UNIVERSITÀ DEGLI STUDI DI TORINO

PhD. Course in Earth Sciences, XXXV Cycle

PhD. Thesis

Sustainability of emissions of an energy- from-waste plant: from CO_2 emissions to bottom and fly ashes, towards their reduction and/or valorization

PhD Candidate: Davide Bernasconi

Supervisor: Prof. Alessandro Pavese

A.A. 2019-2023

Summary

The overwhelming increase of municipal solid waste production, due to the ever-growing urbanization, has prompted the communities to find some solutions. One of them is represented by Waste-to-Energy (WtE) plants, which can recover energy by the incineration of wastes, also allowing a drastic reduction of their volume and mass. However, the process is not perfect, and secondary pollutants are delivered, both solid (i.e., bottom and fly ash, BA and FA) and gaseous (i.e., CO_2), which must be dealt with. This thesis is divided into three main sections, involving all three of the main secondary wastes of a typical MSW WtE plant. In particular, the research effort has been devoted to tackle the management of BA and FA, since their direct recycle in building materials is hampered by their high content of potentially toxic elements (PTEs) like Cu, Cr, Zn, Pb, etc., and their associated anions (chlorides and sulfates).

The first section employs previous research done on the mineralogical and chemical characterization of Turin WtE plant BA as a function of particle size (*s*) to define subclasses for which different combinations of treatments were tested. The coarser BA are composed by mostly inert material (such as ceramics, aggregates, etc..) and do not require strong treatments to meet the law limits for direct reuse in building materials technologies according to Italian law, and for these categories ($s > 1$ mm) a novel steam washing treatment was investigated. Overall, 60 wt% of BA was effectively recovered thanks to a combination of mild dissolution and removal of the dust on the BA grains, together with a relevant reduction of wastewater volume, in the order of 95-98 vol% with respect to the common water washing treatment with L/S around 5-10. On the other hand, the finer fractions are more prone to dangerous leaching and are more difficult to stabilize completely. In this case, an accelerated carbonation method was tested, which was effective in curbing the heavy metals leaching, but did not allow to reach the law limits for chlorides and sulfates.

The second section comprises at first the analysis of the chemical speciation, distribution, and leaching behavior of PTEs as a function of particle size in Turin WtE plant BA. The combination of mineralogy, sequential extractions and geochemical modelling allowed to highlight how the leaching of dangerous heavy metals is dependent more on their speciation rather than simply on the total content. Indeed, heavy metal leaching is strongly correlated to speciation distribution, and in particular to the fraction (F1) associated with salt, carbonate and weak surface sorption. Since the F1-speciation as a function of particle size did not exhibit a definite trend shared by all heavy metals, no grain size separation strategies were used to optimize the following treatments. Then, a multiple-step water washing was assessed by comparison with the conventional batch water washing. A sequential extraction method and dissolution kinetics modelling suggested that the treatment is dominated by kinetics factors, which significantly differs from the conventional washing that takes place at quasi-equilibrium conditions. Although it was effective in reducing pollutants under the legal limits for non-hazardous waste disposal, by using comparatively reduced wastewater and time, the legal limits for non-reactive couldn't be completely reached, owing to the excess release of sulfate and some heavy metals (Cr, Ni). Finally, the washed FA was evaluated as a precursor in phosphate-based materials. This choice was performed due to the good compatibility between phosphate and heavy metals, since the related salts are characterized by a very low K_{sp}. When FA substituted metakaolin in phosphate geopolymer, a progressive decrease of the mechanical properties was observed (up to 75%), which was correlated to its different reactivity in the system conditions, behaving preferentially as a source of alkali that compete with the metakaolin aluminosilicate fraction by precipitating crystalline and amorphous phosphates. Overall, a 10 wt% of metakaolin substitution was found optimal in terms of mechanical properties retention. A similar reactivity was found when FA were introduced into magnesium phosphate cement, although much more limited as the system conditions were less harsh (pH 5 against 1-2). An extensive spectroscopic analysis demonstrated that FA heavy metals become bound to phosphate, which translated into an efficient reduction of heavy metals leaching, thus proving that magnesium phosphate cement can be a promising matrix for treated FA encapsulation.

The third section deals with the thermal stability of weddellite crystals from a new and green method for CO_2 capture and sequestration in stable calcium oxalate by ascorbic acid reducing action. This is crucial to estimate their reuse as solid-state reservoir of pure carbon dioxide and CaO in a circular economy perspective. The combination of *in-situ* high-temperature X-ray powder diffraction and thermogravimetric analysis allowed the definition of three temperature ranges where CO_2 evolved, but only the latter one in pure form (above 550 °C), while for the other two a mixture with water and CO was observed, respectively for 119–255 °C and 390–550 °C. In these cases, a gas separation technology should be used to concentrate the CO_2 for standard application.

List of publications

The PhD work has been performed at the Earth Sciences Department of the University of Turin (Italy) between 2019-2023, and at the Institute of Theoretical and Applied Mechanics of the Czech Academy of Sciences, Centre Telč (Czech Republic) (October-November 2021, July 2022). The PhD work described in this thesis is the results of the following publications:

1. Destefanis, E.; Caviglia, C.; Bernasconi, D.; Bicchi, E.; Boero, R.; Bonadiman, C.; Confalonieri, G.; Corazzari, I.; Mandrone, G.; Pastero, L.; Pavese, A.; Turci, F.; Wehrung, Q. Valorization of mswi bottom ash as a function of particle size distribution, using steam washing *Sustainability (Switzerland)* **2021**, 12, 1–17.

2. Caviglia, C.; Destefanis, E.; Pastero, L.; Bernasconi D.; Bonadiman C.; Pavese, A. MSWI Fly Ash Multiple Washing: Kinetics of Dissolution in Water, as Function of Time, Temperature and Dilution. *Minerals* **2022**, 12, 742.

3. Bernasconi, D.*; Caviglia, C.; Destefanis, E.; Agostino, A.; Boero, R.; Marinoni, N.; Bonadiman, C.; Pavese, A. Influence of speciation distribution and particle size on heavy metal leaching from MSWI fly ash. *Waste Management* **2022**, 138, 318–327.

4. Curetti, N.; Pastero, L.; Bernasconi, D.; Cotellucci, A.; Corazzari, I.; Archetti, M.; Pavese, A. Thermal stability of calcium oxalates from CO_2 sequestration for storage purposes: An in-situ ht-xrpd and tga combined study. *Minerals*. **2022**, *12*, 53.

5. Bernasconi, D.*; Viani, A.; Zarybnicka, L.; Macova, P.; Bordignon S.; Caviglia, C.; Destefanis, E.; Gobetto, R.; Pavese, A. Phosphate-based geopolymer: Influence of municipal solid waste fly ash introduction on structure and compressive strength. *Ceramic International* **2023**, 138, 318–327.

6. Bernasconi, D.*; Viani, A.; Zarybnicka, L.; Macova, P.; Das, G.; Borfecchia, E.; Bordignon S.; Stefancic, M.; Caviglia, C.; Destefanis, E.; Gobetto, R.; Bernasconi A.; Pavese, A. Investigation of MSWI fly ash reactivity into Mg phosphate cement. *in preparation*.

During the PhD, other side-projects and collaborations resulted in the following publications:

7. Bernasconi, D.; Bordignon, S.; Rossi, F.; Priola, E.; Nervi, C.; Gobetto, R., Voinovich, D.; Hasa, D.; Duong, N.T.; Nishiyama, Y.; Chierotti, M.R. Selective synthesis of a salt and a cocrystal of the ethionamide- salicylic acid system. *Crystal Growth & Design* **2020**, *20*, 906-915.

8. Curetti, N.; Bernasconi, D.; Benna, P.; Fiore, G.; Pavese, A. High-temperature ramsdellite–pyrolusite transformation kinetics. *Physics and Chemistry of Minerals* **2021**, *48*, 43

9. Tonon, C.; Bernasconi, D.; Martire, L.; Pastero, L.; Viles, H.; Favero-Longo, S.E. Lichen impact on sandstone hardness is species-specific. *Earth Surface Processes and Landforms* **2022**, 47, 1147-1156.

10. Bernasconi, A.; Bernasconi, D.; Sartori, R.; Francescon, F.; Pavese, A. Fine Fireclay (FC) technological properties and mineralogy by tuning body composition and raw materials particle size distribution. *Ceramic International* **2023**, accepted.

During the PhD, the following conferences have been followed:

Oral presentations

- C. Caviglia, E. Destefanis, L. Pastero, N. Curetti, D. Bernasconi, R. Boero, A. Pavese. "*Carbon Dioxide fixation into minerals*". First Italian Conference on Carbon Dioxide Capture and Utilization, 5-6 December 2019, Bari (ITALY).

- D. Bernasconi, C. Caviglia, E. Destefanis, L. Pastero, C. Bonadiman, A. Pavese, A. Agostino, R. Boero. "*Insight into municipal solid waste fly ash (MSWFA) heavy metals speciation by selective extractions and geochemical modelling*". 23rd EGU General Assembly Conference, 25-30 April 2021, Vienna (AUSTRIA). (*online*)

- N. Curetti, D. Bernasconi, P. Benna, G. Fiore, A. Pavese. "*Kinetic of high-temperature ramsdellite-pyrolusite transformation*". 3rd European Mineralogical Conference, 28 August- 2 September 2021, Cracovia (POLAND). (*online*)

- D. Bernasconi, A. Viani, P. Mácová, L. Zárybnická, C. Caviglia, E. Destefanis, S. Bordignon, R. Gobetto, A. Pavese. "*MSWI fly ash incorporation into acid-based geopolymer: reactivity and performance impact*". 24th EGU General Assembly Conference, 23-27 May 2022, Vienna (AUSTRIA) (*online*)

Poster presentations

- D. Bernasconi, C. Caviglia, E. Destefanis, A. Viani, L. Pastero, R. Boero, N. Marinoni, C. Bonadiman, R. Gobetto, A. Pavese. "*Fly ash from Turin municipal solid waste incineration plant: characterization and treatments towards its revalorization*". International EMU-SIMP school "Minerals and waste" (MINEWA), 20-24 June 2022, Bardonecchia, ITALY.

- D. Bernasconi, Viani, A.; Zarybnicka, L.; Macova, P.; Das, G.; Borfecchia, E.; Bordignon S.; Stefancic, M.; Caviglia, C.; Destefanis, E.; Gobetto, R.; Bernasconi A.; Pavese, A. "*Investigation of Municipal Solid Waste Fly Ash Reactivity into Magnesium Phosphate Cement*". 25th EGU General Assembly Conference, 23-28 April 2023, Vienna (AUSTRIA).

Ringraziamenti

Il mio primo ringraziamento va ai miei genitori, per avermi dato la possibilità di seguire il mio interesse per la ricerca e di concentrarmi su questo corso di dottorato, mostrando molta pazienza durante i periodi di frustrazione che ho attraversato. Ringrazio inoltre il professor Alessandro Pavese, per avermi concesso questa opportunità senza conoscermi in precedenza, spronandomi quando le cose non andavano e per avermi insegnato come la serietà e l'impegno siano fondamentali per l'attività di ricerca. Ringrazio Linda Pastero e Nadia Curetti, le "mamme della diffrazione", per avermi insegnato moltissimo sulla diffrazione di raggi X da polveri e (invano) da cristallo singolo e, in generale, aver sopportato le cavolate che ho fatto e continuo a fare in laboratorio. Ringrazio ancora Enrico e Caterina, per aver condiviso con me le (poche) gioie e (tanti) dolori nel lavorare con le ceneri e per le innumerevoli pause caffè per staccare dai bassifondi del dipartimento. Ringrazio Alberto Viani, che mi ha dato un'assistenza incredibile durante l'autunno in Cechia, rendendo meno solitaria la trasferta, oltre ad avermi insegnato molto sulla mineralogia applicata ai materiali e a continuare a supportare il mio lavoro, condividendo anche di persona l'attività di ricerca.

Ringrazio il mio compare di laboratorio Andrea Cotellucci, anche lui chimico in un mare di geologi, con cui ho condiviso la maggior parte del dottorato e infinite chiacchierate e pettegolezzi. Aggiungo anche Quentin Wherung, che seppur unitosi successivamente, ha dato il suo importante contributo sia in laboratorio che nei momenti di cazzeggio. Ringrazio poi tutti gli altri dottorandi che ho conosciuto a Scienze della Terra, in particolare Stefano, Chiara, Alessandro, Andrea, Claudio e Luca, che non mi hanno mai fatto sentire escluso, nonostante venissi da un altro dipartimento.

Non posso dimenticare poi i compari di chimica, con cui, anche se a distanza, ho condiviso questi anni di dottorato. In particolare, ringrazio Luca, il quale ha sopportato con pazienza quando salivo dalle sue parti per disturbare quando volevo staccare, e Davide, con cui ho condiviso innumerevoli caffè mattutini, spritz, e in generale attività di relax fondamentali per la salute mentale. Ringrazio poi Lele e Alessia, per le chiaccherate e i numerosi consigli per gestire i momenti critici.

Ringrazio gli NMRsti, in particolare il professor Roberto Gobetto, che ha fatto da tramite con il professor Pavese all'inizio di questa avventura e che mi ha seguito durante la mia prima attività di ricerca durante la tesi magistrale. E Simone, per la pazienza e supporto infiniti.

Ovviamente ringrazio la vecchia banda del liceo, Andre, Simo, Antimo, Laur e Dragos, con cui, anche se separati da strade e scelte di vita differenti, rimaniamo ancora il cuore di quella 1C liceo Avogadro.

Infine, ringrazio tutte le persone incontrate durante questo lungo viaggio di 4 anni, e che chi più chi meno, hanno dato un contributo insostituibile alla mia esperienza.

List of Contents

Chapter 1: Introduction

Chapter 2: Materials and Methods

Chapter 3: Valorization of MSWI Bottom Ash as a function of particle size distribution, using steam washing

Chapter 5: MSWI fly ash multiple washing: kinetics of dissolution in water, as function of time, temperature and dilution

Chapter 6: Influence of MSWI-FA introduction on metakaolin phosphate-based geopolymer structure and mechanical properties

Chapter 7: Investigation of MSWI-fly ash reactivity in Magnesium phosphate cement

Chapter 8: Thermal Stability of Calcium Oxalates from CO_2 Sequestration for Storage Purposes: An In-Situ HT-XRPD and TGA Combined Study

Chapter 9: Conclusions and Recommendations

Chapter 1

Introduction

1.1 Background

Municipal solid waste (MSW) represents the leftovers which are generated in urban areas from residential, commercial, institutional, and municipal services sources. The nature and composition of MSW can vary depending on several factors, such as the location, economic and social conditions, and the level of development of the community and therefore can change over time [1,2]. Typically, MSW is composed by a heterogeneous mixture of different types of materials, including: organics, such as food and yard waste, and paper products, which make up the largest portion of MSW, usually around 30-50% in mass or volume; inorganic materials, as plastics, metals, glass, and ceramics, which account for 15-25% of MSW; hazardous materials, such as batteries, pesticides, and medical waste, which make up a small but significant portion of MSW, typically around 1-2%, while the remainder portion is comprised by textiles, rubber, and wood [2,3]. The composition of the global MSW in 2020 is provided in Figure 1.1, in comparison with the one produced in Italy in the same year.[4]

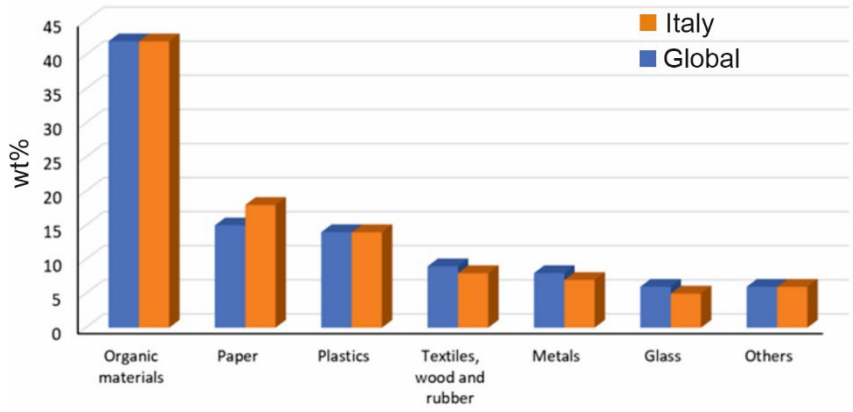

Figure 1.1 Municipal solid waste composition in the world (blue) and Italy (orange) during 2020 [4].

Regardless of its composition, the total MSW production is steadily growing, due to the increase of the world population (which is expected to reach nearly 10 billion by 2050 according to ONU), that is associated to further urbanization and anthropogenic activities. Currently, according to the World Bank, the amount of MSW being produced globally in a year (estimated in 2016) is at least 2.01 billion tonnes, while by 2050 this is expected to increase up to 3.40 billion tons [5]. Such amount can lead to concerns involving public health hazards and environmental degradation, in terms of release of pollutants and greenhouse gases [1,5]. Moreover, the impact on the quality of life and the public image of a community (i.e., “social costs”) are not to be underestimated [5]. Therefore, it is essential to implement effective waste management strategies that on one hand aim to prevent these problems and on the other hand ensure the safe and sustainable disposal of MSW. The traditional approach to MSW disposal has been to bury it in landfills, usually due to relatively economic realization and maintenance costs. However, this method has several drawbacks, in terms of contamination of soil and groundwater and production of greenhouse gases, together with the intrinsic volume limitation as it depends on the available land [6]. Moreover, landfill as the final destination of the waste is strongly contradicting the circular economy principles that many institutions are implementing, since it does not

provide the materials reintroduction into the productive cycle [7]. As a result, there is increasing pressure on municipalities to find more sustainable solutions.

In Europe, the European Union Waste Framework Directive of 2008 establishes a waste management hierarchy that prioritizes different methods and politics according to their environmental impact (Figure 1.2) [8,9]. The first and most important step is to prevent the generation of waste in the first place, by reducing the consumption of products, designing products for a longer lifespan, and encouraging the use of more sustainable materials. Secondly, to reuse materials and products as much as possible, by repairing or using the products for a different purpose. The third step consists in the recycle of materials and products, through a careful collection and processing of waste materials so that they can be used to make new products. Then, the recovery of energy from waste through incineration (Waste-to-Energy, WtE), i.e., by burning MSW to generate heat and electricity. The final step is to dispose of waste that cannot be prevented, reused, recycled, or used for energy recovery, through landfilling [8]. According to Eurostat, the use of different strategies for managing MSW in the EU-28 during 2020 involved mainly recycling and composting (47%), followed by incineration (29%) and landfilling (24%), with significant scattering between the countries [10]. The northern Member States (i.e., Denmark, Germany, Belgium, Sweden) have almost completely abandoned the landfill strategy (0-5 %), while in the southern-eastern Member States (i.e., Hungary, Romania, Greece, Spain, Slovakia) it is still a relevant practice (40-80%). In Italy the situation is similar to the European average, with distribution of 48% recycling, 25% incineration and the remainder as landfilling [10].

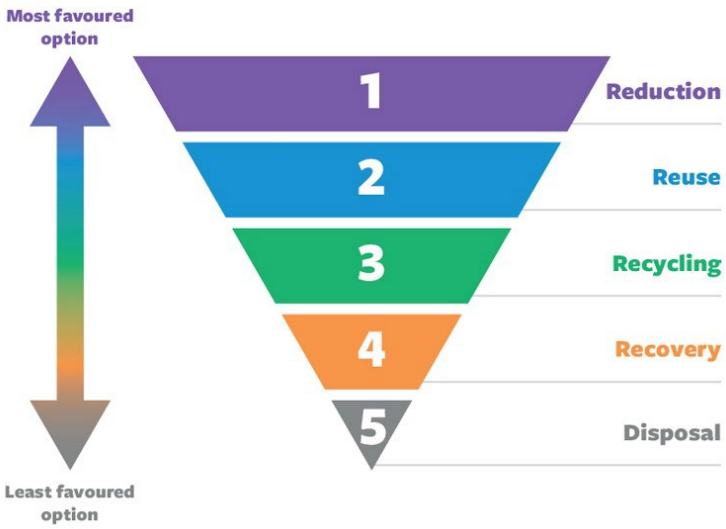

Figure 1.2 Waste management hierarchy [8].

1.2 Waste-to-Energy plant

One potential solution for a more sustainable MSW disposal is represented by the Waste-to-Energy plants, whose diffusion has been favored by the many advantages related to their use: important reduction of the waste mass (75%) and volume (90%); destruction of organic pollutants as temperatures above 800°C are reached; possibility to recover materials and energy from wastes that otherwise would be dumped in landfills; limited space is employed, which can be reuse after the plant end life [6]. In Italy, the use of WtE plants for waste management counts a total of 43 operative plants, which treat around 8 million tons of MSW per year [11]. However, the diffusion of WtE plants in Europe, and in Italy, brought some controversy. Indeed, the incineration process is not perfect, and secondary pollution is produced, both solid (i.e., ashes) and gaseous (i.e., CO_2) [12]. These concerns about the environmental and health impacts of incineration, together with relatively high realization and maintenance costs, have prompted the European Union to establish several policies and regulations to

govern the incineration of MSW, to set out specific provisions for the incineration process, including emissions limits for pollutants such as dioxins and heavy metals (Potentially Toxic Elements, PTEs) [8]. At the same time, until the circular economy principles of waste prevention and reuse are fully assimilated by the communities and productive system, this strategy remains a relevant alternative to landfill in dealing with non-recyclable MSW [6]. Therefore, it is fundamental to invest time and resources into the study of incineration secondary wastes, in terms of their chemical/physical characteristics and recycle opportunities.

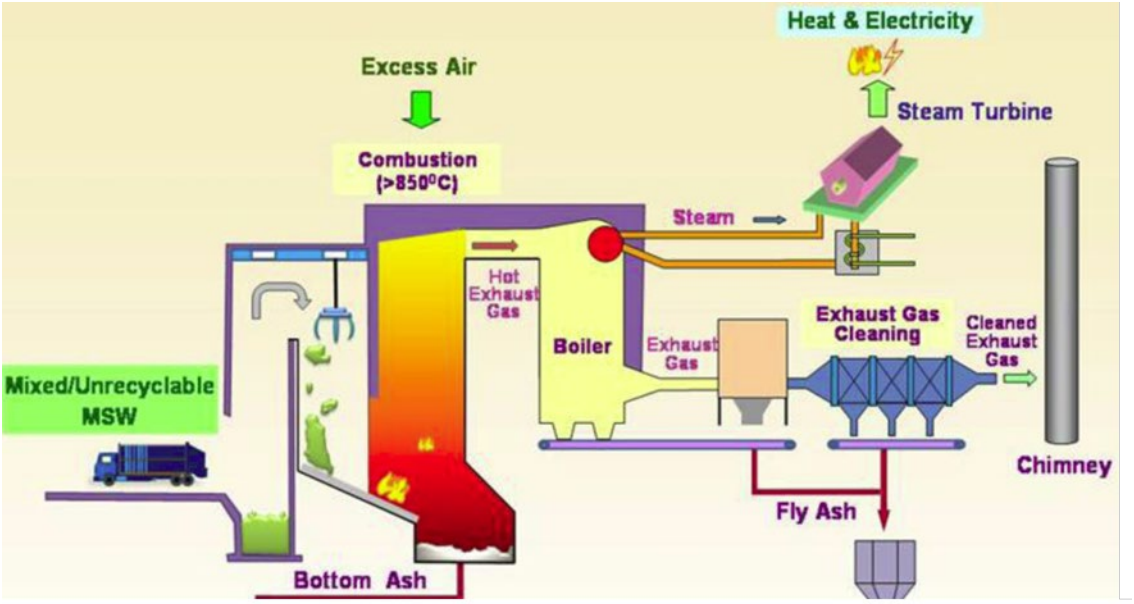

Figure 1.3 General scheme of a WtE plant [13].

In Figure 1.3, the schematic diagram of a typical MSW WtE plant is presented [13]. After being collected and separated from the recyclable portion, the MSW is usually incinerated in a grate-firing furnace, but other incineration techniques exist, such as fluidized-bed firing and rotary-kiln system [14]. The firing temperature lies typically between 850-1000°C, where primary air is blown continuously into the bed from the bottom. The incineration of MSW is a mixed process of gas-phase combustion and heterogeneous combustion: the initial step is a drying phase, whose duration depends on the moisture content of the MSW feed; then, the thermal decomposition starts, involving volatilization and decomposition reactions of the combustible substances in MSW, which generate a variety of volatile hydrocarbons and carbon sequestration products; finally, at high temperatures, the gaseous and solid combustible substances produced by drying and thermal decomposition become flame and start the combustion of the remainder portion. The hot flue gas produced in the combustion chamber is converted in steam and electricity through a boiler [13,14]. The volatile compounds, along with dust particles, are transported through the flue gas, which is purified using a multi-stage cleaning system. Fly ash particles enriched in heavy metals, salts and organic pollutants are collected at the heat recovery section or removed from the flue gas by fabric filters or electrostatic precipitators [13]. Water is injected directly into the flue gas for wet flue gas cleaning where mainly HCl, HF and NH_3 are removed (acidic scrub water). In a second step, NaOH is added to remove SO_x as sodium sulphate solution (neutral scrub water). The combustion of plastics and organics produces also CO_2, which usually accounts for 10-12% vol of flue gas [13]. Overall, the waste incineration process results in the production of two main solid residues: bottom ash and fly ash.

1.2.1 Bottom ash

Bottom ash (BA) comprises a major part of the solid residues remaining after waste incineration (around 23% wt of the initial MSW mass) [15]. The BA represents the unburnt fraction that remains at the bottom of the combustion chamber, and after it is collected it is usually quenched with water. The chemical composition of BA is highly dependent on the waste feed and the elemental partitioning occurring during incineration, while the particle size distribution is quite wide, spanning from above 10 millimeters to tens of micrometers. In general, it is enriched of high boiling points elements (Table 1.1; i.e., Si, Ca, Al, Fe or Ti), that are mostly not volatilized during incineration [14]. Due to the high temperature conditions mainly silicate and aluminosilicate glasses and minerals are formed, although most reactions are not completed, due to the short incineration process (30 min-1 h). Indeed, BA doesn't reach a thermodynamic equilibrium state and for this reason its mineralogical composition is dominated by an amorphous glass fraction (70-90% wt.) [14,15]. The crystalline phases can be divided into refractory minerals which are already present in the waste input (e.g. quartz, feldspars, ceramics) and minerals formed during the incineration process or the cooling step (e.g. melilites, wollastonite, lime) [14,16]. Although BA is considered as a non-dangerous waste, it still requires some management treatments before being used as supplementary filler material for example in road constructions (applied in the Netherlands and France), as the kinetically interrupted transformations leave a relatively unstable material, potentially prone to releasing PTEs (i.e., Cu, Ni, Pb) [14-16].

1.2.2 Fly ash

Fly ash accounts for around 2% wt. of the waste input mass and forms in the flue gas purification system, consisting mainly of aluminosilicates, oxides, soluble salts, heavy metals and residual toxic organic compounds [13-15]. In particular, atmophile/biophile heavy metals (Table 1.1; i.e., Zn, Hg, Pb and Cd) tend to concentrate in FA as leachable species, together with halogens, sulfur and alkali. This is related to the vaporization (i.e., Zn-Cd-Pb chloride: 800-1000 °C) and condensation/crystallization reactions that take place at the firing stage and during the flue gas purification process, respectively [13]. When the flue gas temperature decreases, the volatilized elements may undergo homogeneous nucleation reactions due to supersaturation, or they may condense heterogeneously on the surface of ash particles and filters. This is favored by higher furnace temperatures, which increases the amounts of dust particles, as well as elevated chlorine and sulphur concentration in the flue gas [14,15]. The relevant Cl content in FA (10 wt.%) originates mostly from the combustion of plastics (PVC). Due to the high concentration of pollutants, together with the comparatively small particle size (from 10 to 200 μm) with respect to BA, fly ash is often considered a hazardous waste, and has to be disposed under strict regulations and at great costs or has to be treated properly [15].

Table 1.1 Average chemical composition of BA and FA [13].

	Concentration (mg/kg)	
Element	**Bottom ash**	**Fly ash**
Al	22'000 - 73'000	49'000 - 90'000
As	0.1 - 190	37 - 320
Ba	400 - 3'000	330 - 3'100
Ca	370 - 123'000	74'000 - 130'000
Cd	0.3 - 70	50 - 450
Cl	800 - 4'200	29'000 - 210'000
Cr	23 - 3'200	140 - 1'100
Cu	190 - 8'200	600 - 3'200
Fe	4'100 - 150'000	12'000 - 44'000
Hg	0.02 - 8	0.7 - 30
K	750 - 16'000	22'000 - 62'000
Mg	400 - 26'000	11'000 - 19'000
Mn	80 - 2′400	800 - 1′900
Mo	2 - 280	15 - 150
Na	2'800 - 42'000	15'000 - 57'000
Ni	7 - 4'200	60 - 260
Pb	100 - 13'700	5'300 - 26'000
S	1'000 - 5'000	11'000 - 45'000
Sb	10 - 43	260 - 1'100
Si	91'000 - 308'000	95'000 - 210'000
V	20 - 120	29 - 150
Zn	610 - 7'800	7'000 - 70'000

1.3 Research aim and strategy

In this thesis, the research effort has been devoted to tackle the management of the two main solid wastes of a typical MSW WtE plant (Turin Gerbido WtE plant, Italy), i.e., BA and FA, both of which are affected by pollutants release tendency. In particular, the attention has been focused in correlating the PTEs leaching behaviors with the ash mineralogical and chemical characteristics, by using a sieving pretreatment that can help in optimizing and tuning the related treatments. In addition, the curbing methods here employed have been designed with the aim of exploiting resources already available by the plant (i.e., steam) and successfully treating as much BA/FA portions as possible. Moreover, since a portion of the plant emissions consists in CO_2, part of the research activity has been dedicated on assessing the thermal stability of the calcium oxalate crystals obtained by a new and green method for carbon dioxide capture and sequestration with oxalic acid. The main work of this thesis can be divided into three distinct sections, as follows:

1. The first section deals with the mineral and chemical characterization of Turin WtE plant BA as a function of particle size and describes the application of a novel steam washing treatment on the coarser fraction (particle size> 1 mm), while an accelerated carbonation method is tested on the remainder portion.

2. The second section describes the approach used in the study of Turin WtE plant FA, which involved at first the analysis of chemical speciation, distribution and leaching behavior of PTEs as a function of particle size, followed by the assessment of a water-washing treatment and then the evaluation of washed FA as a precursor in phosphate-based materials.

3. The third section is about the thermal stability of weddellite crystals from CO_2-capture, to estimate their reuse as solid-state reservoir of pure carbon dioxide and CaO in a circular economy perspective.

The mineralogical/geochemical approach employed during this thesis is supported by the analogies between the MSW incineration ash production and composition and the mineralogical/petrological natural processes and products. For example, the BA oxides composition, in terms of Al, Fe, Si, Ti, K and Na, is very close to the continental crust one. On the other hand, it displays an increased content of Ca, P and other elements (i.e., Cl, Zn, Cu, S, Pb, Br, Mo and Sn), due to the anthropogenic activities that determine an artificial enrichment with respect to the natural processes [16,17].

In the continental crust, the most common mineral phases are a combination of these elements, mainly different types of silicates from magmatic origin: quartz, feldspars, pyroxenes, which also contain Fe and Mg. Moreover, the rocks interaction with the atmosphere (geochemical reactions) can determine further minerogenetic processes, which produce, for example, clay minerals, by weathering of silicate minerals, and carbonates, mostly occurring after reaction with atmospheric CO_2 and H_2O [16]. All these minerals are also present in waste residues, as they are just the results of the transformation of natural resources, and these processes at high or low temperature often mimic those occurring in nature [16,17]. This context has prompted the necessity to extend the term “mineral” from the simple natural crystalline compounds to account for the variety of mineral-like phases observable in wastes [16,17]. Indeed, it is possible to distinguish between natural minerals that do not change throughout the product cycle (i.e., extraction, manufacturing, incineration), like quartz, and artificial minerals that are analogous to natural ones. One example is mullite, which is a main product of ceramic industry but also naturally found in shales included and heated by volcanic magmas [16]. Moreover, one must consider synthetic phases, that can be chemically different but share structural similarities and reactivity with natural minerals, like apatites and perovskites [16]. All these can be observed more or less intact in the incineration residues, as they are characterized by a relevant stability. On the other hand, mineral-like phases of new formation are also present, that have analogous in natural environments, for example melilites and feldspars, together with phases of further weathering (i.e., calcite, ettringite) [16,17]. The main difference with respect to the natural processes is related to the time. Here, the reactions and transformations are extremely more rapid, and far-from equilibrium phases are often formed (i.e., glasses), which are characterized by an higher intrinsic instability that may negatively affect the release of PTEs [16].

Overall, the BA formation by heating the waste to high temperatures shares similarities with contact metamorphism phenomena, although kinetically stopped by the water quenching [16]. At the same time, the FA condensation during the cooling of the hot flue gas can be compared to (pseudo)pneumatolytic processes. The PTEs leaching behaviors can be compared to natural weathering and minerals-environment interactions [16,17]. All this points to handle the study of these wastes using the same tools employed in the study of natural materials (i.e., rocks, minerals, volcanic glasses) and provides hope for their possible revalorization as secondary raw materials.

1.4 Outline of the thesis

The outline of the thesis and the connections between the main chapters are given in Figure 1.4. The thesis work is divided into three different sections, while a summary of the content of each chapter is provided as follows:

Chapter 2 describes the sampling of the MSWI ash from the Turin plant and provides the experimental details about the main characterization techniques and analytical methods employed. Additional information is provided in each chapter for more specific materials and methods.

Chapter 3 provides initially the BA characterization trends as a function of particle size, in terms of minerals, chemical composition and PTEs leaching. Then, the steam washing method is described and its effectiveness on the treatment of the coarser BA fraction is evaluated by leaching tests, while details of its mechanism of action are inferred by microscopy and X-ray absorption spectroscopy. Finally, an accelerated carbonation treatment on the finer fraction is applied and discussed.

Chapter 4 summarizes the FA characterization trends as a function of particle size, in terms of minerals, chemical composition and PTEs leaching. In addition, the speciation distribution of selected heavy metals is determined, together with their pH-dependent leaching profiles, to evaluate what are the key parameters affecting their release. On this basis, the potential benefit of a sieving pretreatment in managing FA is discussed.

Chapter 5 describes the phenomenology associated with a water washing multi-cycle treatment of FA. The effect of temperature, water-to-solid (L/S) ratio, and number of washing cycles is assessed for the removal of salt and PTEs, while further information to interpret the leaching process is provided by a sequential extraction method and dissolution kinetics modelling.

Chapter 6 summarizes the results about the introduction of washed MSWI fly ash into metakaolin phosphate-based geopolymers, a recycling opportunity. A complete structural analysis of the resulting materials is provided through a combined spectroscopical, diffractometric and morphological approach. The information so derived about the FA role in the system is then used to interpret the observed differences on the mechanical properties.

Chapter 7 provides the analysis of the filler/active role of washed FA when added in the mixture for the preparation of magnesium phosphate cement. The potential reactivity of FA grains is discussed by employing a combination of different spectroscopies, while its effect on the cement system is evaluated by calorimetric and morphological techniques and compressive strength measurements.

Chapter 8 discusses the thermal decomposition of weddellite obtained from the oxalate carbon capture method, by coupling in-situ high-temperature X-ray powder diffraction and thermogravimetric analysis, to evaluate the dehydration, decarbonation, and the possible production of unwanted volatile species during heating.

Chapter 9 gives an overview of the conclusion derived from this thesis. Additionally, recommendations regarding future research are presented.

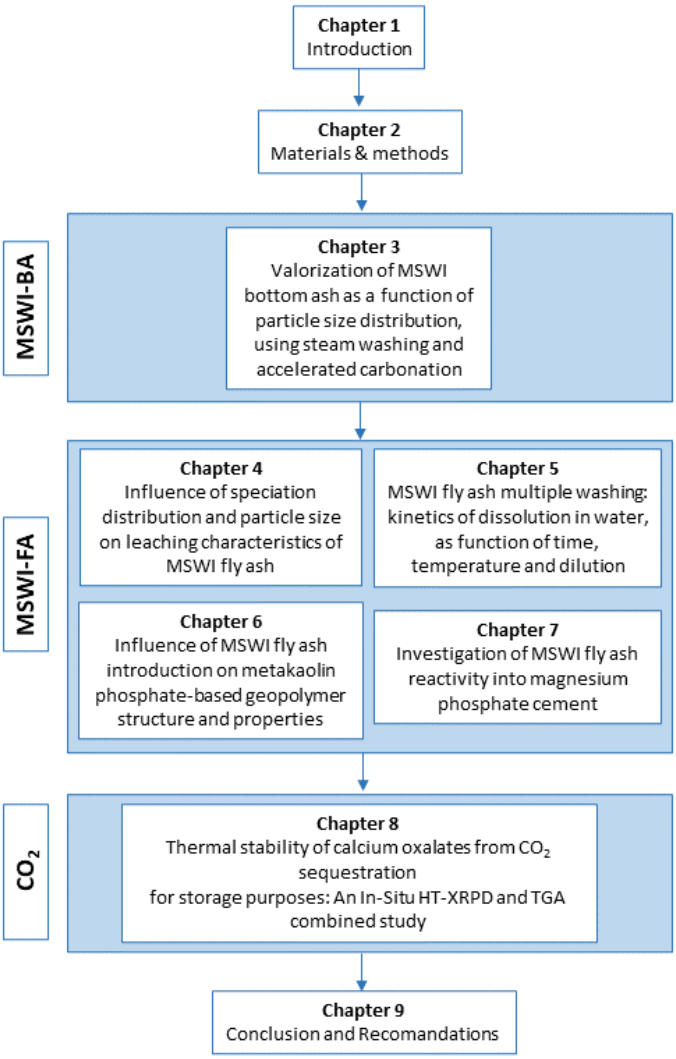

Figure 1.4 Outline of the thesis

1.5 References

1. Edjabou, M.E.; Takou, V.; Boldrin, A.; Petersen, C.; Astrup, T.F. The influence of recycling schemes on the composition and generation of municipal solid waste. *J. of Cleaner Prod.* **2015**, 295.
2. Chen, Y.C Effects of urbanization on municipal solid waste composition. *Waste Manag.* **2018**, 79, 828-836.
3. Edjabou, M.E.; Jensen, M.B.; Götze, R.; Pivnenko, K.; Petersen, C.; Scheutz, C.; Astrup, T.F. Municipal solid waste composition: Sampling methodology, statistical analyses, and case study evaluation. *Waste Manag.* **2015**, 36, 12-23.
4. U.S. Environmental Protection Agency, https://www.epa.gov/.
5. Kaza, S.; Yao, L. C.; Bhada-Tata, P.; Van Woerden. F. *What a Waste 2.0 : A Global Snapshot of Solid Waste Management to 2050.* Washington, D.C.: World bank. **2018**. isbn: 9781464813290.
6. Hussein, I.A.S.; Mona, S.M.M. Solid waste issue: Sources, composition, disposal, recycling, and valorization. *Egyptian J. of Petrol.* **2018**, 27, 1275-1290.
7. European Commission. *Closing the loop - An EU action plan for circular economy*. **2015**.
8. European Council. "Directive 2008/98/EC." In: Official Journal of the European Union 56.C 378 (**2013**), pp. 1–44.
9. Scarlat, N.; Fahl, F.; Dallemand, J.F. Status and Opportunities for Energy Recovery from Municipal Solid Waste in Europe. *Waste and Biomass Valor.* **2019**, 10, 2425-2444.
10. Eurostat. *Treatment of waste by waste category, hazardousness and waste management operations - Eurostat*. **2021**. url: https://ec.europa.eu/eurostat/web/products- datasets/- /env_ wastrt.

11. ISPRA, https://www.catasto-rifiuti.isprambiente.it/index.php?pg=.
12. Makarichi, L.; Jutidamrongphan, W.; Techato, K. The evolution of waste-to-energy incineration: A review. *Renew. and Sustain. Energy Rev.* **2018**, 812–821.
13. Niessen, W.R. *Cobustion and Incineration processes.* C.R.C. Press. **2002**. isbn: 9780824706296.
14. Chandler, A.j. *Municipal Solid Waste Incinerator Residues.* Elsevier Science. **1997**. isbn: 9780080537184
15. Youcai, Z. *Municipal Solid Waste Incineratoion: Bottom and Fly Ash.* Elsevier Science. **2017**. isbn: 9780128121658.
16. Tribaudino, M.; Vollprecht, D.; Pavese, A. *Minerals and Waste.* Springer. **2023**. isbn: 978-3-031-16134-6.
17. Dijkstraa, J.J.; Comans, Rob N.J.; Schokker, J.; van der Meulen, M.J. The geological significance of novel anthropogenic materials: Deposits of industrial waste and by-products. *Anthopocene* **2019**, 28, 100229.

Chapter 2

Materials and Methods

2.1 Bottom and fly ash

BA was provided by the municipal solid waste incinerator of the metropolitan area of Turin (Northern Italy, Figure 2.1). Bottom ashes were collected at the plant after cooling, from a falling stream of wet material, for a total of 20 kg, thus obtaining a general sample. Each general sample was first homogenized by stirring; then, divided by mechanical quartering, using a riffle splitter [1,2], to have representative subsamples, each one of 2 kg. A total of three representative subsamples were prepared. The residual water content, around 17 %wt, was obtained by measuring the difference by weight between pristine BA, and BA after drying at 105 ◦C for 24 hours (Figure 2.1, left).

Approximately 6 kg of FA from the MSWI plant of Turin (Northern Italy) were sampled during a period of six weeks, to cover the seasonal fluctuations of the urban waste production. The in-situ sampling relies on mechanical homogenization of 100 kg of FA, from which sub-samples are obtained by quartering. Given the fine particle size (<0.5 mm), sub-samples of 2 kg are representative, according to [3]. The samples, initially stored in polyethylene bottles at room temperature, were then mixed and homogenized by a riffle splitter, avoiding mechanical crushing and milling. They were eventually dried in an oven at 105°C for 24 hours. FA sample batches of about 100 g were prepared by quartering for leaching tests, chemical and mineralogical analyses.

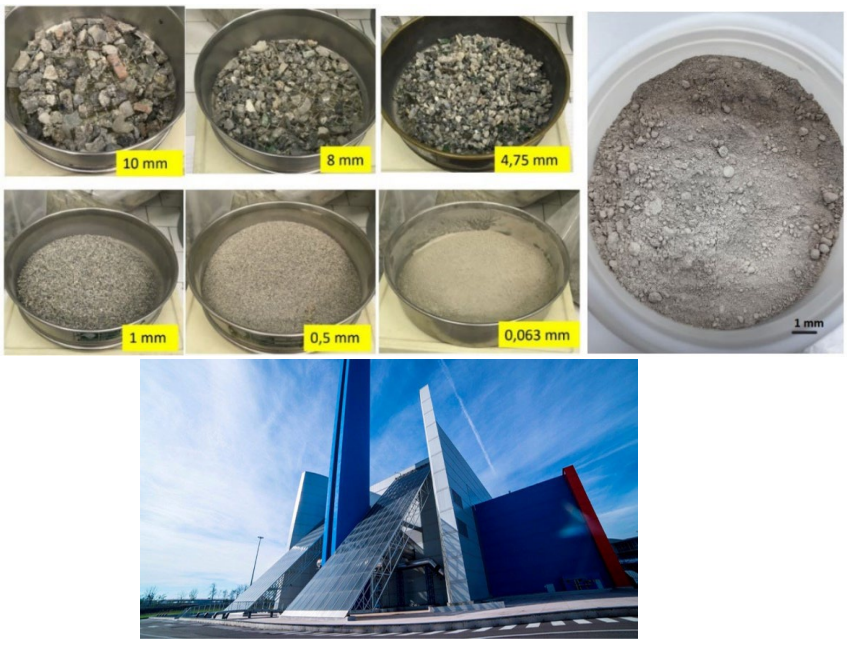

Figure 2.1 Examples of BA after sieving (top, left) and FA (top, right). Turin WtE plant (bottom).

2.2 X-ray Powder Diffraction (XRPD)

The mineralogical composition was determined using a para-focusing geometry Rigaku Miniflex 600, with Cu-Kα incident radiation and operating at 40 kV-15 mA. The diffractometer is equipped with a D/teX 250 silicon strip 1D detector and an optic configuration consisting of a fixed divergence slit

(1/2°) and anti-scatter slit (1/2°). XRPD patterns were collected on pre-dried powdered samples between 3° and 70° 2θ, with a 2θ-step size of 0.02 and scan speed of 0.5°/min, using a side-loading zero-background sample holder. The amorphous phase content was inferred by Rietveld analysis, using high purity calcined α-Al2O3 or ZnO as an internal standard (10-15 wt%). Data refinements were carried out by the software GSASII [4]. The Rietveld strategy involved the refinement of 12-15 Chebyshev polynomial background coefficients, sample displacement parameter, cell parameters, phase fractions, isotropic crystal size and isotropic micro-strain of each phase. When necessary (i.e., gypsum), preferential orientation has been accounted for using MD or spherical harmonics corrections. The PDXL2 software (Rigaku) and PDF-4 2020 database enabled the phase identification.

2.3 Scanning Electron Microscope-Energy Dispersive Spectroscopy (SEM-EDS)

Secondary electrons (SE) and back scattered electrons (BSE) analyses were performed by a Scanning Electron Microscope JSM IT300LV High Vacuum – Low Vacuum 10/650 Pa – 0.3–30 kV (JEOL USA Inc.), equipped with SE and BSE detectors (typical experimental conditions: W filament, EHT 15 kV, standard probe current and working distance 7 mm for images and high probe current and working distance 10 mm was employed for chemical analysis in energy dispersive (EDS) mode). Before the analysis, the samples, either in powder or embedded in resin, have been carbon coated. EDS spectra and maps have been acquired and analyzed by AZtec software (Oxford Instruments).

2.4 X-ray Fluorescence Spectroscopy (XRF)

X-ray fluorescence (XRF) allowed the quantification of the element contents ($Z \geq 11$) on dried powdered samples pressed into pellets, using a THERMO Niton XL3T GOLDD, equipped with a Large Drift Detector (LDD), with a surface area of 25 mm^2 , Si chip thickness of 500 µm, energy resolution of 135 eV @ Mn Kα. Accuracy and precision for major elements (above 1 wt%) are ∼3% for Si, Ti, Fe, Ca and K, and ∼7% for Mg, Al, Mn, Na. For minor/trace elements (below 1 wt%), they are better than ∼10%. The used XRF spectrometer operates with an Ag target, maximum current of 100 µA and voltages between 8 and 50 kV. Each analysis was repeated 5 times on 8 mm diameter circular areas, including 4 sequential measurements at different voltages, in combination with 38 filters to improve the response of the material in the energy range of the data collection: main Al / Fe (40 kV); low Cu, 20 kV; high Mo (50 kV); light no filter (8 kV). The XRF spectra were processed by the commercial b-Axil software, derived from the IAEA's QXAS academic software.

2.5 Leaching Test

The batch (static) leaching tests, according to EN 12457-2 [5], was employed for ash samples. More specifically, the test involves the immersion of the powdered samples in ultrapure water solution at natural pH, with a liquid-to-solid ratio set to 10 and 24 hours shaking. Then, the liquid fraction has been filtered through a 0.45 µm pore size membrane and recovered for analysis. The results are then compared to the Italian law limit [6,7].

2.6 Electrolytic conductivity and pH measurements

Electrolytic conductivity and pH-value of the leachates were measured by an EC-meter Mettler Toledo FiveEasy F30 (accuracy ∼0.5% and resolution ∼0.01-1 µS/cm), and a pH-meter Hanna HI2211 (accuracy ∼0.01; calibration at 9.18 and 12.45, and automatic compensation of temperature),

respectively. For in-situ recordings, an ES-2 Decagon Devices probe, with accuracy and resolution of ~10 and ~1 µS/cm, respectively, was employed.

2.7 Ionic Chromatography (IC)

Ion Chromatography (IC) measurements were carried out to measure the major anions and cations in leachates, using a Metrohm 883 Basic IC plus instrument, with a loop of 20 mL, and calibration relying upon 8 analysis spots on a reference sample (detection limit: 10 µg/L). When necessary, liquid samples have been diluted to around 200 µS/cm of electrolytic conductivity.

2.8 Inductively coupled Plasma-Mass Spectrometry (ICP-MS)

Minor and trace element analyses of leachates were measured using an Agilent 7500 ICP-MS. The samples were first filtered through a 0.45 µm pore size membrane, then acidified using a HNO_3 solution and analysed. When necessary, liquid samples have been diluted to around 200 µS/cm of electrolytic conductivity. Accuracy and precision, based on replicated analyses on standards, are estimated as better than 10% for all elements, i.e. above the detection limit (1 ppb).

2.9 References

1. Gerlach, R.W.; Dobb, D.E.; Raab, G.A.; Nocerino, J.M., Gy sampling theory in environmental studies. 1. Assessing soil splitting protocols. *J. Chemometrics* **2002**, 16.
2. Petersen, L.; Minkkinen, P.; Esbensen, K.H. Representative sampling for reliable data analysis: theory of Sampling. *Chemomet. Intell. Lab. Syst.* **2005**, 77, 261–277.
3. CEN -TR 15310-1 technical report. **2006** https://www.nen.nl/en/cen-tr-15310-1-2006-en-38640.
4. Toby, B. H.; Von Dreele, R. B. GSAS-II: the genesis of a modern open-source all-purpose crystallography software package. *J. of Appl. Cryst.* **2013**, 46 544-549.
5. Lin, W.Y.; Heng, K.S.; Nguyen, M.Q.; Ho, J.R.I. Evaluation of the leaching behavior of incineration bottom ash using seawater: a comparison with standard leaching tests. *Waste Manag.* **2017**, 62, 139–146.
6. Ministerial Decree n. 186 Dated 5 April 2006. Regulatory That Modified Ministerial Decree Dated 5 February 1998. Official Gazette n. 115. 19 May 2006. Available online: http://www.gazzettaufficiale.it/eli/gu/2010/12/01/281/sg/pdf (accessed on 9 April 2022).
7. G.U. Ministerial Decree 27/09/2010-Definition of the Criteria of Admissibility of Landfill Waste. Serie Generale n-281. 1 December 2010. Available online: https://www.gazzettaufficiale.it/eli/id/2010/12/01/10A14538/sg (accessed on 9 April 2022).

Chapter 3

Valorization of MSWI Bottom Ash as a function of particle size distribution, using steam washing

3.1 Introduction

BA's bulk chemical and phase compositions are heterogeneous, as both depend on the particle size distribution, which ranges from a few µm to 25 mm. In a previous work, our group has extensively characterized Turin plant BA as a function of their particle size, bringing to light trends in terms of pollutants contents [1]. More in detail, BA exhibits a particle size distribution similar to materials like coarse sands (D_{50} = 4 mm), with about 70 wt% that lies above 1 mm grain size. The definition of 10 classes allowed to recognize a marked Si content decrease upon decreasing grain size, whereas Ca exhibits a reverse trend. Altogether, heavy metals concentration tends to increase in finer BA. All particle size classes display a mineralogical composition dominated by an amorphous phase (>70 wt%), along with minor crystalline components, such as quartz, calcite, cristobalite, Fe oxides, melilite, halite and feldspar. Unburnt/partially burnt materials account for around 3–4 wt%. Electrolytic conductivity measurements in combination with leaching tests suggest gathering the ten subclasses in two, above and below 1 mm grain size, as the latter exhibits around 3 times the release of chlorides and heavy metals (mainly Cu) with respect to the former. The particle size separation is the foundation for a better tuned treatment aimed at improving the BA environmental impact for a variety of application, involving in particular the construction sector, in which BA are commonly employed as sublayer material [1]. Several treatments have been designed to reduce the BA's release of dangerous substances, namely stabilization with cement [2,3], washing with water [4-6], natural and accelerated carbonation (i.e. promoted in a sealed chamber with CO_2 saturated atmosphere) [7], vitrification [8-10]. Specifically, washing with water-based solutions (largely adopted in the Netherlands), in combination with physical separation as a function of particle size, is very effective in removing water soluble salts and reducing concentrations of heavy metals and organic matter. On the other hand, this method generates important volumes of secondary wastewater, that must be dealt with [11-13].

In this context, this study aims to assess the possibility of treating BA by exploiting the incineration process' steam, nowadays only destined for electricity generation and domestic water warming, thus obtaining a much-reduced wastewater volume. In particular, BA is grouped into three main classes: $s \geq 4.75$, $4.75 > s \geq 1$ and $s < 1$ mm. BA ($s \geq 4.75$ mm) is treated by "steam washing" only. Environmental compatibility of BA ($4.75 > s \geq 1$) is improved by means of both steam washing and accelerated carbonation, and attention is paid to expand as much as possible the *s*-range for which steam washing suffices. As for BA ($s < 1$ mm), whose heavy metals content is the largest one, only accelerated carbonation is applied. Accelerated carbonation's efficacy is explored by changing temperature, treatment time and liquid (water)-to-solid (BA) ratio, at a CO_2-pressure of 2 bar. This process, involving the reaction of CO_2 with alkaline minerals in BA, leads to a decrease of eluates' pH and formation of carbonate compounds (mainly $CaCO_3$), which either immobilize in their crystal structures heavy metals, such as Cu-Pb-Cr-Cd, or partially passivate the BA's surface [7]. Ideally, the same CO_2 produced by the plant could be directly employed for the treatment. However, it must be kept in mind that, given the incineration fumes CO_2 content of only about 10-15 vol%, the gas must be concentrated by separation exploiting solid state CO_2 exchangers to achieve 100% saturation.

3.2 Materials and Methods

3.2.1 Particle size distribution

The BA's particle size distribution was determined by sieving, with openings from 1 to 4.75 mm (Figure 3.1). BA were partitioned as a function of *s* into three classes: $s \geq 4.75$, $4.75 > s \geq 1$ and $s < 1$ mm, corresponding to 39, 36 and 25 wt%, respectively. The BA fraction with $4.75 > s \geq 1$ mm was further divided into two sub-classes: $4.75 > s \geq 2$ and $2 > s \geq 1$ mm, representing 22 and 14 wt% of the whole BA, respectively, in order to evaluate how far can steam washing be applied to successfully treat this waste.

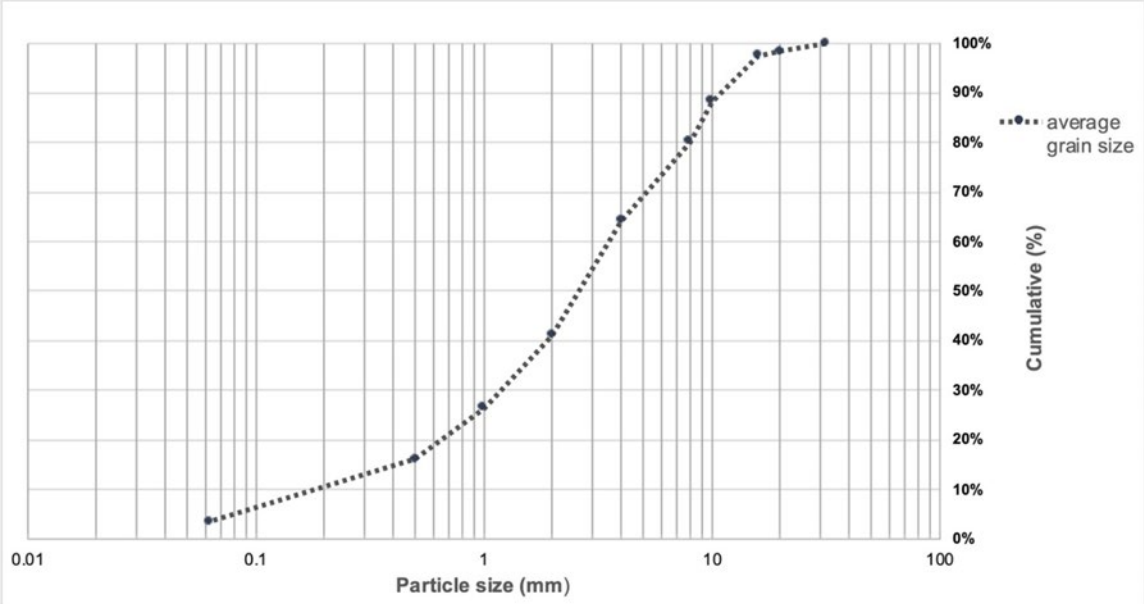

Figure 3.1 Particle size distribution of BA.

3.2.2 Steam washing

Laboratory steam washing experiments were carried out on BA using steam from deionized water (total balance: 0.02 L/kg/s), at P ~ 2 bar, T ~ 80 °C and exploring treatment times from 60 to 600 secs. These conditions, which do not correspond to an equilibrium regime of steam, are compatible with a steam flux from turbines and allow for the recovery of a considerable fraction of thermal energy. A steam generator prototype designed by ETG s.r.l, in collaboration with the Earth Science Department of the University of Turin, was employed (Figure 3.2). A steam flow, conveyed through a pipe, is released by a nozzle and directed onto a BA sample (30–40 g) laid on a grid, under which condensation water is then collected. The process takes place without restraining walls, to avoid steam oversaturation. The steam's temperature is measured by an E + E Elektronik EE 33 sensor (operating range −40 °C < T < 180 °C, 0 < Hr <100%; accuracy for T and Hr: ±0.2 °C and Hr = ±1.3%, respectively). The flow is determined through an E + E Elektronik EE 75 flow sensor that measures the gas velocity (sensitivity range: 0 < V < 40 m/s; accuracy: from 0.06 m/s to 2 m/s; operating conditions: −40 < T < 120 °C, maximum pressure ~10 bar) and provides a pressure estimate by Bernoulli's equation.

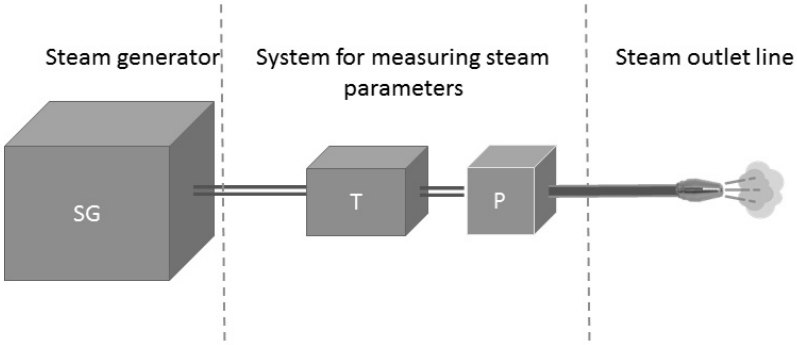

Figure 3.2 Layout of the steam washing apparatus. SG: steam generator; T and P: temperature and pressure regulators.

3.2.3 Accelerated carbonation

The reactor used in the present investigation was specifically designed for such laboratory treatment by Maina G. s.r.l. (Pecetto, Turin-I), and its layout is shown in Figure 3.3.

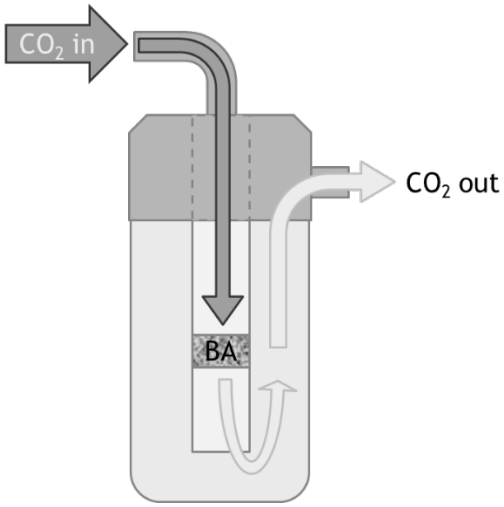

Figure 3.3 Layout of the laboratory reactor used for the accelerated carbonation tests.

CO_2 was provided by a gas tank and its pressure gauged via a manometer at the reactor. Experiments were carried out in closed system mode, which is achieved as follows: 1) the system is warmed up to a given temperature by a H_2O-thermal reservoir surrounding the reactor and heated by a coiling resistance; 2) temperature is measured in the reservoir and inside the reactor by thermocouples; 3) a feed-back control system makes it possible to keep the temperature constant in the reactor; 4) carbon dioxide is allowed to flow in until achievement of the chosen pressure; 5) the system is isolated, so that any in/out CO_2-exchange is prevented and carbonation starts occurring. Accelerated carbonation experiments were restricted to the BA belonging to the classes $2 > s \geq 1$ and $s < 1$ mm, since they display an higher specific surface area, which favors the carbonation reactions.

The parameters used in the carbonation experiments (T < 60–80 °C; duration of carbonation: $t \leq$ 180 min; $P_{CO2} \leq$ 2–3 bar; CO_2-saturation) are in keeping with those of previous works [14-18]. The liquid (i.e., water)-to-solid (i.e., BA) ratio was set to 0.3, as wet carbonation has been proved to be more effective with respect to the dry version. Low temperature carbonation reactions at 6 °C were performed by cooling the reactors outside walls with cold water.

3.2.4 Thermogravimetry (TGA) –Fourier Transform Infrared Spectroscopy (FTIR) analysis

The amount of sequestered CO_2 was assessed by comparing the TGA-curves of treated *versus* untreated samples. About 10 mg of material was placed in a Pt crucible and heated from 30 to 900°C (heating rate of 20 °C/min) under dynamic inert atmosphere (N_2 100%, flow rate: 35 mL min^{-1}) in a Pyris 1 TG analyzer (PerkinElmer, Waltham, MA, USA). The gas evolved upon heating was piped (gas flow 65 mL min^{-1}) *via* a pressurized heated (280 °C) transfer line (Redshift S.r.l., Vicenza, Italy) and analyzed continuously by a FTIR spectrophotometer (Spectrum 100, PerkinElmer), equipped with a thermostatic conventional gas cell. Time resolved spectra were collected in the 4000-600 cm^{-1} wavenumber range with a resolution of 0.4 cm^{-1} and analyzed with the Spectrum software (PerkinElmer) to identify the nature of volatiles. Infrared profiles, of each single species desorbed from the samples, were obtained from the intensity of a representative peak of the investigated species as a function of temperature.

3.2.5 Solid-State Nuclear Magnetic Resonance Spectroscopy (SSNMR)

^{13}C MAS SSNMR spectroscopy allowed insights into the mechanism of carbon dioxide capture. ^{13}C MAS spectra were recorded by a Jeol ECZR 600 instrument, operating at 600.17 and 150.91 MHz, respectively, for ^{1}H and ^{13}C nuclei. Sample preparation was as follows: (1) the ferromagnetic fraction was manually removed by a magnet from 5 g of BA with $s < 1$ mm; (2) the remaining portion was desiccated and further manually ground; (3) the powders were packed into a cylindrical zirconia rotor with a 3.2 mm o.d. and a 60 µL volume. ^{13}C MAS spectra were collected at a spinning speed of 20 kHz, using a recycle delay of 20 s and a number of scans in the range 1100–3100, as a function of the sample. A ^{13}C 90° pulse of 2 µs was employed. A two-pulse phase modulation (TPPM) decoupling scheme was used, with a radiofrequency field of 108.5 kHz. The ^{13}C chemical shift scale was calibrated by the methylene signal of an external standard glycine (at 43.5 ppm).

3.2.6 PHREEQC modelling

Wastewater solutions, resulting from steam condensation and subsequent percolation through BA, were modelled by calculating the saturation indices (SI) of the possible mineral phases that might precipitate, using the PHREEQC with MINTEQ v.4 database [19]. The measured composition of the major cations and anions and pH were provided as input.

3.2.7 X-ray Absorption Spectroscopy (XAS)

The experiments were performed at BM23 of European Synchrotron Facility (ESRF). All samples were finely ground and 13mm pellets were prepared with similar weight (around 150 mg), for measurements in fluorescence mode. The reference minerals samples were all collected in transmission mode, by calculating the optimal mass for an absorption jump around 1 and mixing the amount with BN to reach 100 mg for the pelletization. Cu K-edge XAS spectra were collected using a Si(111) double crystal monochromator. XAS scans were acquired in the 9500-10635 eV range, with an energy step of 5 eV in the pre-edge region, of 0.2 eV in the XANES region and a constant k step of k = 0.035 $Å^{-1}$ in the EXAFS region. For each BA samples, a number of scans between 3-5 was employed, while 1-2 was used for reference minerals. The Linear combination Fitting of XANES, $\chi(k)$ EXAFS function and its Fourier transform (FT) were extracted and calculated using the Athena software from the Demeter package. After energy alignment and normalization to the edge-jump using Athena the $\mu x(E)$ curves were averaged, after checking for signal reproducibility. The corresponding k^2-weighted $\chi(k)$ functions was Fourier-transformed (FT) in the Δk = (2-11.0) $Å^{-1}$ range.

3.3 Results

3.3.1 Steam washing

3.3.1.1 *BA s ≥ 4.75 mm*

The electrolytic conductivity of the eluates from steam washed BA (*s* ≥ 4.75 mm) decreases as a function of the treatment time (Figure 3.4), achieving a saturation over 180 s, thus suggesting that the efficacy of the steam washing treatment does not increase monotonically with time. Table 3.1 reports the heavy metal concentrations observed in eluates as a function of the steam washing duration, up to 240 s, *i.e*. once the steam washing treatment has amply achieved its maximum capacity, for this particle size class. A 60 s steam washing removes the finest dust deposited on the surface of the particles and efficiently solubilizes species like chlorides that are markedly over the Italian threshold. A 60 s steam washing on 30 g BA (*s* ≥ 4.75 mm) requires a total of about 35 mL water (*i.e*. 1.2 mL/g), of which 90 wt% is free steam (*i.e*. dispersed in environment), 5 wt% is retained on the BA surface and the remainder 5 wt% is collected as waste water. Such figures change into 90% free steam, 3% retained by BA and 7% wastewater, if the treatment time is 240 s. Increasing the washing duration significantly improves the removal of chlorides, sulfates and Cu: a 120 s steam washing yields a Cu reduction of 50 wt%, though copper still remains over the legal threshold (0.1 mg/L against 0.05 mg/L), whereas Cd and Ni are definitely below. Increasing the steam washing time to 240 s yields a further reduction of Cu, though at the cost of an overuse of steam.

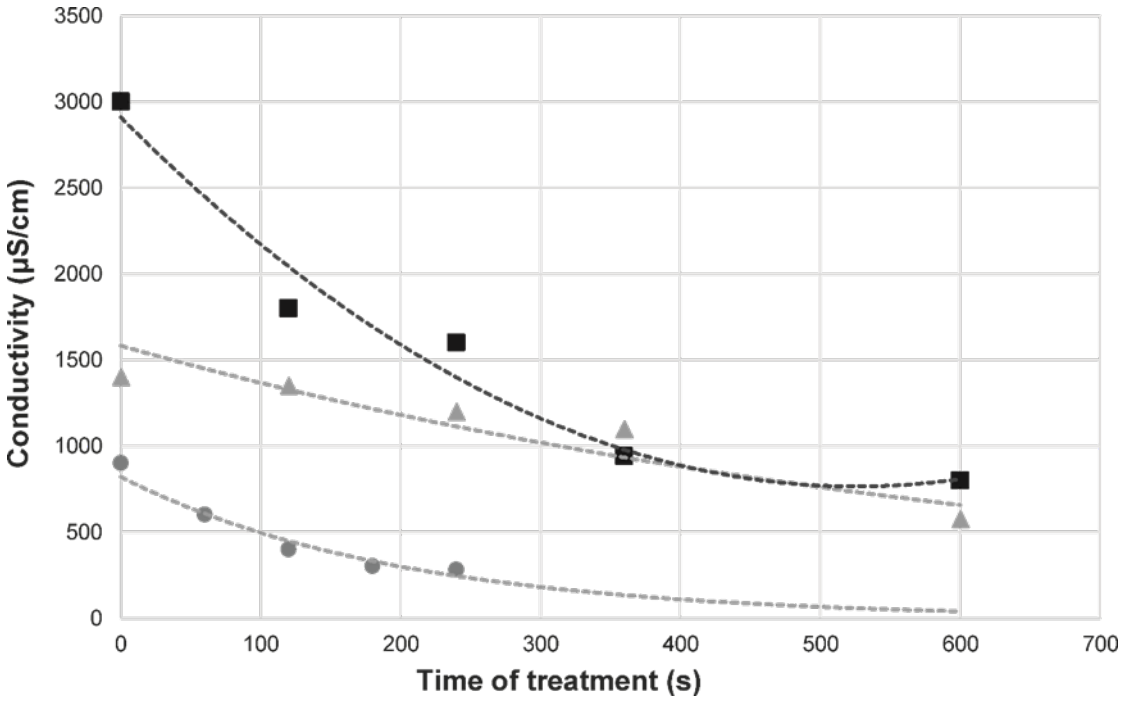

Figure 3.4 Conductivity (µS/cm) versus time (s) of BA leachates after steam washing treatments (circles: BA ≥ 4.75 mm; triangles: 4.75 > *s* ≥ 2 mm; squares: 2 > *s* ≥ 1 mm). Dotted lines: trends.

Table 3.1. Analyses of leaching test BA ($s \geq 4.75$ mm) treated by steam washing for 60, 120, 180 and 240 s, and comparison with Italian legal limits (Min. Dec. 186/2006). Be, V, As, Se and Hg are not reported, as they are below the detection limits. All concentration values are expressed in mg/L.

s ≥ 4.75 mm, steam washing	Cl^-	SO_4^{2-}	NO_3^-	Zn	Ba	Cd	Co	Cr	Cu	Ni	Pb
Unwashed	254	52	0.4	0.02	0.02	0.02	0.03	0.03	0.23	0.01	0.02
Steam Washing (60 sec)	93	35	0.2	0.02	0.02	0.02	0.03	0.03	0.21	0.01	0.02
Steam Washing (120 sec)	31	19	n.d.	n.d.	n.d.	n.d.	n.d.	0.01	0.1	0.002	0.01
Steam Washing (180 sec)	42	13	0.33	n.d.	n.d.	n.d.	n.d.	0.003	0.1	0.002	0.002
Steam Washing (240 sec)	40	19	0.137	n.d.	n.d.	n.d.	n.d.	0.003	0.04	0.002	0.001
Italian Legisl. Limits (mg/L)	**100**	**250**	**50**	**3**	**1**	**0.005**	**0.25**	**0.05**	**0.05**	**0.01**	**0.05**

3.3.1.2 *BA 4.75 > s > 1 mm*

The BA fraction with $4.75 > s \geq 1$ mm was further split into two sub-classes, to improve the efficacy of the treatment: $4.75 > s \geq 2$ mm and $2 > s \geq 1$ mm. The first group underwent steam washing for 120-600 s and the resulting leachates were analyzed. A 600 s steam washing on 30 g BA ($4.75 > s \geq 2$ mm) requires a total of 35 ml water (*i.e*. 1.2 mL/g), of which 85 wt% is free steam, 2 wt% is retained on the BA surface and the remainder 13 wt% is collected as wastewater. Regarding the environmentally dangerous chemical species concentrations observed in leachates, a comparison between unwashed and washed material shows that copper, the most abundant species to be removed, is reduced below the legal threshold using steam washing with a duration of 600 s (Table 3.2). This treatment, effective for such grain size class, yields a BA 5 %wt. loss. On the other hand, in the case of BA with $2 > s \geq 1$ mm, the leachates compositions of the unwashed bottom ashes show Cu concentrations up to four times as large as those of the unwashed sample with $4.75 > s \geq 2$ mm, as reported by Table 3.3. Steam washing effectively reduces chloride, sulfates and heavy metals release, but it fails in reducing copper below the legal threshold, even by 600 s treatments. The wastewater amounts to about 12-13%, and the weight loss around 10%.

Table 3.2 Analyses of leaching test BA ($4.75 > s \geq 2$ mm) treated by steam washing for 60, 120, 180 and 240 s, and comparison with Italian legal limits (Min. Dec. 186/2006). Be, V, As, Se and Hg are not reported, as they are below the detection limits. All concentration values are expressed in mg/L.

4.75 > *s* ≥ 2 mm steam washing	Cl^-	SO_4^{2-}	NO_3^-	Zn	Ba	Cd	Co	Cr	Cu	Ni	Pb
Unwashed	258	115	n.d.	0.012	n.d.	0.001	n.d.	0.008	0.3	0.004	0.001
Steam Washing (120 sec)	220	100	n.d.	0. 012	n.d.	0.001	n.d.	0.008	0.215	0.002	0.003
Steam Washing (240 sec)	200	90	n.d.	0.07	n.d.	0.015	n.d.	0.006	0.08	0.001	0.03
Steam Washing (360 sec)	186	79	n.d.	n.d.	n.d.	n.d.	n.d.	n.d.	0.07	n.d.	n.d.
Steam Washing (600 sec)	80	44	n.d.	n.d.	n.d.	n.d.	n.d.	n.d.	n.d.	n.d.	n.d.
Italian legislation thresholds (mg/L)	100	250	50	3	1	0.005	0.25	0.05	0.05	0.01	0.05

Table 3.3 Analyses of leaching test BA ($2 > s \geq 1$ mm) treated by steam washing for 60, 120, 180 and 240 s, and comparison with Italian legal limits (Min. Dec. 186/2006). Be, V, As, Se and Hg are not reported, as they are below the detection limits. All concentration values are expressed in mg/L.

2 > *s* ≥ 1 mm steam washing	Cl^-	SO_4^{2-}	NO_3^-	Zn	Ba	Cd	Co	Cr	Cu	Ni	Pb
Unwashed	600	250	n.d.	0.031	n.d.	0.001	0.003	0.02	1.3	0.004	0.003
steam washing (120 s)	550	200	n.d.	n.d.	n.d.	0.005	0.006	0.02	0.9	0.001	0.003
steam washing (240 s)	410	180	n.d.	n.d.	n.d.	n.d.	n.d.	n.d.	0.7	n.d.	n.d.
steam washing (360 s)	118	67	n.d.	n.d.	n.d.	n.d.	n.d.	n.d.	0.5	n.d.	n.d.
steam washing (600 s)	16	11	n.d.	n.d.	n.d.	n.d.	n.d.	n.d.	0.2	n.d.	n.d.
Italian legislation thresholds (mg/l)	100	250	50	3	1	0.005	0.25	0.05	0.05	0.01	0.05

3.3.2 Accelerated carbonation

3.3.2.1 *BA 2 > s > 1 mm*

Given that the BA fraction with 2 > s ≥ 1 mm contributes just by 14 wt%, the exploration of the effects induced by accelerated carbonation was performed by keeping fixed a 60 min treatment and P_{CO2}= 2 bar, while varying temperature between 20 °C and 60°C with water-to-solid ratios of 0.2. The observed weight increase owing to carbonation is rather modest, about 1%. The pH of the leaching solutions decreases up to 9.5 and 8.4, in the case of carbonation at 20 °C and 60 °C, respectively. For the lower temperature, Cu remains above the legal limit, while the other heavy metals do not show significant differences when compared with the pristine material (Table 3.4). An increase of carbonation temperature to 60 °C determines a Cu leaching concentration below the legal threshold (< detection limit versus 0.5 mg/L), although the chloride content remains high (> 100 mg/L).

Table 3.4 Analyses of leaching test BA (2 > s ≥ 1 mm) treated by accelerated carbonation for 60 min, and comparison with Italian legal limits (Min. Dec. 186/2006). Be, V, As, Se and Hg are not reported, as they are below the detection limits. All concentration values are expressed in mg/L.

2 > *s* ≥ 1 mm acc. carbonation	Cl^-	SO_4^{2-}	NO_3^-	Zn	Cd	Co	Cr	Cu	Ni	Pb
2 > *s* ≥ 1 mm not carbonated	500	132	n.d.	0.03	0.002	0.003	0.018	0.64	0.004	0.003
2 > *s* ≥ 1 mm carbonated 20°C	455	100	n.d.	0.03	0.002	0.004	0.015	0.5	0.007	0.003
2 > *s* ≥ 1 mm carbonated 60°C	440	120	n.d.	n.d.	n.d.	n.d.	n.d.	n.d.	n.d.	n.d.
Italian legislation limits (mg/L)	100	250	50	3	0.005	0.25	0.05	0.05	0.01	0.05

3.3.2.1 *BA s < 1 mm*

The accelerated carbonation experiments were performed setting pressure, treatment duration, grain size and gas composition as fixed "parameters" (P_{CO2}= 2 bar, 60 min, *s* < 1 mm, 100% CO_2). At *T*= 20 °C, an increase of weight after carbonation of ~5.3 is observed, respectively, while the pH value of the solution after leaching changed from 11.5 to 8.9-8.5, respectively. At raised temperature (60 °C), similar weight increase is measured (around 5.5), while the pH value further decreased to 8 for all the samples under investigation. At *T*=6 °C carbonated BA undergo an increase of weight of ~3.7%, and the aqueous solution pH measured after the leaching test is 7.9. The related leaching tests yield the results shown in Table 3.5, where it is apparent that, although the Cu release is reduced up to 85% (at 60 °C), it is lies above the legal limit, as chlorides. Since similar values were obtained at 20 and 60 °C, the former condition has been further tested by increasing the treatment time (to 180 min). An average BA's weight increase of ~5.6 % was observed, along with an acidification of the leachate up to 7.6. All the heavy metals are reduced to below the legal thresholds after 180 min treatment, but chloride and sulfate concentrations that remain high (Table 3.6).

Table 3.5 Analyses of leaching test BA (s < 1 mm) treated by accelerated carbonation for 60 min, and comparison with Italian legal limits (Min. Dec. 186/2006). Be, V, As, Se and Hg are not reported, as they are below the detection limits. All concentration values are expressed in mg/L.

s < 1 mm	Cl^-	SO_4^{2-}	NO_3^{2-}	Zn	Ba	Cd	Co	Cr	Cu	Ni	Pb
Not carbonated	1336	448	2.7	0.09	0.1	0.12	0.15	0.16	3.18	0.07	0.02
Carbonated (6 °C)	1300	470	n.d.	0.11	0.1	0.16	0.13	0.12	0.7	0.03	0.01
Carbonated (20 °C)	1185	354	0.62	0.11	0.13	0.14	0.16	0.14	0.79	0.06	0.1
Carbonated (60 °C)	791	153	3.4	0.01	0.07	n.d.	n.d.	0.01	0.48	0.04	n.d.
Italian law threshold (mg/L)	100	250	50	3	1	0.005	0.25	0.05	0.05	0.01	0.05

Table 3.6 Analyses of leaching test BA (s < 1 mm) treated by accelerated carbonation at 20 °C, and comparison with Italian legal limits (Min. Dec. 186/2006). Be, V, As, Se and Hg are not reported, as they are below the detection limits. All concentration values are expressed in mg/L.

s < 1 mm	Cl^-	SO_4^{2-}	NO_3^-	Zn	Ba	Cd	Co	Cr	Cu	Ni	Pb
Not carbonated	1336	448	2.7	0.09	0.1	0.12	0.15	0.16	3.18	0.07	0.02
Carbonated (60 min)	1185	354	0.62	0.11	0.13	0.14	0.16	0.14	0.79	0.06	0.1
Carbonated (180 min)	510	348	n.d.	n.d.	n.d.	n.d.	n.d.	n.d.	n.d.	n.d.	n.d.
Italian legisl. limits (mg/L)	100	250	50	3	1	0.005	0.25	0.05	0.05	0.01	0.05

3.4 Discussion

3.4.1 Steam washing

In general, steam washing affects BA by a combination of mild dissolution and mechanical removal of the fine dust adherent to the surface of the particles. Figure 3.4 shows BA before and after steam washing, for all grain sizes under study, using an optical microscopy. Small-size particles, adherent to the surface, are apparent in untreated BA samples, whereas they are absent in samples that have undergone steam washing. Table 3.7 sets out the chemical composition of the wastewaters. It shows that Na/K-chloride and Ca-sulfate underwent dissolution into water (pK_{sp} = −1.58, −0.85, and 4.36, respectively). This is further confirmed by observing the presence of Na^+, K^+ and Ca^{2+} to counterbalance chloride and sulfate. PHREEQC modelling of the wastewater indicates a solution undersaturated with respect to NaCl, KCl, $CaSO_4$, and supersaturated in Ca-carbonates (calcite), Fe carbonates and Fe hydroxides, that can potentially precipitate into the residual solid (Figure 3.5). It is also apparent that Cu phases are supersaturated in these conditions (i.e., cuprite and Cu hydroxide); however, it was not possible to clearly identify them by XRPD and SEM analyses. It is also worth to keep in mind that such calculations are obtained assuming thermodynamic equilibrium is reached, which may not represent the real conditions. SEM analyses of the solid residue confirm the presence of these phases, especially calcite, Fe oxides and hydroxides, apatite and quartz, together with slag phases. In addition, SEM observations yield an average particle size of the solid residue of about 300–800 μm, corroborating the removal of the fine fraction (BA with *s* < 1 mm) from the surface of coarser BA during treatment (Figure 3.6).

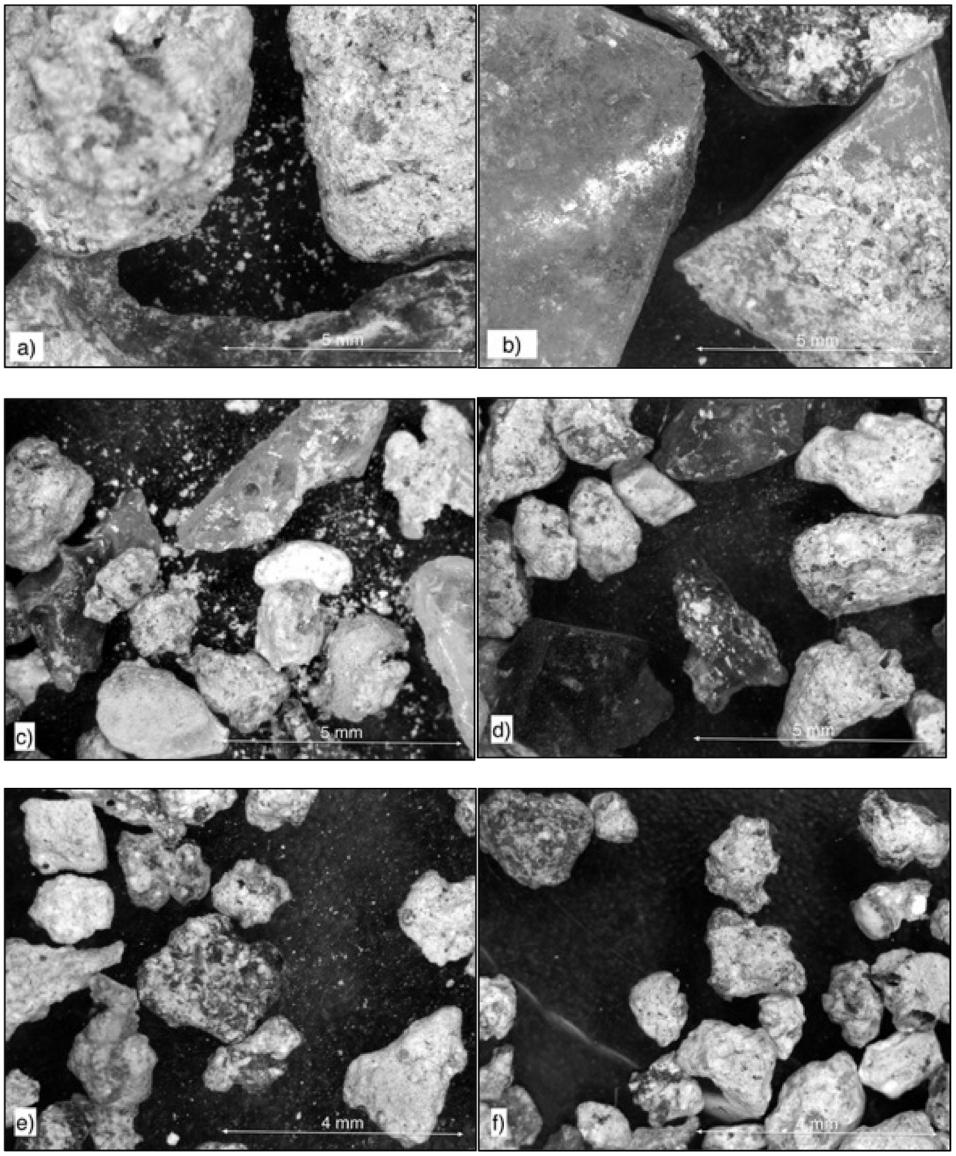

Figure 3.4 BA with *s* ≥ 4.75 mm before (**a**) and after (**b**) steam washing; BA with 4.75> *s* ≥ 2 mm before (**c**) and after (**d**) steam washing. Optical magnification 7.7×.; BA with 2 > *s* ≥ 1 mm before (**e**) and after (**f**) steam washing.

Table 3.7. Wastewater composition of steam washing on BA with s ≥ 4.75 mm, 4.75 > s ≥ 2 mm, 2 > s ≥ 1 mm (240, 600, 600 s). Be, V, As, Se and Hg are not reported, as they are below the detection limit. All concentration values are expressed in mg/L.

Wastewater	Cl^-	SO_4^{2-}	NO_3^-	Ni	Zn	Ba	Cd	Co	Cr	Cu	Pb
s ≥ 4.75 mm (240 s)											
Average	214	33	0.26	0.001	0.002	<LOQ	0.002	<LOQ	0.02	0.2	<LOQ
St. Dev.	16.26	6.66	0.02	0.001	0.001	<LOQ	0.001	<LOQ	0.01	0.01	<LOQ
4.75 > *s* ≥ 2 mm (600 s)											
Average	150	51	0	0.001	0.01	<LOQ	< LOQ	<LOQ	0.003	0.3	<LOQ
St. Dev.	43.59	17.93	0	0.001	0.02	<LOQ	< LOQ	<LOQ	0.004	0.001	<LOQ
2 > *s* ≥ 1 mm (600 s)											
Average	504	250	0.2	<LOQ	0.001	< LOQ	0.002	0.001	0.05	1.05	<LOQ
St. Dev.	53.95	0.83	0.01	<LOQ	0.001	< LOQ	0.001	0.001	0.03	0.001	<LOQ

Figure 3.4 PHREEQC modelling results of BA (2 > s ≥1 mm) wastewater solution, using MINTEQ v.4 database. In the table the main obtained minerals with their saturation indices (SI) are reported. SI is calculated by SI = log (IAP/K), where IAP is the ionic activity product of the ions forming the mineral and K is its

thermodynamic equilibrium constant. When SI < 0, the mineral is undersaturated in solution, otherwise it is supersaturated.

Mineral	SI
Anhydrite	−1.38
Aragonite	1.38
Brucite	−3.46
Calcite	1.56
$Cu(OH_2)$	1.70
Cr_2O_3	6.40
Cuprite	1.53
$CuSO_4$	−13.55
Dolomite	1.40
$Fe_2(SO_4)_3$	−44.1
Ferrihydrite	4.36
Goethite	7.05
Gypsum	−1.13
Halite	−5.28
Hematite	16.5
Lime	−17.5
Maghemite	8.71
Magnesite	−1.31
Magnetite	19.28
Nesquehonite	−4.10
Periclase	−8.20
Portlandite	−7.57
Siderite	−4.33
Tenorite	2.97
Zincite	−2.13
$Zn(OH)_2$	−3.00
ZnO	−1.99

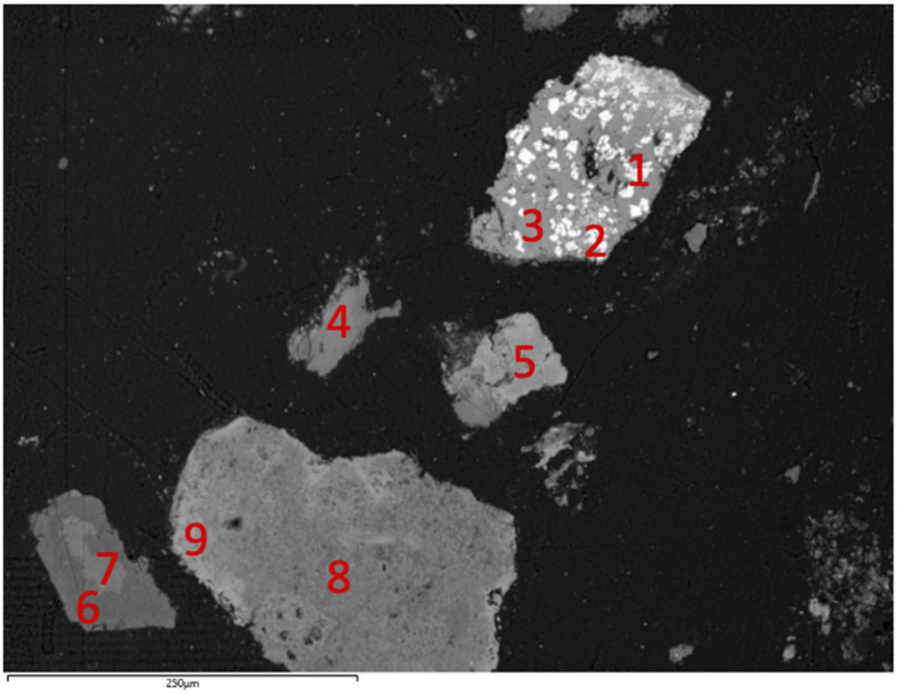

Figure 3.6 BSE image of the solid residue removed during steam washing. SEM-EDS observations show a complex composition of both crystalline and slag phases (where no mineral could be identified the composition is reported in cement notation): 1. FeOx; 2. TiO_2; 3. Pyroxene; 4. Apatite; 5. CAS; 6. Mg-spinel; 7. CA; 8. Calcite; 9. Quartz. (Experimental conditions: W filament, accelerating voltage 15 kV, working distance 10 mm, high probe current, magnification 200×).

A possible confirmation of the above description can be derived by Cu K-edge XAS analysis, performed on ground pellets of BA 4.75 > *s* ≥ 2 and three replicas of treated BA after 600 s (Figure 3.7). The pristine BA Cu K-edge XANES white line showed features from both Cu^+ and Cu^{2+} oxidation states, indicating the non-homogenous oxidizing conditions of the combustion chamber. The profile was satisfactorily modelled using Linear Combination Fitting contributions mainly from tenorite (CuO), followed by cuprite (Cu_2O) and chalcocite (Cu_2S), together with malachite ($Cu_2(OH)_2CO_3$), this latter probably formed during the water quenching used in the plant to cool down the material. By considering the EXAFS and Real space spectra it was possible to bring to light many similarities between tenorite and pristine BA, suggesting that in this sample the Cu environment can be approximate to a bulk CuO domain. When the treated samples are considered, a marked reduction of CuO is observed, while the other contributions increase. Due to the nature of the treatment, it's unlikely that these differences are the result of chemical redox transformations. A possible interpretation can be found assuming that the steam washing has removed the CuO particles on the BA larger grains, thus changing the overall Cu speciation distribution and the resulting leaching profile, as tenorite has been proposed as one of the main solubility controlling minerals in BA [20]. This seems to be in accordance with the EXAFS and Real Space analysis, where the treated BA spectra seems more dampened in intensity and without the higher coordination shells of CuO bulk. The differences in the other contributions between the treated BA are probably related to the relevant heterogeneity of this material with respect to the scale of XAS beam size, as the treatments are performed on tens of grams of coarse grains (2<*s*<1 mm), since the leaching tests require large quantities to be significant. To tackle this limitation, three spectra on different pellets of pristine BA were collected, confirming CuO as the main speciation contribution. This, coupled with measurements on pellets of independently treated samples, which have shown a similar trend with respect to CuO, seems to support the hypothesis derived above.

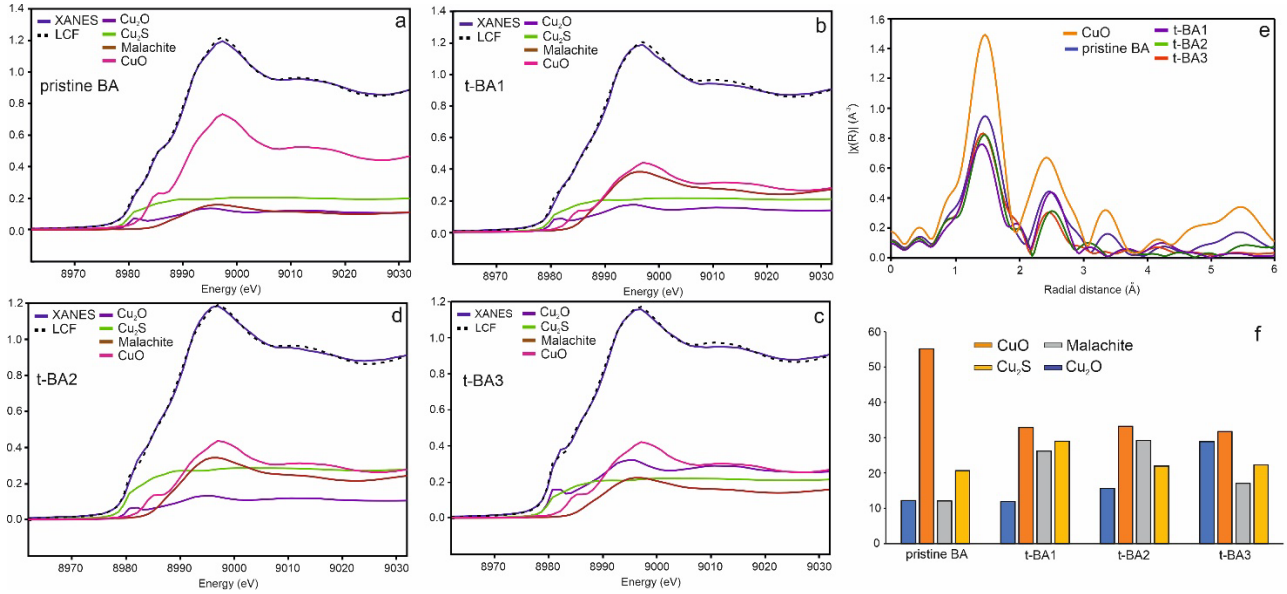

Figure 3.7 BA Cu K-edge XANES profile with LCF of a) pristine BA, b) t-BA1 c) t-BA2, d) t-BA3. e) Real space spectra of BA samples and CuO. f) Results of LCF quantifications.

Table 3.8 reports the global mass balance related to steam washing treatments, in terms of (i) dissipated steam (i.e., dispersed in the environment); (ii) retained water (i.e., adsorbed by the BA surface); (iii) wastewater (i.e., water collected from BA percolation, and giving a leachate); (iv) weight loss (i.e., difference in mass between treated and untreated BA). Note that the i) can potentially be recovered up to ~80%.

Table 3.8. Mass balance of the steam washing treatment referred to the three grain size classes investigated. The weight loss refers the BA weight difference after and before treatment; retained water, dissipated steam and wastewater fractions are referred to the initial water balance. Weight loss is expressed on dry weight.

Grain Size BA	Time (s)	Retained Water (wt%)	Dissipated Steam (wt%)	Wastewater (wt%)	Weight Loss (wt%)
≥4.75 mm	240	3	91	6	0.4
4.75 mm > s ≥ 2 mm	600	2	85	13	5
2 mm > s ≥ 1 mm	600	13	75	12	10

By comparing the retained water figures of the BA classes having 2 ≤ s < 4.75 mm and 1 ≤ s < 2 mm, the relevant impact of the surface area is apparent. By taking into account the calculations of the total amount of water employed during the treatment (*i.e.*, 1,2 ml/g_{BA}) and the maximum wastewater percentage (13%), it is possible to estimate the mean amount of wastewater generated (*i.e.,* 0,16 ml/g_{BA}). This number is markedly lower than the one obtained during a common water washing treatment with L/S around 5-10 (*i.e.,* 3-8 ml/g_{BA}, assuming an 80 % of wastewater percentage), in order of 95-98%. In the case of BA (s < 1 mm), steam washing is difficult, as it induces flocculation phenomena that require additional dispersants to properly counterbalance agglomeration (for example, Na-silicate ~0.1 wt%; Na-carbonate ~0.02 wt%; phosphonate ~0.06 wt%).

3.4.2 Accelerated carbonation

The carbonation process was investigated by TGA-FTIR, comparing the thermal behavior of carbonated BA with pristine BA samples. Figure 3.8 shows the case of BA with s < 1 mm, at T= 60 °C, P_{CO2}= 2 bar, 60 min. FTIR allowed to determine the volatiles released, which were identified as H_2O and CO_2. In the temperature range from 30 to 540 °C both samples exhibited a qualitatively similar thermal behavior, characterized by the release of physisorbed and chemisorbed H_2O and small amounts of CO_2. At higher temperature, an important weight loss occurs for both samples. This process, which achieved its maximum rate at ~747 °C, was characterized by release of CO_2 and therefore is ascribed to the decomposition of carbonate, in agreement with literature. The weight loss observed in the temperature range between 560 and 840 °C was 6.50 and 11.1%, for BA and carbonated-BA, respectively, yielding a net sequestered CO_2 amount as large as about 4-5 wt%. Such figures provided by TGA are comparable with those from weight increase measurements, which range from 5.3 to 5.6%.

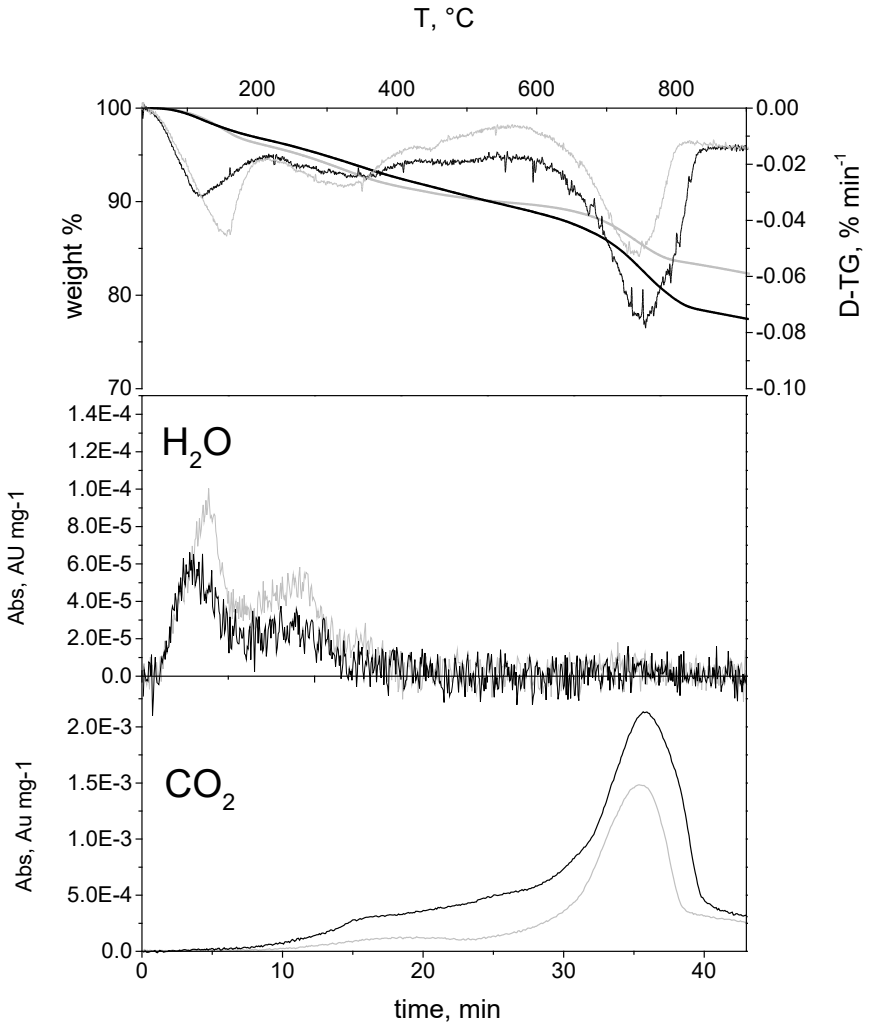

Figure 3.8 BA with *s* < 1 mm. Grey lines: BA not treated; black lines: BA carbonated; Solid lines: TG; Dashed lines: derivatives recorded as function of temperature for untreated sample (grey) and carbonated sample (black).

In addition, ^{13}C MAS SSNMR measurements, was used to shed light on the nature of the phases that develop upon carbonation. ^{13}C MAS spectra (Figure 3.9) were recorded from one untreated and two carbonated BA samples. All three spectra exhibit signals in the carbonate region, which corresponds to 165-170 ppm. In particular, the apparent peak at 168.2 ppm is attributable to calcite. The broad peak centered at about 108 ppm is a spurious signal due to the rotor background, visible because of the low content of C in the sample. Comparing the carbonated-BA samples with the untreated one, a remarkable increase of the calcite signal intensity is visible, thus confirming a relationship between carbonation process and Ca-carbonate formation. Moreover, the remarkable peak broadening clearly indicates the low crystallinity of such carbonates. Further investigations are required to unravel the still unidentified additional peak at about 166.4 ppm, which is particularly evident in the untreated sample.

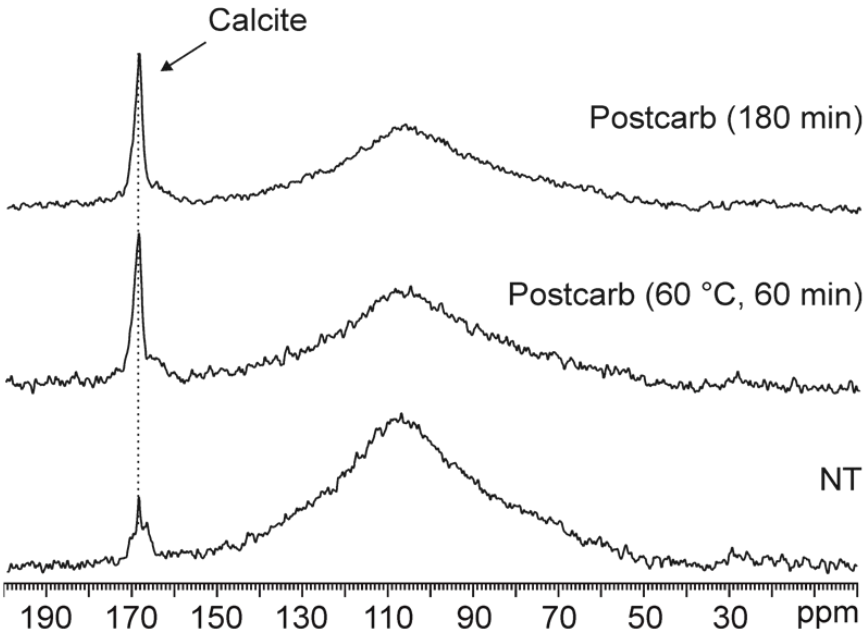

Figure 3.9 ^{13}C (150 MHz) MAS spectra of untreated (NT) and two carbonated, T = 60 ◦C, P_{CO2} = 2 bar, t = 60 min and L/S = 0.3, (Postcarb) BA samples (s < 1 mm), acquired at room temperature at a spinning speed of 20 kHz. The broad peak at about 108 ppm is a spurious signal due to the rotor background.

XRPD measurements and Rietveld refinements, carried out on all treated and untreated samples, yield a slight average increase in calcite of ~3 wt% due to carbonation (Table 3.9). Therefore, it can be concluded that ~40–50 wt% of the provided CO_2 has been sequestered into crystalline calcite, while the remainder is segregated into amorphous products. Moreover, since no crystalline phase potentially able to react directly with CO_2 is present (i.e., portlandite, periclase, etc..), it must be assumed that the amorphous fraction of BA is involved in the carbonation process. On the one hand, SSNMR agree to attribute to calcite a prominent role in sequestering CO_2; on the other hand, it also shows a broadening of the calcite signals, thus suggesting occurrence of low crystallinity/amorphous structures and carbonate other than calcite. This is in keeping with the composition provided by for BA (s < 1 mm), in which the following molar ratios Pb/Ca = 3.5×10^{-4}, Zn/Ca = 1.4×10^{-2}, Cu/Ca = 7.5×10^{-3}, confirm that Ca-carbonate is by far the most likely to form. The low leaching of Cu-Ni-Cr-Pb-Cd in the observed pH range (8–8.5), the stability of carbonate in a CO_2-saturated solution and the low solubility products of transition metal carbonate (~10^{-9}–10^{-14}, for copper-lead carbonate) point to heavy metals entering carbonate structures that exhibit different degrees of crystallinity and which reaction kinetics are promoted by an higher temperature (i.e., 60 °C). Carbon EDS maps (~25 106 analysis points) recorded by SEM-EDS (Figure 3.10) from a suite of treated versus untreated BA grains yield an average increase of carbon (ΔC) from 8.6(±3) to 15.7(±5) wt%. The "flat" gaussian distribution of ΔC (μ = 7.1, σ = 6.8) implies ΔC > 0 with a probability larger than 83.7%, thus hinting at carbonation processes spread across the sample's surface.

Table 3.9 Phase compositions on BA s < 1 mm and after carbonation (T = 60 °C, 60 min).

Table 3.9 Phase compositions on BA *s* < 1 mm and after carbonation (*T* = 60 °C, 60 min).

	Amorphous	Quartz	Calcite	Halite	Feldspar	Hematite	Melilite
BA s < 1 mm	80	3	3	2	4	3	5
Postcarb	82	2	6	1	3	2	4

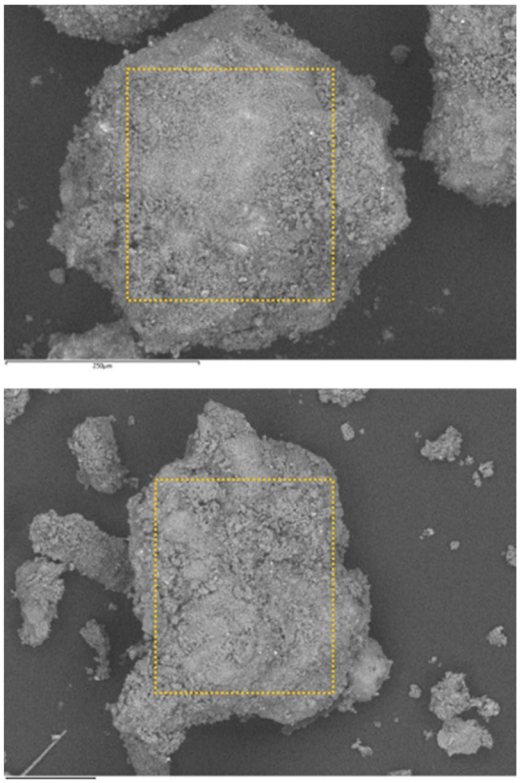

Figure 3.10 SEM images of carbonated BA samples (*s* < 1 mm). SEM-EDS observations show BA grains < 1 mm after treatment, highlight the complex and aggregate structure of such particles.

3.5 Conclusions

Steam washing on BA with *s* > 4.75 is effective to remove pollutant substances after 240 s of treatment; the measured concentrations of heavy metals, chlorides and sulfates in the eluates lie below the Italian legal thresholds. Therefore, steam washed BA (*s* ≥ 4.75 mm) are potentially suitable for reuse in environmental applications. Steam washing enables recovering of the BA fraction with 4.75 > *s* ≥ 2 mm, by increasing the treatment duration to 600 s. By considering the particle size distribution of the employed BA, steam washing allows one to recover about 60 wt% of the total BA, resorting to a wastewater volume far smaller than that required by conventional washing. The treatment mechanism mainly involves a combination of mild dissolution and dust removal, this latter possibly confirmed by the XAS analysis of Cu behavior, the main pollutant in the BA under study. In the case of BA with 2 > *s* ≥ 1 mm (amounting to ~14 wt%), steam washing is effective in decreasing chlorides and sulfates, and after 600 s it can reduce chlorides under Italian legal threshold, *i.e.* 100 mg/L. Although Cu is significantly reduced by 50%, it still remains above the legal threshold. On the other hand, accelerated carbonation of 60 min (*closed system mode*) reduces all the heavy metal and chloride concentrations below the legal thresholds. In the case of BA with *s* < 1 mm, accelerated carbonation is effective in reducing heavy metals after 180 min treatment. Chlorides and sulfates yet remain over the legal threshold. XRPD, TGA coupled with FTIR and NMR analyses show that carbonation mainly takes place in terms of formation of carbonate compounds, which are represented by calcite (major phase) with a low degree of crystallinity.

Overall:

- BA with $s \geq 4.75$ mm (39 wt%) and $4.75 > s \geq 2$ mm (22 wt%), for a total of ~61 wt%, are recoverable by steam washing. Estimating a weight loss ~0.6-1.9 wt% (% recalculated on the whole grain size of BA), the net recoverable BA amount is ~60 wt%;

- the remaining ~39 wt%, constituted by the $2 > s \geq 1$ mm (14 wt%) and $s < 1$ mm (25 wt%) fractions, can be partially recovered by a combination of steam washing and accelerated carbonation. In particular: i) the first fraction requires steam washing to reduce chlorides/sulfates and carbonation to treat heavy metals. In this view, an appropriate choice of the treatment durations might allow an affordable strategy to recover such BA fraction; ii) the second fraction requires a long duration carbonation (180 min), to achieve an appropriate reduction of heavy metals release. However, BA with $s < 1$ mm remain difficult to treat by steam washing, because of flocculation.

3.6 References

1. Caviglia, C.; Confalonieri, G.; Corazzari, I.; Destefanis, E.; Mandrone, G.; Pastero, L.; Boero, R.; Pavese, A. Effects of particle size on properties and thermal inertization of bottom ashes (MSW of Turin's incinerator). *Waste Manag.* **2019**, *84*, 340–354
2. Sorlini, S.; Collivignarelli, M.C.; Abbà, A. Leaching behaviour of municipal solid waste incineration bottom ash: From granular material to monolithic concrete. *Waste Manag. Res.* **2017**, *35*, 978–990.
3. Silva, R.V.; de Brito, J.; Lynn, C.J.; Dhir, R.K. Environmental impacts of the use of bottom ashes from municipal solid waste incineration: A review. *Resour. Conserv. Recycl.* **2019**, *140*, 23–35.
4. Alam, Q.; Schollbach, K.; Florea, M.V.A.; Brouwers, H.J.H. Investigating washing treatment to minimize leaching of chlorides and heavy metals from MSWI bottom ash. In Proceedings of the 4th International Conference on Sustainable Solid Waste Management, Limassol, Cyprus, 22–25 June **2016**.
5. Alam, Q.; Florea, M.V.A.; Schollbach, K.; Brouwers, H.J.H. A two-stage treatment for Municipal Solid Waste Incineration (MSWI) bottom ash to remove agglomerated fine particles and leachable contaminants. *Waste Manag.* **2017**, *67*, 181–192.
6. Alam, Q.; Lazaro, A.; Schollbach, K.; Brouwers, H.J.H. Chemical speciation, distribution and leaching behavior of chlorides from municipal solid waste incineration bottom ash. *Chemosphere* **2020**, *241*, 124985.
7. Asal, S.; Laux, S.J.; McVay, M.C.; Townsend, T.G. Blending organic material with municipal solid waste incinerator bottom ash to promote in-situ carbonation in road base. *Waste Manag. Res.* **2019**, *37*, 951–955.
8. Kavouras, P.; Kaimakamis, G.; Ioannidis, T.A.; Kehagias, T.; Komninou, P.; Kokkou, S.; Pavlidou, E.; Antonopoulos, I.; Sofoniou, M.; Zouboulis, A.; et al. Vitrification of lead-rich solid ashes from incineration of hazardous industrial wastes. *Waste Manag.* **2003**, *23*, 361–371.
9. Xiao, Y.; Oorsprong, M.; Yang, Y.; Voncken, J.H.L. Vitrifcation of bottom ash from a municipal solid waste incinerator. *Waste Manag* **2008**, *28*, 1020–1026.
10. Stabile, P.; Bello, M.; Petrelli, M.; Paris, E.; Carroll, M.R. Vitrification treatment of municipal solid waste bottom ash. *Waste Manag.* **2019**, *95*, 250–258.
11. Lin, Y.C.; Panchangam, S.C.; Wu, C.H.; Hong, P.K.A.; Lin, C.F. Effects of water washing on removing organic residues in bottom ashes of municipal solid waste incinerators. *Chemosphere* **2011**, *82*, 502–506.
12. Keulen, A.; van Zomeren, A.; Harpe, P.; Aarnink, W.; Simons, H.A.E.; Brouwers, H.J.H. High performance of treated and washed MSWI bottom ash granulates as natural aggregate replacement within earth-moist concrete. *Waste Manag.* **2016**, *49*, 83–95.
13. Quek, A.; Xu, W.; Guo, L.; Wu, D. Heavy metal removal from incineration bottom ash through washing with rainwater and seawater. *Int. J. Waste Resour.* **2016**, *6*, 1–9.

14. Fernández Bertos, M.; Simons, S.J.R.; Hills, C.D.; Carey, P.J. A review of accelerated carbonation technology in the treatment of cement-BAed materials and sequestration of CO_2. *J. Hazard. Mater.* **2004**, *112*, 193–205.
15. Van Gerven, T.; Van Keer, E.; Arickx, S.; Jaspers, M.; Wauters, G.; Vandecasteele, C. Carbonation of MSWI-bottom ash to decrease heavy metal leaching, in view of recycling. *Waste Manag.* **2005**, *25*, 291–300.
16. Baciocchi, R.; Costa, G.; Lategano, E.; Marini, C.; Polettini, A.; Pomi, R.; Postorino, P.; Rocca, S. Accelerated carbonation of different size fractions of bottom ash from RDF incineration. *Waste Manag.* **2010**, *30*, 1310–1317.
17. Nam, S.-Y.; Seo, J.; Thriveni, T.; Ahn, J.-W. Accelerated carbonation of municipal solid waste incineration bottom ash for CO_2 sequestration. *Geosystem Eng.* **2012**, *15*, 305–311.
18. Pan, S.Y.; Chang, E.E.; Chiang, P.C. CO_2 capture by accelerated carbonation of alkaline wastes: A review on its principles and applications. *Aerosol Air Qual. Res.* **2012**, *2*, 770–791.
19. Parkhurst, D.L.; Appelo, C.A.J. *PHREEQC (Version 2.12.5.669)—A Computer Program for Speciation, Batch-Reaction, One-Dimensional Transport, and Inverse Geochemical Calculations*; U.S. Geological Survey: Reston, VA, USA, **2005**.
20. Meima, J.A.; Comans, R.N.J. The leaching of trace elements from municipal solid waste incinerator bottom ash at different stages of weathering. *Appl. Geochem.* **1999**, 14, 159–162.

Chapter 4

Influence of speciation distribution and particle size on heavy metal leaching from MSWI fly ash

4.1 Introduction

MSW-FA, which forms in the purification system, accounts for about 1-3 % of the total incinerated waste and tend to be concentrated in atmophile/biophile heavy metals (Zn, Cu, As, Hg, Pb and Cd), together with halogens, sulfur and alkali [1]. Since a sieving pre-treatment was effective on tuning the BA treatments (see ***Chapter 3***), a similar approach has been initially employed for the study of this waste. In previous investigations, many efforts have been made to evaluate the distribution of chemical elements and the related enrichment in FA particle size fractions. Liao et al. (2007) found that Pb and Zn frequently occur in small particle size fractions; Cu, Ni and Cr are mostly concentrated in larger particle sizes; As, Cd, Co and Mo do not show any correlation with particle size [2]. Zhang et al. (2008) claimed that Cu, Pb, Zn, Cd and Hg concentrate in fine fractions, whereas Cr and Ni seem independent of the particle size [3]. Lanzerstorfer (2015) observed opposite trends of concentration versus particle size, in the case of (Cd, Cr, Cu, Ni, Mo, Pb, Zn) and (Al, As, Ba, Fe, Si, Ti), while the content of Ca, Mg, Na, Co, Mn, Sb and Sr was independent of particle size [4]. Finally, Raclavská et al. (2017) investigated three different FA samples, detecting a systematic increase of As, Ca, Cd, Cl, Cr, Cu, Hg, Mg, Pb, S, Sb, Sn and Zn in the fine fractions [5]. All these valuable studies aim to help understand the FA particle formation mechanisms and the role of heavy metals during the combustion process through the chemical composition of the resulting fly ash. All this in view of assessing the potential sources of hazard and designing efficient control/purification plants [6]. On the other hand, this background must also be related to the actual heavy metal leaching behaviour, which plays a crucial role in driving the destination and management of this waste. Indeed, the design of suitable management strategies can greatly benefit from the understanding of the correlation between leaching from FA and technologically relevant characteristics, such as particle size and chemical and phase composition. In this light, the present work aims to get an insight into the relations between i) heavy metal leaching, ii) particle size, iii) heavy metal speciation distribution and iv) heavy metal solid content, in FA. The particle size is used as a technological parameter that allows the separation of the original waste into classes. This would answer the following question, which impact upon the waste management: “are particle size separation strategies suited to develop treatments to curb heavy metal leaching from MSWI-FA?”. The experimental data are complemented with geochemical modelling at equilibrium conditions to help interpretation.

4.2 Materials and Methods

4.2.1 Particle size distribution

The particle size distribution of FA was determined by sieving, in combination with mechanical shaking over one hour, using stainless steel mesh screens with openings of 500, 250, 149, 105, 53 and 25 µm. Such openings were chosen on the basis of preliminary electrolytic conductivity tests on 10 different particle size

fractions, which allowed to pick out the partitioning reported above as the one that best highlights differences. The particle size distributions of four independent FA samples were measured to account for possible fluctuations. Every sample will be hereafter referred by the code "FA_X", where X represents the mesh opening of the related particle size class (FA_bulk means "undifferentiated fly ash sample").

4.2.2 pH-dependent batch (static) leaching tests

The pH-dependent leaching tests were performed at 8 different pH values (2-14), according to the SW-846 Test Method 1313 [7], using a liquid-to-solid ratio of 10. Additions of 2M HNO_3 or 1M KOH solutions enabled the control of the pH values, following pre-titration tests to determine the acid neutralization capacity of the material. After 24 hours, the samples were filtered, and the liquid residues analysed by IC and ICP-MS.

4.2.3 Sequential extractions procedure

The heavy metals speciation in BA and FA can be investigated by a sequential extraction method, often used in soil science, which is based on the hypothesis that it is possible to selectively extract heavy metals associated with specific phases by employing progressively stronger reactants. Here, a four-step sequential extraction method was applied (after [8]). The details about the procedure are provided below and outlined in the Table 4.1.

Step 1 (exchangeable fraction, water and acid-soluble): an aliquot of 40 ml of acetic acid (0.11 mol/L) was added to 1 g of dry FA in a 100 ml glass container. The mixture was shaken for 16 h (overnight) with a magnetic stirrer at room temperature at a speed of 40 rpm. The extract was separated from the solid residue by filtration through a 0.45 µm cellulose nitrate filter (47mm diameter). The extract was analysed immediately or stored at 4 °C. The solid residue was washed with deionized water and underwent step 2.

Step 2 (reducing conditions): in a 100 ml glass container, an aliquot of 40 ml of hydroxylammonium chloride (0.1 mol/L, adjusted to pH 2 with nitric acid) was added to the residue obtained in step 1. The mixture was shaken for 16 h (overnight) with a magnetic stirrer at room temperature at a speed of 40 rpm. The extraction procedure was then performed as described above. After washing with deionized water, the solid residue underwent step 3.

Step 3 (oxidizing conditions): an aliquot of 10 ml of hydrogen peroxide (8.8 mol/L) was carefully added in small aliquots to the residue obtained in step 2 in a 100 ml glass container. The container was covered with a watch glass and left at room temperature for 1 h with occasional manual shaking. The procedure was continued for another hour at 85 °C and the volume reduced to a few ml by further heating of the uncovered glass container. A further aliquot of 10 ml of hydrogen peroxide (8.8 mol/L) was added to the residue. The container was covered again and heated at 85 °C for 1 h. The cover was removed, and the volume reduced almost to dryness. After cooling, 50 ml of ammonium acetate (1 mol/L adjusted to pH 2 with nitric acid) were added to the residue. The mixture was shaken for 16 h (overnight) with a magnetic stirrer at room temperature at a speed of 40 rpm. The extraction procedure was then continued as described in the previous steps. After washing with deionized water, the solid residue was digested with strong acids (step 4).

Step 4 (remaining residue): a digestion of this fraction has been carried out using the last step of Tessier's procedure. The solid residue was digested with a 5:1 mixture of hydrofluoric and perchloric acids. The solid was first dissolved in a Teflon beaker with a solution of concentrated $HClO_4$ (2 ml) and HF (10 ml) to near dryness. Subsequently, a second aliquot of $HClO_4$ (1 ml) and HF (10 ml) was added, and again the mixture was evaporated to near dryness. Finally, $HClO_4$ (1 ml) alone was added, and the sample was

evaporated until the appearance of white fumes. The residue was dissolved in 12N HCl and diluted to 25 ml. The resulting solution was then analysed by ICP-MS.

Table 4.1. Sequential extraction method parameters.

Steps	Reagents and extraction conditions	Target phases
Step 1	40 ml acetic acid (0.11 M), pH 5.5	water and acid-soluble (carbonate and salt)
Step 2	40 ml hydroxylammonium chloride (0.1 M) and adjusted to pH 2 with 10 M HNO_3	easily reduced (iron oxyhydroxide)
Step 3	20 ml hydrogen peroxide (8.8M); 50 ml ammonium acetate (1 M) adjusted to pH 2 with 10 M HNO_3	oxidizable (organic matter and sulfide)
Step 4	12 ml HF conc. (10 mL) - $HClO_4$ conc. (2 mL)	residual

4.2.4 Ascorbic acid and Ammonium oxalate extractions

Low crystallinity Fe- and Al-hydroxide amounts were estimated by means of an extraction procedure with ascorbic acid and ammonium oxalate, respectively, according to [9], their concentrations were then used to model the surface adsorption of heavy metals.

4.2.5 Geochemical modelling

The Visual MINTEQ software version 3.1 [10], a solution thermodynamic geochemical code, was employed to model the heavy metals concentration/speciation in the leachates of bulk FA. The software is able to simulate the solution composition by calculating the saturation indexes of the possible solubility controlling phases, i.e, logSI = logIAP/logK_s (IAP: ion activity product; K_s: solubility constant of the mineral at the given temperature), taking into account possible ions adsorption mechanism on reactive surfaces, i.e., Fe/Al/Mn hydroxides (HFO), through a surface complexation model [10]. The calculation stability was evaluated by the charge difference (CD), i.e.,

$$CD = 100 * Abs\frac{\sum \mathrm{A} - \sum \mathrm{C}}{\sum \mathrm{A} + \sum \mathrm{C}}$$

where ∑A is the sum of anions (eq/kg solvent) and ∑C the sum of cations (eq/kg solvent). A CD value between 5-10% was considered acceptable [10].

Here, the employed strategy involved a two-step calculation:

1. calculation of all possible logSI at each pH by giving as input the solution chemistry as measured by ICP-MS/IC. The employed thermodynamic K_s database was minteq [10]. The saturation index is defined as logSI = logIAP-logK_s. When IAP is lower than *K*s, a negative value will result, which means that the solution is undersaturated with respect to that mineral (and thus that the solid should not be able to form). The reverse situation, i.e. that IAP is higher than *K*s, results in a positive value, thus reflecting over- or supersaturated conditions. The choice of potentially solubility controlling solids used for the calculations was based on the approach of Meima and Comans [11], i.e. by (i) likeliness of their presence or formation in municipal fly ash under the experimental conditions (ii) calculated log saturation indices relatively close to zero (-1 < logSI < 1) (iii) model-predicted curve shapes following the measured data in the concentration vs. pH graphs. After an initial screening as per i) and ii), the iii) step was derived by calculating the leachate composition in equilibrium with the selected mineral, using the 'infinite solid approach' outlined by Meima and Comans [11], where the solid is assumed to be present in sufficient amounts not to be completely dissolved during the simulation (i.e., the concentration of the solid is sufficient to maintain equilibrium in solution at all times.)

2. the calculation of a certain heavy metal equilibrium concentration at a specific pH value, taking into account possible ions adsorption mechanism on HFO surfaces. A multi-surface approach was employed [12], which exploits the heavy metal concentrations from leaching at the lowest pH (pH 2, which is assumed to be the maximum heavy metal availability) and uses a parameterized ''sub-model" for reactive surfaces, the "Three Plane CD-MUSIC model" [12] with surface charging parameters for ferrihydrite from [13]. The input was obtained by introducing as starting value the selected heavy metal lowest pH concentration and fixing: the major cations and anions concentrations (measured at that pH value), as spectator ions; the other heavy metals concentrations (measured at that pH value), thus assuming no coprecipitation; the concentration of HFO as determined by extraction procedure with ascorbic acid and ammonium oxalate, according to [9]. Then the pH was varied following the experimental values of the pH-dependent leaching tests. The key parameters are outlined in Table 4.2

Table 4.2. Parameters of the employed geochemical modelling, step 2.

Concentrations of different elements	As input the metal concentration that was modelled (i.e. Cu, Ni, Cr, Cd, Mn, Pb or Zn) was set as extracted at pH 2. The other metals were fixed at the concentration of the pH-dependent experiment (at each pH) in the same way as the spectator anions and cations, namely: Ca^{2+}, K^{+}, Na^{+}, Mg^{2+}, Al^{3+}, Fe^{3+}, Cl^{-}, SO_4^{2-}, NO_3^{-}, PO_4^{3-}, CO_3^{2-} Dissolved inorganic carbon (DIC): Assumed to be in equilibrium with the atmosphere.

	NO_3^-: Calculated from added acid. Sometimes adjusted to improve charge balance in the simulations. CO_2: atmospheric pressure Temperature: fixed to 25 °C
Sorption to Fe/Al-hydroxides	The concentration of HFO that could adsorb metals was calculated from oxalate extracted Al and Fe (i.e., 0.8 g/L). A molar weight of 89 g mol^{-1} was used for ferrihydrite and a molar weight of 78 g mol^{-1} for $Al(OH)_3$. The sum was parameterized as ferrihydrite. Adsorption was modelled with a surface complexation model, the "Three Plane CD-MUSIC model" [12] surface charging parameters for ferrihydrite from [13]

4.3 Results

4.3.1 Particle size distribution

The particle size distribution of the FA_bulk sample is displayed in Figure 4.1. The distribution ranges from 25 to 500 µm, and over 90 wt% FA lies between 250 and 53 µm. The calculated D_{50} is ~87 µm and expectedly indicates a small grain size and a large specific surface area, related to a tendency of FA to leach out contaminants [14]. Each particle size class is formally identified by its mesh opening value.

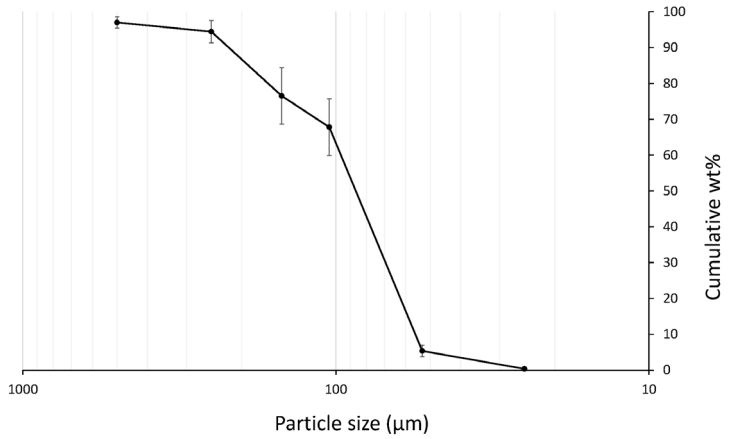

Figure 4.1 Particle size distribution of fly ash. X-axis: particle size (µm), log_{10}-scale; Y-axis: cumulative weight percentage. The reported particle size distribution is the average of measurements on four independent samples; error bars are determined as the related expected standard deviations.

4.3.2 Chemical composition

The chemical composition (FA_bulk and each particle size fraction) in terms of elements with Z≥11, including heavy metals, is reported in Table 4.3. Light elements such as carbon, oxygen, boron and nitrogen were preliminarily observed in FA_bulk *via* elemental analyser. They are estimated ("RES" contribution) by mass balance with respect to the concentrations of the other elements, measured by XRF, setting the total

to 100. Uncertainties were estimated to be as large as 2 e.s.d, a figure exceeding the lower detection limit for each element. The reported element concentrations are the average of 5 independent measurements, carried out on different points of a given sample. The FA_bulk composition is shown in Figures 4.2a and 4.2b The most abundant major elements are Na (27.6 wt%), Ca (12.9 wt%), Cl (10.1 wt%), S (10.3 wt%) and K (4.7 wt%). Among the heavy metals, apart from iron (commonly considered as a major element for geological matrices), Zn, Ti and Pb exhibit the largest concentrations (1.38-0.31 wt%); all the other reported species are equal to or lower than 0.1 wt%. Note that some elements are still a source of hazard even at a very low concentration, owing to their high toxicity (*i.e.,* Cd and Ni, CLP regulation 2008). Figures 4.2c and 4.2d show the FA composition with respect to its particle size. An increase in some major elements (K, Mg, Fe, Cl, S) and in almost all heavy metals (Cr, Cd, Cu, Pb, Zn, Mn) occurs with a decrease in the particle size. Conversely, Ca, Al and, to a lesser extent, Si and Ti exhibit higher concentrations in the coarser fractions.

Table 4.3 Chemical composition of solid FA by XRF. Element concentrations reported as wt%. Uncertainties, estimated as 2 e.s.d, are larger than the lower detection limit for each element.

(wt %)	FA_500	FA_250	FA_149	FA_105	FA_53	FA_25	FA_BULK	Average Error
(major elements)								
Si	3.1	2.9	2.6	2.4	2.4	2.7	**2.7**	0.1
Ti	0.51	0.59	0.48	0.46	0.43	0.43	**0.48**	0.01
Al	2	1.7	1.4	1	0.7	0.9	**1.2**	0.3
Fe	0.26	0.32	0.61	0.68	0.71	0.76	**0.75**	0.01
Mg	1.02	1.1	1.8	2.1	2.3	2.2	**3.2**	0.08
Ca	11	13.9	12.6	12.4	11.3	10.4	**12.9**	0.1
Na	21.3	23.4	24.6	26.7	27.3	28.4	**27.6**	0.1
K	2.04	2.2	3.62	4.18	4.46	3.85	**4.65**	0.03
P	0.26	0.4	0.46	0.48	0.5	0.53	**0.47**	0.04
Cl	4.84	6.26	8.48	9.53	8.89	6.85	**10.11**	0.06
S	3.54	3.71	7.21	8.56	9.63	9.56	**10.3**	0.06
(Minor/heavy metal)								
As	0.006	0.001	0.001	0.002	0.001	0.001	**0.002**	0.003
Ba	0	0	0.014	0.015	0.015	0.011	**0.03**	0.004
Bi	0.002	0.004	0.005	0.007	0.009	0.006	**0.007**	0.001
Cd	0.004	0.004	0.008	0.008	0.009	0.007	**0.01**	0.001
Cr	0.018	0.029	0.046	0.049	0.05	0.041	**0.05**	0.002
Cu	0.026	0.03	0.051	0.061	0.066	0.052	**0.066**	0.003
Mn	0.04	0.015	0.047	0.091	0.062	0.065	**0.074**	0.005
Ni	0.01	0.012	0.045	0.07	0.065	0.062	**0.064**	0.005
Pb	0.093	0.102	0.238	0.292	0.296	0.232	**0.311**	0.004
Rb	0.003	0.004	0.007	0.008	0.009	0.007	**0.005**	0.001
Zn	0.585	0.647	1.085	1.217	1.336	1.241	**1.383**	0.008
Sn	0.01	0.013	0.041	0.054	0.064	0.05	**0.07**	0.003
Sb	0.011	0.014	0.015	0.018	0.022	0.022	**0.027**	0.002
Sr	0.008	0.015	0.02	0.02	0.019	0.016	**0.021**	0.001
Zr	0.002	0.003	0.005	0.005	0.005	0.004	**0.005**	0.001

RES	49.31	42.63	34.51	29.59	29.35	31.6	**23.52**	0.3

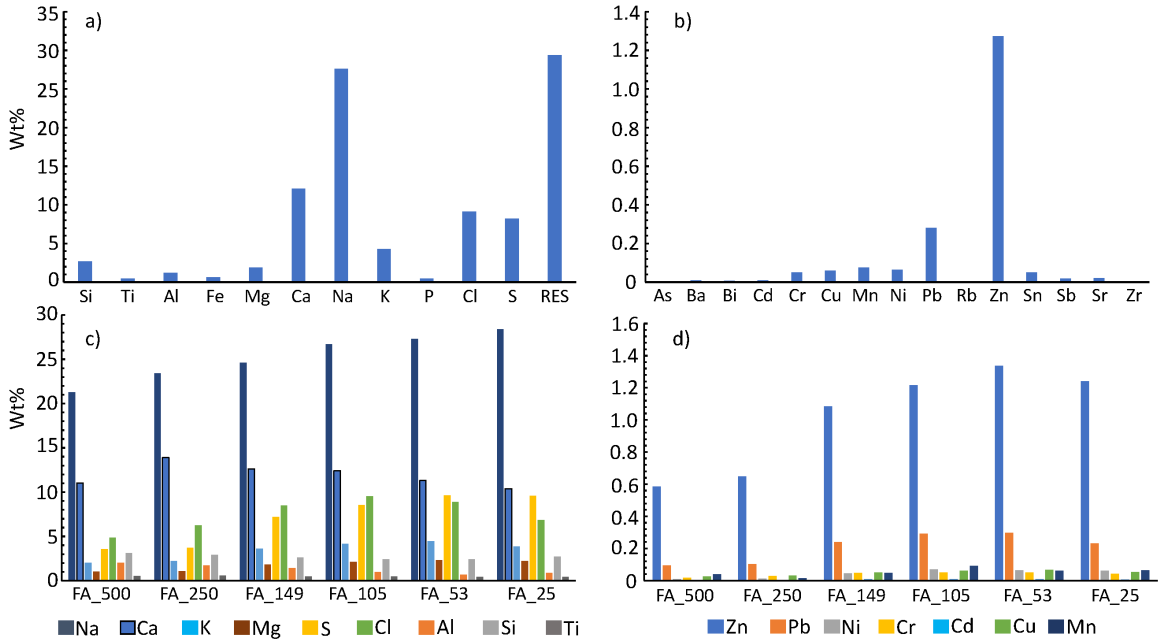

Figure 4.2 FA chemical composition, from XRF. a) Major elements (bulk); b) Minor/trace elements, such as heavy metals (bulk); c) Major elements as function of particle size; d) Minor/trace elements as function of particle size. RES: light elements, below atomic number 11 (such as C, O, B or N) were not measured.

4.3.3 Mineralogy

The mineralogical composition of the samples under investigation was determined by XRPD, in combination with Rietveld profile analysis (as an example, Figure 4.3), and the results are reported in Table 4.4. The main minerals are represented by: chloride (halite: NaCl; sylvite: KCl) and sulfate (anhydrite: $CaSO_4$; gypsum: $CaSO_4 \cdot 2H_2O$; syngenite: $K_2Ca(SO_4)_2 \cdot H_2O$). Anhydrite is expected to occur in fresh FA, while gypsum and syngenite are supposed to be products of secondary reactions (hydration), the latter due to a high concentration of K. The other mineral phases are calcite ($CaCO_3$), gehlenite ($Ca_2Al[AlSiO_7]$) and quartz (SiO_2), along with a relevant amorphous fraction ranging from 36 to 65 wt%. The latter also includes minor minerals, not revealed by XRPD because of their low abundance and/or crystallinity, but inferred by SEM-EDS, as stated below.

Table 4.4 Phase composition of the FA particle size fractions.

	FA_500	**FA_250**	**FA_149**	**FA_105**	**FA_53**	**FA_25**	**FA_bulk**
				wt%			
Halite	6	7	9	10	16	20	14
Sylvite	3	4	5	7	9	13	8
Syngenite	3	3	5	5	6	6	8

Bassanite	1	1	1	2	2	3	1
Anhydrite	7	9	9	10	12	12	10
Calcite	8	7	7	5	5	6	5
Quartz	3	2	1	1	2	1	1
Gehlenite	5	3	4	4	2	3	3
Amorphous	64	64	59	56	46	36	50

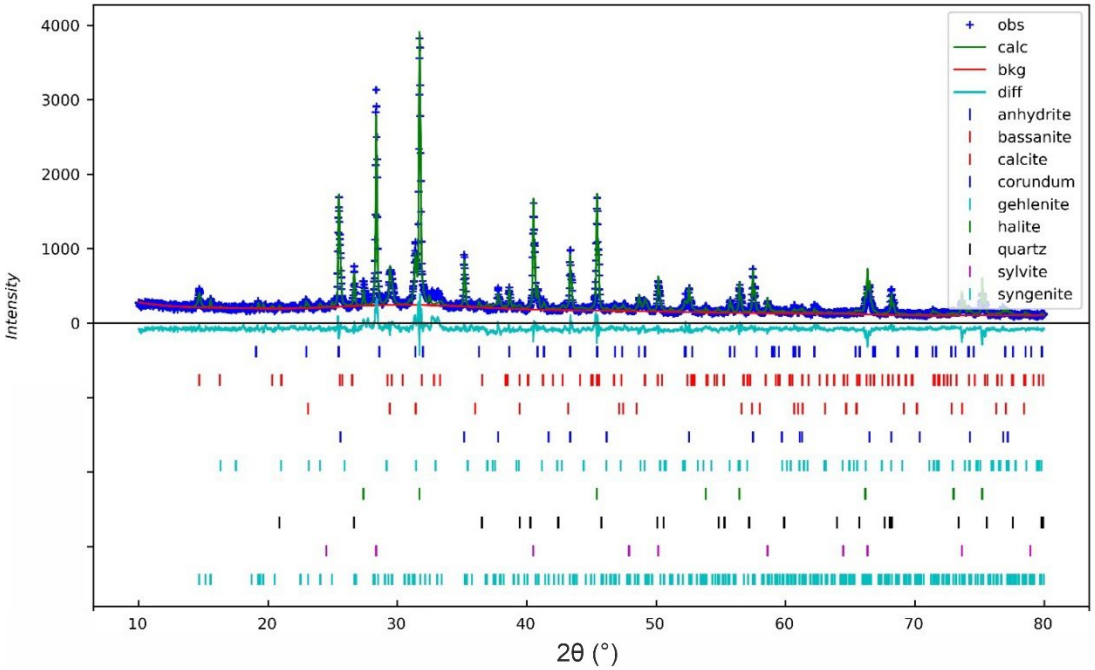

Figure 4.3 GSASII Rietveld output for FA_25, with corundum as internal standard (10% wt), with R_{wp} of 9.8.

4.3.4 Morphology

FA particles are aggregates of various phases. In this respect, SEM observations allowed to acquire information about morphology, chemical composition and texture of the minerals constituting the FA samples, as a function of the particle size (see Figure 4.4). The particle size distribution of FA inferred from imaging is in a good agreement with that determined by sieving. Agglomerates of very fine particles, due to their large and highly reactive surface areas [15], are widespread, especially in the case of coarse fractions. FA particles exhibit irregular morphologies, and the smaller grains are often observed to adhere to the surface of larger ones. The SEM-EDS mapping of polished sections of (Figure 4.5) enabled to get insight into the chemical composition and infer information on the occurring mineral phases. Particles > 100 µm are often composed of an aluminosilicate core surrounded by a rim of chloride adherent to the surface. In addition, phases not detected by XRPD, because of their modest abundancy and/or low crystallinity, are revealed by SEM-EDS (for example Fe and Mn oxides, and Ca-Mg silicates).

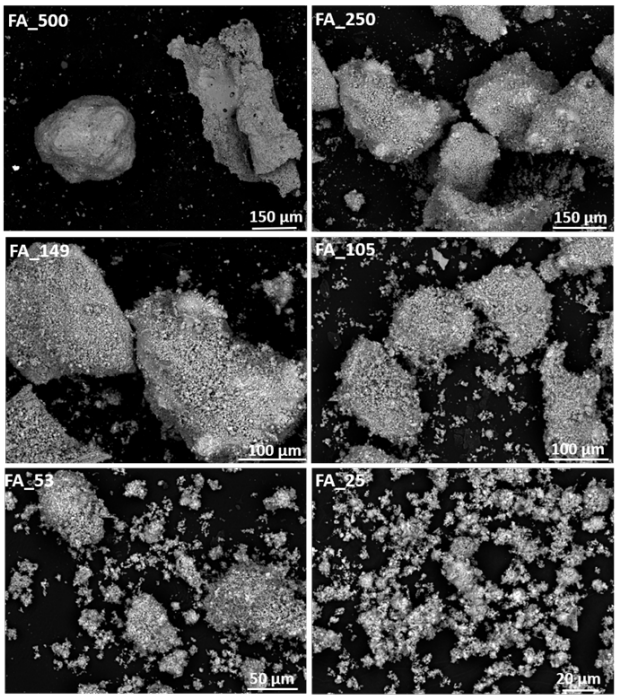

Figure 4.4 Backscattered electron SEM images on FA of different particle size fractions.

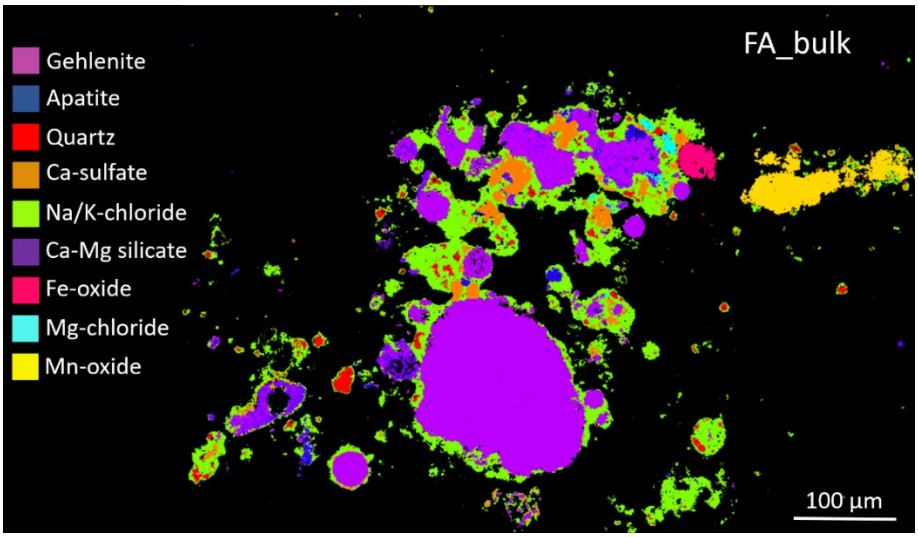

Figure 4.5 Backscattered electron SEM images of a FA polished section. Colours identify phases, recognised by SEM-EDX mapping: purple, melilite (gehlenite); green, Na/K-chloride; magenta, Fe-oxide; yellow, Mn-oxide; orange, Ca-sulfate; red, quartz; blue, apatite; light blue, Mg-chloride; dark violet, Ca-Mg silicate.

4.3.5 Leaching tests

Leaching tests were carried out on both FA_bulk and each particle size class (see Table 4.5). Electrolytic conductivity measurements *versus* time and weight loss after leaching *versus* particle size are reported in Figure 4.6 top and bottom, respectively. Electrolytic conductivity is related to the dissolution of soluble and

abundant phases (chloride and sulfate), which concentrate in the finest fractions (Table 4.4). Hence, an inverse correlation between particle size and electrolytic conductivity holds, as it does for weight loss.

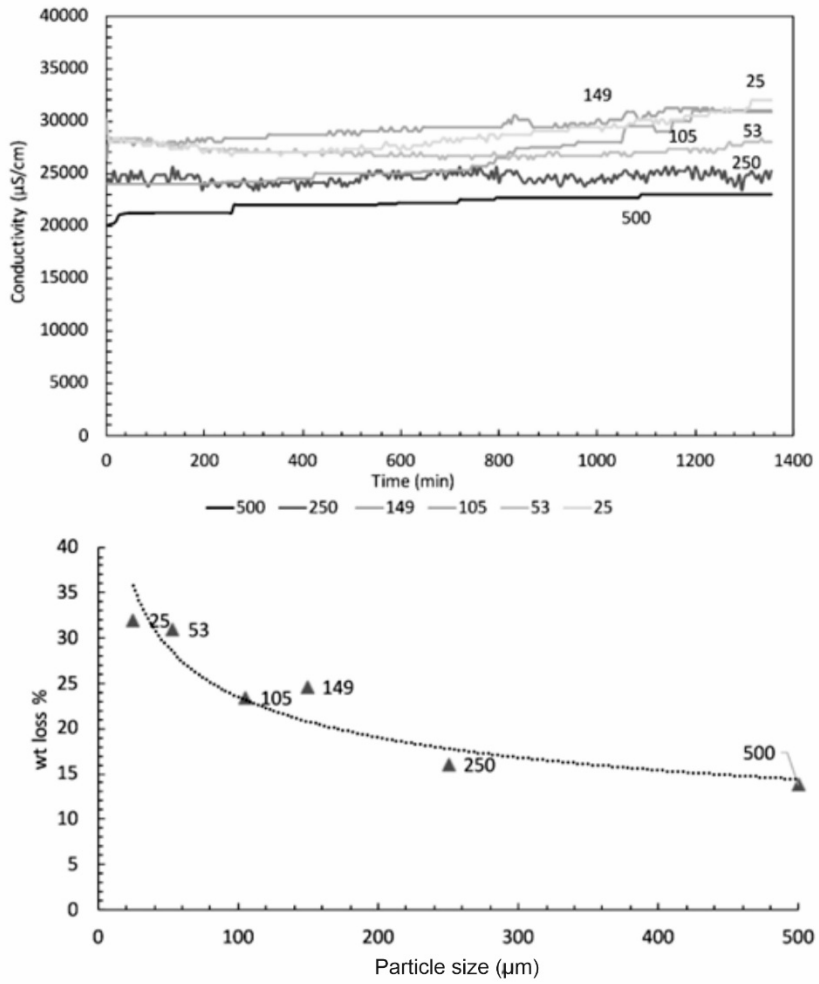

Figure 4.6 Electrolytic conductivity (µS/cm) *versus* time (min) of fly ash particle sizes, from 500 to 25 µm (top). Weight loss % of fly ash in each particle size class after leaching (bottom). Measurements were made on dried samples. Dotted line: tendency line

Table 4.5 Element concentrations in leachates from bulk FA and its particle size fractions. Note that Sb is not shown because its concentration is under the detection limit in all analysed samples. Although the same holds for Cu, its behaviour it is still discussed since this species represents a major pollutant in the bottom ash from the same MSWI plant. * Min. Decr. 27/09/2010, about disposal of waste in landfill, (transposition of 2003/33/EC); ** Min. Decr. 186/2006, about waste reuse. DOC: Dissolved Organic Carbon; TDS: Total Dissolved Solids; d.l.: detection limits.

	FA_bulk L/S 10	FA_500 L/S 10	FA_250 L/S 10	FA_149 L/S 10	FA_105 L/S 10	FA_53 L/S 10	FA_25 L/S 10	Not reactive*	Not dangerous*	Hazardous	Reuse**
conductivity (µs/cm)	31700	26000	29000	32200	34300	31400	35000				
pH	9	9.2	9.3	9	8.9	9.1	8.8				5.5-12
weight loss %	25	14	16	25	23	31	32				
Na (mg/L)	4474	3920	3638	4651	5251	4631	5320				
K (mg/L)	5120	4689	4460	5631	6218	5508	6203				
Mg (mg/L)	22	0.49	4.64	0.94	24.23	26.16	62.12				
Ca (mg/L)	799	930	1477	1280	1266	904	855				
Cl^- (mg/L)	11000	8582	11482	13281	12878	10027	12377	80	1500	2500	100
Br^- (mg/L)	118	<d.l.	92.16	<d.l.	<d.l.	89.76	112.13				
F^- (mg/L)	<d.l.	<d.l.	<d.l.	<d.l	<d.l.	<d.l.	<d.l.	1	15	50	1.5
SO_4^{2-} (mg/L)	6700	5499	4779	6430	6279	6371	6538	100	2000	5000	250
Cr (mg/L)	1.8	1.319	1.686	1.213	2.05	1.801	1.885	0.05	1	7	0.05
Ni (mg/L)	0.004	0.007	0.005	0.008	0.006	0.005	0.005	0.04	1	4	0.01
Cu (mg/L)	0.018	<d.l.	<d.l.	<d.l.	<d.l.	<d.l.	<d.l.	0.2	5	10	0.05
Zn (mg/L)	0.078	0.721	<d.l.	0.303	0.301	<d.l.	0.322	4	5	20	3
Ba (mg/L)	0.86	0.695	1.071	0.779	0.594	0.683	0.673	2	10	30	1
Pb (mg/L)	0.155	0.711	<d.l.	0.814	0.105	0.521	0.18	0.05	1	5	0.05
As (mg/L)	0.004	0.001	<d.l.	0.003	<d.l.	0.001	<d.l.	0.05	0.2	2.5	0.05
Cd (mg/L)	0.003	<d.l.	<d.l.	<d.l.	0.96	0.68	1.26	0.004	0.1	0.5	0.005
Hg (mg/L)	<d.l.	0.001	0.007	<d.l.	<d.l.	<d.l.	<d.l.	0.001	0.02	0.2	
TDS (mg/L)	15500	13000	14500	16100	17150	15700	17500	400	6000	10000	
DOC (mg/L)	<5	<5	<5	<5	<5	<5	<5	50	80	100	30

The pH values (8.8-9.3) do not significantly change with particle size (Table 4.5). Na^+, K^+ and Cl^- are related to halite and sylvite dissolution that is weakly pH-dependent, thus inversely correlated to the particle size (Table 4.4). Sulfates are associated with anhydrite and syngenite dissolution and follow a similar trend. Ca leaching, in turn, is not entirely attributable to dissolution of sulfate/carbonate: in fact, it displays high concentration values in the 250-105 µm fractions, though calcite is poorly soluble at a natural pH of ~9. Some metals exhibit concentrations that are under the legal limits for both “not reactive” and “reuse” categories. It is the case of Zn, Cu, Cd and Ni, which therefore do not contribute to a potentially toxic leaching, according to the Italian law. Instead, high leaching concentrations are measured for Pb and Cr, up to 3, 4 and 50 times the legal limits, respectively. Pb and Zn show high concentrations in the leaching solutions from the coarsest fraction (up to 50 times larger than leaching from bulk), though both metals’ contents increase with a decrease in the particle size. Other heavy metals show an inverse trend. The Cd concentration in the leachate of bulk FA is below the legal limit, while very high leaching was measured from the fine fractions, up to about 2 mg/L. Cr shares a similar trend, being leached out by the finer fractions, as expected, and each particle size class exhibits a chromium concentration over 50 times the legal limit. Finally, no trend is revealed for Ni, which yields a leaching concentration of around 0.005 mg/L for all the particle size classes, against a legal limit of 0.01 mg/L.

4.3.6 Speciation distribution

On the basis of the results obtained from leaching tests, the heavy metals chemical speciation was investigated, to better the mechanisms underlying leaching.
A four-step sequential extraction protocol was applied. Four different classes were defined, for sequential extraction: acid-soluble exchangeable (F1), reducible (F2), oxidizable (F3) and residual (F4). F1 points to speciation types that are prone to a comparatively low acidic dissolution and hence potentially responsible for most of the heavy metal leaching. F4-speciation is virtually insoluble, unless a very strong acid attack is used [8]. F2/F3-speciations are intermediate between F1 and F4, in terms of stability to an acid treatment. All the results from sequential extraction experiments are shown in Figure 4.7.

F1. This fraction involves those substances that dissolve into neutral or slightly acid media (5< pH <7), *i.e*. chlorides and carbonates. It also includes leaching of metals weakly adsorbed on particles' surface through electrostatic interactions [16]. F1-speciation can account for up to 40%, as in the case of Pb and Zn (Figure 4.7), and its importance is expected to increase with particle size decrease, in keeping with the element concentrations. This is visible in the case of Cu, Cr, Cd, and Ni, comparing the largest particle size class with the smallest. An inverse trend reveals for Pb and Zn, which show F1-speciation contributions in the coarse fractions of about 20% larger than those in the smallest fraction. Such a difference reflects a possible preferred association of Zn with calcite-structure carbonates [17]. Pb is expected to speciate in a similar way, presumably entering low crystallinity aragonite-type structures and assuming a higher coordination than in trigonal carbonate [18]

F2. This fraction accounts for heavy metals bound to Fe/Al/Mn oxide, and which are leached out by chemical reduction. The leaching of heavy metals from Fe/Al/Mn oxide is very sensitive to pH [19] as discussed in the next section, where the geochemical modelling clearly points out an important correlation between surface complexation on Fe/Al (hydr)oxide and leaching at pH < 8, for all the examined metals. Figure 4.7 shows that the speciation of Zn, Pb, Cr, Cd, Ni and Cu is ascribable to F2-like mechanisms in terms of an average ranging from 15 to 25%. For the reason stated above, the abundance of Fe and Al deeply affects the F2-speciation. Fe and Al follow two opposite trends, the former being more concentrated in the fine fractions, the latter in the coarse fractions. This results in a compensation that gives a comparatively little difference of F2-speciation contributions between the particle size classes.

F3. This fraction includes the heavy metals from organic matter and sulfides. The organic matter is due to unburnt substances, like polycyclic aromatics [19]. Since the organic matter in FA is generally decomposed by incineration, F3 is expected to be small. Our measurements show a F3-type speciation for Cd, Cr, Ni, Pb and Zn, smaller than 5%. Cu, conversely, displays a fraction as large as 24%, thus proving its high affinity for organic complexation [20,21].

F4. This fraction accounts for residual heavy metals hosted by *quasi*-indissoluble phases, such as phosphate and silicate. Their high stability against dissolution implies that the related heavy metal fraction is not leached out until strong acid mixtures are employed (*i.e*. aqua regia digestion). As shown in Figure 4.7, almost all metals exhibit F4-type as the most abundant speciation. XRPD measurements on a sample before acid digestion show the presence of silicate phases, mainly quartz and gehlenite, which can potentially host heavy metals in their crystal structure. The SiO_4 tetrahedrons of gehlenite organize in tetragonal ring chains, thus providing room to heavy metals.

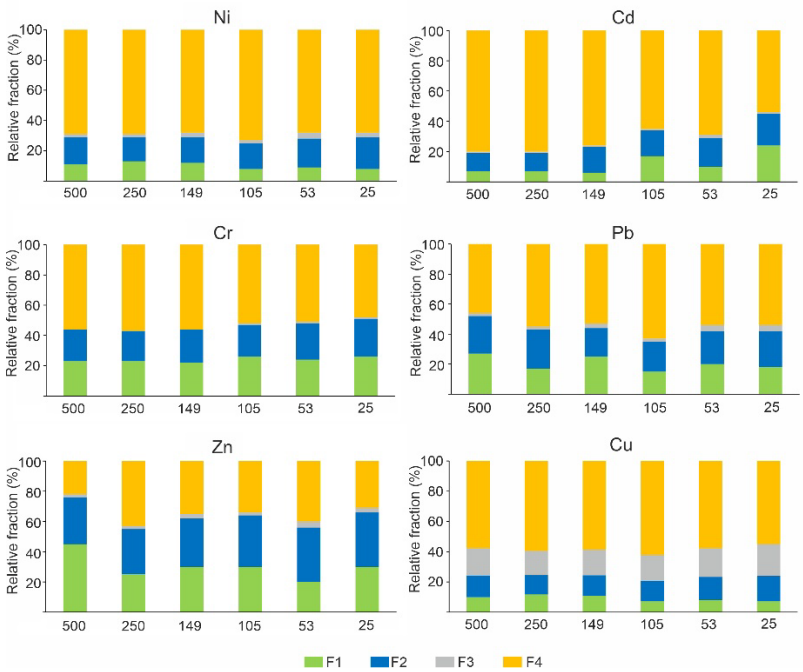

Figure 4.7 Chemical speciation distribution of heavy metals in the different FA particle size fractions.

4.4 Discussion

4.4.1 Geochemical modelling

The understanding of the heavy metal leaching from FA can benefit from comparing experiments as a function of pH with geochemical modelling. Ions follow three different trends *versus* pH [19]: oxyanionic (metal leaching increasing with pH), cationic (metal leaching decreasing with pH) and amphoteric (metal leaching decreasing up to a given pH value and increasing beyond). These different behaviours are ascribed to a combination and competition of: i) precipitation of solubility controlling minerals, ii) surface complexation/precipitation on Fe/Al/Mn (hydr)oxide (*i.e*. Surface Complexation Model, SCM) and iii) solid and dissolved organic matter [11]. In the experiments of heavy metal leaching *versus* pH, the investigation was restricted to bulk FA, only, as the pH value changes comparatively little between particle size classes (see Table 4.4). Figure 4.8 shows the leaching of Cd, Cr, Cu, Ni, Pb and Zn as a function of pH in the leachates, along with the predictions from geochemical modelling.

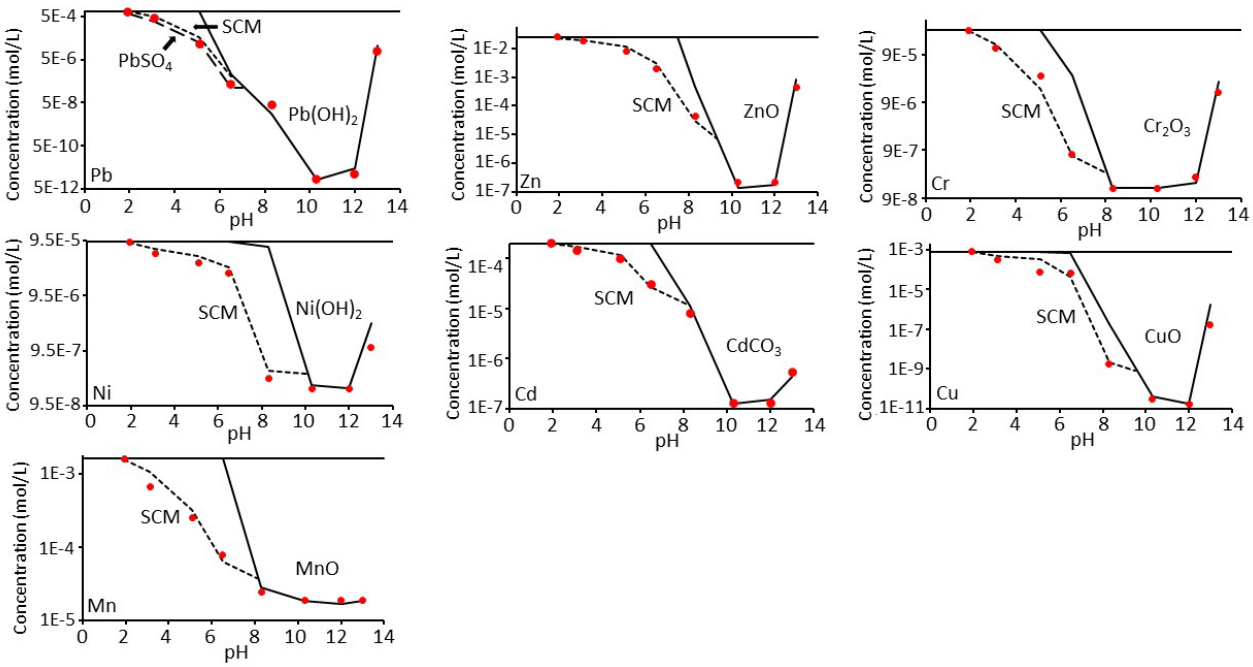

Figure 4.8 Experimental heavy metals leaching (dots); models: surface complexation on Fe/Al/Mn (hydr)oxide (dotted line) and solubility curve of minerals (solid line).

***Copper*.** The leaching profile follows an amphoteric trend, peaking at 7.8 mmol/L with pH around 2, and rapidly decreasing to extremely low concentrations, at pH>7. Cu^{2+} leaching predictions agree with previous studies (Zhang et al., 2016). Precipitation as tenorite (CuO) is suggested at neutral to alkaline pH values, thus indicating CuO as the possible solubility controlling mineral (Fig. 4.8). This, coupled with a relatively low total copper concentration (0.066 wt%), may explain why no leaching is observed at native pH around 9. With pH < 8, Cu^{2+} is undersaturated with respect to any of the possible solid phases available in the MINTEQ database, hence hinting that, at acidic pH values, mechanisms other than precipitation/dissolution are involved in driving the leaching behaviour [21], as proven by the enhancement of agreement by introducing SCM. The mismatch between theoretical values and observations might be ascribed to neglecting possible interactions with organic matter, which has a role for copper, as also suggested by the sequential extraction results related to the F3-speciation for Cu.

***Lead*.** The leaching concentration of Pb follows an amphoteric pattern, decreasing to a minimum at pH around 6-8 and then increasing again at pH > 12. At alkaline conditions, the dissolution/precipitation of Pb hydroxide, *i.e*. $Pb(OH)_2$, is proposed as a solubility controlling mechanism. When pH changes from neutral to acidic, the leaching profile agrees with the dissolution curve of anglesite, $PbSO_4$, which however appears to be undersaturated at pH 2. In literature, $Pb_5(PO_4)_3Cl$ is proposed as a possible solubility controlling phase in this pH range; yet, the modelled solubility curve shows high undersaturation with respect to experimental concentrations, meaning that its dissolution is not responsible for Pb leaching [22]. A better agreement is achieved for low pH values, where adsorption on Fe/Al(hydr)oxide is accounted for via SCM, indicating a possible combination of dissolution and surface complexation at pH < 8.

***Nickel*.** As with Pb, Ni leaching displays an amphoteric trend, gradually decreasing up to pH 8, and then increasing for pH over 12. The model identifies amorphous Ni-hydroxide as a possible solubility controlling phase for alkaline pH, in keeping with not observing crystalline $Ni(OH)_2$ by XRPD and with results from a similar study on coal fly ash [19]. The surface complexation mechanism on Fe/Al (hydr)oxide yields results matching the Ni-leaching behaviour at acidic pH, although the discrepancy in terms of oversaturation at pH

3-6 hints at a possible role of the organic matter interaction, which contributes to Ni speciation, though in terms of a few percentage points (see F3-speciation, in Fig. 4.8).

***Manganese*.** The leaching profile of Mn exhibits a cationic trend. The dissolution/precipitation of MnO accounts for the leaching concentration at alkaline pH. This is confirmed by SEM-EDS analyses, which allowed to observe MnO in FA. At pH around 7, surface complexation on Fe/Al (hydr)oxide provides a good agreement between predicted and experimental Mn concentrations.

Chromium. The leaching of Cr follows an amphoteric leaching trend, decreasing to its minimum at pH around 6, and then increasing with pH > 12. In the pH range 7-12, the precipitation/dissolution model agrees with observations, and solid Cr_2O_3 seems to control leaching of Cr in this pH range. At lower pH values, the surface complexation model describes adequately the leaching behaviour of Cr, confirming the limited influence of dissolved organic matter, as even suggested by the low F3-speciation contribution.

Zinc. Zn follows a weakly amphoteric leaching trend, decreasing to a minimum at pH around 8 and then increasing again at pH > 12. The precipitation/dissolution of zincite, ZnO, is responsible for leaching at alkaline pH, though $Zn(OH)_2$ is a further possible solubility controlling phase in such a pH range [19]. As seen with Cr, at lower pH values SCM reproduces the leaching pattern.

***Cadmium*.** The leaching profile of Cd shows a amphoteric trend, decreasing as pH increases up to pH around 9. The dissolution/precipitation of otavite, $CdCO_3$, accounts for the leaching at alkaline pH, in accordance with an earlier study [22]. At pH < 7, surface complexation on Fe/Al (hydr)oxide provides an agreement between predicted and experimental concentrations.

4.4.2 Correlation analysis

The heavy metal leaching from FA as a function of particle size is a complex process involving different but interconnected aspects that require a combination of complementary pieces of information (bulk chemistry, phase compositions characterization, metal speciation and geochemical modelling) to be understood. The element distribution observable in the different particle size fractions can be related to the vaporization and condensation/crystallization reactions that take place at the firing stage and during the flue gas purification process, respectively [23]. Chloride of heavy metals such as Zn, Cd and Pb easily evaporate on heating (800-1000 °C), thus enriching flue gases, which then condense and lead to crystallization on cooling [24]. FA particles develop large surface area upon which further condensation/crystallization processes can occur, as pointed out in the section devoted to morphology. This mechanism also explains the abundance of Na-K chloride that adhere to the surface of FA particles (Figure 4.5). Iron concentrates in the fine fractions of FA. This is in keeping with the observation that, on the one hand, heavy metal abundance is related to small particle size and, on the other hand, heavy metals often exhibit an affinity with Fe (hydr)oxide surfaces, as shown in the previous section [23]. Large FA particles are mainly constituted of glass pieces, metal fragments and dust, which the hot flue gas transported and deposited on the electro-filter walls, thus contributing to the concentration of some elements, such as Si and Al (aluminosilicate residue).

Despite the intrinsic heterogeneity of this type of material [25], similar general trends are observable, when XRPD results are considered. Salt (chloride and sulfate) concentrate in the fine fractions, in accordance with leaching tests, up to 55 wt% in the 25 μm fraction. Conversely, quartz, calcite and Ca-aluminosilicate are seen in association with larger particle size fractions. The amorphous phase's abundance seems to follow a trend directly proportional to particle size, being more concentrated in the coarse fractions. This observation agrees with the occurrence of aggregates and conglomerates in large particle size classes of FA, as shown by SEM images. Such aggregates might be composed of amorphous particles, whose surface is expected to be more reactive than crystals' and prone to clustering phenomena. In addition, glass cullet and even electro-

filter fragments are visible in coarse fractions (500 and 250 μm), thus contributing further to the amorphous content.

The degree of correlation of heavy metal leaching (HML) with some relevant variables, such as speciation relative fractions (F1 and F2), content of each heavy metal *per* size class (HMSC) and particle size (*s*), is investigated. An inspection of Figure 4.9 and 4.10 suggests that mostly linear trends are clearly recognizable. The CANOVA technique [26] that discloses possible non-linear correlations is hampered here by the unavoidable limitations in the particle size sampling (6 classes). On the other hand, such a particle size partitioning was chosen to maximize differences between classes and therefore it helps highlight correlations. In this view, the correlation coefficients of Pearson (*r*) and Spearman (ρ), as reported in Table 4.6, are analyzed, paying attention to their absolute values and signs and using a confidence level of 95% (*t*-test of Student). A relatively high positive linear correlation holds in the case of the F1-HLM pair, for each heavy metal under study. F2 and HLM exhibit low correlation (<|*r*|> < 0.37), but the case of Cd (*r* ∼0.79), although *r* and ρ are not statistically significant (just below the *t*-test). Moreover, the correlation coefficients' signs change with the heavy metals involved, so that the global efficacy of F2 on HML suffers from a compensation of the contributions. Particle size and HLM correlates with 0.2 < |*r*| < 0.73, for any heavy metal under investigation, but with correlation coefficient signs positive and negative. Examining <|*r*|>, one can roughly establish the following order of correlation degree between leaching and parameters: F2<HMSC<*s*<F1.

F2 (the fraction related to Fe/Al hydroxides) becomes relevant only when pH < 5 (acidic regime), as pointed out in section 4.4.1. Hence, a correlation with HML in water (leachates' natural pH ∼9) is reasonably weak. HMSC provides the maximum heavy metal "potential" leaching availability, which is reduced to the "real" availability *via* the solubility of the mineral phases hosting metals [8,19]. Although the FA heavy metal distribution usually shows an enrichment in the finest fraction [5], the hosting mineral phase distribution does not necessarily share the same trend, as it is affected by the physical-chemical behaviour of the other elements (Ca, S, C, Si, Al, Cl) that participate in the complex FA formation process. This may result in a relatively low correlation between HML and HMSC. The influence of *s* on HML can be related to the particles surface area that is provided to the dissolution process. This parameter seems to impact on HML more than HMSC and F2, as suggested by the general increase of correlation coefficients. Finally, the F1-speciation is by far the most prominent aspect in affecting HML, because it is directly related to the most easily soluble fraction. In fact, only in this case all the heavy metals under study exhibit robust correlation coefficients (*r*>0.85) sharing the same positive sign. Although a moderate correlation holds between F1-speciation and *s*, as suggested by <|*r*|> ∼0.6, yet the scattering of the correlation signs makes it difficult to assert any general direct proportionality law linking *s* to F1 (Table 4.6).

Table 4.6. Correlation coefficients between i-ii) relative fractions (F1 and F2), iii) heavy metal XRF content *per* size class (HMSC), iv) particle size (*s*) and heavy metal concentrations in leachates (HML); v) particle size and F1. *r*: Pearson (linear) correlation coefficient. ρ: Spearman (non-parametric) correlation coefficient. <|*r*|>: average of the absolute values of the Pearson correlation coefficient. *: significance level ≥ 95%, according to the *t*-test of Student.

	F1-HML	**F2-HML**	**HMSC-HML**	**s-HML**	**s-F1**
***r*(Zn)**	0.92*	-0.36	-0.29	0.41	0.37
ρ(Zn)	0.87*	-0.08	-0.22	0.45	0.2
***r*(Cr)**	0.91*	0.79	0.74	-0.77	-0.81

ρ(Cr)	0.89*	0.72	0.71	-0.73	-0.80
***r*(Ni)**	0.87*	0.28	0.41	-0.22	-0.51
ρ(Ni)	0.84*	0.25	0.35	-0.20	-0.45
***r*(Pb)**	0.85*	0.37	0.25	0.28	-0.23
ρ(Pb)	0.81	0.06	0.27	0.27	-0.25
***r*(Cd)**	0.90*	0.53	0.35	-0.64	-0.71
ρ(Cd)	0.88*	0.49	0.18	-0.71	-0.67
<|*r*|>	0.89*	0.37	0.44	0.54	0.6

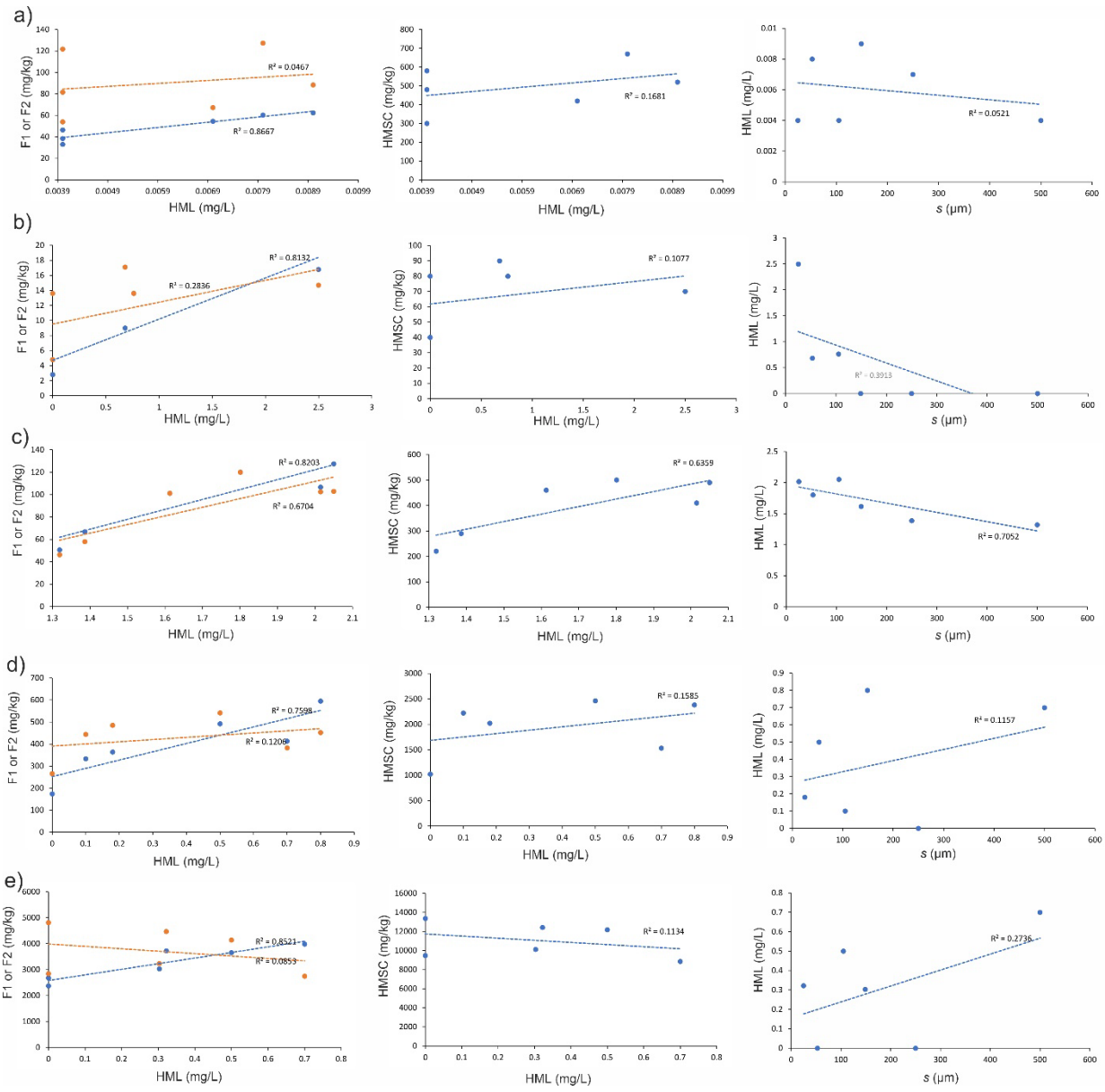

Figure 4.9 Linear correlation between extracted fractions (F1 and F2, blue and orange, respectively) and leachate concentration (HML), with respect to particle size (*s*) (right). Linear correlation between relatively weight percentage (HMSC) and HML, with respect to *s* (middle). Linear correlation between Cr HML (right) and *s* (right). a) Ni; b) Cd; c) Cr; d) Pb; e) Zn.

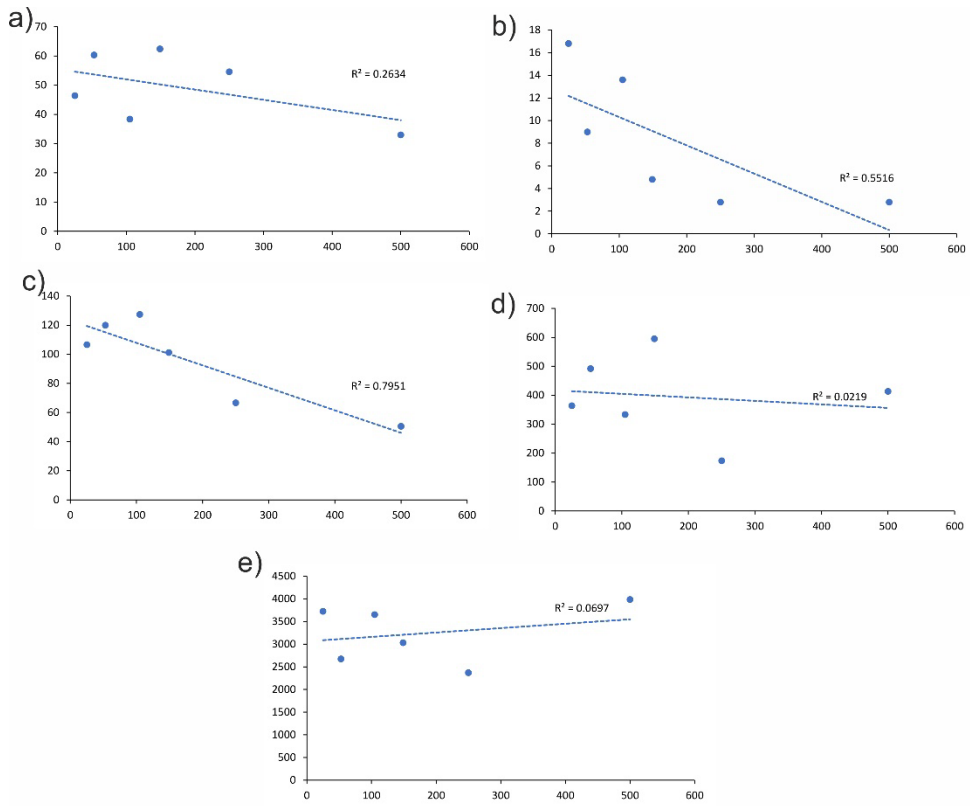

Figure 4.10 Linear correlation between F1 relative fraction of heavy metals and FA particle size (*s*). a) Ni; b) Cd; c) Cr; d) Pb; e) Zn.

The discussion above is summarized by Figure 4.11, in which the total concentrations of anions (for the sake of completeness) and heavy metals in leachates are shown with respect to *s*. They both exhibit irregular trends. The total leaching of chloride and sulfate displays a maximum variation of ∼25% between particle size classes (from 15000 to 20000 mg/L). The total heavy metal leaching changes for classes from 53 to 250 µm in the range 2-3 mg/L; however, the coarsest (500 µm) and finest (25 µm) fractions give leachates with total heavy metal concentrations over 4 mg/L. This shows the absence of any monotonic trend between total leaching and *s*, in keeping with the analysis of the previous section, pointing to a low practical efficacy of grain size separation strategy, on the contrary of what is seen to hold for bottom ash from the same plant [27].

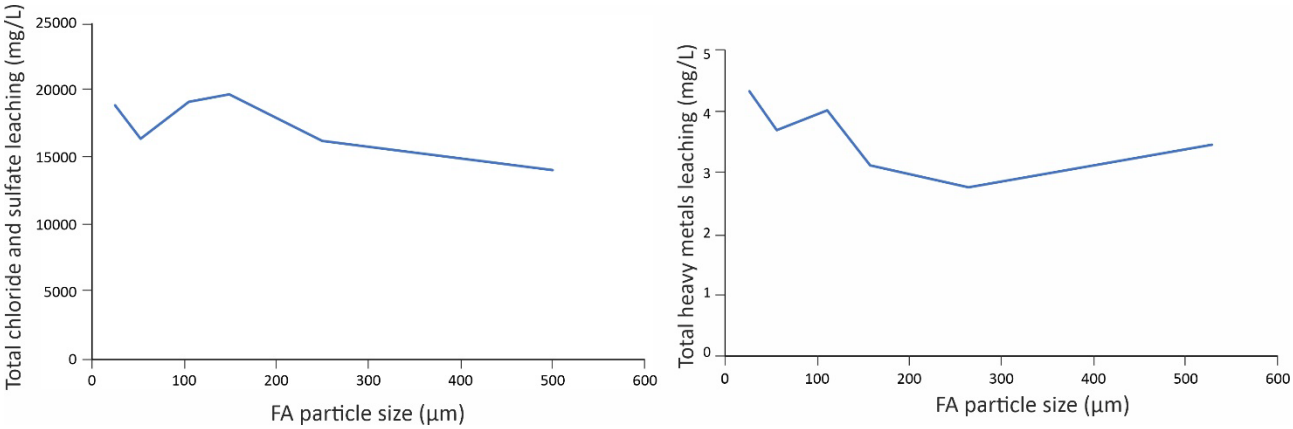

Figure 4.11 Total leachate concentration of chloride and sulfate (left), and total concentration of heavy metals (namely Cu, Ba, As, Zn, Ni, Cr, Cd, Pb; right) with respect to particle size.

4.5 Conclusions

The relations between leaching behaviour of MSWI-FA (plant of Turin), chemical composition, particle size and speciation distribution were investigated. Zn and Pb are the most abundant heavy metals followed by Mn, Cu, Cr and Cd. Such species increase their concentrations with decreasing of particle size; chloride and sulfate behave alike. Alkaline metals, Al and Si, exhibit an opposite trend. Heavy metal leaching is primarily governed by salt dissolution (chloride and sulfate, mostly) and weak surface sorption (F1-speciation). It is significantly affected by Al/Fe (hydr)oxide surface complexation (F2-speciation) at acidic regime, as shown by experiments as a function of pH and thermodynamic geochemical modelling. Moreover, heavy metal leaching correlates with F2-speciation, heavy metal concentration *per* particle size class (HMSC), particle size (*s*) and F1-speciation, according to the following order of relevance: F2<HMSC<*s*<F1. However, a very high positive linear correlation holds between heavy metal leaching and F1 relative fraction, only. This indicates that F1 is a valuable marker of the potential heavy metal leaching. Notwithstanding the complexity of the whole sequential extraction method, it should still be implemented at the F1-speciation level to become a reference check of leaching behaviour. In this way, it can be taken into account the potential heavy metal leaching associated with an acid rain scenario, whose pH lies in the interval of F1-speciation determination (5-5.5). Still, kinetics (long-term leaching) should also be considered to fully translate in real scale the results here discussed, which assume that the thermodynamic equilibrium is reached. Moreover, F1-speciation moderately correlates with *s*, and the correlation sign changes as a function of the species involved (Pb-Zn and Cr-Cu-Mn-Ni have opposite trends). Therefore, despite the chemical composition of FA shows an enrichment of contaminants in the fine fractions, the supposed increase of leaching with decrease of grain size does not hold for all of the heavy metals under investigation. Indeed, no significant differences in terms of magnitude are observable when the total salt and total heavy metal leaching is considered. As a consequence, grain size separation pre-treatments are expected to be of comparatively modest efficiency in tailoring leaching curbing methods.

4.6 References

1. Joseph A.M.; Snellings R.; Van den Heede P.; Matthys S.; De Belie N. The Use of Municipal Solid Waste Incineration Ash in Various Building Materials: A Belgian Point of View. *Materials* **2018**, 11, 141.

2. Liao C.; Wu C.; Yan Y. The characteristics of inorganic elements in ashes from a 1 MW CFB biomass gasification power generation plant. *Fuel Proc. Tech.* **2017**, 88, 149-156.
3. Zhang H.; He P.; Shao L.M. Fate of heavy metals during municipal solid waste incineration in Shanghai. *J. Hazard. Mat.* **2008**, 156, 365-373.
4. Lanzerstorfer C. Cyclone fly ash from a grate-fired biomass combustion plant: dependence of the concentration of various components on the particle size. *Fuel Proc. Tech.* **2015**, 131, 382-388.
5. Raclavská H.; Corsaro A.; Hartmann-Koval S.; Juchelková D. Enrichment and distribution of 24 elements within the sub-sieve particle size distribution ranges of fly ash from wastes incinerator plants. *J. Environ. Manag.* **2017**, 203, 1169-1177.
6. Kanhar, A.H.; Chen, S.; Wang, F. Incineration Fly Ash and Its Treatment to Possible Utilization: A Review. *Energies* **2018**, 13, 6681.
7. SW-846 Test Method 1313: Liquid-Solid Partitioning as a Function of Extract pH Using a Parallel Batch Extraction Procedure **2017**, https://www.epa.gov/hw-sw846/sw-846-test-method-1313-liquid-solid-partitioning-function-extract-ph-using-parallel-batch.
8. Bruder-Hubscher V.; Lagarde F.; Leroy M.J.F.; Coughanowr C.; Enguehard F. Application of a sequential extraction procedure to study the release of elements from municipal solid waste incineration bottom ash. *Anal. Chim. Acta* **2020**, 451, 285-295.
9. ISO 12782-1:2012 Soil quality — Parameters for geochemical modelling of leaching and speciation of constituents in soils and materials — Part 1: Extraction of amorphous iron oxides and hydroxides with ascorbic acid **2012**, https://www.iso.org/standard/51697.html.
10. Gustafsson J.P. **2013** Visual MINTEQ 3.1. http://vminteq.lwr.kth.se/.
11. Meima J. A.; Comans R. N.J. The leaching of trace elements from municipal solid waste incinerator bottom ash at different stages of weathering. *Appl. Geochem.* **1999**, 14, 159-171.
12. Hiemstra, T.; van Riemsdijk, W.H., On the relationship between charge distribution, surface hydration, and the structure of the interface of metal hydroxides. *J. Colloid Interface Sci.* **2006**, 301, 1–18.
13. Tiberg, C.; Sjöstedt, C.; Persson, I.; Gustafsson, J.P. Phosphate effects on copper(II) and lead(II) sorption to ferrihydrite. *Geochim. Cosmochim. Acta* **2013**, 120.
14. Chang, F. Y.; Wey, M. Y. Comparison of the characteristics of bottom and fly ashes generated from various incineration processes. *J. Hazard. Mat.* **2006**, 138(3), 594-603.
15. Cosgrove T. Colloid Science Principles, Methods and Applications; Blackwell Publishing Ltd. **2005** Hoboken, NJ, USA.
16. Jiao F.; Zhang L.; Dong Z.; Namioka T.; Yamada N.; Ninomiya Y. Study on the species of heavy metals in MSW incineration fly ash and their leaching behavior. *Fuel Proc. Tech.* **2016**, 152, 108-115.
17. Yuan K.; Soo Lee S.; De Andrade V.; Sturchio N.C.; Fenter P. Replacement of Calcite (CaCO3) by Cerussite (PbCO3). *Environ. Science & Tech.* **2016**, 50, 23, 12984–12991.
18. Munemoto T.; Fukushi K.; Kanzaki Y.; Murakami T. Redistribution of Pb during transformation of monohydrocalcite to aragonite. *Chem Geol.* **2014**, 387, 133-143.
19. Zhang Y.; Cetin B.; Likos W.J.; Edil T.B. Impacts of pH on leaching potential of elements from MSW incineration fly ash. *Fuel* **2016**, 184, 815-826.
20. Chakraborty P.; Chakrabarti C. L. Chemical speciation of Co, Ni, Cu, and Zn in mine effluents and effects of dilution of the effluent on release of the above metals from their metal-dissolved organic carbon (DOC) complexes. *Anal. Chim. Acta* **2018**, 571, 260–269.
21. Dijkstra J.J.; Van Zomeren A.; Meeussen J. C. L; Comans R. N. J. Effect of Accelerated Aging of MSWI Bottom Ash on the Leaching Mechanisms of Copper and Molybdenum. *Environ. Science & Tech.* **2006**, 40, 4481–4487.
22. Zhang Y.; Jiang J., Chen M. MINTEQ modeling for evaluating the leaching behavior of heavy metals in MSWI fly ash. *J. Environ. Sciences* **2008**, 20, 1398-1402,
23. Zhou J.; Wu S.; Pan Y.; Zhang L.; Cao Z.; Zhang X.; Yonemochi S., Hosono S.; Wang Y.; Oh K.; Qian G.

Enrichment of heavy metals in fine particles of municipal solid waste incinerator (MSWI) fly ash and associated health risk. *Waste Manag.* **2015**, 43, 239-246.

24. Tang Q.; Liu G.; Zhou C.; Sun Distribution of trace elements in feed coal and combustion residues from two coal-fired power plants at Huainan, Anhui, China. *Fuel* **2013**, 107, 315–322.
25. Lindberg D.; Molin C.; Hupa M. Thermal treatment of solid residues from WtE units: A review. *Waste Manag.* **2015**, 37, 82-94.
26. Wang Y.; Li Y.; Cao H.; Xiong M.; Shugart Y.Y.; Jin L. Efficient test for nonlinear dependence of two continuous variables. *BMC Bioinformatics* **2015**, 16, 260.
27. Destefanis, E.; Caviglia, C.; Bernasconi, D.; Bicchi, E.; Boero, R.; Bonadiman, C.; Confalonieri, G.; Corazzari, I.; Mandrone, G.; Pastero, L.; Pavese, A.; Turci, F.; Wehrung, Q. Valorization of MSWI Bottom Ash as a Function of Particle Size Distribution, Using Steam Washing. *Sustainability* **2020**, 12, 9461.

Chapter 5

MSWI fly ash multiple washing: kinetics of dissolution in water, as function of time, temperature and dilution

5.1 Introduction

MSWI-FA is classified as a hazardous waste by the European regulatory authorities [1] and, in the previous chapter, a detailed investigation of Turin plant MSWI-FA compositional characteristics has been conducted, showing the relatively high content of chlorides and heavy metals. Because of these features, the recycling of MSWI-FA for profitable applications is challenging. For instance: the presence of carbonate salt and metal oxides leads to a highly basic natural pH (~10–12) [2-5]; the chloride content promotes corrosion of reinforced concrete structures [6]; the high water-absorption capacity of hygroscopic $CaCl_2$ causes low workability of lime scrubber-treated MSWI-FA [7]. The revalorization of MSWI-FA, or at least its safe disposal, is primarily related to being able to enhance its stability in water and curb as much as possible its heavy metal leaching, using treatments of low environmental impact that are economically sustainable. Among the most common treatments to remove/curb chloride and heavy metals (primarily Zn, Pb, Cu, and Cd) are: washing with deionized water or added with basic leaching solvents [8-10]; thermal treatments in rotary kilns [11]; bioleaching (or microbial leaching, a biohydrometallurgical technology that can be applied for metal recovery) [12]; electrolytic treatments [13,14]; carbonation, reacting with CO_2 to produce stable carbonate [15]. Washing treatments, especially with acid additives, have been shown to provide the highest efficacy in terms of heavy metal removal, but they usually require a long time and a considerable amount of water (liquid-to-solid, L/S, ratio of 25 and duration of 1-24 h, [16]), often in combination with additives that improve the solving capacity of the solution but at the cost of managing further potential pollutants [17]. In the present work, water washing cycles were performed to help answer the following general question: “To which extent can the original fly ash be transformed into a product that is a non-hazardous waste, and possibly reusable, exploiting a treatment that relies upon iterative water washings only and uses comparatively small liquid/solid ratios?” In particular, the focus is on how such a treatment changes the mineralogical phase composition and heavy metal speciation distribution, to shed light on its efficacy to reduce chloride, sulfate, and heavy metal leaching from MSWI-FA.

5.2 Materials and Methods

5.2.1 Water washing set-up

Each water washing cycle is constituted by a water flow traversing MSWI-FA, implemented according to the water washing “falling head” (FH-WW) geometry (Figure 5.1). MSWI-FA particles are loosely packed by mechanical compacting, to have an average dry density in the range of 0.6–0.7 g/cm^3. Deionized water is used to fill the free head (Chamber 1, Figure 5.1). Water washing flows downwards through MSWI-FA inducing mineral dissolution reactions [18], which are affected by (i) mineral solubility and related kinetics, (ii) degree of packing, and (iii) total time of water percolation; the latter is proportional to the amount of water used. MSWI-FA is laid on a paper filter (with a thickness of 0.21 mm and a particle retention of 10 μm)

that retains the solid fraction, letting the resulting solution pass through and be collected in the second chamber of Figure 5.1. Such a process is formalized by Darcy's law [19]:

$$\frac{\Delta V}{A \times \Delta t} = \frac{\Delta h}{\Delta t} = -K\frac{h}{H}$$

where A = head's section; ΔV = head's change in Δt; h = head's height; Δh = height's change in Δt; H = thickness of the sample; K = hydraulic permeability. K has long been known to primarily depend on particle size and bulk density, both varying as a function of time because of the changes induced by the dissolution of the mineral particles [20]. The dependence of K on t is associated with changes of MSWI-FA's packing, induced by particle readjustment and mineral dissolution. An L/S ratio of 5 was chosen for each step.

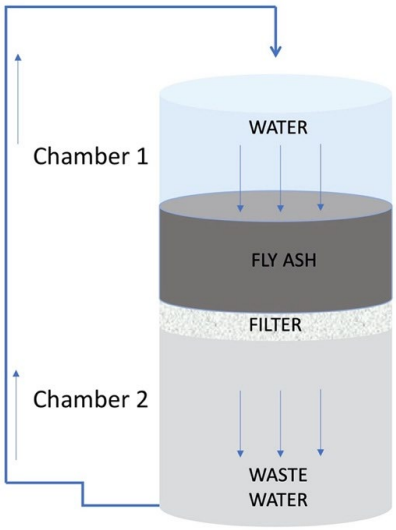

Figure 5.1 Scheme of the multi-step water washing.

The wastewater that is collected from percolation is supposed to undergo depuration of the contaminant species leached out from MSWI-FA, and then used as a regenerated solvent for a new washing step. Here, the focus is on the assessment of the methodology using a low electrolytic conductivity water, thus clean deionized water is employed for each step. Specifically, attention is concentrated on (i) the role of the washing water's initial temperature (T) in relation to the kinetics of the dissolution reactions, and (ii) effects induced by washing cycles.

For comparison, batch water washing treatments (24 h shaking; L/S between 2 and 50) were performed in triplicate to determine the concentrations of chloride, sulfate, and heavy metals that are leached out as a function of L/S.

5.2.2 Sequential extraction procedure

A modification of the four-step sequential extraction method employed in the previous chapter has been here introduced, to get an insight into heavy metal speciation distribution before and after treatment. In particular, an additional step was added at the beginning, to recognize the water/exchangeable fraction F0. Practically, an aliquot of 8 ml of magnesium chloride (1 M) was added to 1 g of dry FA in a 100 ml glass container. The mixture was shaken for 16 h (overnight) with a magnetic stirrer at room temperature at a speed of 40 rpm. The extract was separated from the solid residue by filtration through a 0.45 µm cellulose

nitrate filter (47mm diameter). The extract was analyzed immediately or stored at 4 °C. The solid residue was washed with deionized water and underwent step 2.

5.3 Results

5.3.1 Washing tests

Room-temperature washing tests provide a reference for MSWI-FA dissolution as a function of L/S, assuming a constant treatment duration of 24 h; data are set out in the Table 5.1 and summarized in Figure 5.2 a,b. For convenience, the leached ions are divided into two main categories: $\Sigma_{major\ ions}$, i.e., the sum of Na, K, Ca, Mg, bromide, fluoride, chloride, sulfate, and nitrate; and $\Sigma_{heavy\ metals}$, i.e., the sum of Cr, Ni, Cu, Zn, Cd, Fe, Ba, and Pb. The $\Sigma_{heavy\ metals}$ exhibits high sensitivity to the L/S ratio, as suggested by a change of 75–80% on the L/S-range 5–50. This hints at an expected relevant role of L/S in promoting removal of heavy metals. As for $\Sigma_{major\ ions}$, a change of 25–30% occurs in the L/S-range 5–50; such a figure is comparable to the one observable in the case of weight loss. At L/S 10, the concentrations of chloride and sulfate become weakly dependent on time for a treatment duration over 10 min, approaching the almost invariant values of 8698 ± 100 and 3085 ± 91 mg/L, respectively, and reaching the highest EC values (Figure 5.3). Conversely, heavy metals do not show definite trends as a function of washing time, as proven by the comparatively small oscillations in concentration observable in the range of 10–1440 min (average ± e.s.d.: Cr = 6.08 ± 0.02 mg/L, Ni = 0.32 ± 0.06 mg/L, Zn = 3.99 ± 0.07 mg/L, Cd = 4.65 ± 0.05 mg/L, Fe = 22.4 ± 1.22 mg/L, Pb = 1.29 ± 0.55 mg/L).

Table 5.1. Concentration of fly ash washing solutions from the Turin plant, compared with the legislation limits: * Decr. Min. Amb. 27/09/2010 about the landfill of waste; ** D. M. 186/2006 on waste reuse. Concentrations expressed in mg/L.

	L/S 2	L/S 5	L/S 10	L/S 20	L/S 50	Inert*	Non hazardous*	Hazardous	Reuse**
conductivity (µs/cm)	102000	52000	32000	19000	8600				
pH	12	12	12	12	12				5.5-12
weight loss %	5	10	12	18	21				
Na (mg/L)	17424	5353.2	3138	1417.2	589.32				
K	19362	6324	3195	1567.2	636.6				
Ca	1503.6	1334.4	1263.9	832.56	345				
Mg	17.364	17.256	8.613	33.924	17.004				
Chloride	43888	15763	8698	5266	1217	80	2500	2500	100
Bromide	517	225	115	68	19				
Fluoride	13	15		2.2		1	15	50	1.5
Sulfate	6719	3774	3085	804	600	100	5000	5000	250
Nitrate	n.d.	n.d.	n.d.	n.d.	n.d.				50
Cr	11.772	12.87	6.081	25.512	12.648	0.05	1	7	0.05
Ni	0.49692	19.068	0.3219	0.186	0.06126	0.04	1	4	0.01
Cu	0.001	0.001	0.001	0.001	0.001	0.2	5	10	0.05
Zn	7.02	7.056	3.999	24.276	17.262	4	5	20	3

Cd	9.198	10.374	4.65	1.926	0.9264	0.004	0.1	0.5	0.005
Fe	67.14	30	22.245	13.092	8.526				
Ba	18.786	29.136	13.797	12.264	1.005	2	10	30	1
Pb	12.918	12.918	12.918	3.468	12.858	0.05	1	5	0.05

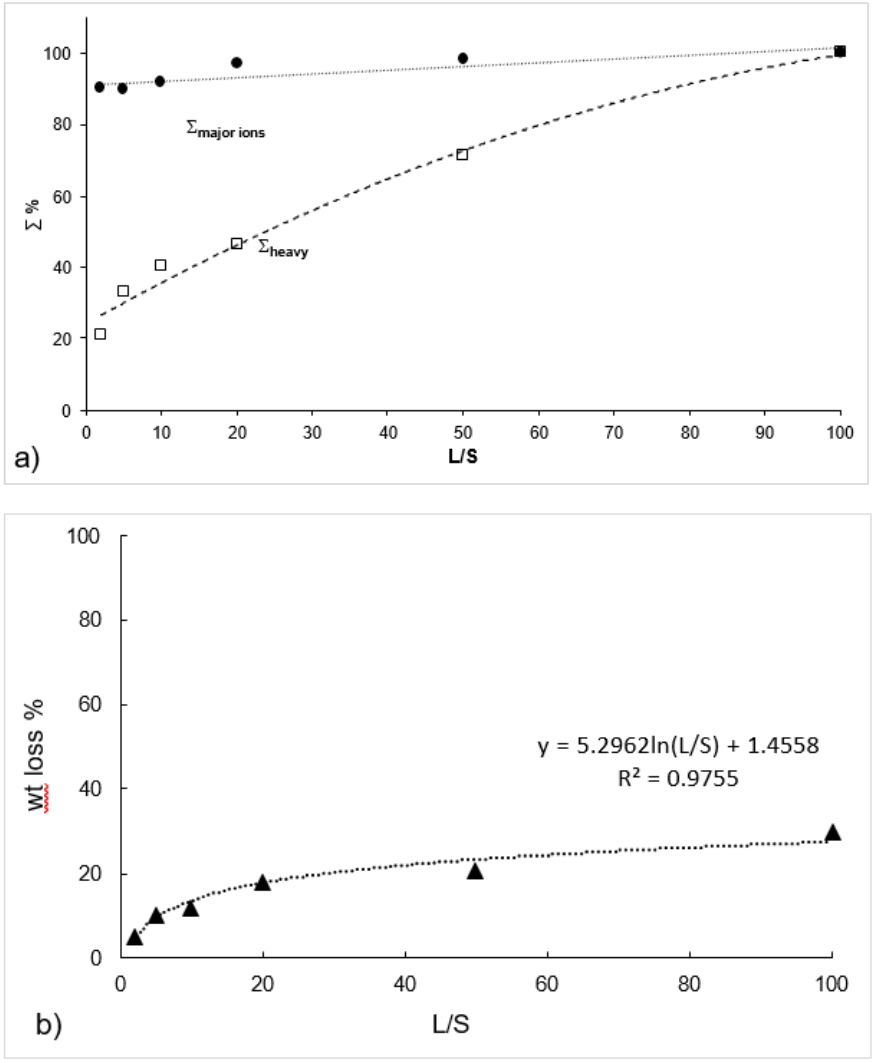

Figure 5.2 Washing treatments: 24 h duration. (**a**) $\Sigma_{major\ ions}$ = Na, K, Ca, Mg, bromide, fluoride, chloride, sulfate, and nitrate (filled circles), and $\Sigma_{heavy\ metals}$ = Cr + Ni + Cu + Zn + Cd + Fe + Ba + Pb (empty squares), versus L/S. Figures are normalized to their maximum values in terms of $\Sigma_{major\ ions}$ and $\Sigma_{heavy\ metals}$. (**b**) Weight loss (triangles) of MSWI-FA versus L/S because of mineral dissolution due to washing.

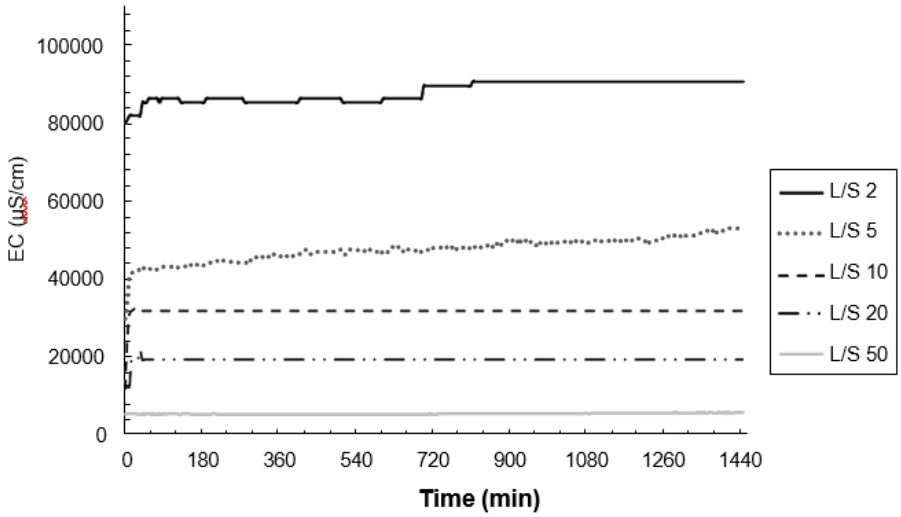

Figure 5.3. Time (min) *versus* EC (µS/cm) of fly ash washing test at different L/S ratios, from 2 to 50.

XRD measurements on original MSWI-FA reveal (Table 5.2) the occurrence of minerals such as halite (NaCl; 12 wt%), sylvite (KCl; 8 wt%), syngenite ($K_2Ca(SO_4)_2 \cdot H_2O$; 7wt%), anhydrite ($CaSO_4$; 10 wt%), calcite ($CaCO_3$; 6 wt%), quartz (SiO_2; 2 wt%), and gehlenite ($Ca_2Al_2SiO_7$; 4 wt%), along with over 50 wt% of amorphous fraction. The washing treatment induces partial hydration of anhydrite into either bassanite ($CaSO_4$ $0.5H_2O$), for L/S=2, or gypsum ($CaSO_4 \cdot 2H_2O$), for L/S > 2, while highly soluble salt (halite, sylvite, and syngenite) are almost completely dissolved for L/S > 5, thus resulting in a relative increase of the less soluble phases, such as quartz (5 wt%) and anhydrite (17 wt%). The fly ash particle size distribution becomes coarser after washing, since the finer fraction, represented mainly by salts, has dissolved.

Table 5.2 Mineralogical composition (wt%) of fly ash: fly ash before washing test and fly ash residual solid (Res) after washing test at different L/S. Crystalline phase content is estimated with an error of 1% wt, while amorphous fraction content is estimated with an error of 5% wt.

wt%	Bulk Fly Ash	Res.L/S 2	Res.L/S 5	Res.L/S 10	Res.L/S 20	Res.L/S 50
Halite	12	6	4			
Sylvite	8	2				
Calcite	6	6	6	7	8	7
Syngenite	7	5	2			
Anhydrite	10	12	13	14	15	14
Quartz	2	2	4	6	5	6
Bassanite		8				
Gypsum			11	12	10	12
Gehlenite	4	5	6	6	6	6
Amorphous	51	54	54	55	56	55

5.3.2 Falling Head Water Washing

The change in composition of the solution from the water suspension with MSWI-FA is shown as a function of the washing steps (N_{ws}), setting L/S=5, T=25 or 80 °C. In particular, three classes of observables are considered, namely, pH, $C_t(\Sigma_{major\ ions})$, and $C_t(\Sigma_{heavy\ metals})$, to help point out the changes induced in MSWI-FA because of a flow of washing water. $C_t(\Sigma_{major\ ions})$ and $C_t(\Sigma_{heavy\ metals})$ define the cumulative leaching concentration as a function of the washing steps and provide a measure of the capacity of FH-WW to extract and bring into solution contaminants, thus removing them from the dry residue (Figure 5.4). Firstly, it is possible to notice that water takes ~2 min to pass through a MSWI-FA sample at T = 80 °C, and ~4 min in the case of T = 25 °C, because of an increase of the dissolution kinetics with temperature, thus accelerating percolation. All this is in keeping with the fact that, at 80 °C, the weight loss after 5 and 12 washing steps is 18 and 21 wt%, respectively; such figures change into 17 and 19% at room temperature. In all cases (Figure 5.4, top and bottom) the cumulative leaching concentration increases very rapidly and then shows steady trends: quasi-flat for $\sum_{major\ ions}$ versus relatively steep for $\sum_{heavy\ metals}$, the latter exhibiting a *T*-dependent slope ($dC_t(\sum_{heavy\ metals})/dN_{ws}$ = 0.612 and 2.603 mgL^{-1}/cycle, for *T* = 25 and 80 °C, respectively; N_{ws}-range = 5–12). The concentration trends qualitatively suggest that: (i) the effect of temperature is modest on chloride and sulfate removal, while becoming more relevant for heavy metals; (ii) the achievement of a quasi-steady state for most of the ions is observable after 6–7 washing cycles, though Ca^{2+}, Pb, Zn, and SO_4^{2-} continue slightly increasing their concentrations from the ninth washing treatment onwards. Conversely, the pH trend, expressed as the average between the values measured at T = 25 ◦C and 80 °C, oscillates around a basic value of the averaged value of 11.2 ± 0.4 (Figure 5.5) and stabilizes around 10.9.

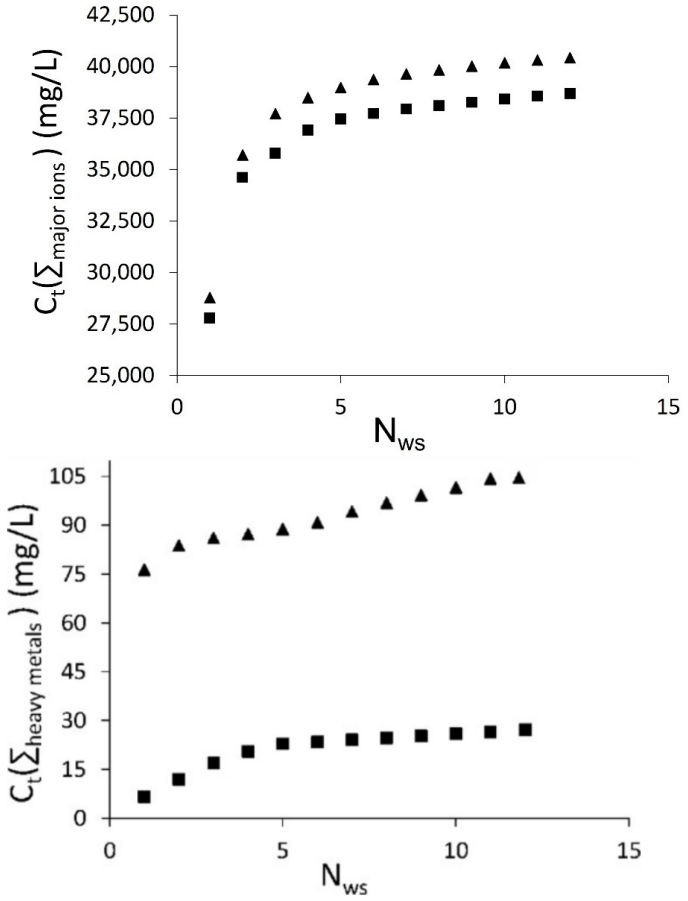

Figure 5.4 Cumulative leaching concentration (Ct) $\Sigma_{major\ ions}$, top, and $\Sigma_{heavy\ metals}$, bottom, versus number of washing steps (N_{ws}) at 25 (squares) and 80 ℃ (triangles).

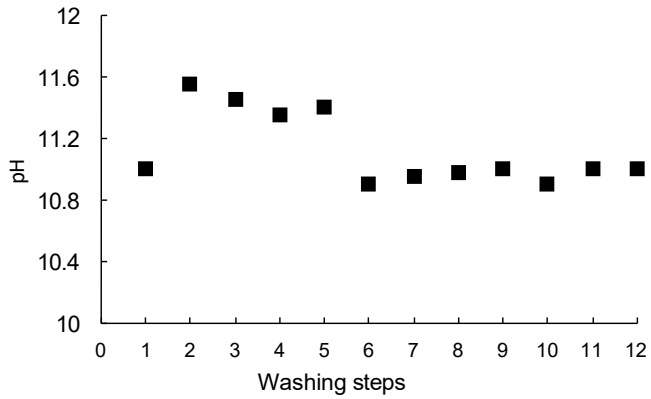

Figure 5.5 Average pH values as a function of N_{WS} (number of washing steps).

5.3.3 Leaching Tests

Leaching tests (Table 5.3), applied to the dry solid residue after FH-WW (N_{ws} up to 30), show that Cr, Ni, Cd, sulfate, and fluoride are still over the Italian legal limits for reuse [21]. Comparing N_{ws}=5 with N_{ws}=12, a significant difference is apparent in the case of Na, K, Ca, chloride, sulfate, and Cr, which exhibit high sensitivity to dilution.

Table 5.3 Leaching test (L/S = 10) of the solid residue of FA after five- and twelve-step FH-WW at 80 ℃ and five-, twelve-, and thirty-step FH-WW at 25 ℃. Legend 1: Nws = 5, L/S = 5, T = 80 ℃; 2: Nws = 12, L/S = 5, T = 80 ℃; 3: Nws = 5, L/S = 5, T = 25 ℃; 4: Nws = 12, L/S = 5, T = 25 ℃; 5: Nws30, L/S = 5, T= 25 ℃; 6: 24 h washing L/S = 50, T = 25 ℃; 24 h washing, L/S = 5, T = 25 ℃. Legal limits according to: [21,22].

	1	2	3	4	5	6	7	Not Reactive	Non Hazardous	Hazardous	Reuse
E.Cond. (µs/cm)	1650	1037	1858	1500	1340	1400	3160				
pH	9.6	9.6	9.7	9.2	9.2	9.1	9.4				5.5–12
Na (mg/L)	36	15	45	25	20	41	167				
K(mg/L)	37	31	58	15	9	31	159				
Ca (mg/L)	440	240	409	329	311	273	365				
Mg (mg/L)	0.3	0.2	0.3	0.3	0.2	0.6	7				
Chloride (mg/L)	51	43	100	83	73	125	500	80	2500	2500	100
Bromides (mg/L)	0.5	n.d.	3.4	2.8	n.d.	1.1	n.d.				
Fluorides (mg/L)	n.d.	1.1	1.7	2	1.2	0.5	n.d.	1	15	50	1.5
Sulfate (mg/L)	574	431	860	662	578	475	920	100	5000	5000	250
Nitrate (mg/L)	0.4	n.d.	n.d.	0.8	n.d.	1.3	n.d.				50
Cr (mg/L)	0.18	0.10	0.08	0.03	0.06	0.13	0.25	0.05	1	7	0.05
Ni (mg/L)	0.09	0.08	0.02	n.d.	0.05	0.06	0.11	0.04	1	4	0.01
Cu (mg/L)	0.04	0.05	n.d.	n.d.	n.d.	n.d.	n.d.	0.2	5	10	0.05
Zn (mg/L)	0.1	0.2	n.d.	n.d.	0.005	0.05	0.04	4	5	20	3
Cd (mg/L)	0.02	0.02	n.d.	n.d.	n.d.	n.d.	n.d.	0.004	0.1	0.5	0.005
Ba (mg/L)	0.12	0.12	0.04	0.08	0.06	0.11	0.1	2	10	30	1
Pb (mg/L)	0.04	0.05	n.d.	n.d.	n.d.	0.005	n.d.	0.05	1	5	0.05

At T = 25 °C, leaching tests indicate that a five-step treatment is not sufficient to reduce Cr, Ni, Cd, fluoride, and sulfate below the legislation limits for reuse (Table 5.3). Conversely, a twelve-step treatment gives leachates in which all the analyzed heavy metals lie under the legal limits, along with chloride, whereas only sulfate still lies above the limit (Table 5.3). For comparison, the leachates of a conventional water washing treatment of fly ash at L/S 50 and 24 h versus a thirty-step washing test at T = 25 °C are reported in Table 5.3 and Figure 5.6; a modest decrease both of chloride and sulfate is observable, with respect to N_{ws}=12. Note that the case of N_{ws}=80 (not reported here) still shows a sulfate concentration over the legal limit for reuse. The extrapolation of the sulphate concentration versus N_{ws} proves that a number of washing steps as large as 370 is supposed to provide a leachate within the legal limits for reuse. As to the heavy metals, no significant decrease is observable when comparing N_{ws}=12 with N_{ws}=30.

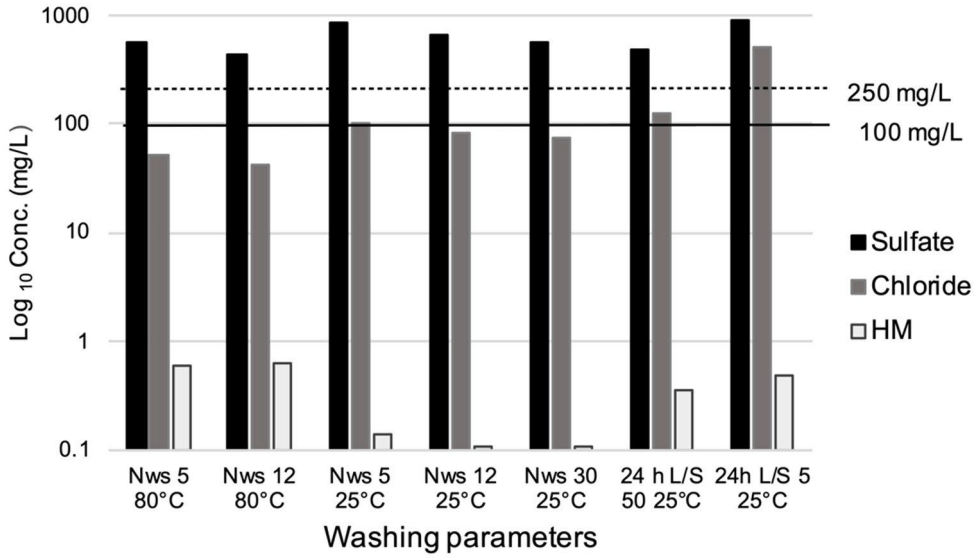

Figure 5.6 Leaching tests on FA treated by FH-WW, as a function of temperature (25–80 °C) and Nws (5–30); for comparison, the cases of 24 h washing with L/S = 50 and 5 are reported. Attention is focused on chloride, sulfate, and heavy metal (HM) concentrations. Dotted line and solid line: legal limits for reuse in the case of sulfate (250 mg/L) and chloride (100 mg/L), respectively.

5.4 Discussion

5.4.1 Kinetics modelling

The FH-WW related phenomenology can be better analyzed by employing the kinetics reaction formalism and using the cumulative leaching concentrations as experimental variables (Figure 5.4). In a liquid/solid reaction system, the kinetics rate is generally influenced by chemical species diffusion through the solvent, diffusion through the solid layer, and/or possible chemical reactions at the solid particles' surface [23]. This is described by the shrinking core model (SCM), which assumes homogeneous spherical particles and derives two formulations to take chemical reactions or diffusion through the outer layer into account [24,25]:

$$1-(1-\alpha)^{\frac{1}{3}} = k_R t$$

$$1-3(1-\alpha)^{\frac{2}{3}}+2(1-\alpha) = k_D t$$

where α represents the relative cumulative leaching with respect to the maximum after 12 steps; k_D (diffusion) and k_R (reactions) are the reaction rate constants; t is the time calculated by multiplying the number of steps by the mean water contact time (i.e., 4 and 2 min for 25 and 80 ℃, respectively). Table 5.4 and Figure 5.7 show how the second SCM formulation better fits both heavy metals and major ions data, though all the correlation coefficients are not ideal ($R^2 < 0.95$).

Table 5.4 Linear correlation coefficient of SCM plots.

	Temperature (°C)	R^2 (R)	R^2 (D)
$\Sigma_{\text{heavy metals}}$	25	0.93	0.93
	80	0.91	0.93
$\Sigma_{\text{major ions}}$	25	0.91	0.93
	80	0.92	0.94

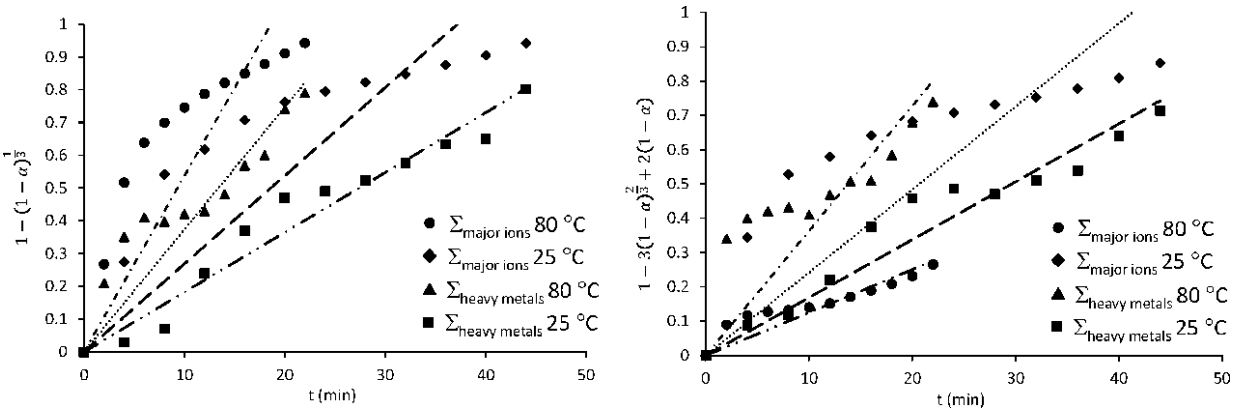

Figure 5.7 SCM plots when chemical reactions (left) or diffusion (right) are considered the rate-determining step.

Considering the cumulative leaching concentration trends, it is possible to parametrize the process by a second-order rate law. This empirical approach has been successfully employed in similar fields, involving heavy metals extraction from sludge [26,27]. After [28] the formulation can be written as:

$$\frac{dC_t}{dt} = k(C_s - C_t)^2$$

$$\frac{t}{C_t} = \frac{1}{kC_s^2} + \frac{t}{C_s}$$

where C_t represents the cumulative leaching concentration at time t, k is the leaching rate constant, and C_s the cumulative leaching concentration at saturation conditions (i.e., $t \to \infty$, which implies $N_{ws} \to \infty$). The resulting plots are displayed in Figure 5.8, where good agreement between model and experiments is proven by the high correlation coefficient in all cases ($R^2 > 0.98$).

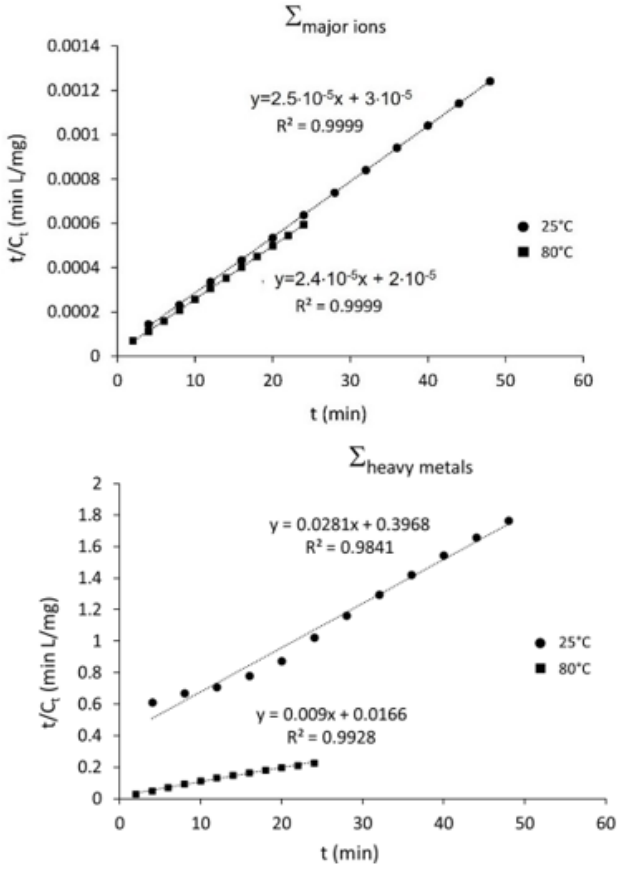

Figure 5.8 Empirical second-order reaction model plots for $\sum_{heavy\ metals}$ (bottom) and $\sum_{major\ ions}$ (top).

Table 5.5. Kinetical parameters derived from the empirical second-order reaction model.

	***Cs* (mg/L)**	***k* (L mg^{-1} min^{-1})**	**R^2**
$\Sigma_{heavy\ metals}$	35.71	3.2×10^3	0.9841
	111.11	7.4×10^5	0.9982
$\Sigma_{major\ ions}$	40,000	5.3×10^{13}	0.9999
	42,478	7.2×10^{13}	0.9999

The relevant difference between the curves' slopes at the beginning ($N_{ws} < 5$) and at the end ($N_{ws} > 5$) of the washing process in Figure 5.4 suggests that the reaction is divided into two stages: (i) an intense and fast dissolution occurs at the start, due to the scrubbing action of the water flow and the soluble salt clustering on particle surface, as shown [29]; (ii) a slower chemical species diffusion develops from solid into solution, successively. Leaching tests on FH-WW treated samples (Table 5.3 and Figure 5.6) indicate that FH-WW at 25 ℃ gives a dry product that is less prone to heavy metal leaching than its counterpart at 80 ℃. Although such an issue is unexpected, it is confirmed by full reproducibility of the observations. This effect is possibly engendered by the residue of incomplete dissolution reactions boosted by high temperature and interrupted before completion because of kinetic reasons, thus leaving the solid portion still reactive to water.

A comparison with conventional single-step washing treatments at L/S = 50 and L/S = 5 (duration: 24 h) shows the higher efficiency of FH-WW on chloride and heavy metal removal. In particular, by comparing the

washing treatment relying on L/S = 50 and t = 24 h against FH-WW with N_{ws} = 30, it is evident that FH-WW not only provides an improvement in terms of dry product leaching (chloride and heavy metals), but also allows saving both water (L/S = 50 versus 5) and time (24 versus 2.5 h).

MSWI-FA is easily converted into non-hazardous waste, whereas it is more complex to achieve the conditions required for non-reactive waste. In particular, sulfate is the contaminant that shows the lowest sensitivity to those of FH-WW's parameters (temperature and N_{ws}) that are technologically manageable. An increase in the L/S ratio, i.e., a dilution of the solution, leads to a decrease in leachate's sulfate concentration, as proven by the leaching tests on fly ash treated with L/S = 5 and 50; yet, this is a strategy difficult to be developed on a large scale. The phase compositions of the FA after FH-WW (Table 5.6) do not show significant differences between samples washed with five- or twelve-step treatments, at 25 and 80 ℃, in terms of occurring minerals and their relative amounts. In all cases, the soluble chloride is not detectable anymore, while the most abundant crystalline phase is represented by anhydrite that is not associated with any of its hydration products, such as bassanite and gypsum. This is likely related to the off-equilibrium conditions due to the kinetics driving the process. Conversely, the standard washing treatment (static batch and 24 h duration) provides better approximate equilibrium conditions. Nonetheless, the relatively large amount of anhydrite and its slow kinetics of dissolution [30] are probably the reason why there is still relevant sulfate concentration in leachates even after 30 steps.

Table 5.6 Mineralogical composition (wt%) of fly ash after FH-WW. Crystalline phase content is estimated with an error of 1% wt, while amorphous fraction content is estimated with an error of 5% wt.

wt%	5-Step at 25 °C	12-Step at 25 °C	5-Step at 80 °C	12-Step at 80 °C	30-Step
Calcite	8	7	9	8	6
Anhydrite	15	14	17	16	13
Quartz	8	10	7	10	10
Gehlenite	7	8	8	7	9
Amorphous	62	61	60	59	62

5.4.2 Speciation distribution

The MSWI-FA leaching of heavy metals is rationalized through their speciation distribution, which was obtained by the five-class sequential extraction method. The five classes are defined as follows: easily exchangeable (F0), carbonates (F1), reducible (F2), oxidizable (F3), and residual (F4). F0 and F1 point to speciation types that are prone to a comparatively low acidic dissolution and, hence, are potentially responsible for most of the heavy metal leaching. F4 speciation is associated with virtually insoluble phases, unless a very strong acid attack is used [31]. F2 and F3 speciation types are intermediate between F1 and F4. In so doing, the speciation distribution of pristine MSWI-FA, five- and twelve-step washing treatments at 80 ℃, was determined. All the results from sequential extraction experiments are shown in Figure 5.9

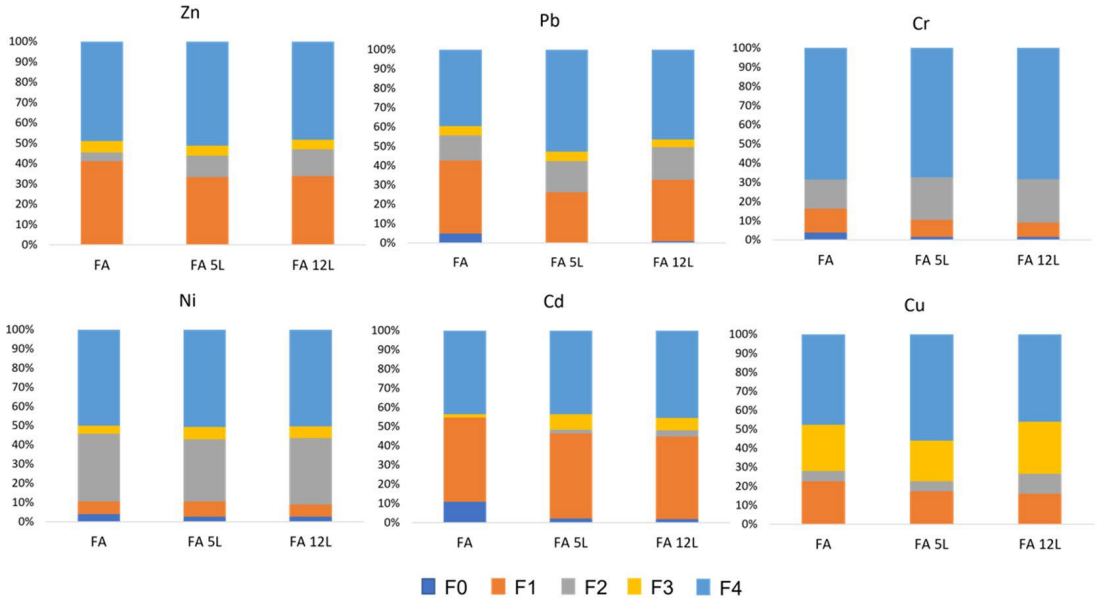

Figure 5.9 Speciation distribution of the main heavy metals for pristine FA and FA that underwent five- and twelve-step washing treatments at 80 °C. 5 L: N_{ws} = 5; 12 L: N_{ws} = 12.

Leaching tendency is mainly correlated with F0 and F1, which represent the fractions associated with crystal/glass particles prone to species exchange and carbonate, respectively [32]. Although F4 provides the highest fraction percentage for all heavy metals (between 40–65%), it is constituted of very low soluble phases, and therefore gives a relatively modest contribution to leaching. Conversely, the average large values of F0 + F1, which lie over 20% for most species, can explain the observed relevant heavy metal leaching. The FH-WW treatment markedly reduces the contribution of F0 and, to a lesser extent, F1's. The largest reduction involves Pb (16%) and is associated with chloride and carbonate [33,34]. For N_{ws} > 5, a steady improvement is not observed in terms of leaching reduction, save at the cost of a significant increase in the washing cycles (see Figure 5.4). Eventually, in the case of Ni, Cr, and Cd, the residual F0+F1 cumulative fraction (15–50%) is sufficient to leach out heavy metals whose concentrations lie above the legislated limits for FA reuse.

5.5 Conclusions

Falling head water washing (FH-WW) treatment was investigated to reduce chloride, sulfate, and heavy metal leaching from municipal solid waste incineration fly ash, which has a phase composition provided by amorphous (50 wt%), halite (12 wt%), sylvite (8 wt%), anhydrite (10 wt%), and, to a lesser extent, by quartz, calcite, and gehlenite (12 wt%). FH-WW relies upon soluble phase dissolution and removal of the related species that are dragged away by the gravity-driven flow of solvent traversing a FA sample. This is shown by the speciation distribution analysis, which proves the changes in terms of chloride/sulfate/heavy metals leaching from FA to be related to a reduction of the F0 + F1 solid fraction, i.e., ion exchangeable and carbonate phases. Dissolution kinetics is the key reaction governing the cleaning process of FH-WW, which, in this respect, differs much from conventional washing that takes place at quasi-equilibrium conditions. A more detailed analysis by employing an empirical second-order kinetics model suggests that a two-step mechanism is involved. At first, a very fast dissolution occurs, related to the readily soluble fraction present on the FA particle surface, followed by a much slower diffusion step. FH-WW yields a dry product with reduced contaminant leaching with respect to that from FA treated using conventional washing at L/S = 50

for 24 h, thus providing comparatively relevant water (L/S = 5 versus 50) and time (2.5 versus 24 h) savings. The use of high-temperature water in FH-WW, i.e., 80 °C, does not provide significant enhancement in terms of leaching behavior of the treated FA. Altogether, room temperature FH-WW is a successful strategy to take chloride and many heavy metals below the legal limits for reuse, whereas it fails for sulfate, Cr, and Ni. However, not all contaminants are reduced below the legal limits required for a non-hazardous waste classification.

5.6 References

1. Directive 2008/98/EC of the European Parliament and of the Council of 19 November 2008 on Waste and Repealing Certain Di- rectives. Available online: https://eur-lex.europa.eu/legal-content/EN/TXT/?uri=CELEX%3A02008L0098-20180705 (accessed on 9 April 2022).
2. Ginés, O.; Chimenos, J.M.; Vizcarro, A.; Formosa, J.; Rosell, J.R. Combined use of MSWI bottom ash and fly ash as aggregate in concrete formulation: Environmental and mechanical considerations. *J. Hazard. Mater.* **2009**, *169*, 643–650.
3. Colangelo, F.; Messina, F.; Cioffi, R. Recycling of MSWI fly ash by means of cementitious double step cold bonding pelletization: Technological assessment for the production of lightweight artificial aggregates. *J. Hazard. Mater.* **2015**, *299*, 181–191.
4. Yakubu, Y.; Zhou, J.; Ping, D.; Shu, Z.; Chen, Y. Effects of pH dynamics on solidification/stabilization of municipal solid waste incineration fly ash. *J. Environ. Manag.* **2018**, *207*, 243–248.
5. Ferraro, A.; Farina, I.; Race, M.; Colangelo, F.; Cioffi, R.; Fabbricino, M. Pre-treatments of MSWI fly-ashes: A comprehensive review to determine optimal conditions for their reuse and/or environmentally sustainable disposal. *Rev. Environ. Sci. Biotechnol.* **2019**, *18*, 453–471.
6. Zhou, Y.; Gencturk, B.; Willam, K.; Attar, A. Carbonation-induced and chloride-induced corrosion in reinforced concrete structures.
   J. Mater. Civ. Eng. **2015**, *27*, 04014245.
7. Cho, B.H.; Nam, B.H.; An, J.; Youn, H. Municipal Solid Waste Incineration (MSWI) Ashes as Construction Materials—A Review.
   Materials **2020**, *13*, 3143.
8. Kang, D.; Son, J.; Yoo, Y.; Park, S.; Huh, I.-S.; Park, J. Heavy-metal reduction and solidification in municipal solid waste incineration (MSWI) fly ash using water, NaOH, KOH, and NH_4OH in combination with CO_2 uptake procedure. *Chem. Eng. J.* **2020**, *380*, 122534.
9. Nordmark, D.; Lagerkvist, A. Controlling the mobility of chromium and molybdenum in MSWI fly ash in a washing process.
   Waste Manag. **2018**, *76*, 727–733.
10. Chen, X.; Bi, Y.; Zhang, H.; Wang, J. Chlorides Removal and Control through Water-washing Process on MSWI Fly Ash. *Procedia Environ. Sci.* **2016**, *31*, 560–566.
11. Huber, F.; Blasenbauer, D.; Mallow, O.; Lederer, J.; Winter, F.; Fellner, J. Thermal co-treatment of combustible hazardous waste and waste incineration fly ash in a rotary kiln. *Waste Manag.* **2016**, *58*, 181–190.
12. Gomes, H.I.; Funari, V.; Ferrari, R. Bioleaching for resource recovery from low-grade wastes like fly and bottom ashes from municipal incinerators: A SWOT analysis. *Sci. Total Environ.* **2020**, *715*, 136945.
13. Kirkelund, G.M.; Skevi, L.; Ottosen, L.M. Electrodialytically treated MSWI fly ash use in clay bricks. *Constr. Build. Mater.* **2020**,
    254, 119286.
14. Huang, T.; Zhou, L.; Liu, L.; Xia, M. Ultrasound-enhanced electrokinetic remediation for removal of Zn, Pb, Cu and Cd in municipal solid waste incineration fly ashes. *Waste Manag.* **2018**, *75*, 226–235.
15. De Boom, A.; Aubert, J.E.; Degrez, M. Carbonation of municipal solid waste incineration electrostatic

precipitator fly ashes in solution. *Waste Manag. Res.* **2014**, *32*, 406–413.
16. Phua, Z.; Giannis, A.; Dong, Z.L.; Lisak, G.; Ng, W.J. Characteristics of incineration ash for sustainable treatment and reutilization. *Environ. Sci. Pollut. Res.* **2019**, *26*, 16974–16997.
17. Kanhar, A.H.; Chen, S.; Wang, F. Incineration Fly Ash and its treatment to possible utilization: A review. *Energies* **2020**, *13*, 6681.
18. Li, L.; Steefel, C.I.; Yang, L. Scale dependence of mineral dissolution rates within single pores and fractures. *Geochim. Cosmochim. Acta* **2008**, *72*, 360–377.
19. Atangana, A. Chapter 2: Principle of Groundwater Flow. In *Fractional Operators with Constant and Variable Order with Application to Geo-Hydrology*; Atangana, A., Ed.; Academic Press: Cambridge, MA, USA, 2018; pp. 15–47, ISBN 9780128096703.
20. Chen, L.; Kang, Q.; Viswanathan, H.S.; Tao, W.Q. Pore-scale study of dissolution-induced changes in hydrologic properties of rocks with binary minerals. *Water Resour. Res.* **2014**, *50*, 9343–9365.
21. Ministerial Decree n. 186 Dated 5 April 2006. Regulatory That Modified Ministerial Decree Dated 5 February 1998. *Official Gazette n. 115.* 19 May 2006. Available online: http://www.gazzettaufficiale.it/eli/gu/2010/12/01/281/sg/pdf (accessed on 9 April 2022).
22. G.U. Ministerial Decree 27/09/2010-Definition of the Criteria of Admissibility of Landfill Waste. *Serie Generale n-281*. 1 December 2010. Available online: https://www.gazzettaufficiale.it/eli/id/2010/12/01/10A14538/sg (accessed on 9 April 2022).
23. Gharabaghi, M.; Irannajad, M.; Azadmehr, A. Leaching kinetics of nickel extraction from hazardous waste by sulphuric acid and optimization dissolution conditions. *Chem. Eng. Res. Des.* **2013**, *91*, 325–331.
24. Levenspiel, O. *Chemical Reaction Engineering*, 3rd ed.; Wiley: New York, NY, USA, 1998.
25. Souza, A.D.; Pina, P.S.; Lima, E.V.O.; da Silva, C.A.; Leão, V.A. Kinetics of sulphuric acid leaching of a zinc silicate calcine. *Hydrometallurgy* **2007**, *89*, 337–345.
26. Lee, I.H.; Wang, Y.J.; Chern, J.M. Extraction kinetics of heavy metal-containing sludge. *J. Hazard. Mater.* **2005**, *123*, 112–119.
27. Sakultung, S.; Pruksathorn, K.; Hunsom, M. Simultaneous recovery of valuable metals from spent mobile phone battery by an acid leaching process. *Korean J. Chem. Eng.* **2007**, *24*, 272–277.
28. Ho, Y.S.; Harouna-Oumarou, H.A.; Fauduet, H.; Porte, C. Kinetics and model building of leaching of water-soluble compounds of Tilia sapwood. *Sep. Purif. Technol.* **2005**, *45*, 169–173.
29. Bernasconi, D.; Caviglia, C.; Destefanis, E.; Agostino, A.; Boero, R.; Marinoni, N.; Bonadiman, C.; Pavese, A. Influence of speciation distribution and particle size on heavy metal leaching from MSWI fly ash. *Waste Manag.* **2022**, 138, 318–327.
30. Mbogoro, M.; Snowden, E.; Edwards, M.; Peruffo, M.; Unwin, P. Intrinsic Kinetics of Gypsum and Calcium Sulfate Anhydrite Dissolution: Surface Selective Studies under Hydrodynamic Control and the Effect of Additives. *J. Phys. Chem. C* **2011**, *115*, 10147–10154.
31. Bruder-Hubscher, V.; Lagarde, F.; Leroy, M.J.F.; Coughanowr, C.; Enguehard, F. 523 Application of a sequential extraction procedure to study the release of elements from municipal solid waste incineration bottom ash. *Anal. Chim. Acta* **2002**, *451*, 285–525.
32. Jiao, F.; Zhang, L.; Dong, Z.; Namioka, T.; Yamada, N.; Ninomiya, Y. Study on the species of heavy metals in MSW incineration fly ash and their leaching behavior. *Fuel Process. Technol.* **2016**, *152*, 108–115.
33. Funatsuki, A.; Takaoka, M.; Oshita, K.; Takeda, N. Methods of determining lead speciation in fly ash by X-ray absorption fine-structure spectroscopy and a sequential extraction procedure. *Anal. Sci.* **2012**, *28*, 481–490.
34. Zhang, Y.; Cetin, B.; Likos, W.J.; Edil, T.B. Impacts of pH on leaching potential of elements from MSW incineration fly ash. *Fuel* **2016**, *184*, 815–825.

Chapter 6

Influence of MSWI-FA introduction on metakaolin phosphate-based geopolymer structure and mechanical properties

6.1 Introduction

The ever-increasing necessity to reduce the environmental footprint of the building materials has prompted more sustainable alternatives to ordinary Portland cement (OPC) [1]. In this scenario, the interest for geopolymers has steadily grown. They represent an amorphous ceramic-like class of materials usually obtained by reacting an aluminosilicate "source" with a strong alkali base at room temperature, so as to generate a highly reticulated matrix of poly(siloxo)/poly(sialate) (Si-O-Si-O-/Si-O-Al-O-) units [2,3]. The resulting product exhibits high mechanical performance and fire resistance [4]. Initially, metakaolin (MK), from the calcination of natural kaolinite at >700 °C, was chosen as an aluminosilicate source because of its reactivity related to a large amorphous fraction and fine particle size. However, environmental concerns due to the high temperatures needed for its production and the exploitation of natural resources for kaolinite, motivated efforts steered to an at least partial replacement of MK [4]. Ground blast furnace slag (GBFS), coal fly ash (CFA) and also municipal solid waste incineration fly ash (MSWI-FA) have been/are being tested, alone or in blends, to reduce the amount of required MK and provide a recycling opportunity for these solid waste residues thereby [5,6,7]. Another possible route for geopolymers preparation involves the use of an acid solution, like phosphoric acid (H_3PO_4), to dissolve/depolymerize the network of the raw material and produce a new polymeric structure formed by polysilicoalumino-phospho (-Al-O-P-O-Si-) units [3,8]. This system, which can be defined as a *phosphate-based geopolymer* (PBG), has hitherto received less attention than the alkali-based analogues, although it performs better in terms of thermal stability, and resistance to corrosion and efflorescence [4]. In this view, PBG provides a promising matrix to incorporate and functionalise waste residues. Few studies have hitherto investigated the implementation of solid waste residues in PBG, and they mostly focused on CFA. In particular, Guo et al. [9] show that a substitution of MK with CFA up to 30 wt% provides a material exhibiting good mechanical properties. In addition, Wang et al. [10] tested both low- and high-calcium CFA, concluding that the former acts as secondary aluminosilicate precursor while the latter behaves as a rapid setting agent, through calcium phosphate phases precipitation.

Here, the replacement of MK with previously water-washed MSWI-FA in phosphate-based geopolymers is explored. Indeed, treated MSWI-FA has been widely tested as a supplementary cementitious material to partially replace raw materials in OPC and low-energy cements, such as alinite and calcium sulfoaluminate cements [11-13]. In PBG systems, the metal ions provided by the MSWI-FA may be involved in reactions with phosphoric acid to form metal phosphates. The aim of the present study is twofold: 1) contributing to understand both the products and reaction mechanism that governs the MSWI-FA/MK-PBG interaction, paying special attention to the PBG molecular framework modifications; 2) determining the relationship between replacement of MK with MSWI-FA and mechanical properties of the resulting material.

6.2 Materials and Methods

6.2.1 Materials

Industrial metakaolin was obtained from České lupkové závody, a.s. (Czech Republic), which is produced by heating kaolinite at 750° C for 2h. Reagent grade phosphoric acid solution (85% wt) was bought from Lach-ner s.r.o (Czech Republic). The washed MSWI-FA was milled in a steel ball mortar (RM 200, Retsch, Germany) to a particle size < 63 μm. The BET surface area, mean particle size, chemical composition, and mineralogical composition of the used raw materials are presented in Table 6.1 and 6.2. The results reported therein are the average of 3 repetitions on different samples.

Table 6.1 Chemical composition (wt%) and main physical properties of MK and MSWI-FA. Uncertainties of about 2-3%.

Raw materials	Chemical composition (wt %)										BET (m^2g^{-1})	D_{50} (μm)	D_{90} (μm)
	Al_2O_3	Fe_2O_3	TiO_2	K_2O	CaO	SiO_2	MgO	SO_3	P_2O_5	Others			
MK	42.70	1.09	1.80	0.83	0.58	52.45	0.18	0.07	0.08	0.14	12.8	3.0	10.0
MSWI-FA	7.37	8.99	2.87	0.45	44.38	22.51	6.98	5.23	0.38	0.86	15.7	8.8	29.1

Table 6.2 Mineralogical composition (wt %) of MK and MSWI-FA, using the Rietveld analysis on X-ray powder diffraction patterns. The uncertainties are ±0.2 wt % (crystal phases) and ±5 wt % (amorphous phase).

	MK	MSWI-FA
Quartz	3.9	4.3
Kaolinite	2.2	
Anatase	1.1	
Illite	1.2	
Mullite	1.6	
Calcite		7.5
Anhydrite		9.6
Larnite		3.0
Gehlenite		6.2
Periclase		4.0
Gypsum		4.5
Bassanite		1.1

Ettringite		3.8
Merwinite		1.7
Perovskite		2.3
Amorphous	90	52

6.2.2 Geopolymer formulation

Table 6.3 reports details about the formulation of the investigated MSWI-FA geopolymer pastes, which rely upon hand-mixing homogenized blends of MK and MSWI-FA into diluted phosphoric acid solution. The resulting slurry was stirred manually for 5 min and then cast into cubic polytetrafluoroethylene (PTFE) molds ($10 \times 10 \times 10$ mm^3), which were kept on vibration for 1 min to remove possible air bubbles. The molds were successively wrapped in plastic foils to prevent evaporation and subjected to a two-step curing treatment, consisting of 24 h at room temperature and 24 h at 60 °C. Such a curing method was chosen because of its proven efficacy to reduce cracks in the resulting material [14]. Eventually, the geopolymer samples were aged at room temperature, for as long as 60 days. An Al/P nominal molar ratio of 1.1, as such a figure allows a satisfactory workability of the paste according to preliminary tests. The samples of the present study are univocally identified by the label "PBGX", where "X" is the wt% of MSWI-FA in replacing MK.

Table 6.3 Formulations of MK/MSWI-FA geopolymer pastes. The Al/P mole ratio was determined on the basis of the chemical composition of MSWI-FA and MK, and of their proportion in the solid mixtures. The molar ratio of Al/P was kept to 1.1 by adjusting the mass of phosphoric acid. L/S: mass ratio between the diluted phosphoric acid solution (L) and the mass of the used raw materials (S). M: molarity of the diluted phosphoric acid solution.

Sample	**Solid binder**		**Al/P**	**L/S**	**M**
	MK (wt %)	**MSWI-FA (wt %)**			**(mol L^{-1})**
PBG0	100	0	1.1	0.90	12
PBG10	90	10	1.1	0.90	12
PBG20	80	20	1.1	0.93	10
PBG30	70	30	1.1	0.95	9
PBG50	50	50	1.1	1.00	6

6.2.3 Fourier-transform Infrared Spectroscopy Attenuated total reflection (FTIR-ATR)

FTIR-ATR spectra were collected on a Fourier transform Equinox 55 (Bruker) spectrophotometer equipped with an ATR device; the resolution was set at 2 cm^{-1} for all spectra. A spectral range of 600−4000 cm^{-1} was scanned, using KBr as a beam splitter.

6.2.4 Solid state Nuclear magnetic Resonance (SSNMR)

All SSNMR measurements were recorded at room temperature on a solid-state NMR spectrometer (JNM-ECZ600R, JEOL RESONANCE Inc., Japan) at a magnetic field of 14.1 T, operating at ^{1}H, ^{27}Al, ^{29}Si, and ^{31}P Larmor frequencies of 600.1, 156.4, 119.2, and 242.9 MHz, respectively. The raw materials and ground PBG samples were packed into 3.2 mm zirconia rotors and spun at a MAS frequency of 15, 15 and 20 kHz for ^{27}Al, ^{29}Si, and ^{31}P MAS spectra, respectively. A ^{27}Al, ^{29}Si and ^{31}P pulse of 12 μs, 4 μs and 3 μs were employed. ^{1}H, ^{27}Al, ^{29}Si, and ^{31}P chemical shifts scales were referenced through the resonances of adamantane, aluminium nitrate, silica and $(NH_4)H_2PO_4$, respectively. The deconvolution analysis was conducted using the related in-built feature of Delta 6.1 (Jeol), while the estimated error in the calculated fraction percentage is in range of ± 1%.

6.2.5 Mechanical tests

Compressive strength tests were performed on early (7 days) and long-aging (60 days) PBG paste cubes' (1x1x1 cm), measuring 5 replicates by means of an Instron 3345 (Instron, USA) loading frame, at loading speed of 0.2 mm/min and load cell of 5 kN.

6.2.6 Mercury intrusion Porosimetry (MIP)

Porosity was measured by mercury intrusion technique on long-aging (60 days) PBG paste cubes (1x1x1 cm), using a Mercury porosimeter (Autopore IV 9500, Micromeritics Corporation, USA).

6.3 Results

6.3.1 Mineralogical analysis (XRPD)

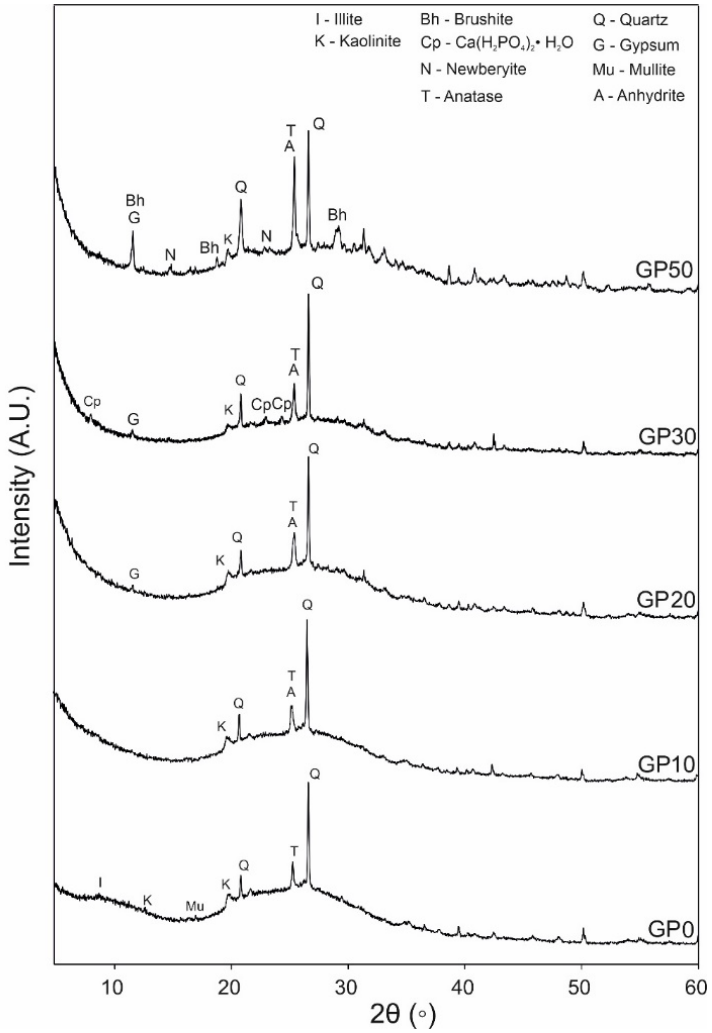

Figure 6.1 XRPD patterns of metakaolin, MSWI-FA and PBG0-10-20-30-50 samples, cured for 60 days.

The PBG0 pattern (Figure 6.1) is characterized by an evident amorphous "hump" around 2θ-25°, in agreement with expectations motivated by the known amorphous nature of these materials [15]. The residual minerals in MK (Table 6.2) are still observable in all of the PBG-samples. The introduction of MSWI-FA, up to a replacement of MK in terms of 20 wt%, exhibits a comparatively modest effect on the crystalline components of PBGX. The MSWI-FA's phases, which likely react in the acidic phosphate environment, are calcite, ettringite and periclase [16]; the secondary products that form in PBGX (likely Ca and Mg phosphates) are either non-crystalline, similarly to what observed in the Mg- or Ca-Mg phosphate cements [17], or in a too low abundance to allow detection. With the introduction of larger fractions of MSWI-FA (PBG30 and PBG50), new crystalline phosphates appear: in PBG30, monocalcium phosphate monohydrate [MCPM, $Ca(H_2PO_4)_2{\cdot}H_2O$]; in PBG50, brushite ($CaHPO_4{*}2H_2O$) and newberyite ($MgHPO_4{\cdot}H_2O$). As to the effect on the PBG-structure, in previous works the occurrence of different coexisting frameworks (amorphous silica and aluminophosphate) was supposed from the qualitative analysis of the XRPD background profile [3,18]. In the present investigation, a reduction of the main amorphous "humps" around 2θ-24° and 2θ-12° with the increase of the MSWI-FA content is apparent. This points to a decrease of the geopolymer matrix extent, in

combination with a shift from a pure PBG-system to a Ca(Mg)-phosphate cement (CMPC)/PBG composite. Further confirmation is obtained from the results of spectroscopic measurements, as reported below.

6.3.2 FTIR-ATR

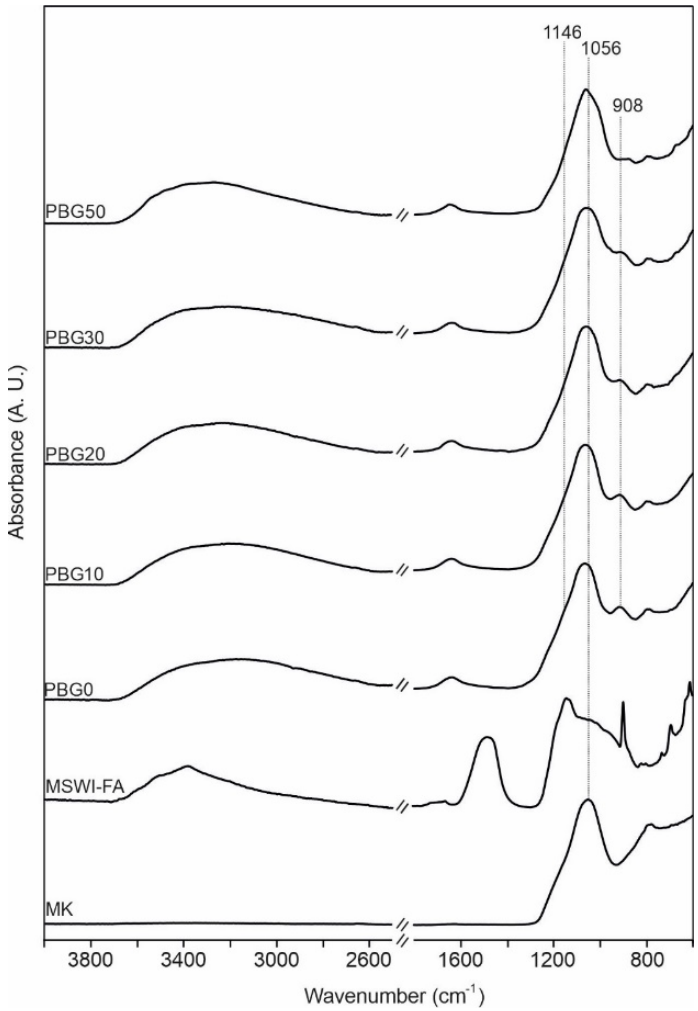

Figure 6.2 Infrared spectra of metakaolin, MSWI-FA and PBG0-10-20-30-50 samples cured for 60 days.

Figure 6.2 displays the FT-IR spectra of MK, MSWI-FA and PBG-samples. The infrared spectrum of the raw materials is characterized by a main feature at 1056 cm^{-1}, related to the Si-O-Al stretching vibrations of the aluminosilicate amorphous fraction, along with a doublet around 790-770 cm^{-1} of the residual quartz [18]. In case of MSWI-FA, the broad peak between 1200-1000 cm^{-1} encompasses contributions from all the different Si-O and Al-O stretching vibrations of the crystalline and amorphous aluminosilicates. Particularly evident are also the peaks related to calcite, i.e., $\nu_{2,asym}$ and $\nu_{3,asym}$ CO_3^{2-} bands at 1380 and 870 cm^{-1}, respectively [19], along with the ν_{sym} O-H doublet between 3500-3400 cm^{-1} of the hydrous phases, like gypsum [20].

The FT-IR spectrum of PBG0 preserves many of the pure MK's features. Yet, some differences are worth being stressed: although the discrimination between ν(Si-O), ν(Al-O) and ν(P-O) is complex, owing to their overlap in the spectral region 1200-1000 cm^{-1} [9,27], a blueshift to 1065 cm^{-1} of the main band occurs. This suggests a rearrangement of the Si-O, Al-O and P-O bonds due to the geopolymerization reactions [21]. In addition, two new bands at 1146 and 908 cm^{-1} can be assigned to ν_{asym} P-O-Al and ν_{asym} P-O-P, respectively

[18], thus confirming the presence of a reticulated aluminophosphate framework. The same features are preserved in the spectra of the samples PBG10 and PBG20, although the vibrations at 1146 and 908 cm^{-1}, associated with the geopolymer structure, seem to have a relatively lower intensity. This suggests that the lower aluminium content of MSWI-FA with respect to MK's negatively affects the development of the aluminophosphate matrix. The main peak blueshift, i.e. 1060 cm^{-1}, is less marked in PBG30 than PBG0-10-20, indicating a reduced rearrangement of the Si-O and Al-O bonds, which remain similar to MK's, thus pointing to a more limited reactivity of the raw materials' mixture. In addition, a new peak at 970 cm^{-1} hints at the presence of the crystalline phosphate phase $Ca(H_2PO_4)_2{\cdot}H_2O$ [22].

6.3.3 SSNMR

The SSNMR is a powerful tool in the structural characterization of geopolymers, due to its capacity to selectively probe specific elements (nuclei) regardless of the occurrence of a long-range order [23]. All the main species involved in the geopolymerization process were investigated: ^{27}Al, ^{31}P and ^{29}Si.

6.3.3.1 ^{27}Al MAS

^{27}Al MAS spectra of the raw materials are shown in Figure 6.3, while the PBG-samples' spectra are shown in Figure 6.4 (left). The MSWI-FA spectrum displays a broad peak at around 60 ppm, which is related to the Al tetrahedra (Al^{IV}) speciation in the residue aluminosilicate glass fraction, while the relatively narrow peak at around 13 ppm arises from a crystalline phase and is assigned to $Ca_6Al_2(SO_4)_3(OH)_{12}{\cdot}26H_2O$ (ettringite), in agreement with literature data [24]. The broader peak tail centred at 9.5 ppm can reasonably originate from a limited fraction of Al octahedra (Al^{VI}) in aluminosilicate glass. The ^{27}Al MAS spectrum of MK is also dominated by the amorphous tetrahedral Al peak at 60 ppm, while additional contributions can be observed at around 30, 12, and 2 ppm, assigned to pentacoordinated Al, octahedral Al of mineral impurities and MK hexacoordinated Al (25).

The PBG0 spectrum is dominated by a peak at about -12 ppm, assigned to octahedral [AlO_6] units linked to tetrahedra [PO_4]. Al^{VI} represents the main aluminium coordination in condensed aluminophosphate geopolymers, at variance with traditional basic geopolymers, wherein Al^{IV} dominates [3,26]. The Al^{IV} signal characteristic of MK is slighlty visible at about 60 ppm, indicating that the dealumination of the raw material was almost complete. The spectrum profiles from MSWI-FA-bearing PBG samples exhibit peaks whose positions are similar to those in PBG0, though they differ in terms of intensity, thus indicating that MSWI-FA affects the degree of geopolymerization.

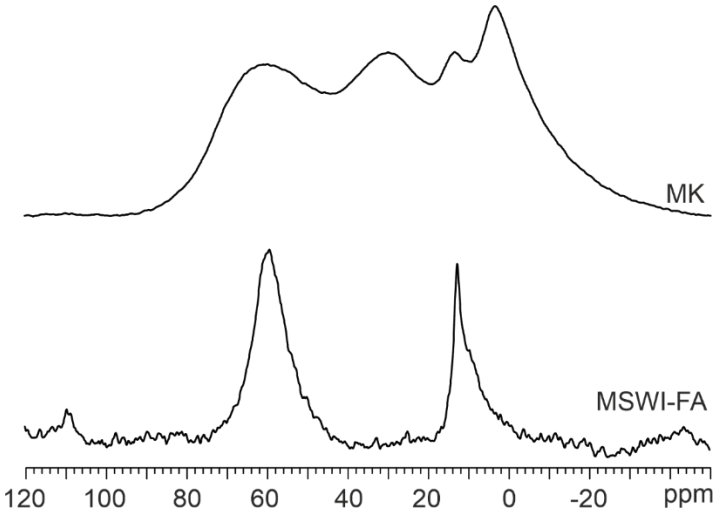

Figure 6.3 ^{27}Al MAS spectra of the raw materials.

6.3.3.2 ^{29}Si MAS

^{29}Si chemical shift is particularly sensible to the coordination number and nature of second coordination sphere atoms. In particular, SiO_4 tetrahedra are represented by Q^n (n=0, 1, 2, 3, 4), where n is the number of bridging oxygens, and their shifts are −60 to −81 ppm (Q^0), −68 to −83 ppm (Q^1), −74 to −93 ppm (Q^2), −91 to −101 ppm (Q^3), and −102 to −118 ppm (Q^4) respectively [23]. When Si atoms are replaced by Al atoms, the Si-O-Al units are usually expressed as Q^n(mAl) (m, n = 1, 2, 3, 4), and their chemical shift ranges for Q^4(1Al), Q^4(2Al), Q^4(3Al), Q^4(4Al) between −96 to −106 ppm, −91 to −99 ppm, −85 to −94 ppm, and −81 to −91 ppm, respectively [23].

^{29}Si MAS spectrum of MSWI-FA (Figure 6.5) is characterized by a very broad peak between -60 and -115 ppm, which encompasses all the different silicate/aluminosilicate environments present in the residue, such as Q^0 (i.e., larnite, see Table 6.2) and Q^1 (i.e., melilite) units at -63 and -71 ppm and the higher cross-linked Q^4(mAl) units of the glass fraction (from -80 to -115 ppm) [27]. ^{29}Si MAS spectrum of MK is instead localized between -85 and -115 ppm, as only Q^4(mAl) units are present in the amorphous fraction [27].

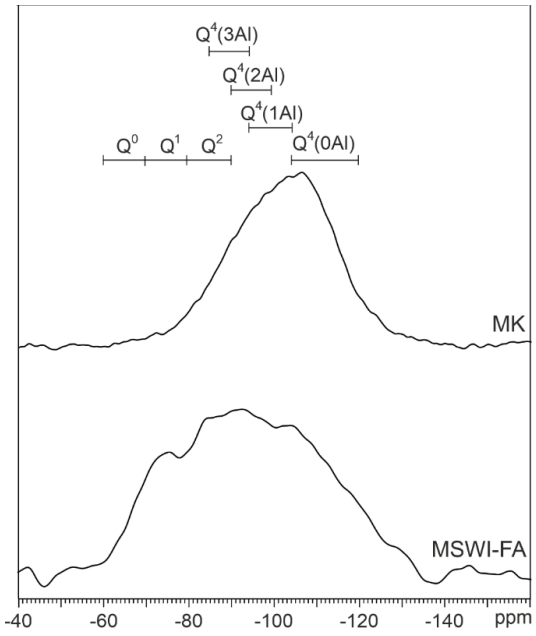

Figure 6.5 ^{29}Si MAS spectra of MK and MSWI-FA.

Figure 6.4 shows the ^{29}Si MAS spectra of the PBG-samples. The acidic dissolution of MK leads to the release of Al^{3+} and depolymerization of the Si-O layers [8,10,21]; whereas phosphate anions are energetically favoured to make bonds with aluminium to build up the geopolymer structure [3], the residual [SiO_4] are supposed to rearrange into an amorphous silica phase, leading to a composite-like system [3]. In MK, the Si speciation is represented by Q^4_{Si}(mAl), i.e. Si-tetrahedron with four bridging oxygens and m-Al atoms in the second coordination sphere. Once geopolymerization has occurred, in PBG0 prevails a Q^4_{Si}(0Al) component at -112 ppm, associated with a highly reticulated amorphous silica phase. Note that the MK dissolution implies a decrease of abundance of the speciation related to Q^4_{Si}(3Al) and Q^4_{Si}(2Al), whose signals lie in the range 85-95 ppm [3]. Upon increasing the MSWI-FA content, the spectra become less and less resolved.

6.3.3.3 ^{31}P MAS

In a similar way, differences are visible in the ^{31}P MAS spectra (Figure 6.4). The reference sample PBG0 displays a single and broad peak between -5 and -20 ppm, characteristic of amorphous condensed phosphate units [23]. Upon increasing the MSWI-FA content, the peak maximum shifts towards a lower field and the peak asymmetry decreases. In PBG30 and PBG50, new and sharper resonances appear; they are consistent with MCPM (-0.1 and -4.5 ppm) [17], in the first case, and with brushite (1.1 ppm) [17] and newberyite (-7.4 ppm) [28], in the second case. An additional peak at about -1.6 ppm is visible in the PBG50 ^{31}P MAS spectrum, close to the reference value of -1.5 ppm for monetite ($CaHPO_4$) [27], though the latter phase has never been detected by X-ray diffraction in our samples.

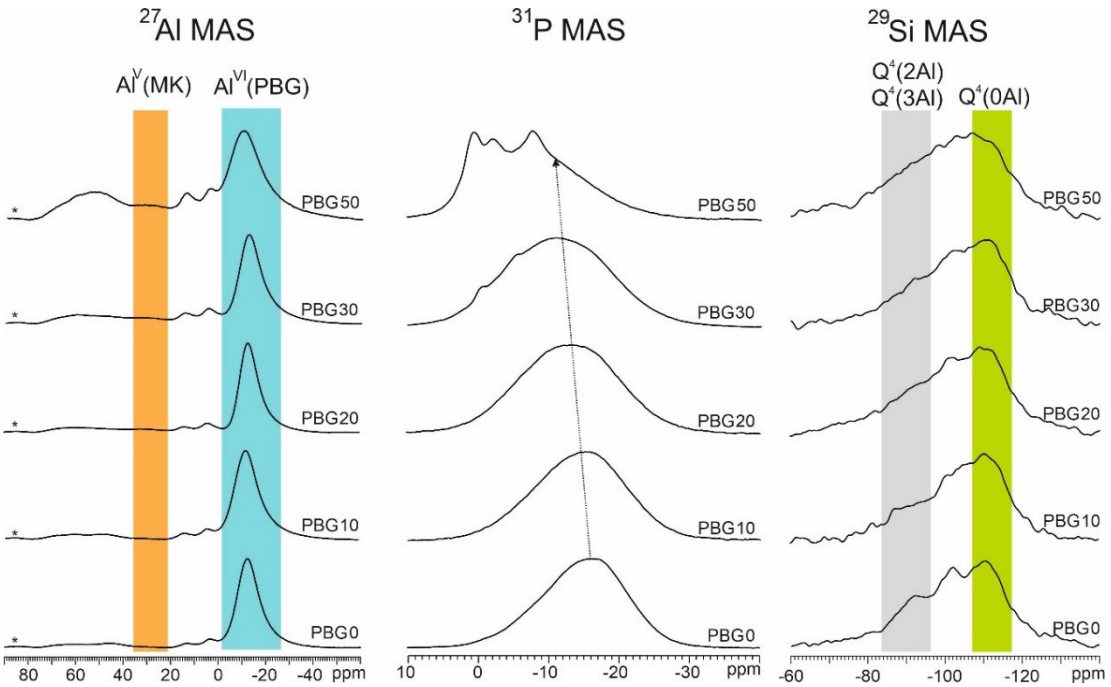

Figure 6.4 ^{27}Al MAS (left), ^{31}P MAS (middle) and ^{29}Si MAS (right) spectra of PBG samples cured for 60 days.

6.3.3.4 Spectra deconvolutions

Spectral deconvolutions allowed to interpret the role of MSWI-FA in affecting the PBG-structure. The assignments are shown in Figure 6.6. The analysis of the ^{27}Al MAS spectra indicates a secondary contribution due to the [AlO_4] units in PBG-samples at around 45 ppm [27]. The contributions of the Al^{VI} and Al^{IV} speciations in the PBG-samples are shown in Figure 6.7, with respect to the unreacted Al^{V} of MK. This

represents a highly distorted coordination in MK, which provides the Al fraction most prone to participate in the geopolimerization process [3] and it was therefore chosen as indicator of the raw material reaction degree. The absence of MK Al^{V} peak is apparent in PBG0 and PBG10, while at a higher degree of substitution, this contribution becomes more relevant, while at the same time the aluminophosphate Al fraction decreases.

The broad ^{31}P peak was modelled with three contributions, centred at -7, -12 and -17 ppm, which are assigned to the $Q^{1}_{P}(0Al)$, $Q^{1}_{P}(1Al)$, $Q^{1}_{P}(2Al)$ units, respectively [27], where $Q^{n}_{P}(mAl)$ indicates $[PO_4]$ units bridged with n P-tetrahedra and m Al-polyhedra. In Figure 4, the most important contribution in PBG0 is from the $Q^{1}_{P}(2Al)$ unit, confirming the presence of a highly cross-linked aluminophosphate matrix [23,27]. In PBG10 and PBG20, the $Q^{1}_{P}(2Al)$ content decreases in favour of $Q^{1}_{P}(0Al)$ and $Q^{1}_{P}(1Al)$. This indicates, in combination with the ^{27}Al MAS NMR spectra, that an increase of MSWI-FA leads to a general reduction of the PBG-matrix. Such an effect becomes even more apparent in PBG30 and PBG50.

The deconvolution of the ^{29}Si MAS spectra (Figure 6.7) is performed assuming that the main contribution to the signal is due to silicon from MK, because of the abundance of the species in MK. The $Q^{4}_{Si}(0Al)/[Q^{4}_{Si}(3Al) + Q^{4}_{Si}(2Al)]$ ratio (0.57 in MK) steadily changes from 1.30, in PBG0, to 0.66, in PBG50. This hints at a progressive decrease in metakaolin dissolution.

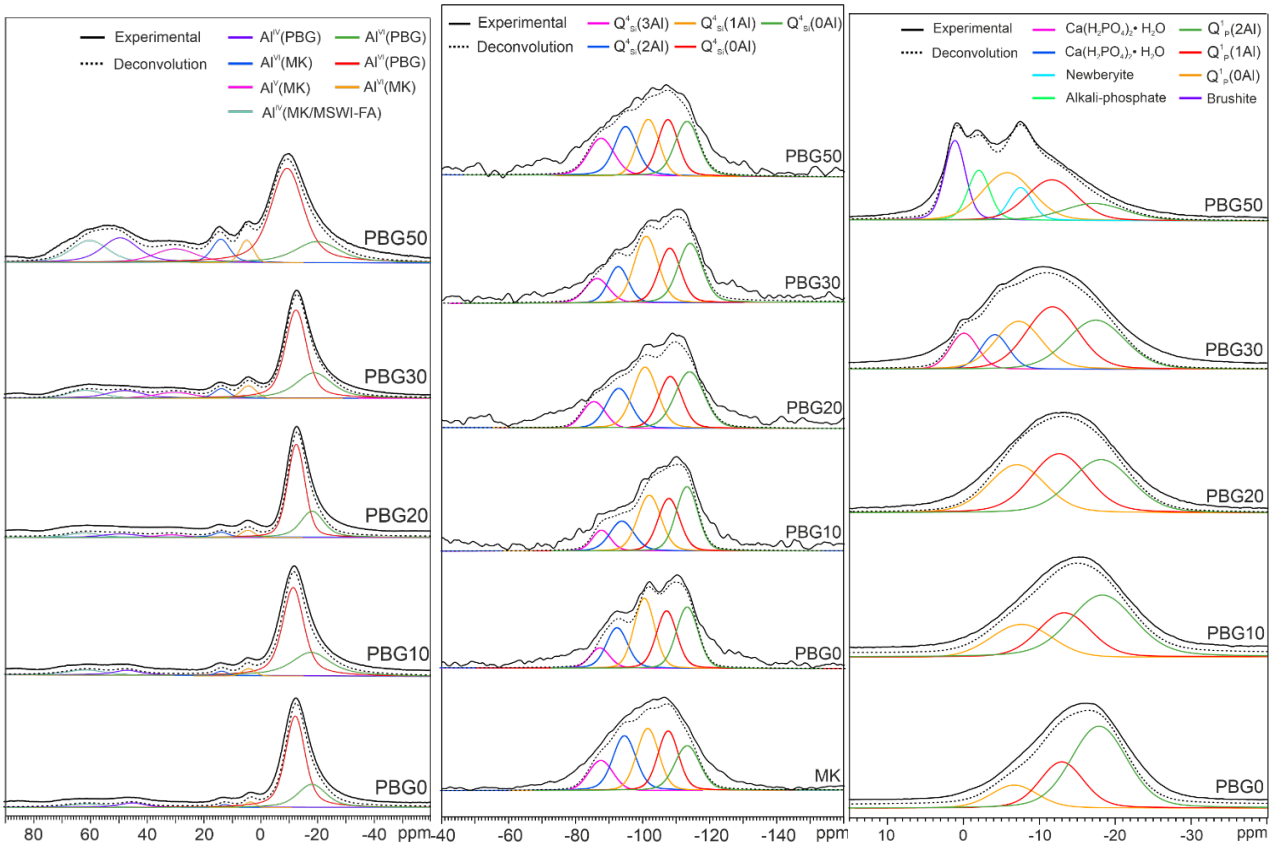

Figure 6.6 ^{27}Al MAS (left), ^{29}Si MAS (middle) and ^{31}P MAS (right) spectra with deconvolution of PBG samples cured for 2 months. The dotted line represents the sum of all contributions. Experimental spectra are displaced vertically for the sake of clarity. To take into account the asymmetry of the Al^{VI} (PBG) signal at around -12 ppm, two peaks were used to model it, as previously applied [27], which describe two different Al^{VI} local environments in the PBG structures, while the sum of their relative intensity, together with the Al^{IV}(PBG) peak at around 48 ppm, was considered to represent the samples degree of geopolymerization.

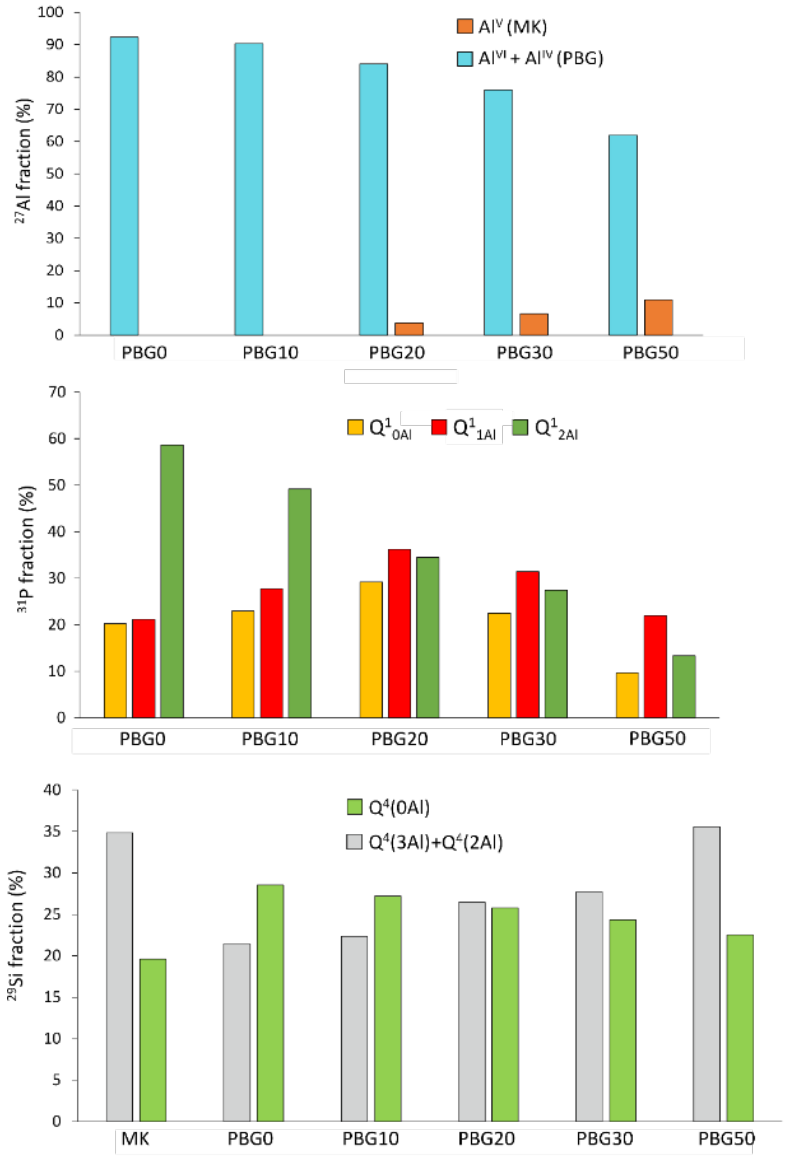

Figure 6.7 ^{27}Al MAS (top), ^{31}P MAS (middle) and ^{29}Si MAS (bottom) deconvolution data of PBG samples cured for 60 days.

6.3.4 Morphology observation

The microstructure of MSWI-FA, as revealed by SEM, is shown in Figure 6.8. The morphological and mineralogical heterogeneity is proven by the occurrence of micrometric and sub-micrometric particles, of spherical, needle-like and more complex shapes, retaining features like an amorphous material. In Figure 6.9, the micrographs of the internal surface of PBG0 and PBG30, in secondary electron mode, are displayed. PBG0 appears compact in agreement with its pervasive amorphous matrix. Some isolated fragments of unreacted MK (i.e., anatase and kaolinite) can be distinguished, along with microcracks. As expected, the EDS analyses revealed a composition rich in Al, Si and P. However, the two different amorphous systems, i.e., aluminophosphate and silica, are highly intermixed and not easily distinguishable from one another by SEM-EDS [3]. The matrix of PBG30 is similar to PBG0's, but more heterogeneous and with higher porosity. The composition of the matrix indicates an enrichment in alkali, i.e., Ca and Mg, confirming a degree of MSWI-FA particle dissolution, as discussed above. The increasing porosity is even more evident for PBG50 sample

(Figure 6.10), where relatively large pores favour the growth of acicular and needle-like Ca-phosphate crystals from the residual pore solution. In addition, the microstructure appears less dense, formed by loosely bound particles rather than a condensed and compact matrix.

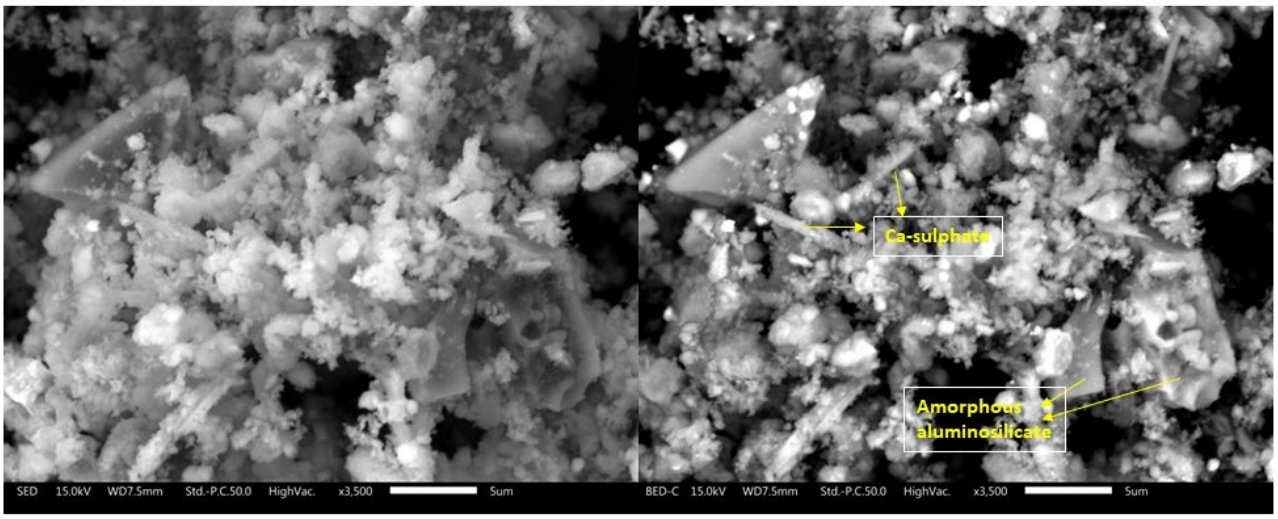

Figure 6.8 SE (left) and BSE (right) images of washed MSWI-FA particles.

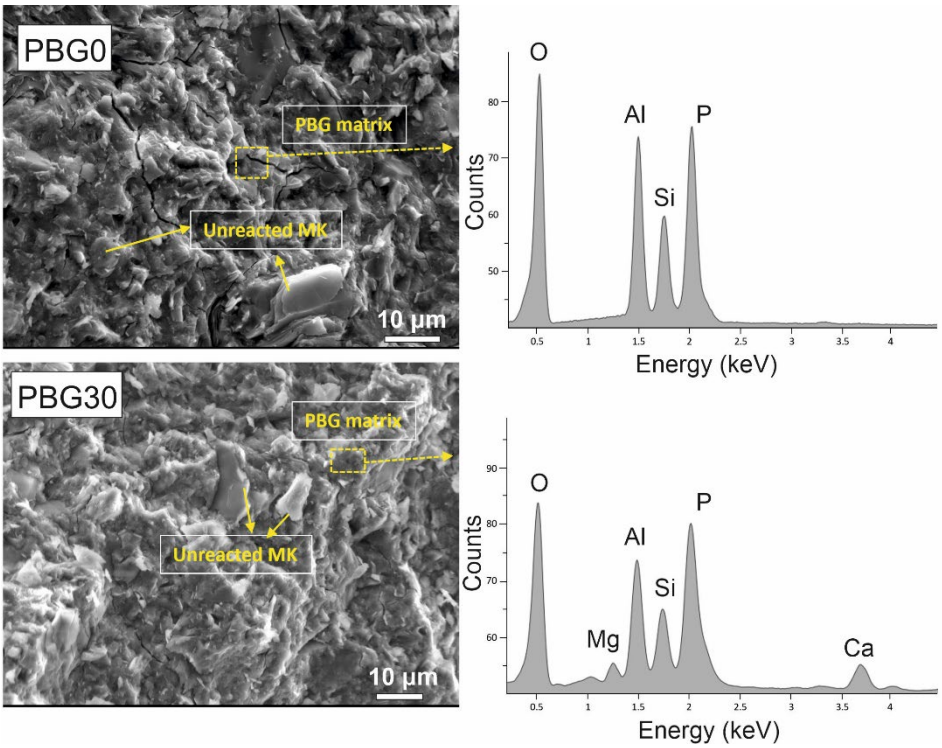

Figure 6.9 SEM micrographs of PBG0 and PBG30 samples cured for 60 days.

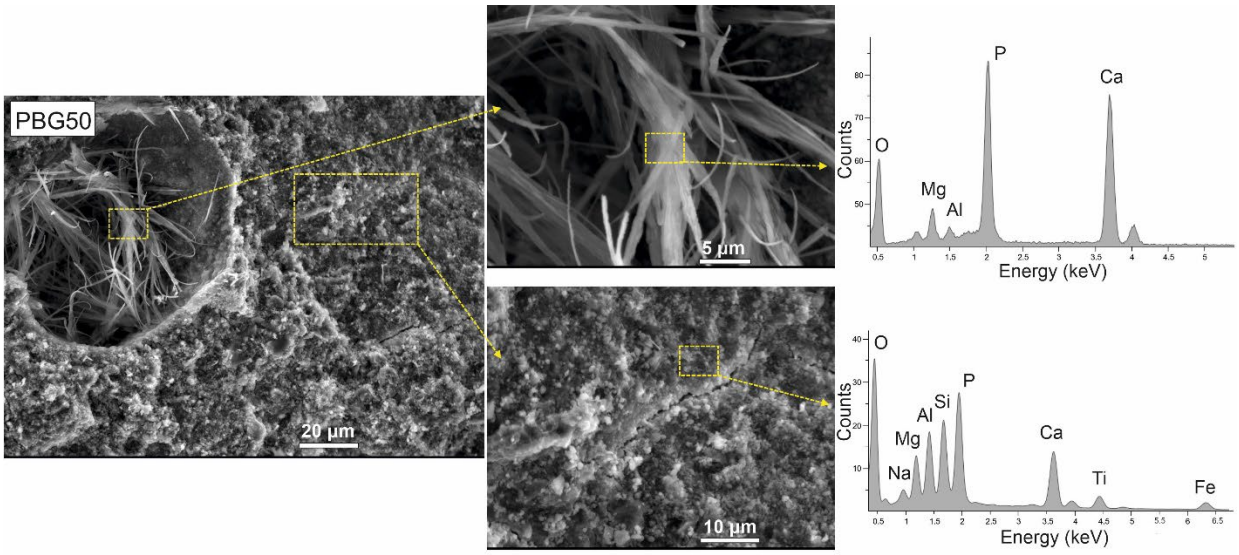

Figure 6.10 SEM micrographs (bulk and pore's content) of PBG50 sample cured for 60 days.

The cross section in backscattered mode of PBG30 (Figure 6.11, top) shows Ca-phosphate evenly distributed in the PBG-matrix. Therefore a 30 wt% of MK substituted with MSWI-FA allows an intermix of these two binding phases, leading to the cementation of the unreacted particles. Although the phosphate crystals and the unreacted MSWI-FA particles embedded in the PBG-matrix can potentially reinforce the resulting material, the increasing presence of pores, which act as stress concentrators, ultimately impairs the compressive strength (see next paragraph).

On the other hand, the PBG50 cross-section (Figure 6.11, bottom) indicates a distribution of larger and more heterogenous particles, related to the increase of the MSWI-FA content and the reduced participation of MK to the final material. It is worth noticing how the P-map well correlates with Ca and Mg's, while the distribution of Al is concentrated on the unreacted particles, indicating that in this case most of the binding action is due to Ca/Mg-phosphates.

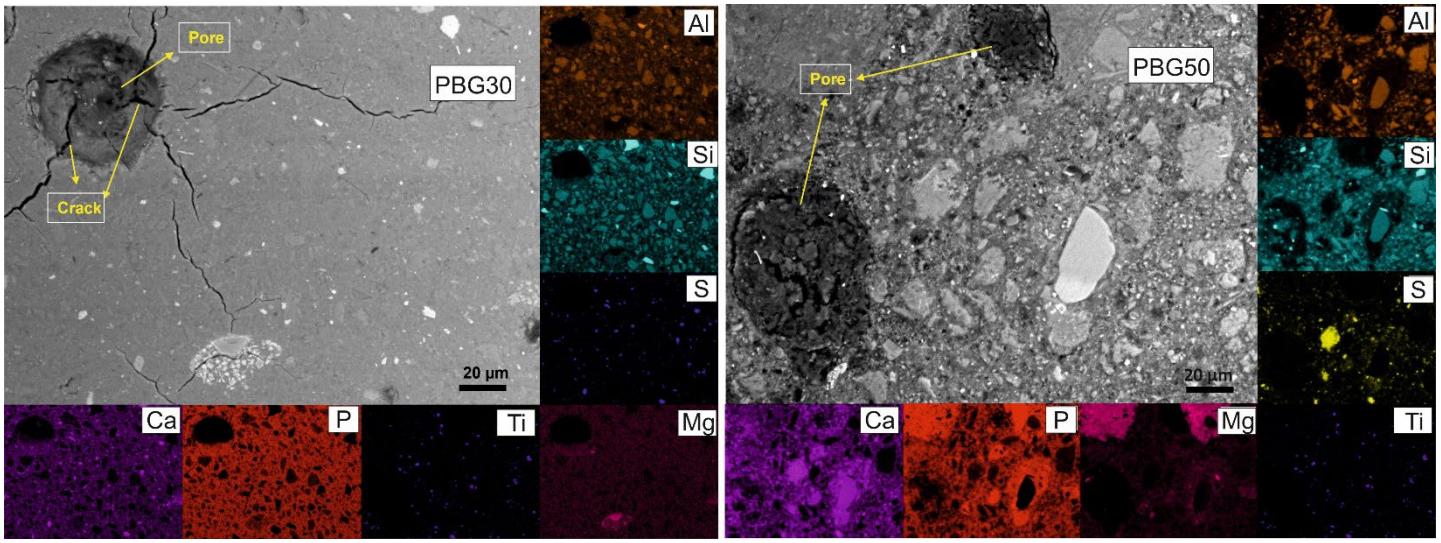

Figure 6.11 Backscattered images of PBG30 and PBG50 cross-sections, with major elements' EDS maps.

6.3.5 Setting time, compressive strength and porosity

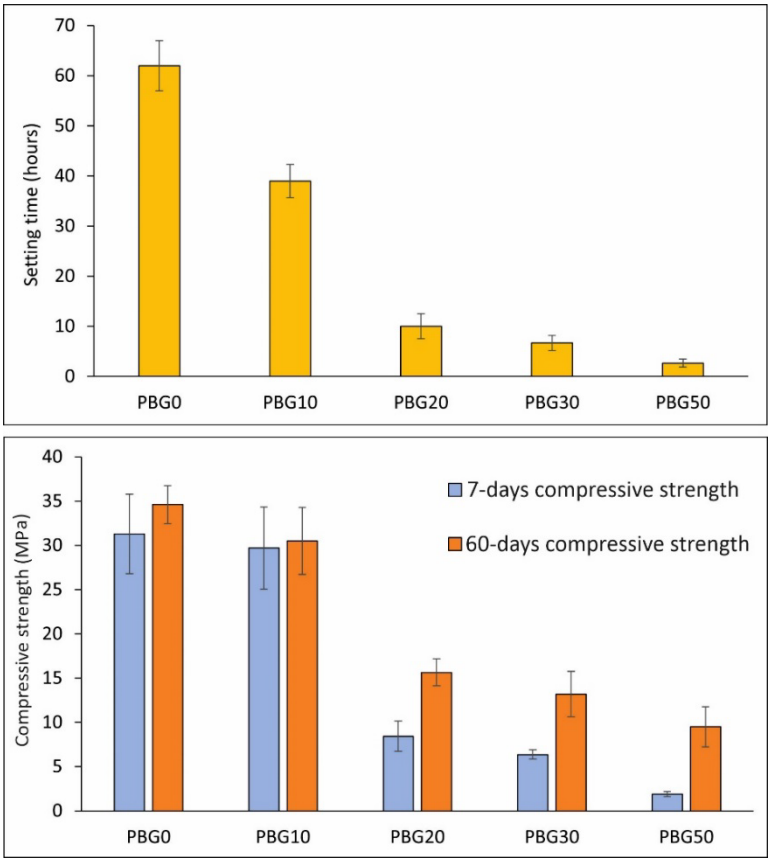

Figure 6.12 Setting time (top) and early and long-aging compressive strength values (bottom) of PBG samples. Uncertainties determined as standard deviation of each measurement batch.

The setting times of the PBG samples are illustrated in Figure 6.12 (top). PBG0 exhibits a final setting time of over 60 h, in agreement with the values reported in literature, which, in some cases can reach 18-20 day, as a function of the mix composition and curing mode [18]. Such behaviour is due to the slow kinetics of the dealumination and polycondensation reactions [4]. Therefore, for practical purposes, in order to speed up the process, curing at high temperature is advisable [4,14]. Owing to the quick acid-base reactions involving the MSWI-FA alkali (Ca and Mg) with phosphate, the addition of MSWI-FA markedly shortens the setting time to a few hours or even less in the case of high substitution degrees. Such fast kinetics are reported for acid-base Mg phosphate cements and alkali-activated fly-ash-based binders [29]. It is worth noticing that even PBG10, which is structurally and microstructurally similar to PBG0, displays a significant shortening of the setting time, of about 30%.

The compressive strength changes from early (7 days) to long-aging (60 days) of the PBG-samples are displayed in Figure 6.12 (bottom). In all of the cases, the aging time positively affects the mechanical properties, testifying the strengthening effect of the geopolymerization and phosphate crystallization progress. The reference PBG0 reaches over 90% of the 60-day figure in the first week (i.e, 31.3 *versus* 34.6 MPa), suggesting that, at such conditions, the curing treatment of 24 h at 60 °C effectively speeds up the poly-condensation reactions towards their completion. A similar behaviour is revealed by PBG10, which displays close values of compressive strength between early and long-aging curings, 29.4 and 30.7 MPa,

respectively. A significant change apparently takes place at higher MSWI-FA substitution degrees, with PBG20, PBG30 and PBG50 that exhibit 46%, 38% and 27% of the PBG0's strength from 60-days curing. This is likely related to the gradual crystallization of Ca/Mg-phosphates from the acidic pore solution. Such a process contributes to build up a microstructure resembling that of a composite material with crystals embedded in an amorphous matrix (see Figure 6.10, top). The development of such a microstructure, which reduces crack deflection and propagation [30], and induces a well-known toughening in ceramics [31,32] and in acid-base cements [33], is nevertheless accompanied by a significant increase in porosity, as proven by SEM observations. Therefore, the detrimental effect due to porosity seems to prevail over the expected improvement of the mechanical properties because of a composite-like microstructure, at MSWI-FA introduction >10 wt%. The poorer performance of PBG20-30-50 than PBG10 is also ascribable to the abundance in the unreacted MSWI-FA fraction of low-strength phases (e.g. gypsum).

The total porosity measured by mercury intrusion is reported in Table 6.4. Given that the vacuum conditions required by measurements cause partial dehydration of the samples, the related results must be considered from a qualitative standpoint only. PBG0 exhibits low porosity (~1 %), confirming the presence of a pervasive and compact aluminophosphate matrix. A similar value (3.5 %) is observed for PBG10, while an increase to about 8% occurs in PBG20 and PBG30. The reduction of the paste setting time and fluidity in presence of MSWI-FA, along with the CO_2 production due to the dissolution of calcite, favour the development of a higher porosity, promoted by gas/air entrapment. This agrees with the high values of porosity observed in PBG50.

Table 6.4. Porosity measurements on PBG samples cured for 60 days. Standard deviation is around 15-20% of the average value.

Sample	Porosity (%)	Average pore size (nm)
PBG0	0.98	83.1
PBG10	3.80	42.3
PBG20	8.07	54.2
PBG30	7.57	26.6
PBG50	38.6	50.8

6.4 Discussion

The effects of the partial replacement of MK with of MSWI-FA in the phosphate-based geopolymer system can be explained by considering the reaction conditions, the chemical/phase composition of the involved waste and the key parameters of the formulation (i.e., Al/P and L/S). In the PBG0 formulation, all of the available phosphate groups can potentially react with MK. Therefore, the highly acidic environment boosts MK depolymerization/dissolution, thus providing the building blocks necessary for the PBG condensation reactions, and eventually leading to the formation of Al-O-P linkages and amorphous SiO_2, as

detected by SSNMR (section 6.3.3). The introduction of MSWI-FA causes a decrease of the overall content of Al_2O_3 in the mixture, because of the lower amount of alumina provided by MSWI-FA with respect to MK. The constraint of a fixed Al/P ratio reduces, as a consequence, the available phosphate partaking in the reactions. On the one hand, the liquid-to-solid ratio has to be increased to preserve an acceptable workability of the paste; on the other hand, MSWI-FA competes with MK for the available phosphate by precipitating Ca/Mg-phosphate hydrate phases. Such acid-base reactions are generally characterized by fast kinetics [21,32], all the more here favoured by the rapid dissolution of MSWI-FA Ca/Mg-bearing amorphous and crystalline phases (i.e., calcite, periclase, ettringite; Table 6.4). By way of example, this explains the crystallization of brushite in PBG50, as observed by XRPD. Being a kinetically-driven process, precipitation occurs owing to a high Ca oversaturation and a relatively low brushite solubility product ($Ksp=10^{-6.5}$) [33], notwithstanding a Ca/P molar ratio lower than the theoretical one (0.83 instead of 1). A quick subtraction of both phosphate and water not only accelerates the paste hardening (Figure 8), but also hinders the MK dealumination, as shown by ^{27}Al and ^{29}Si MAS spectra, although such acid-base reactions are highly exothermic and thus induce an increase in the paste temperature that could boost MK dissolution. As a net result, the availability of Al for the condensation reactions to build up the geopolymer framework is reduced. A fraction of Al from MSWI-FA participates in the formation of the PBG-matrix, but its contribution does not fully compensate for the replaced MK. All this is testified by the detailed ^{31}P MAS analysis in Figure 6.7, which evidences that the reticulated $Q^1_P(2Al)$ component significantly decreases with the MSWI-FA introduction.

Mechanical properties measured on long-aging samples and microstructural features correlate. In fact, low degrees of MK substitution with MSWI-FA (i.e., 10 wt%) modestly stymie the amount of the geopolymer matrix, so that the PBG0's mechanical properties are still preserved. At a higher content of MSWI-FA, the precipitation of secondary products (i.e. brushite and MCPM) and the indirect inhibiting effects on MK dealumination and geopolymer matrix generation result in a shift from a pure PBG-system to a progressively more porous CMPC/PBG composite, which thing is detrimental to the mechanical performance (Figure 6.13). It is worth attention that, as shown in Figure 6.11, PBG and $CaHPO_4$ exhibit an excellent intermixing, at least up to 30 wt% of substitution. On the other hand, the dilution effect due to the large gap in Al_2O_3 content between the two raw materials, along with the progressive increase of the internal porosity in the MSWI-FA bearing PBG-samples and the presence of low-strength phases in the ash residue (i.e. gypsum), worsen the mechanical properties of the output composite. A similar detrimental dilution effect was observed by Wang et al. (2020) [10], who describe a 30% decrease of the 28-day compressive strength in a PBG-system containing 30 wt% of CFA. Yet, the significant reduction of the final setting time promoted even by low MSWI-FA contents can potentially be of interest, as the long PBG reaction kinetics is one of the main drawbacks in terms of practical application [4], along with the relatively high cost of both MK and phosphoric acid. In this view, even a partial MK substitution with MSWI-FA can help mitigate technical problems and economic impact related to PBG use/production.

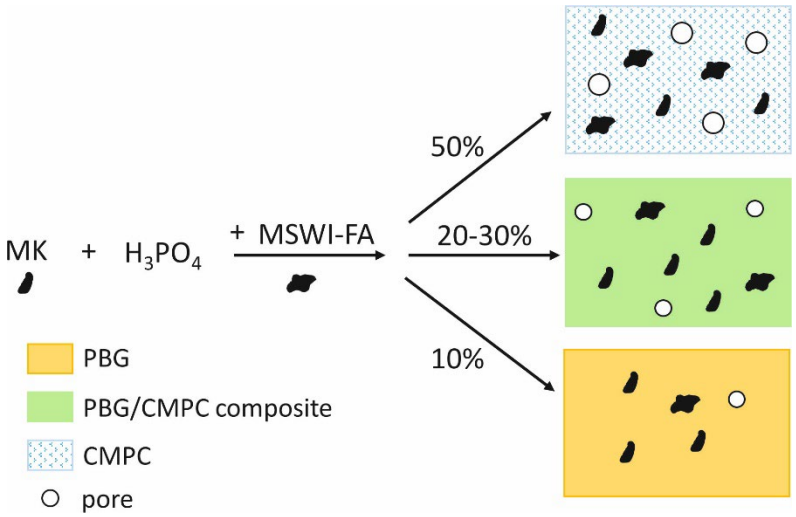

Figure 6.13 Schematic representation of the influence of MSWI-FA degree of substitution in the production of PBG.

6.5 Conclusions

Water-washed MSWI-FA has been introduced for the first time into metakaolin/phosphate-based geopolymer. It has been shown that some fractions of MSWI-FA participate in the reaction with the phosphoric acid, and amorphous phosphate hydrates form exploiting metal ions, such as Mg^{2+}. The replacement of MK with MSWI-FA makes available Ca^{2+}, whose mobilization leads to the precipitation of crystalline Ca-phosphates. Yet, the lower amount of available aluminium provided by MSWI-FA in comparison with pure MK and the competition of the metal ions from ash for phosphates, hinder the development of the aluminophosphate geopolymer matrix. Using Al/P~1.1, at 10 wt% of MK substitution with MSWI-FA the extent of geopolymerization is still satisfactory, in terms of relative contribution of Q^1_P(2Al) and octahedral Al, and the mechanical performance turns out to be comparable to the one exhibited by the reference sample, PBG0. At higher degrees of substitution (30-50 wt%), the nature of the resulting material gradually shifts from that of a PBG-system to a Ca/Mg-phosphate cement/PBG composite. Although a well-mixed microstructure is preserved up to 30 wt% substitution, the increasing porosity and the presence of low-strength phases lead to a decline of the mechanical performance.

6.6 References

1. Coppola, L.; Bellezze, T.; Belli, A.; et al. Binders alternative to Portland cement and waste management for sustainable construction—part 1. J. *Appl. Biomater. Funct. Mater.* **2018**, 16, 186-202.
2. Davidovits, J. Geopolymers: ceramic-like inorganic polymers. *J. Ceram. Sci. Technol.* **2017**, 8, 335-350
3. Davidovits, J. Geopolymer Chemistry and Applications. 5th Ed.; Geopolymer Institute, **2020**.
4. Wang, Y. S.; Alrefaei, Y.; Dai, J. G. Silico - Aluminophosphate and alkali-aluminosilicate geopolymers: a comparative review, *Front. Mater.* **2019**, 6, 1–17.
5. Liu, J.; Wang, Z.; Xie, G.; Li, Z.; Fan, X.; Zhang, W.; Xing, F.; Tang, L.; Ren, J. Resource utilization of municipal solid waste incineration fly ash - cement and alkali-activated cementitious materials: A review *Sci. Total Environ.* **2022**, 852, 158254.

6. Zhan, X.; Wang, L.; Wang, L.; Wang, X.; Gong, J.; Yang, L.; Bai, J. Enhanced geopolymeric co-disposal efficiency of heavy metals from MSWI fly ash and electrolytic manganese residue using complex alkaline and calcining pre-treatment. *Waste Manag.* **2019**, 98, 135–143.
7. Zheng, L.; Wang, C.; Wang, W.; Shi, Y.; Gao, X. Immobilization of MSWI fly ash through geopolymerization: Effects of water-wash. *Waste Manag.* **2011**, 31, 311–317.
8. Katsiki, A. Aluminosilicate phosphate cements–a critical review. *Adv. Appl. Ceram.* **2019**, 118, 274-286.
9. Guo, H.; Yuan, P.; Zhang, B.; Wang, Q.; Deng, L.; Liu, D. Realization of high-percentage addition of fly ash in the materials for the preparation of geopolymer derived from acid-activated metakaolin. *J. Clean. Prod.* **2021**, 285, 125430.
10. Wang, Y. S.; Alrefaei, Y.; Dai, J. G. Influence of coal fly ash on the early performance enhancement and formation mechanisms of silico–aluminophosphate geopolymer. *Cement Concr. Res.* **2020**, 127, 105932.
11. Ginés, O.; Chimenos, J.M.; Vizcarro, A.; Formosa, J.; Rosell, J.R. Combined use of MSWI bottom ash and fly ash as aggregate in concrete formulation: Environmental and mechanical considerations. *J. Hazard. Mater.* **2009**, 169, 643–650
12. Cho, B.H.; Nam, B.H.; An, J.; Youn, H. Municipal Solid Waste Incineration (MSWI) Ashes as Construction Materials—A Review. *Materials* **2020**, 13, 3143.
13. Yin, K.; Ahamed, A.; Lisak, G. Environmental perspectives of recycling various combustion ashes in cement production—A review. *Waste Manag.* **2018**, 78, 401–416.
14. Lin, H.; Liu, H.; Li, Y.; Kong, X. Properties and reaction mechanism of phosphoric acid activated metakaolin geopolymer at varied curing temperatures. *Cem. Concr. Res.* **2021**,144, 106425.
15. Celerier, H.; Jouin, J.; Tessier-Doyen, N.; Rossignol, S. Influence of various metakaolin raw materials on the water and fire resistance of geopolymers prepared in phosphoric acid, *J. Non Cryst. Solids* **2018**, 500, 493-501.
16. Damons, R.E.; Petersen, F.W. An Aspen Model for the Treatment of Acid Mine Water. *EJMP & EP* **2002**, 2, 69-81.
17. Legrand, A.P.; Sfihi, H.; Lequeux, N.; Lemaître, J. ^{31}P Solid-State NMR study of the chemical setting process of a dual-paste injectable brushite cements. *J. Biomed. Mater. Res.* **2009,** 91B, 46-54.
18. Mathivet, V.; Jouin, J.; Gharzouni, A.; Sobrados, I.; Celerier, H.; Rossignol, S.; Parlier, M. Acid-based geopolymers: Understanding of the structural evolutions during consolidation and after thermal treatments. *J. Non Cryst. Solids* **2019**, 512, 90-97.
19. Kim, Y.; Caumon, M.C.; Barres, O.; Sall, A.; Cauzid, J. Identification and composition of carbonate minerals of the calcite structure by Raman and infrared spectroscopies using portable devices. *Spectrochim. Acta A Mol. Biomol.* **2021**, 261, 119980.
20. Jones, F. Infrared investigation of barite and gypsum crystallization: Evidence for an amorphous to crystalline transition. *CrystEngComm* **2012**,14, 8374-8381.
21. Zribi, M.; Baklouti, S. Investigation of Phosphate based geopolymers formation mechanism. *J. Non Cryst. Solids* **2021**, 562, 120777.
22. Sánchez-Enríquez, J.; Reyes-Gasga, J. Obtaining $Ca(H_2PO_4)_2{\cdot}H_2O$, monocalcium phosphate monohydrate, via monetite from brushite by using sonication. *Ultrason. Sonochem.* **2013**, 20, 948-954.
23. Edén, M. NMR studies of oxide-based glasses. *Annu. Rep. Prog. Chem., Sect. C: Phys. Chem.* **2012**, 108, 177–221.
24. Skibsted, J.; Pedersen, M. T.; Holzinger J. Resolution of the Two Aluminum Sites in Ettringite by ^{27}Al MAS and MQMAS NMR at Very High Magnetic Field (22.3 T). *J. Phys. Chem. C* **2017**, 21, 4011-4017.
25. Abdelrahman, O.; Garg N. Impact of Na/Al Ratio on the Extent of Alkali-Activation Reaction: Non-linearity and Diminishing Returns. *Front. Chem*. **2022**, 9.

26. Dong, T.; Xie, S.; Wang, J.; Chen, Z.; Liu, Q. Properties and characterization of a metakaolin phosphate acid–based geopolymer synthesized in a humid environment. *J. Aust. Ceram. Soc.* **2020**, 56, 175–184.
27. Celerier, H.; Jouin, J.; Gharzouni, A.; Mathivet, V.; Sobrados, I.; Tessier-Doyen, N.; Rossignol, S. Relation between working properties and structural properties from ^{27}Al, ^{29}Si and ^{31}P NMR and XRD of acid-based geopolymers from 25 to 1000°C. *Mater. Chem. Phys.* **2019**, 228, 293-302.
28. Scrimgeour, S.N.; Chudek, J.A.; Cowper G.A.; Lloyd C.H. (^{31})P solid-state MAS-NMR spectroscopy of the compounds that form in phosphate-bonded dental casting investment materials during setting. *Dent Mater.* **2007**, 23, 934-43.
29. Lee, W.; Van Deventer, J. The effect of ionic contaminants on the early-age properties of alkali-activated fly ash-based cements, *Cem. Concr. Res.* **2002**, 32, 577–584.
30. Mecholsky, J. Toughening in glass ceramic through microstructural design. In: Bradt, R.C.; Evans, A.G.; Hasselman, D.; Lange, F.F. editors. Fracture mechanics of ceramics, vol. 6. New York, NY: Plenum Press, **1983**
31. Serbena, F.C.; Mathias, I.; Foerster, C.E.; Zanotto, E.D. Crystallization toughening of a model glass-ceramic. *Acta Mater.* **2015**, 86, 216–28.
32. Apel, E.; Deubener. J.; Bernard, A.; Holand, M.; Muller, R.; Kappert, H. Phenomena and mechanisms of crack propagation in glass-ceramics. *J. Mech. Behav. Biomed. Mater.* **2008**, 1, 313–25.
33. Wagh, A. S. Chemically Bonded Phosphate Ceramics (Second Edition), Elsevier, **2016**.
34. Viani, A.; Lanzafame, G.; Chateigner, D.; El Mendili, Y.; Sotiriadis, K.; Mancini, L.; Zucali, M.; Ouladdiaf B. Microstructural evolution and texture analysis of magnesium phosphate cement. *J. Am. Ceram. Soc.* **2020**, 103, 1414– 1424.

Chapter 7

Investigation of MSWI-fly ash reactivity in Magnesium phosphate cement

7.1 Introduction

Magnesium potassium phosphate cement (MKPC) is an example of chemically bonded ceramics in which the hardening occurs at room temperature through the acid-base aqueous reaction between an alkaline magnesia source (MgO; periclase) and a phosphate source (KH_2PO_4), according to the following chemical equation [1]:

$$MgO + KH_2PO_4 + 5H_2O \rightarrow MgKPO_4 \cdot 6H_2O \quad (1)$$

Such a reaction is fast, exothermic and its mechanism has been described as a multi-step process, starting from i) MgO dissolution and complexation of cations, ii) formation of an amorphous gel-like phase by interaction with phosphate anion and iii) partial/total crystallization of $MgKPO_4 \cdot 6H_2O$ (K-struvite) in proximity or around the unreacted MgO particles [1,2]. As a result, the mechanical strength is ascribable to a network of K-struvite crystals embedded in an amorphous matrix, thus producing a sort of composite material [3,4]. In the conventional non-stoichiometric MgO-excess formulations, where a Mg/P molar ratio > 1 is employed (usually up to 6-8), the unreacted oxide fraction behaves as a filler, further reducing the porosity of the cement [4]. MKP-based cements (MKPC) are nowadays object of an increasing interest because of their excellent properties, such as high early age and long-term strengths, resistance to the sulfate attack, rapid setting, *quasi*-neutral pH, low shrinkage, good water resistance, high adhesive properties [5]. Therefore, they have been proposed for several applications: waste stabilizations/solidifications, rapid rehabilitations of infrastructures, and biomedical materials [5]. In the former case, blends with various waste (coal fly ash, ground blast furnace slag) have been studied, to reduce the cost of raw materials, which limits the use of this class of binders on a large-scale [6,7]. Comparatively few papers report investigations on MSWI-FA incorporation into MKPC. Su et al. 2016 focused on the synergistic effect of MSWI-FA in the stabilization of Pb/Cd-loaded MKPC, which demonstrated good efficacy in the former case, owing to the fly ash's pore-filling and heavy metal adsorption properties [8]. Yang et al. (YEAR) tested the performance of MSWI-FA in MKPC different formulations, concluding that 10% wt. of MSWI-FA is the optimal addition, due to a 20% higher 60-day compressive strength and 20% smaller 60-day shrinkage deformation [9]. However, no in-depth analysis was provided about the effect of the cement environment, i.e., pH and chemical conditions, on MSWI-FA.

In the present work, the incorporation of washed/steam-washed MSWI-FA into MKPC is studied, paying special attention to the waste participation to the cement reaction. In particular, the occurrence of dissolution reactions involving MSWI-FA components is thoroughly assessed, together with the chemical characterization of the related secondary products. All this in order to provide a mechanistic understanding of MSWI-FA behaviour within MKPC, as it is fundamental for the design of the optimal conditions to recycle this waste in MKPC. The strategy we follow takes the *reactivity* of MSWI-FA into account, in terms of *effective* MgO "equivalent" [6]. Two formulations are studied: in one, MSWI-FA is considered a *fully inert system*, replacing both MgO and KH_2PO_4; in the other, MSWI-FA is *fully reactive*, thus replacing MgO only. Moreover, a MSWI-FA diluted suspension in KH_2PO_4 saturated solution is also investigated, to evaluate the maximum

extent of the waste reactivity and compare its behaviour with the one observed in the cement pastes. The obtained samples are characterized by X-ray powder diffraction, scanning electron microscopy coupled with energy dispersive spectroscopy, isothermal conduction calorimetry techniques, in addition to compressive strength and leaching performances. Moreover, due to the presence of significant amorphous components in the cement and MSWI-FA, spectroscopies such as SSNMR (on ^{27}Al, ^{29}Si, ^{31}P) and synchrotron Zn K-edge X-ray absorption spectroscopy are used.

7.2 Materials and Methods

7.2.1 Materials

The raw materials employed in this study were reagent grade MgO (assay 99.8%), reagent grade KH_2PO_4 (assay 99.8%) (Lach-ner s.r.o) and MSWI-FA from an incineration plant located in Turin (Italy). MgO powder was calcinated for 1 h in laboratory furnace at 1500 °C, then milled for 1 min in a Mini-Mill Pulverisette 23 (Fritsch) at 30 oscillations/min. Particle size analysis and specific surface area were conducted in triplicate, resulting in an average particle size d_{50} of 7.2 µm and a BET surface area of 2.98 m^2g^{-1}. The washed MSWI-FA was filtered and ground in a mortar (RM 200, Retsch, Germany) to a size < 63 µm. The chemical compositions of the raw materials were determined by X-Ray Fluorescence measurements and are reported in Table 7.1.

Table 7.1 Chemical composition (wt %) and main physical properties of MSWI-FA. Uncertainties of about 2-3%.

aw naterial	**Chemical composition (wt %)**										**BET (m^2g^{-1})**	**D_{50} (µm)**	**D_{90} (µm)**
	Al_2O_3	Fe_2O_3	TiO_2	K_2O	CaO	SiO_2	MgO	SO_3	P_2O_5	Others			
MSWI-FA	9.12	8.21	1.57	0.62	43.54	24.51	6.53	4.51	0.27	1.12	13.2	7.9	32.5

7.2.2 Formulation design

The formulation details of the investigated MKPC pastes are reported in Table 7.2. Although it is usually applied in commercial mixes, the retarder addition was here avoided because the objective was to explore the reactivity of MSWI-FA in the pure MgO- KH_2PO_4 system. In the reference paste (REF), a M/P molar ratio of 1.75 and water-to-binder weight ratio (*w*/b) of 0.45 were used, to favour the dissolution of MSWI-FA particles and resulting cations/anions mobilization [1]. The ash residue was implemented at a fixed 30 wt% MgO substitution in both the filler and reactive formulations (MF0 and MF100, respectively). Such value was chosen as it allows to observe the MSWI-FA behaviour without compromising the cement properties [6]. A fixed *effective* MgO/PO_4 of 1.75 and fixed water-to-*effective* binder of 0.45 were considered to calculate KH_2PO_4 and water content. An additional sample was investigated to estimate the potential reactivity of the ash. It consists of a MSWI-FA diluted (at liquid-to-solid ratio of 2) suspension in KH_2PO_4 saturated solution (obtained by dissolving 7 g of salt in 50 ml of ultrapure water).

Table 7.2 Formulations of MKPC pastes

	REF	MF0	MF100
MgO (g)	350	245	245
MSWI-FA (g)	-	105	105
KDP (g)	675.3	472.7	675.3
Water (g)	512.7	358.9	512.7

7.2.3 Solid state Nuclear magnetic Resonance (SSNMR)

All SSNMR measurements were recorded at room temperature on a solid-state NMR spectrometer (JNM-ECZ600R, JEOL RESONANCE Inc., Japan) at a magnetic field of 14.1 T, operating at ^{1}H, ^{27}Al, ^{29}Si, and ^{31}P Larmor frequencies of 600.1, 156.4, 119.2, and 242.9 MHz, respectively. The raw material and ground cement samples were packed into 3.2 mm zirconia rotors and spun at a MAS frequency of 15, 15 and 20 kHz for ^{27}Al, ^{29}Si, and ^{31}P MAS spectra, respectively. A ^{27}Al, ^{29}Si and ^{31}P pulse of 12 µs, 4 µs and 3 µs were employed. ^{1}H, ^{27}Al, ^{29}Si, and ^{31}P chemical shifts scales were referenced through the resonances of adamantane, aluminium nitrate, silica and $(NH_4)H_2PO_4$, respectively. The deconvolution analysis was conducted using the related in-built feature of Delta 6.1 (Jeol), while the estimated error in the calculated fraction percentage is in range of ± 1%.

7.2.4 Isothermal conduction calorimetry (ICC)

Isocalorimetry experiments were conducted with a TAM-Air (TA Instruments) 8-channel instrument. For each formulation, the powder and the liquid were kept separated in an Ad-Mix® ampoule until both were equilibrated at the measurement temperature (20 °C). The liquid was manually injected onto the powder, defining the start of the experiment. The slurry was mixed for 30 s and the heat flow was recorded for 10 h.

7.2.5 Mechanical tests

Compressive strength tests were performed on 28 days PBG paste cubes' (1x1x1 cm), measuring 3 replicates by means of an Instron 3345 (Instron, USA) loading frame, at loading speed of 0.2 mm/min and load cell of 5 kN.

7.2.6 Leaching test

The batch (static) leaching tests, according to EN 12457-2, [10] was employed for MSWI-FA and cement samples. Prior to the test, cement cubes were ground and sieved to obtain a powder with particle size less than 2 mm. More specifically, the test involves the immersion of the powdered samples in ultrapure water solution at natural pH, with a liquid-to-solid ratio set to 10 and 24 hours shaking.

7.2.7 X-ray Absorption spectroscopy (XAS)

The Zn K-edge XANES spectra of the samples were collected at Elettra synchrotron radiation source, beamline XRF. All samples were finely ground and 13mm pellets were prepared with similar weight (around

150 mg), for measurements in fluorescence mode. The reference minerals samples were all collected in transmission mode, at the XAS beamline of Elettra, by calculating the optimal mass for an absorption jump around 1 and mixing the amount with BN to reach 100 mg for the pelletization. Zn K-edge XAS spectra were collected using a Si(111) double crystal monochromator. A number of scans between 3-5 was employed, while 1-2 was used for reference minerals, with an energy step of 5 eV in the pre-edge region, of 0.2 eV in the XANES region and a constant k step of k = 0.035 $Å^{-1}$ in the EXAFS region. The Linear combination Fitting of XANES, energy alignment and normalization to the edge-jump was performed by Athena.

7.3 Results

7.3.1 ICC

The first 50 min of the heat flow (normalized to the amount of MgO) produced during the cement reaction at 20 °C is shown in Figure 7.1 (top). The REF sample displays the typical curve observed in similar pure formulations [1]. An initial endothermic peak is recorded immediately after mixing (Figure 7.2), related to the dissolution of KDP, which is usually neglected as it is followed by two more intense exothermic events. The first one has been assigned to the dissolution of MgO, while the second, characterised by a much broader exothermic peak, relates to the crystallization of MKP. At a slower heat-exchange rate (i.e., at *T* of 5-15 °C, [1]) the calorimetric curve inflection has allowed the identification of a third exothermic event in between those mentioned above, which has been attributed to the formation of an amorphous precursor that later converts to K-struvite [1,2]. Here, the identification of this exothermic event is impaired by the strong signal overlap because of the fast cement reaction kinetics (most of the heat is exchanged in about 20 min) due to the relatively high reactivity of the employed MgO (calcined at 1500 °C). When the normalized heat flow curve of the inert MF0 formulation is considered, no significant differences in terms of time and intensity can be observed for the MgO dissolution (i.e., the first exothermic peak). Interestingly, a change is apparent on the amorphous precursor formation/MKP crystallization peak (i.e., the second exothermic peak), whose maximum starts earlier (10 min with respect to 13 min for REF0) and in general appears to be sharper, thus more 'compressed' in time, indicating an increase of the reaction kinetics of the overall process. On the contrary, MF100 presents a clear delay of the maximum of the MgO dissolution peak (6 min against 5.3 min for REF0), together with an increased intensity, followed by a more developed MKP crystallization peak, while its breath and shape are more similar to REF0 than MF0. All this suggests that a more effective dissolution of MgO occurs, probably related to the higher KH_2PO_4 content in the formulation, which determines an higher amount of product. This is confirmed by the normalized total heat curves, where MF100 displays a significant higher heat release at the end of the experiments, while REF0 and MF0 are very close (1720 J/g against 1425 and 1410 J/g, respectively).

In order to better isolate the potential MSWI-FA contribution to the total exchanged heat and heat flow, an additional experiment has been conducted, where MSWI-FA was mixed with a saturated solution of KH_2PO_4 (liquid-to-solid ratio of 2) inside the calorimeter (Figure 7.1, inset). The intensity of the maxima, normalized to the amount of MSWI-FA, in the inset of Figure 7.1, are about one order of magnitude lower with respect to the cement samples' (0.1 against 1.2 W/g and 74 against 1400-1700 J/g, respectively). Nonetheless, the dissolution of a MSWI-FA fraction in acidic environments (see next sections) and the formation of secondary products occurred. The time scale of the heat flow peak, going to completion in about 40 min, is compatible with the fast kinetics typical of these acid-base reactions [1,11].

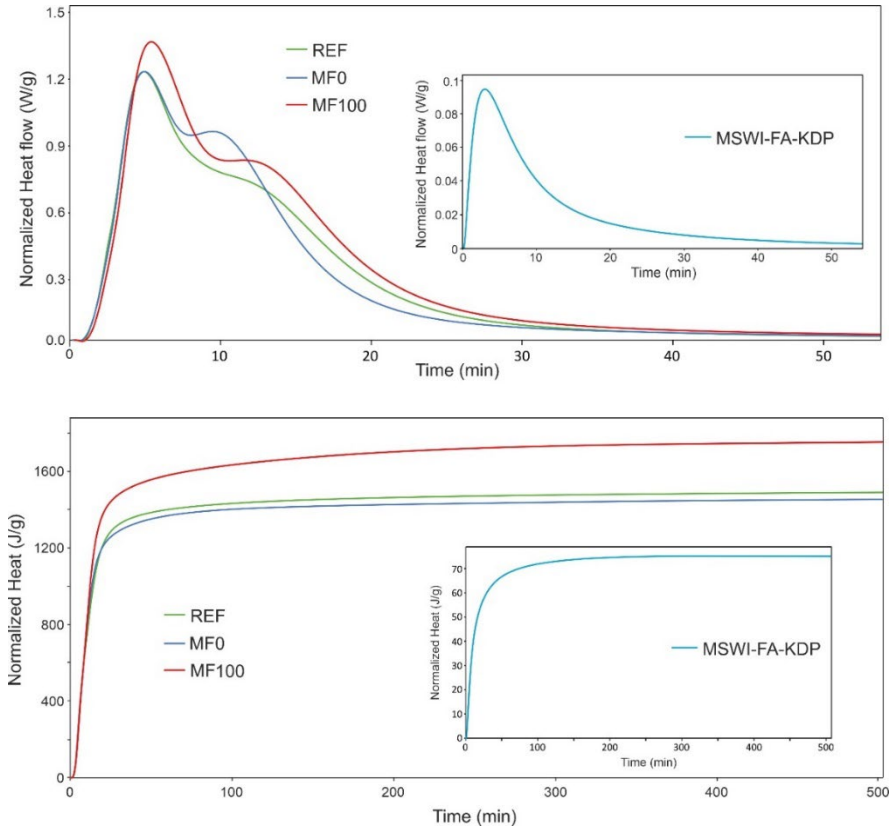

Figure 7.1 Normalized heat flow (top) and total heat (bottom) of cement mixtures. MSWI-FA/KDP suspension curves are represented in the insets.

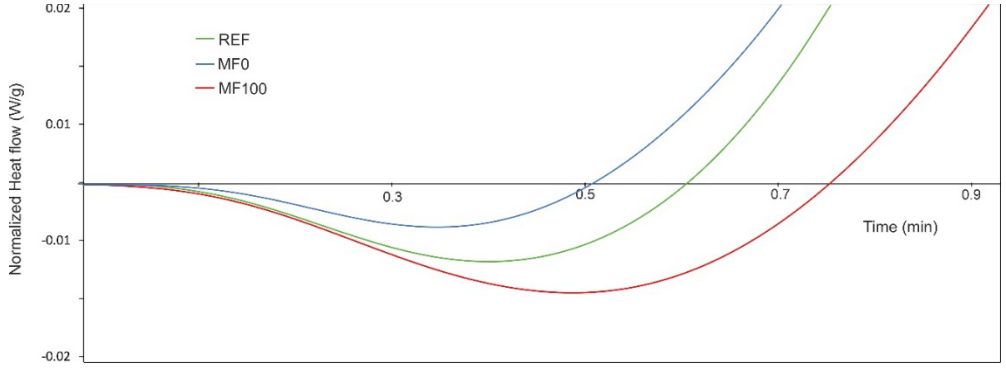

Figure 7.2 First minute of the normalized heat flow curves of cement samples, where the KDP dissolution endothermic peak is visible.

7.3.2 XRPD

The XRPD patterns of MSWI-FA and cement pastes are shown in Figure 7.2. MSWI-FA, after washing treatment, exhibits a complex mineralogy, including sulfate phases (gypsum, anhydrite and ettringite), quartz, calcite, melilite, perovskite, together with a significant amount of amorphous fraction. In the REF sample, the only crystalline phases are represented by K-struvite, along with a residual periclase (MgO), as expected in light of the used Mg/P molar ratio (1.75:1), whereas KH_2PO_4 is not detected. In the case of MF0 and MF100

formulations, additional peaks of quartz and anhydrite related to MSWI-FA are present, together with calcite. Low intensity peaks of arcanite (K_2SO_4) are visible, suggesting a release of sulfate from MSWI-FA. The results of the Rietveld quantitative phase analysis of the pastes are reported in Table 7.3, while an example of the graphical output for MF0 is illustrated in Figure 7.4. As previously observed, the cement products consist of both crystalline and amorphous MKP. With respect to the REF sample, MF0 does not exhibit a significant decrease in residual MgO, conversely, a much higher proportion of the amorphous precursor remains after the experiment. This agrees with the results by ICC, where the first exothermic peak is very similar in the two normalized heat flow curves, while the acceleration of the second event indicates a reaction with higher kinetics, thus favouring amorphous products [1,2]. When MF100 is considered, a lower amount of residual MgO was detected, due to a more efficient dissolution process in presence of a relatively initial higher content of KH_2PO_4. This consumption of MgO did not cause an increase of the products with respect to REF, though the normalized heat curves display comparable K-struvite crystallization peaks, suggesting that a more complex mechanism may be involved.

As a comparison, the phase composition of MSWI-FA/KDP after isocalorimetry is shown in Table 7.4, to emphasize the potential MSWI-FA mineralogical transformations that may occur during the cement reactions. It is apparent that even in this case, some calcite is still present, in agreement with the results on the cement pastes, while a more effective dissolution involved other phases, like ettringite and periclase. In a similar way, arcanite is observed, together with the crystallization of Ca-phosphate (brushite). A marked decrease of anhydrite content is present. It is expected that in this diluted environment anhydrite easily hydrates as gypsum, which was observed (1.6 to 4.3 wt.%) [12]. It is likely that the ions for precipitation of arcanite and brushite are provided by anhydrite dissolution. It is worth noting that the amorphous content increased by 50% (from 53.4 to 77.1 wt.%), indicating that most of the secondary products are poorly crystalline. The significant decrease in gehlenite content suggests that also the MSWI-FA aluminosilicate component can be potentially involved during the cement reaction. Further hints in this sense will be provided in the next sections.

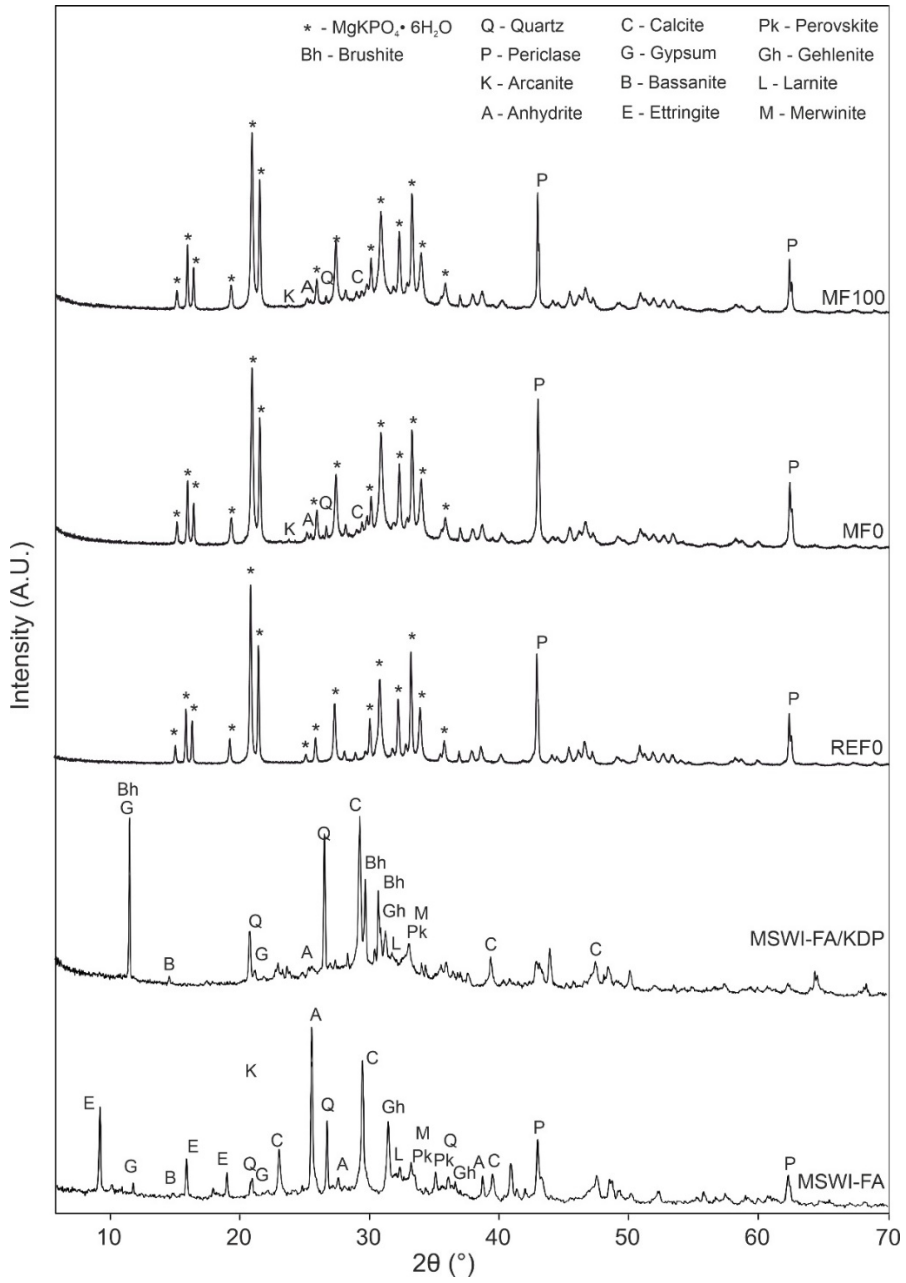

Figure 7.2 XRPD patterns of cement pastes, together with MSWI-FA and MSWI-FA/KDP samples.

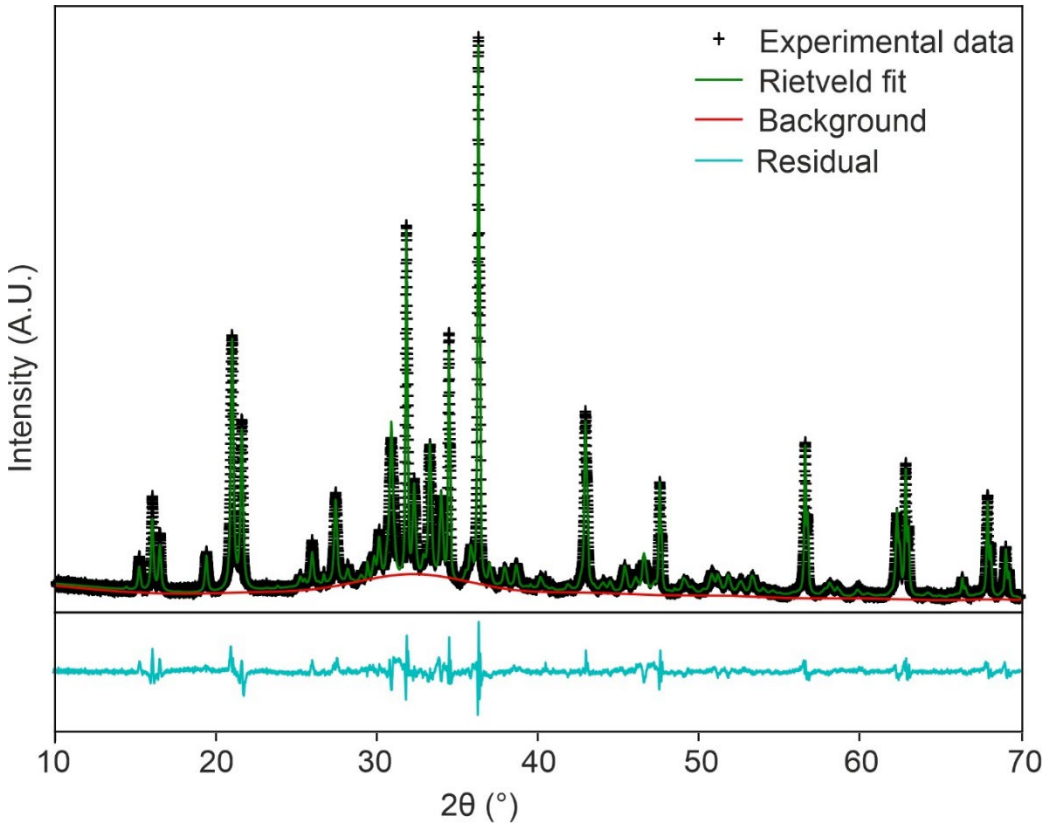

Figure 7.3 GSASII Rietveld refinement output for MF0, with the addition of 10%wt ZnO as internal standard and a final R_{wp} of 8.1.

Table 7.3 Results of quantitative phase analysis with the internal standard method of samples 28 days after the reaction in the calorimeter at 20 °C. The uncertainties are ±0.2 wt % (crystal phases) and ±5 wt % (amorphous phase).

Sample	**REF**	**MF0**	**MF100**
		wt.%	
MKP	65.6	40.1	52.9
Periclase	7.7	7.4	6.1
Quartz		0.2	0.2
Calcite		0.3	0.3
Anhydrite		0.2	0.2
Arcanite		0.2	0.2
Amorphous	26.7	51.6	40.1

Table 4. Results of quantitative phase analysis with the internal standard method of MSWI-FA and MSWI-FA/KDP samples. The uncertainties are ±0.2 wt % (crystal phases) and ±5 wt % (amorphous phase).

Sample	**MSWI-FA**	**MSWI-FA/KDP**
	wt.%	
Quartz	3.2	3.3
Calcite	11.9	5.1
Anhydrite	9.2	1.3
Larnite	1.5	0.8
Gehlenite	2.9	1
Periclase	4.5	-
Gypsum	1.6	4.3
Bassanite	0.2	0.1
Ettringite	9.6	-
Merwinite	0.9	0.6
Perovskite	1.1	0.8
Arcanite	-	3.8
Brushite	-	2.6
Amorphous	53.4	77.1

7.3.3 SSNMR

The ^{31}P MAS spectra of the cement samples are shown in Figure 7.4. All spectra are dominated by a peak at 6.3 ppm, related to the crystalline MKP [2]. The broader signal centred at around 2.1 ppm of much lower intensity has been assigned to the cement amorphous precursor, whose hydrated orthophosphate nature has been assumed by the chemical shift range and previous cross-polarization (CP/MAS) experiments [1,2]. Here, a signal deconvolution approach was employed, to better evaluate differences between the samples. The broad amorphous contribution has been modelled using two components, which are related to two distinct amorphous P environments previously found to exhibit different dynamics under CP conditions [1,2]. It is apparent that the MSWI-FA cement samples present a lower MKP crystalline/amorphous ratio with respect to REF, especially MF0, hinting to different reaction rates, in accordance with the ICC curves. It is also worth noting that, although XRPD and ^{31}P MAS spectra cannot be directly compared, in terms of relative fractions of crystalline and amorphous phases, from a semi-quantitative point of view the general trends obtained by the two techniques are in good agreement.

On the other hand, with respect to the neat MKPC (REF sample), a contribution to the amorphous component from MSWI-FA might be present. Indeed, the MAS spectrum of F (Figure 7.5, bottom) exhibits a sharp peak at around 1.3 ppm, assigned to brushite [13], but it is dominated by a significantly broader asymmetric peak that spans from 7 to -8 ppm. Such large linewidth testifies the presence of different P environments that can result from the reactions between the numerous crystalline and amorphous phases of the fly ash with phosphate. The $^{31}P\{^{1}H\}$ CP/MAS experiment (Figure 7.5, top) produced only the brushite peak and a secondary much smaller resonance at around -7 ppm, possibly related to newberyite ($MgHPO_4 \cdot 3H_2O$) [13]. This information, coupled with the chemical shift range, points to identify most of the amorphous products as either orthophosphate or pyrophosphate with no significant interaction with H.

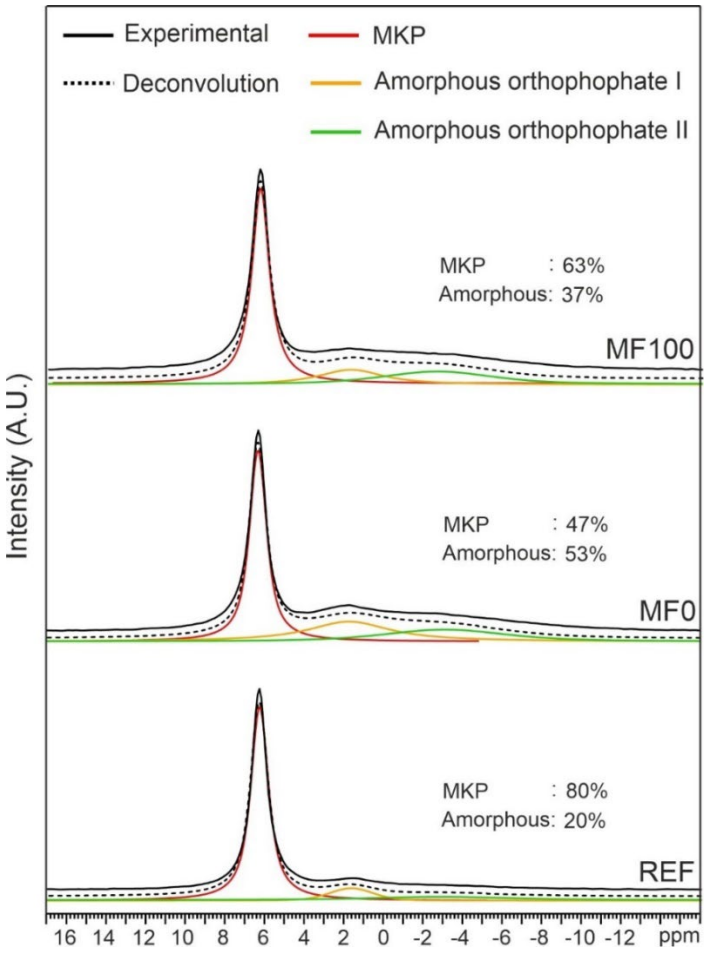

Figure 7.4 ^{31}P MAS spectra of cement samples.

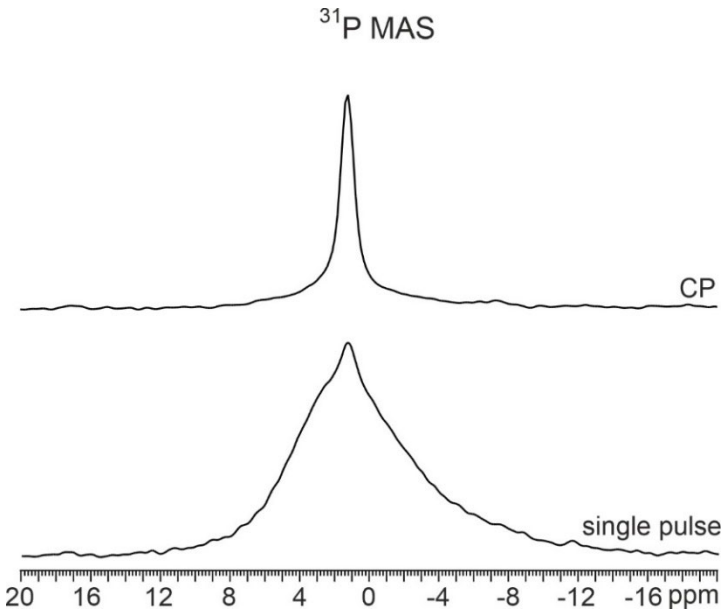

Figure 7.5 ^{31}P MAS and CP/MAS spectra of MSWI-FA/KDP sample.

^{27}Al and ^{29}Si MAS experiments are particularly useful since they allow the direct investigation of MSWI-FA behaviour, as no other source of these elements is present in the mixtures. ^{27}Al MAS spectra of all samples are shown in Figure 7.6, together with the unreacted residue. The MSWI-FA spectrum displays a broad peak

at around 68 ppm, which is related to the Al^{IV} speciation in the aluminosilicate glass fraction, and second signal formed by at least two contributions in the Al^{VI} region (Figure 7.6, left) [14]. The relatively narrow peak at around 13 ppm arises from a crystalline phase and it is assigned to $Ca_6Al_2(SO_4)_3(OH)_{12}\cdot 26H_2O$ (ettringite), in agreement with literature data [15] and the XRPD results reported in Table 7.4. The broader peak centred at 9.5 ppm is reasonably originated by a limited fraction of Al^{VI} in aluminosilicate glass or amorphous aluminium hydroxide phases [14]. When MF spectra are considered in Figure 5, significant differences are apparent in the octahedral region. In particular, in MF100, the ettringite peak markedly reduces and a new broad peak develops at higher field, around -12 ppm. Moreover, the Al^{IV} aluminosilicate glass displays an increased linewidth, which may indicate partial dissolution or alteration. The new Al^{VI} signal centred at around -12 ppm should be related to some secondary product involving MSWI-FA. This product seems to be characterized by a relevant Al local disorder, as testified by the evident tail towards lower ppm, typical of a large distribution of chemical shifts and quadrupolar parameters [16]. It is also worth mentioning that the relative intensity of this peak increases from MF0 to MF100, pointing to the involvement of phosphate ions. Indeed, a very similar profile is observable for the F sample, where this signal is even more apparent (Figure 7.7).

^{29}Si MAS spectrum of MSWI-FA (Figure 7.6, right) is characterized by a very broad peak between -60 and -120 ppm, which encompasses all the different silicate/aluminosilicate environments present in the residue, spanning from the less reticulated Q^0 (i.e., larnite, see Table 4) and Q^1 (i.e., gehlenite) units at -63 and -71 ppm and the higher cross-linked Q^4(mAl) units of the amorphous glass fraction (from -80 to -113 ppm) [16]. MF0 and MF100 exhibit a similar broad profile, which significantly limits the interpretation [16]. Nonetheless, they seem to display a relatively less resolved low field region (Q^0-Q^1) with respect to the unreacted material, thus suggesting, as discussed with XRPD and ^{27}Al MAS SSNMR, that the aluminosilicate fraction of MSWI-FA likely reacted to some extent.

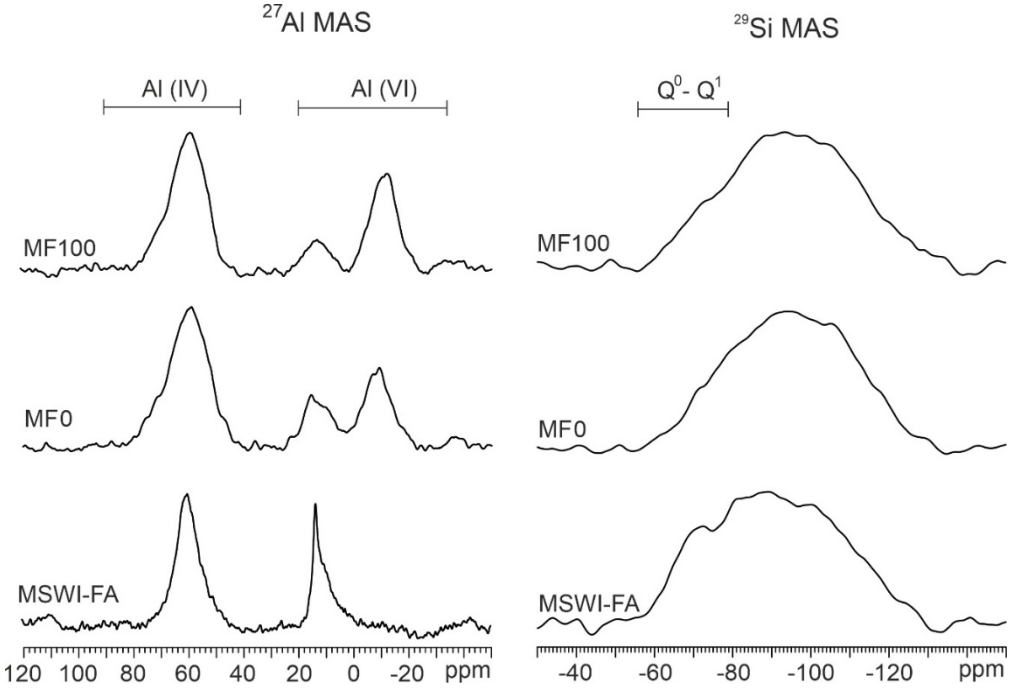

Figure 7.6 ^{27}Al (left) and ^{29}Si (right) MAS spectra of MSWI-FA and cement samples.

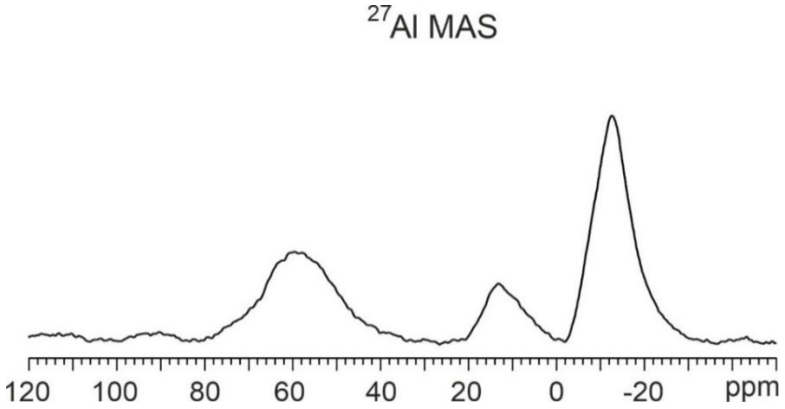

Figure 7.7 ^{27}Al MAS spectrum of MSWI-FA/KDP sample.

7.3.4 XAS

Zn K-edge XAS has been employed to get an insight into the mobilization and reactivity of one of the most abundant MSWI-FA heavy metals. The XANES spectra of MSWI-FA and MF samples, are shown in Figure 7.9, while the full XAS profiles, together with references, are plotted in Figure 7.8. Some differences before and after the cement reaction are apparent, namely, a relative increase of the white line intensity and the appearance of an additional feature around 9675 eV, while MF0 and MF100 samples display very similar profiles. A more detailed analysis was performed using the Linear Combination Fitting (LCF) method, which employs a set of known standards to model and fit the spectrum profile [17]. In case of complex system like MSWI-FA, the selection of the most appropriate standards can be hindered by its non-equilibrium formation processes, which often favour the stabilization of metastable/amorphous phases that can show some structural differences, in terms of number, nature of atoms and geometry of the heavy metal coordination shells, with respect to the related pure crystalline compound [17]. In this sense, the Zn-impregnated Al_2O_3, which presents Zn-aluminate nanospinel domains, has been chosen rather than the pure gahnite, $ZnAl_2O_4$ [18]. All XANES spectra have been modelled using four contributions, which were found enough to account for all the observed features. On average, the residual value (R) of around 0.02, which translated into an error of ± 2.5% on the quantitative data, was considered acceptable [18]. The washed MSWI-FA Zn (Figure 7.9) was found to be present as Zn^{2+} in tetrahedral coordination, with a local environment approximated with Zn-aluminate nanospinel (41%) and Zn-silicate, Zn_2SiO_4 (25%), together with ZnO (16%) and hydrozincite (18%). Both MF samples display similar Zn-aluminate components, but significant differences in the others are present. A decrease of ZnO contributions is evident (11%), together with the disappearance of hydrozincite. The new observed feature is modelled using a Zn-phosphate, namely hopeite ($Zn_3(PO_4)_2{\cdot}4H_2O$), which becomes one of the main contributions to the XANES profile (29-32%). Interestingly, a not-negligible reduction of Zn-silicate is also noticeable (16-18%), suggesting that a partial dissolution of the silicate MNSWI-FA fraction occurs. Indeed, this agrees with what observed in ^{29}Si MAS spectra, namely, the decrease in the intensity in the Q^0-Q^1 region.

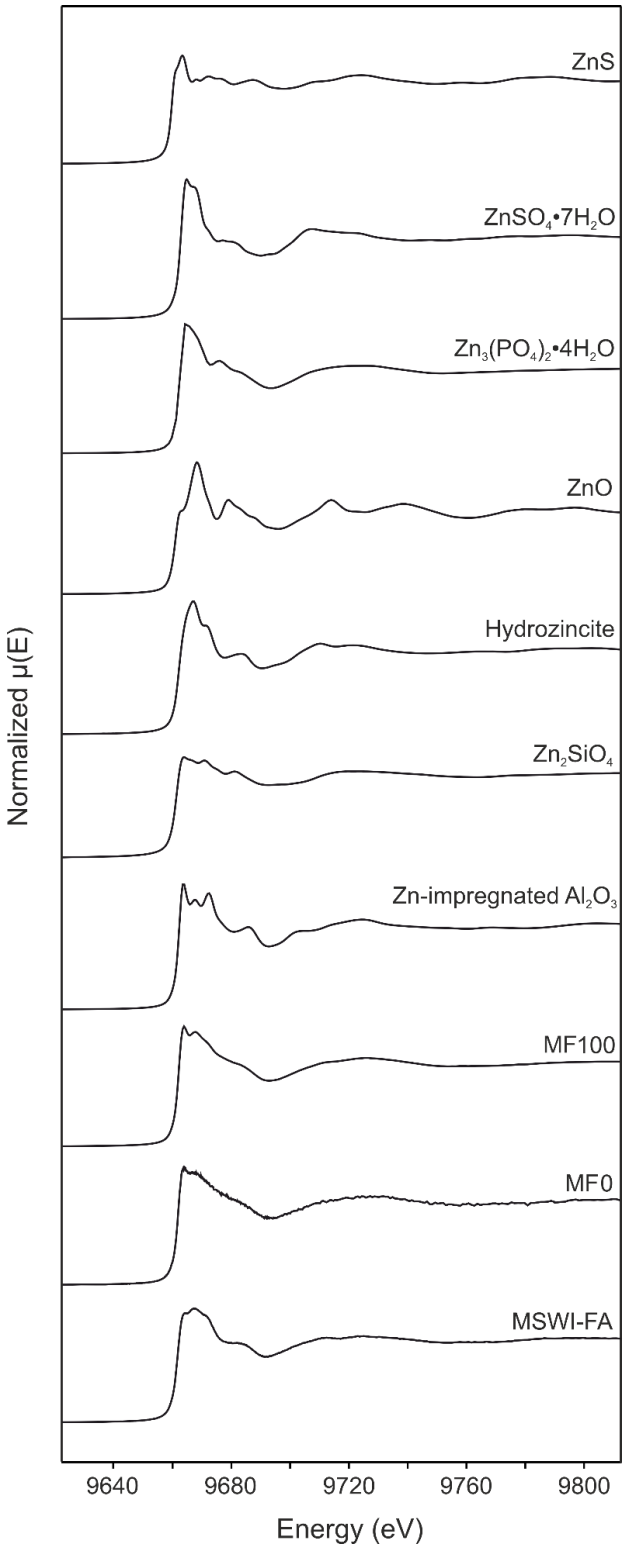

Figure 7.8 Zn *K*-edge XAS spectra of MSWI-FA, MKP samples and references.

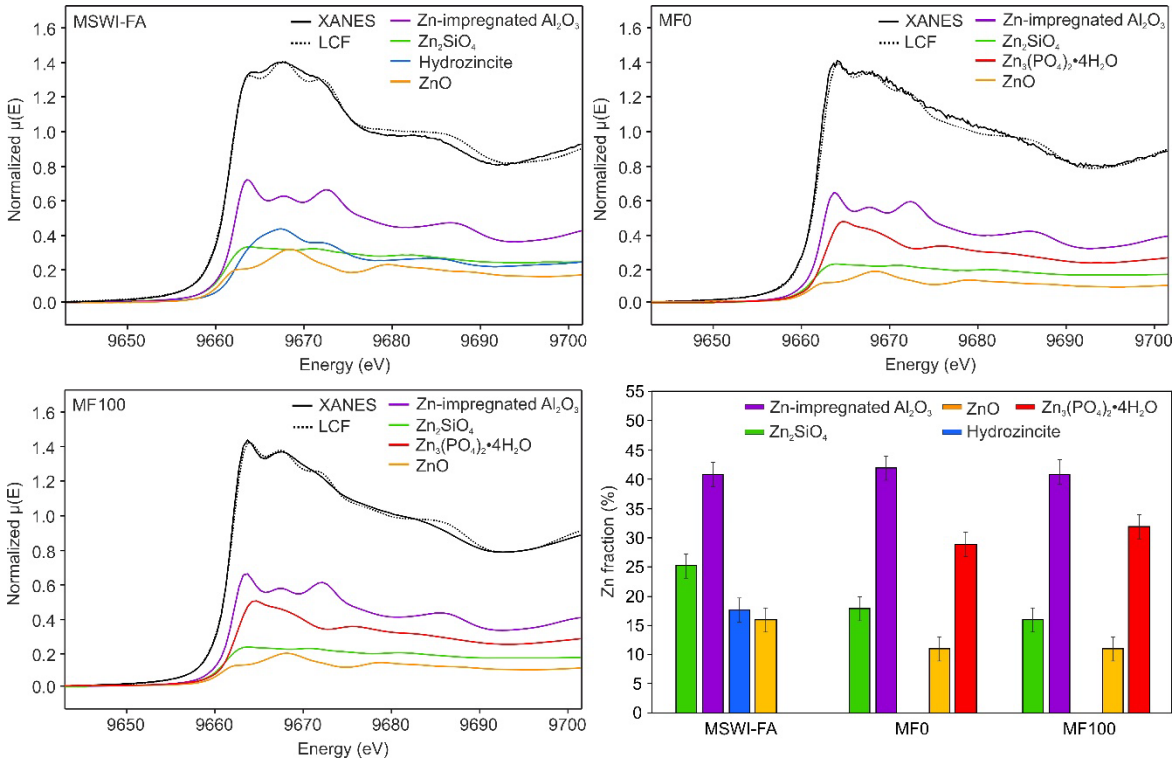

Figure 7.9 Zn *K*-edge XANES spectra of MSWI-FA and MKP samples, with LCF results.

5.3.4 SEM

The cements samples microstructure (Figure 7.10) is mostly determined by the growth of large (above 30-50 µm) and packed K-struvite crystals embedded in an amorphous matrix that present a similar chemical composition (i.e., similar contrast in BSE images) [19]. In the MSWI-FA containing samples, it is possible to observe that the surface of K-struvite crystals is sometimes coated by another crystals, namely arcanite, suggesting that the potassium sulfate precipitates after the K-struvite. In pure cement, K-struvite is known to exhibit both platelet-like and prismatic elongated crystal morphology, depending on crystallization rates and conditions (usually, lower reaction rates favour the platelet-like habit) [1]. This seems the case for MF100 with respect to MF0 (Figure 7.10), in agreement with the ICC curves (Figure 7.1).

MSWI-FA is characterized by a significant heterogeneity in terms of particles shape and chemistry, as shown in Figure 7.11, which makes more difficult the analysis of the cement samples. The MSWI-FA/KDP sample is mainly composed by large aggregates (> 100-150 µm, Figure 7.12), where, together with unreacted spherical particles, elongated crystals of Ca-phosphate are recognizable. Interestingly, the EDS spectrum of the bulk phase mostly presents Al, Si and P, suggesting the development of an aluminophosphate binding phase, in agreement with the spectroscopic analysis. As a way of example, MF0 cross-section BSE image is shown in Figure 7.13, together with EDS map. Overall, the MSWI-FA grains seem to be well embedded in the cement matrix. Indeed, K-struvite growth on spherical particles is noticed in Figure 7.14. Arcanite appears between K-struvite crystals, while in this case no clear Al and Si dissolution is observed for the aluminosilicate grains, possibly due to the limited extension of their reaction rims.

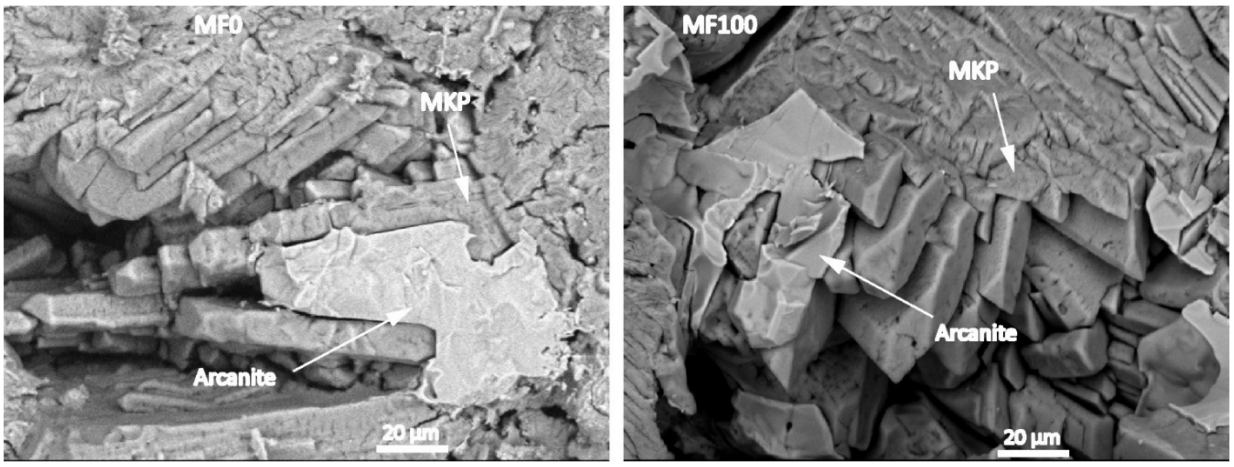

Figure 7.10 BSE images of MF0 (left) and MF100 (right).

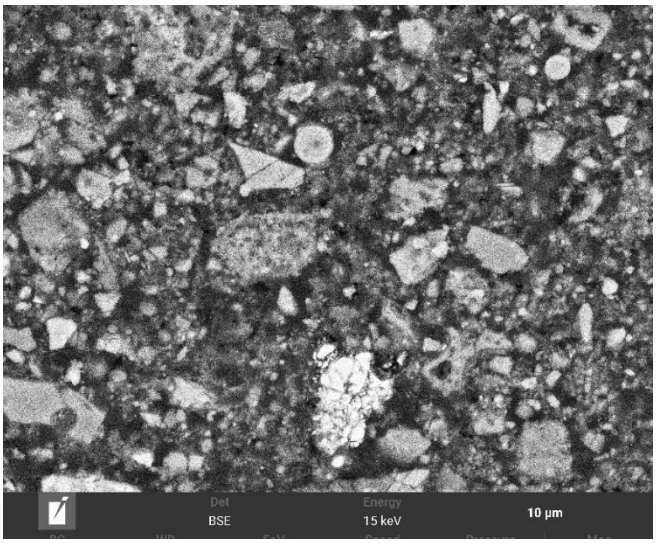

Figure 7.11 BSE image of washed MSWI-FA cross-section.

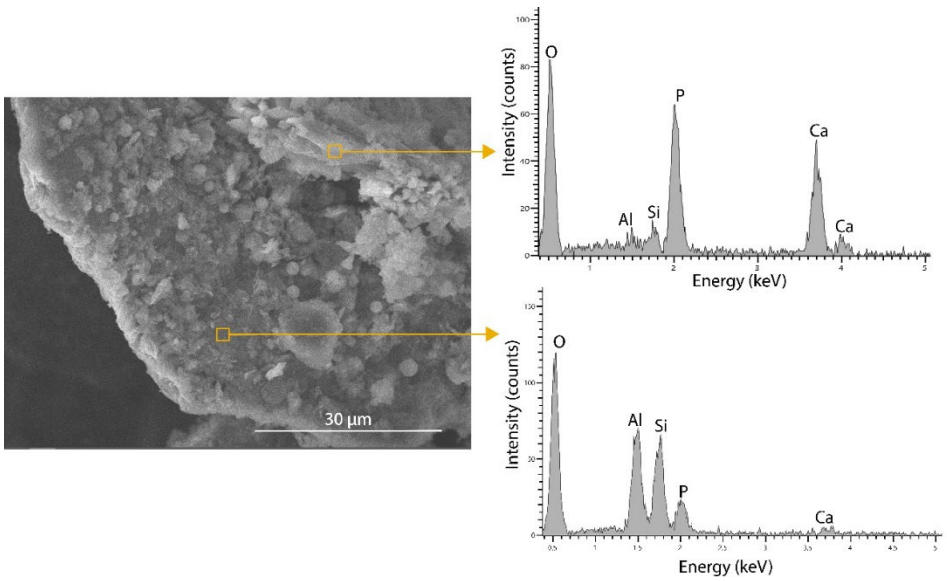

Figure 7.12 SE image of MSWI/KDP sample, with EDS spectra.

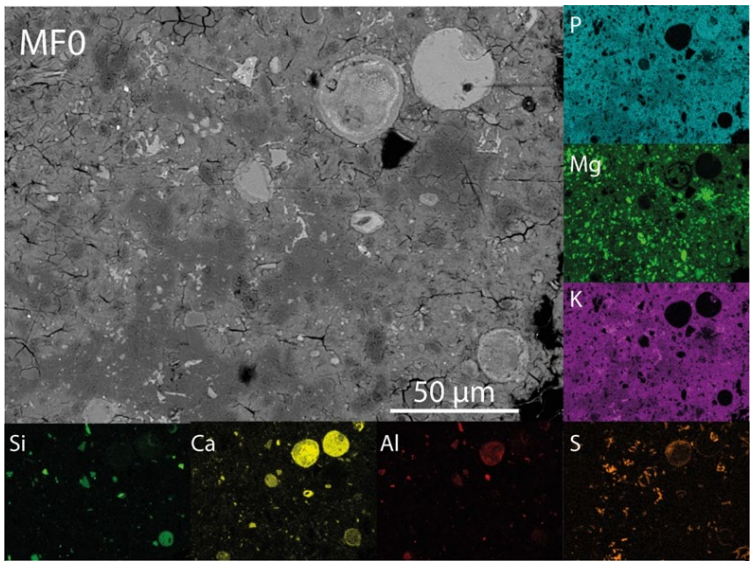

Figure 7.13 BSE images of MF0 cross-section, with EDS map.

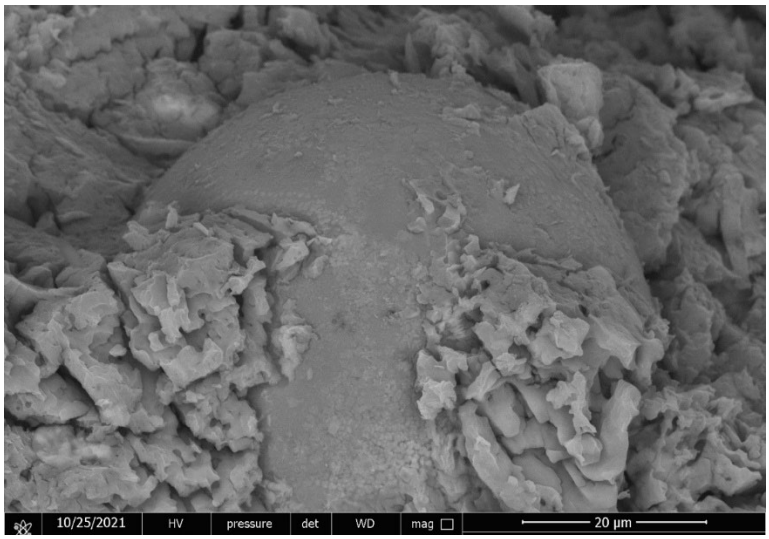

Figure 7.14 MSWI-FA spherical particle with MKP on the surface.

5.3.5 Mechanical and leaching properties

The compressive strengths of the MKPC samples cured for 28 days are illustrated in Figure 7.15 (top). REF and MF0 display comparable values (10.9-10.2 MPa), indicating that the formulation in which the ash is considered as “inert”, MSWI-FA does not significantly alter the cement mechanical performance. A marked increase is then visible for MF100 (15.5 MPa), possibly related to the more efficient MgO dissolution, as seen in the previous section. The mechanical properties of the cement are highly dependent on the amount of water, retardant, M/P ratio, purity of MgO (i.e., industrial grade periclase that has more impurities that could improve the strength). Here, the relatively high water-to-binder ratio of 0.45, the lack of retardant and the use of analytical grade MgO may explain the relatively low values observed. Indeed, comparable values were recently reported for MKPC formulated with similar parameters [20].

The leaching tests of the employed MSWI-FA and related MF samples are set out in Figure 7.15 (bottom). Although the waste residue underwent a washing pre-treatment, residual leaching of Zn, Cu, Ni and Cr was observed. It is known that water washing methods are very effective in removing salts (i.e., chloride) from

MSWI ashes, while the release of heavy metals may require additional treatments to be fully minimized. Here, it is apparent that a marked decrease on all investigated heavy metals leaching occurs, below the limits defined for inert waste and recycled aggregates [21]. It is also worth noting that no significant differences are evident between the two formulations, apart from Cr.

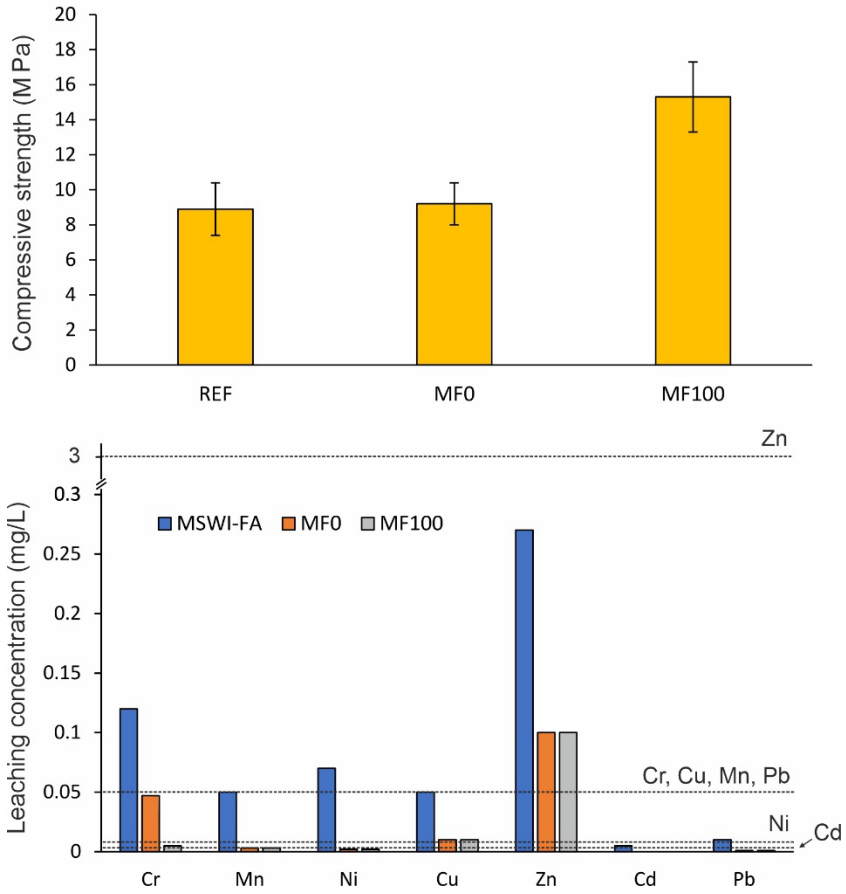

Figure 7.15 28-days compressive strength values of cement samples (top); Leaching test performances, together with MSWI-FA (bottom) and Italian law limit [21].

7.4 Discussion

The behaviour of a waste in a binder is dictated by both the chemical/mineralogical composition of the former and the chemical environment of the latter. MKPC develops through the initial dissolution of MgO in acidic environment (pH usually around 4; KH_2PO_4), followed by hydration reactions that increase the pH in time, usually up to 8-9 [2,11]. MSWI-FA is characterized by a complex phase composition, reported in Table 7.4. The solubility of the MSWI-FA's main phases (i.e., carbonate and sulfate) is promoted at pH < 6; therefore, their dissolution at the beginning of the cement reaction may provide cations (i.e., Ca^{2+} and Al^{3+}) and contribute to the precipitation of secondary products. Moreover, periclase (4 wt.%), together with a significant fraction of amorphous, is likely involved in this process.

This was confirmed by the heat released and the precipitation of Ca-phosphate (brushite) when MSWI-FA was allowed to react with the phosphate solution (Figure 7.1 and Table 7.4). The ^{31}P SSNMR analysis on MSWI-FA/KDP sample clearly indicated the formation of different phosphate (Figure 7.5), mostly amorphous

in nature, as suggested by the increase of the amorphous amount with respect to MSWI-FA. We observed a similar behaviour by adding the same MSWI-FA in metakaolin phosphate geopolymers [22]. In that case, the ash reactions speeded up the hardening process compared to the pure geopolymer, which has slow kinetics, and the pH remains highly acidic (around 2-3). In MKPC the system evolves much faster, as shown with ICC, where, for the sample REF, the maximum of the first exothermic peak was reached in 5 min, concomitantly with the pH increase.

The quick change of pH, combined with the relatively high acid neutralization capacity of the MSWI-FA, may be responsible for the incomplete calcite dissolution, both in the MSWI-FA/KH_2PO_4 suspension and in the MF0/100 samples. The partial dissolution of the abundant sulfate (i.e., gypsum, anhydrite), together with the rapid subtraction of water due to the gelification of the MKP amorphous precursor, have realized the supersaturation conditions required for the precipitation of arcanite (K_2SO_4) [1,11]. Its late precipitation is confirmed by the SEM observation (Figure 7.10), where arcanite is present on the surface of MKP crystals. In the same way, the released Ca can substitute Mg in the MKP, as shown in Figure 7.16.

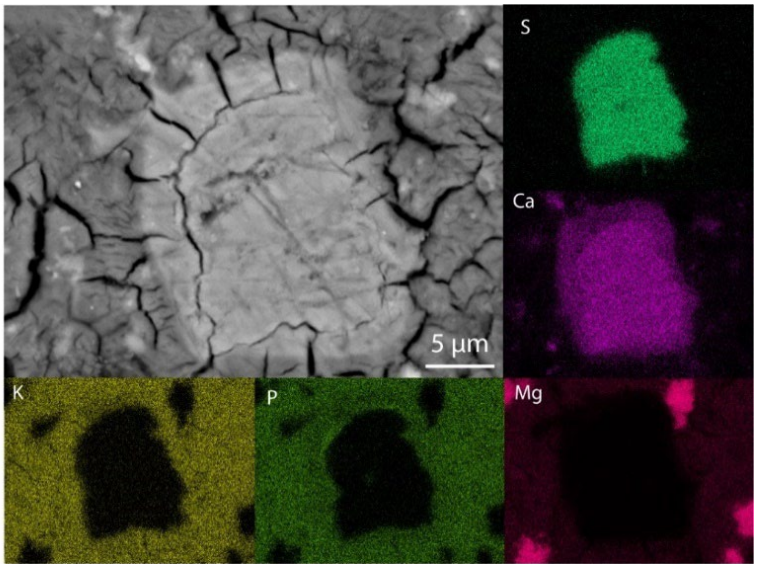

Figure 7.16 MSWI-FA Ca-sulfate particle in the cement matrix, with EDS map.

There are evidence that also the aluminosilicate fraction of MSWI-FA reacted in the cement chemical environment. The phase composition of MSWI-FA/KH_2PO_4 points out a significant decrease in gehlenite content, while the ^{27}Al MAS spectrum clearly shows the presence of a new resonance in the octahedral region at -12 ppm, together with an increase linewidth of the tetrahedral Al (Figure 7.7). This is compatible with the incorporation of at least some of the ions released by the aluminosilicate into new Al-bearing phases. Similar features were also observed in the ^{27}Al spectra of MF sample. The range in chemical shift is the same reported for some aluminophosphate glasses [16] and phosphate geopolymer [22], where the resonances have been assigned to aluminium sited in an octahedron sharing corners with P-coordinated polyhedron, so as to build up the aluminophosphate networks. Although the broad linewidth of the ^{31}P MAS spectrum impaired the unambiguous identification of a new signal between -5 to -30 ppm, as it should be expected, according to this interpretation [22], the SEM results (Figure 7.12) are compatible with this model. The alternative possible scenarios offered by the literature, seem less probable. That is: the tiny ^{31}P resonance at 3 ppm reported in glasses and exhibiting proximity with a similar Al^{VI} environment [23]; the ^{31}P resonance at 5 ppm assigned to Q^0(1Al) units in a geopolymer added with P [24]; the precipitation, upon addition of ground granulated blast furnace slag to MKPC, of a new potassium aluminosilicate phase producing an analogous ^{27}Al MAS signal [7].

The small differences in the ^{29}Si MAS spectra of cement samples compared to MSWI-FA (Figure 7.6) are also compatible with the partial dissolution of gehlenite (a sorosilicate displaying mainly Q^1 units at -71 ppm) and the mobilization of Si. Likewise, Si was mobilized from the zinc silicate as evidenced by the XANES results (Figure 7.9). Altogether, the experimental evidence from spectroscopies indicate the involvement of MSWI-FA in the cement reaction. Even though the SEM-EDS measurements were not conclusive on this hypothesis, in terms of Al and Si mobilization, the intrinsic local nature of the spectroscopies here employed may provide more reliable results. Similar questions on the SEM-EDS approach in inquiring the reactivity of waste residue into MKPC have been recently raised [25].

The significant reduction of heavy metals leaching (Figure 7.15) is also in agreement with this view, since, in addition to the expected physical encapsulation effect of the cement matrix, XANES spectra clearly indicated a chemical stabilization due to the direct reaction of MSWI-FA components (Zn-bearing phases) with phosphate. In fact, in analogy with the Ca carbonates mentioned above, hydrozincite ($Zn_5OH_6(CO_3)_2$) is likely dissolved in the initial acidic conditions and Zn can reach the supersaturation conditions needed to precipitate hydrated Zn-phosphate phases, as they exhibit very low K_{sp} (for example, $Zn_3(PO_4)_2{\cdot}4(H_2O)$, hopeite, has $K_{sp} \sim 10^{-35}$ at 25 °C) [26]. At the same time, ZnO in MSWI-FA may directly react with phosphate, likewise zinc in Zn-phosphate dental cement [27]. Eventually, these processes are kinetically competing with the main reaction involving MgO (for K-struvite, K_{sp} is $\sim 10^{-11}$ at 25 °C) [26]. By taking into account the similarities between the spectroscopic results of MF0 and MF100, although significantly different from the pristine washed MSWI-FA, it seems that the MSWI-FA reactivity is not deeply affected by the type of formulation, i.e., an increase in the KH_2PO_4 content (MF100) does not result in a significant increase of the dissolution/precipitation reactions.

When considering the main reaction pathway, the ICC curves indicated a marked effect on the kinetics rather than on the normalized heat released (MF0, Figure 7.1). The acceleration of the second exothermic peak may be considered the effect of enhanced nucleation of the reaction products. Heterogeneous nucleation is known to be thermodynamically favoured [1]. In MKPC, this role is commonly played by MgO, as confirmed by the positive correlation between its specific surface area and the K-struvite crystallization rates [1]. Therefore, the high specific surface area of the ash provides additional room for nucleation of the reaction products (Figure 7.14). Although less evident, a similar effect is present in MF100, since the delay of the MgO dissolution with respect to REF is not followed by a delay of the K-struvite crystallization. This behaviour can also explain the increase of the amorphous-phase/crystal-phase ratio passing from REF to MF0/100, as their interconversion is hindered in a more kinetically driven reaction pathway [1,2]. On the other hand, the mobilization of Al and Si by the addition of metakaolin in MKPC has been linked to an increase in the amount of amorphous fraction [28]. Although the mechanisms are not yet clarified, an analogous effect can occur here, too, since a similar release of Al and Si is observed. The K-struvite crystallization pathway is the results of a complex interplay between the amount and availability of ions in solution, their mobility and the relative stability of the amorphous precursor, all of which can be affected by impurities and/or additives [5]. Further work should be done to isolate the eventual contribution of the MSWI-FA components on this complex reaction mechanism.

7.5 Conclusions

In this work, the reactivity of washed MSWI-FA when added in MKP cement is investigated, by employing both an “inert” formulation, where MWSI-FA replaces both magnesia and KDP, and a “reactive” formulation, replacing magnesia only. The following conclusions have been achieved:

- SSNMR and XAS agree to indicate that, in both inert and reactive conditions, dissolution/precipitation reactions involving MSWI-FA occur. A fraction of Zn, the most abundant

heavy metal in the waste, becomes bound to phosphate, together with Al and, at a lesser extent, Si. The dissolution of the abundant sulfate leads to the precipitation of K_2SO_4.

- the suspension of MSWI-FA in a KH_2PO_4 saturated solution confirms these results, indicating a mainly amorphous character of the reaction products.
- MSWI-FA determines an increase in the amorphous/crystalline ratio in MKP, as shown by ICC, XRPD and SEM observations, although the precise mechanism has not been clarified.
- In both conditions, the leaching of all the heavy metals investigated is below the legal limit, thus proving that MKPC can be a promising matrix for the MSWI-FA incorporation. Moreover, the reactive formulation demonstrated a 50% increase in the compressive strength, suggesting taking into account the waste when optimizing the binder parameters.

7.6 References

1. Viani, A.; Macova, P. Polyamorphism and frustrated crystallization in the acid-base reaction of magnesium potassium phosphate cements. *CrystEngComm* **2018**, 20 4600–4613.
2. Viani, A.; Mali, G.; Macova, P. Investigation of amorphous and crystalline phosphates in magnesium phosphate ceramics with solid-state ^{1}H and ^{31}P NMR spectroscopy, *Ceram. Int.* **2017**, 6571–6579.
3. Viani, A.; Radulescu, A.; Perez-Estebanez, M. Characterisation and development of fine porosity in magnesium potassium phosphate ceramics. *Mater. Lett.* **2015**, 161, 628–630.
4. Viani, A.; Sotiriadis, K.; Sasek, P.; Appavou, M.S. Evolution of microstructure and performance in magnesium potassium phosphate ceramics: role of sintering temperature of MgO powder. *Ceram. Int.* **2016**, 42.
5. Zhang, Q.; Cao, X.; Ma, R.; Sun, S.; Fang, L.; Lin, J.; Luo, J. Solid waste-based magnesium phosphate cements: Preparation, performance and solidification/stabilization mechanism. *Const. Build. Mat.* **2021**, 123761.
6. Xu, B.W.; Ma, H.Y.; Shao, H.; Lothenbach, B. Influence of fly ash on compressive strength and micro-characteristics of magnesium potassium phosphate cement mortars. *Cem. Concr. Res.* **2017**, 99, 86–94.
7. Gardner, L.J.; Bernal, S.A.; Walling, S.A.; Corkhill, C.K.; Provis, J.L.; Hyatt N.C. Characterisation of magnesium potassium phosphate cements blended with fly ash and ground granulated blast furnace slag. *Cem. Concr. Res.* **2015**, 74, 78–87.
8. Su, Y.; Yang, J.; Liu, D.; Zhen, S.; Lin, N.; Zhou, Y. Effects of municipal solid waste incineration fly ash on solidification/stabilization of Cd and Pb by magnesium potassium phosphate cement. *J. Environ. Chem. Eng*. **2016**, 4, 259–265.
9. Yang, J.; Zhen, S.; Wu, Q. Effect of Municipal Solid Waste Incineration Fly Ash on Properties of Magnesium Potassium Phosphate Paste. *J. of Mat. Civil Eng.* **2019**, 31, 06019013.
10. Lin, W.Y.; Heng, K.S.; Nguyen, M.Q.; Ho, J.R.I. Evaluation of the leaching behavior of incineration bottom ash using seawater: a comparison with standard leaching tests. *Waste Manag.* **2017**, 62, 139–146.
11. Wagh, A..; Jeong, S.Y. Chemically bonded phosphate ceramics: I, a dissolution model of formation. *J. Am. Ceram. Soc.* **2003**, 86, 1838–1844.
12. Mbogoro, M.; Snowden, E.; Edwards, M.; Peruffo, M.; Unwin, P. Intrinsic Kinetics of Gypsum and Calcium Sulfate Anhydrite Dissolution: Surface Selective Studies under Hydrodynamic Control and the Effect of Additives. *J. Phys. Chem. C* **2011**, *115*, 10147–10154.
13. Legrand, A.P.; Sfihi, H.; Lequeux, N.; Lemaître, J. ^{31}P Solid-State NMR study of the chemical setting process of a dual-paste injectable brushite cements. *J. Biomed. Mater. Res.* **2009,** 91B, 46-54.
14. Abdelrahman, O.; Garg N. Impact of Na/Al Ratio on the Extent of Alkali-Activation Reaction: Non-linearity and Diminishing Returns. *Front. Chem.* **2022**, 9.
15. Skibsted, J.; Pedersen, M. T.; Holzinger J. Resolution of the Two Aluminum Sites in Ettringite by ^{27}Al MAS and MQMAS NMR at Very High Magnetic Field (22.3 T). *J. Phys. Chem. C* **2017**, 21, 4011-4017.

16. Edén, M. NMR studies of oxide-based glasses. *Annu. Rep. Prog. Chem., Sect. C: Phys. Chem.* **2012**, 108, 177–221.
17. Godfrey, I.J.; Dent, A.J.; Parkin, I.P.; Maenosono, S.; Sankar, G. Following the Formation of Silver Nanoparticles Using In Situ X-ray Absorption Spectroscopy. *ACS Omega* **2020**, 5, 13664-13671.
18. Pinilla-Herrero, I.; Borfecchia, E.; Cordero-Lanzac, T.; Mentzel, U.V.; Joensen, F.; Lomachenko, K.A.; Bordiga, S.; Olsbye, U.; Beato, P.; Svelle, S. Finding the active species: The conversion of methanol to aromatics over Zn-ZSM-5/alumina shaped catalysts. *J. of Catal.* **2021**, 394, 416–428.
19. Viani, A.; Macova, P.; Sotiriadis, K. Amorphous-crystalline transformation control on the microstructural evolution of magnesium phosphate cements. *Mater. Lett.* **2021**, 129630.
20. Zhou, X.; Zhang, Z.-F.; Bao, C.J.; Yue, Y.C.; Wang, J.S.; Yang, H.; Chen, M.J.; Liu, Y. The stabilization mechanism of high-efficiency magnesium phosphate cement for arsenic remediation in lollingite polluted environments. *J. of Clean.Prod.* **2022**, 378, art. 134580.
21. G.U. Ministerial Decree 27/09/2010-Definition of the Criteria of Admissibility of Landfill Waste. Serie Generale n-281. 1 December **2010**. Available online: https://www.gazzettaufficiale.it/eli/id/2010/12/01/10A14538/sg.
22. Bernasconi, D.; Viani, A.; Zarybnicka, L.; Macova, P.; Bordignon S.; Caviglia, C.; Destefanis, E.; Gobetto, R.; Pavese, A. Phosphate-based geopolymer: Influence of municipal solid waste fly ash introduction on structure and compressive strength. *Ceram. Int.* **2023**, 138, 318–327.
23. Wegner, S.; van Wullen, L;, Tricot, G. The structure of aluminophosphate glasses revisited: Application of modern solid state NMR strategies to determine structural motifs on intermediate length scales. *J. of Non-Cryst. Sol.* **2008**, 354, 1703-1715.
24. Dupuy, C.; Gharzouni, A.; Sobrados, I.; Texier-Mandoki, N.; Bourbon, X.; Rossignol, S. ^{29}Si, ^{27}Al, ^{31}P and ^{11}B magic angle spinning nuclear magnetic resonance study of the structural evolutions induced by the use of phosphor- and boron–based additives in geopolymer mixtures *J. of Non-Cryst. Sol.* **2019**, 119541.
25. Maa, H.; Li, Y. Discussion of the paper "Characterisation of magnesium potassium phosphate cement blended with fly ash and ground granulated blast furnace slag" by L.J. Gardner et al. *Cem. Concr. Res.* **2018**, 245-248.
26. Zhang, Y.; Wan, Z.; Wang, L.; Guo, B.; Ma, B.; Chen, L.; Tsang, D.C.W. Designing Magnesium Phosphate Cement for Stabilization/Solidification of Zn-Rich Electroplating Sludge. *Environ. Science & Tech.* **2022,** 13, 9398-9407.
27. Viani, A.; Sotiriadis, K.; Kumpová, I.; Mancini, L.; Appavou, M.S. Microstructural characterization of dental zinc phosphate cements using combined small angle neutron scattering and microfocus X-ray computed tomography. *Dent. Mat.* **2017***,* 33, 402 – 417.
28. Qin Z.; Ma, C.; Zheng, Z.; Long, G.; Chen, B. Effects of metakaolin on properties and microstructure of magnesium phosphate cement. *Const. Build. Mat.* **2020**, 234, 117353.

Chapter 8

Thermal Stability of Calcium Oxalates from CO_2 Sequestration for Storage Purposes: An *In-Situ* HT-XRPD and TGA Combined Study

8.1 Introduction

Carbon dioxide is one of the main components of the flue gas produced by the combustion of waste in WtE plant (i.e., around 10% vol). This, coupled with the many anthropic manufacturing activities, has brough the concentration of carbon dioxide in the atmosphere from the pre-industrial level of 280 ppm [1] to about 412 ppm in 2019 [2]. For this reason, many CO_2 fixation methods have been proposed, such as Carbon Capture and Storage (CCS) in suitable geological structures, bio-sequestration, catalytical reduction *via* metal-organic complexes, sequestration by amine mixtures, precipitation of carbonate minerals by the carbonation reaction of calcium and magnesium silicates and oxides [3-6]. In this context, our group developed an alternative and green approach for the mineral capture of CO_2, by exploiting the reducing ability of the ascorbic acid to reduce carbon dioxide according to the following red-ox reaction (AA: ascorbic acid; DHA: dehydroascorbic acid) [7-8]:

$AA + 2CO_2 \rightarrow C_2O_4^{2-} + DHA + 2H^+$

In the presence of calcium as a counterion (provided *via* Ca-ascorbate, CaASC), the reaction promotes precipitation of stable and nearly insoluble Ca-oxalate hydrates, mainly dihydrate (weddellite; COD; $CaC_2O_4 \cdot 2H_2O$), with monohydrate as a byproduct (whewellite; COM; $CaC_2O_4 \cdot H_2O$) [7,8]. Moreover, AA/DHA interconversion has been demonstrated at acidic pH (4–6) as the result of delocalization of the reducing hydrogens, potentially leading to a reuse of the reducing agent, when kept in the right conditions [9]. Calcium oxalates find their applications in many fields, from pre- and post-harvesting and storage treatment on many plants intended for human consumption, to metal and hazardous metals (arsenic as an example) immobilization or extraction from minerals to ceramic glazes and for preparation of reagent-grade chemicals [10,11]. In this context, the thermal behaviour of weddellite crystals is crucial in assessing their carbon dioxide storage capacity, disposal, or, eventually, reuse in a circular economy perspective. COD could be considered a solid-state carbon dioxide reservoir, reducing storage and handling safety costs compared to compressed gas. Calcium oxalate can be a potential source of pure CO_2 and CaO, exploiting thermal degradation. CO_2 recovered from calcium oxalate may be used in standard applications, while homogeneous calcium oxide powder can be employed as a reagent in the cement or ceramics industries [12-14]. Nevertheless, the literature reports a comparatively modest number of studies regarding the decomposition of oxalates using in-situ X-ray powder diffraction (XRPD), which is appropriate to provide a complete description and quantification of the crystalline phases appearing at different stages of the reaction. The thermal degradation reactions of calcium oxalate can be described as followed:

The first step (dehydration) represents an endothermic process both in the inert and oxidizing atmosphere, according to the reactions R1 [15-21]:

$CaC_2O_4 \cdot H_2O \leftrightarrow CaC_2O_4 + H_2O$ (reaction R1).

$CaC_2O_4 \rightarrow CaCO_3 + CO$ (reaction R2a)

$CaCO_3 \leftrightarrow CaO + CO_2$ (reaction R3)

R2a is an endothermic reaction under inert conditions, but possibly exothermic in air or oxygen, and R3 is endothermic. The temperatures related to the maximum reaction rate (reactions R1, R2a, and R3) roughly range from 45 to 235 °C, from 250 to 550 °C, and from 550 to 850 °C, respectively, and depend on experimental aspects, such as the preparative routine, the environmental conditions, the heating rate, the presence and nature of the flowing gas, as well as the hydration state of the crystalline phase (COT, COD or COM). Additional reactions may occur in the reaction batch, simultaneously with R2a: disproportionation (R2b) and oxidation (R2c and R2d). The former has been proposed to explain the presence of both CO and CO_2 in the reaction batch:

$2CO \rightarrow C + CO_2$ (reaction R2b)

The disproportionation reaction is considered a very slow process and neglected in many works dealing with calcium oxalate thermal decomposition [19-23]. CO, in turn, may coexist with CO_2 in the carbonate formation range of temperature. The oxidation of CO to CO_2 may be related to the catalytic effect of some parts of the experimental setup (the platinum crucible, for instance) [23-25]:

$CO + 1/2O_2 \rightarrow CO_2$ (reaction R2c)

The occurrence of free carbon is considered a side-effect typical of the decomposition of REE-oxalates, or as a ubiquitous byproduct, even in calcium oxalate decomposition [19-23]:

$C + O_2 \rightarrow CO_2$ (reaction R2d)

Almost all of the papers devoted to determining the thermal stability of oxalate are referred to as calcium oxalate monohydrate. Whewellite shows higher structural order than weddellite that contains loosely bonded zeolitic water molecules free to move in the channels [7]. Accordingly, the transition temperatures are significantly higher for whewellite. The dehydration reaction of weddellite occurs at lower temperatures than whewellite, confirming the hypothesis of weakly bonded water molecules in the channels of weddellite [7,16]. Moreover, the relative storage humidity plays an essential role in the stability of weddellite crystals. It has been demonstrated that the transformation of whewellite in weddellite takes a few minutes when original whewellite crystals are immersed in water [26]. As the humidity decreases, the time required to reach the stability increases. Nevertheless, this is of primary importance when considering the storage of calcium oxalates produced by carbon dioxide reduction.

8.2 Materials and Methods

8.2.1 Materials

Calcium oxalate dihydrate (weddellite) was precipitated from CO_2 by carbon reduction using a Ca-ascorbate aqueous solution exploiting the reaction described above [7,8]. At the beginning of each experiment, the air trapped in the headspace of the vessel is removed by first flowing in pure CO2 through the inlet valve until a slight overpressure, compared to the atmosphere's, is achieved (1.1 bar), and then partially relieving the overpressure *via* a relief valve. This "washing" treatment is repeated three times t<o clear the vessel from the air. Successively, CO_2 is provided *via* a single gas injection until a slight overpressure (1.043 bar) with respect to ambient is achieved (Figure 8.1). Then, the inlet gas valve is closed, and the system is isolated, so that CO_2 neither enters nor escapes. A 1 M CaASC solution in the vessel is continuously stirred to homogenize the distribution of dissolved CO_2, thus avoiding gas gradients from the cap towards the bottom of the reactor. The system was kept sealed to measure the CO_2 captured, *i.e.* the decrease of pressure inside the vessel, starting from a setpoint slightly higher than the atmospheric pressure (1.043 bar).

Successively, the decrease of pressure *versus* time, due to CO_2 capture and Ca-oxalate precipitation, was monitored by the *pressure switch* device. At the end of the experiments, the suspension was vacuum filtered on a cellulose filter with a pore size of 0.45 µm and the crystalline sample was dried overnight at room temperature.

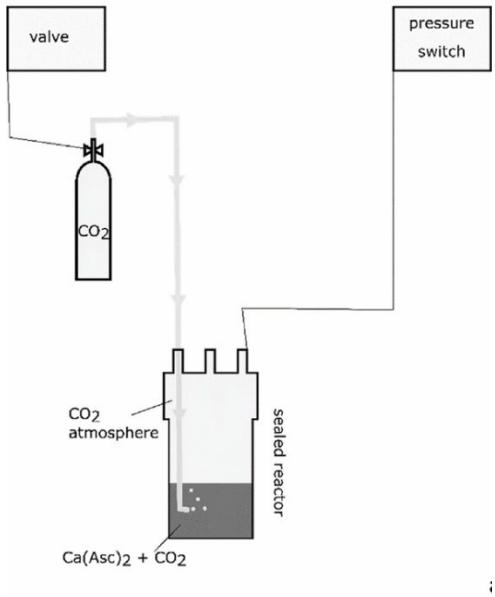

Figure 8.1 Sketch of the CO_2 capture experiment set-up.

8.2.2 *In-situ* High Temperature X-ray Powder Diffraction (HT-XRPD)

In-situ high-temperature XRPD data collections at quasi-equilibrium/equilibrium (data collections at given *T* after the achievement of thermal equilibrium as reported in Table 8.1) were carried out using a Rigaku SmartLab XE (Rigaku, Tokyo, Japan) diffractometer (Bragg-Brentano θ-θ geometry, CuKα radiation, generator operating at 40 kV and 30 mA) equipped with a Rigaku Multipurpose High Temperature Attachment, combined with PTC-EVO temperature control. The actual temperature of the sample was determined using a calibration curve previously defined with Pt thermal dilatation. The samples were heated at a rate of 15 °C/min, in keeping with the heating ramp proposed by Hourlier, 2018[15] and held at the achieved temperature for 30 min. Diffraction patterns were recorded using a CCD detector (Rigaku Hypix 3000), operating as a punctual detector in the range $5 < 2\theta < 80°$ with a speed of 1°/min and step size of 0.01°. The heating rate was maintained constant throughout the XRPD experiments to prevent temperature shifts related to the heat transfer. The temperatures at which XRPD data were collected are reported in Table 8.1 (Ramp#1). Ramp#1 did not allow complete characterization of the recrystallization reactions. Two more runs (Ramp#2 and Ramp#3) were designed and carried out to complement and detail Ramp#1. Phase identification from XRPD data was performed using the DIFFRAC.EVA software (version 11.0.0.3, Bruker) and the PDF-2 database. The GSAS-II Software Package was used for full profile refinements to quantify and characterize the crystal phases occurring in the mixture that develops from the transformations of Ca-oxalate.

8.2.3 Thermogravimetric Analysis-Evolved Gas Analysis (TGA-EGA)

In-situ high Thermogravimetric analysis coupled with infrared spectroscopy (TGA-FTIR) was used to assess the COD thermal behavior and monitor the species evolved during the thermal degradation (CO, CO_2,

and H_2O). In detail, the TGA-FTIR setup was previously cleaned by purging nitrogen and raising the temperature until 930 °C to remove any pollutant from the measure system. After the cleaning cycle, the sample (6.27 mg) was placed in a platinum pan and put in a Pyris 1 thermobalance (Perkin Elmer, Waltham, MA, USA). Then, the sample chamber was sealed at room pressure and gas purged at 35 mL/min for 30 min with an oxygen-nitrogen mixture (33.3% of O_2 in N_2). Thereafter, the sample was heated under flowing of the same oxidant gas mixture from 70 to 900 °C at different heating rates depending on the temperature range: between 72 to 250 °C, a slow heating rate (2 °C/min) was chosen to better discriminate zeolitic and structural water. At a higher temperature (250 to 900 °C), the sample was heated at 15 °C/min to identify the nature and monitor the evolution of the gaseous species that evolved during the formation of solid phases other than hydrated oxalates investigated by XRPD experiments.

The gas that evolved during the heating ramp was piped (gas flow 65 mL/min) via a pressurized transfer line (Redshift S.r.l., San Giorgio in Bosco (PD), Italy) and analyzed continuously by FTIR spectrophotometer (Spectrum 100, Perkin Elmer), equipped with a thermostatic conventional gas-flow cell. Temperature/time-resolved spectra were ac- quired in the 4000–600 cm^{-1} wavenumber range and analyzed with the Spectrum software (version 10, Perkin Elmer, Waltham, MA, USA). Temperature-resolved infrared profiles of the evolved gases were obtained from the absorbance variation at a specific wavenumber characteristic of each gaseous species of interest (1650, 2185, and 2359 cm^{-1} for H_2O, CO, and CO_2, respectively). The deconvolution of the FTIR and derivative thermogravimetry (DTG) curves was performed using the Fityk 0.9.8 free software and choosing a Voigt or a splitted Voigt (for strong peak asymmetry) peak profile to fit the experimental data.

Table 8.1 Temperatures of the measurements in the HT-XRPD in situ experiments (Ramp#1 to #3).

Step#	Ramp#1 (°C)	Ramp#2 (°C)	Ramp#3 (°C)
1	26	25	25
2	47	47	86
3	274	102	97
4	410	158	108
5	460	212	119
6	487	273	130
7	605	329	141
8	881	410	152
9	22	420	163
10		430	174
11		440	185
12		450	196
13		460	207
14		605	218
15		660	230
16		715	241
17		826	384
18		439	395
19		22	406
20			417
21			428
22			439
23			450
24			461
25			472
26			483
27			494
28			748
29			760
30			771
31			782
32			793
33			804
34			815
35			826
36			837
37			848
38			859
39			870
40			881
41			22

8.3 Results

8.3.1 HT-XRPD

Figure 8.2 shows the results of *in-situ* HT-XRPD experiments, by heating weddellite according to Ramp#1, to investigate the correlation between solid-state phases stable within a temperature range and gases evolving from thermal degradation of calcium oxalate.

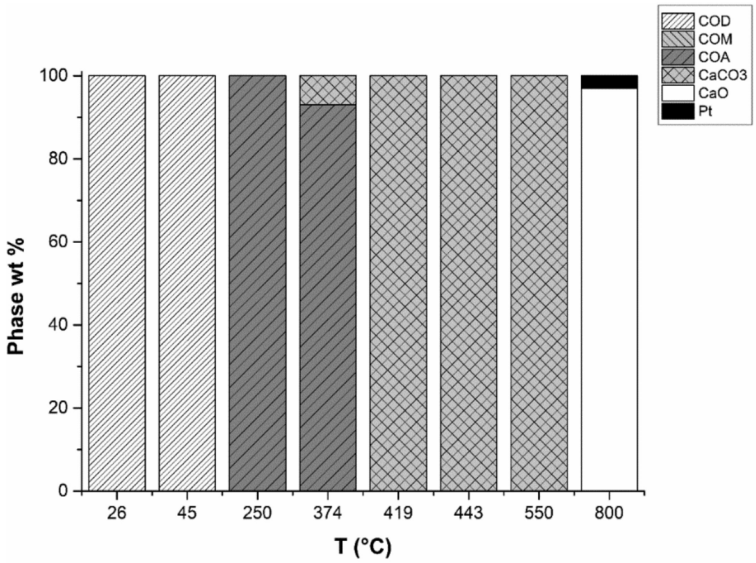

Figure 8.2 Ramp#1: The transitions between crystal phases are not well distinguished. Weddellite to whewellite transition is missing, as the anhydrous phase abruptly appears at 250 ℃. The same applies for CaO, which suddenly crystallizes at 800 ℃. Pt signal comes from the sample holder.

During the first two steps (26 and 45 ℃), calcium oxalate dihydrate is the stable phase. The transition from COD to COA occurs between 45 and 250 ℃ and a COM fraction is not recorded. At 250 ℃, weddellite is fully dehydrated, with COA identified as the sole crystalline phase. At 374 ℃, some calcium carbonate (calcite) appears and at 419 ℃ it completely replaces COA. Calcium carbonate, in turn, is stable until the last-but-one step, at 550 ℃, where the onset of the decarbonation reaction is detected. Calcium carbonate lasts up to 800 ℃. Starting from this temperature only CaO occurs (Pt diffraction signal comes from the powder sample holder). Ramp#2 represents an intermediate experiment intended to find the proper measurement conditions in terms of temperature. Eventually, Ramp#3 (Figures 8.3-8.4) was designed to detail the crystalline phase transitions. The first transition between weddellite and whewellite approximately starts at 110 ℃ and achieves completion at 140 ℃ (Figure 8.4). During this first transition, the weight loss recorded by TGA analysis is related to zeolitic water. Between 140 and 150 ℃, in a very narrow T-range, the sole stable phase is the calcium oxalate monohydrate that undergoes further dehydration between 150 and 180 ℃, losing the tightly bonded structural water. COA is stable up to 410 ℃. The onset of the decarbonation reaction is detectable from 360 ℃. In the range 410–680 ℃, calcium carbonate is the unique stable phase, but at higher temperatures, it is progressively replaced by CaO. At the end of the reaction (800 ℃), the final crystalline product is fine-grained pure lime. Note that, in any explored ramp, the Pt signal from the sample holder becomes visible due to the volume loss of the sample.

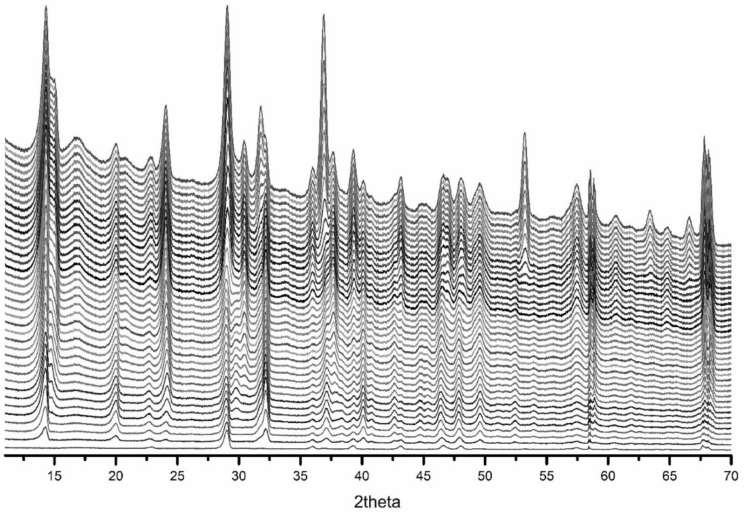

Figure 8.3 Raw data of HT-XRPD *in-situ* measurement (Ramp#3).

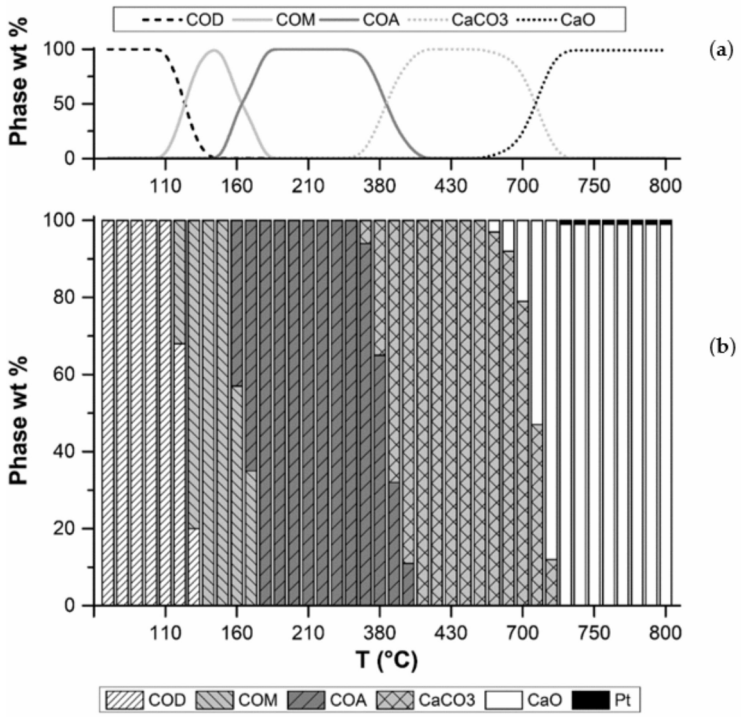

Figure 8.4 Ramp#3. The HT-XRPD refinement and quantitative analysis highlight the thermal stability range of the phases coming from COD thermal degradation (**a**) and the transition between crystalline phases (**b**).

8.3.2 TGA-EGA

The thermal decomposition of the sample was monitored in the temperature range between 70 and 900 °C (2 °C/min up to 250 °C and 15 °C/min from 250 to 900 °C) and shows three weight loss processes, as illustrated in Figure 8.5. The first process, which occurs between 70 and 200 °C (maximum rate at 136 °C), corresponds to a weight loss of 25.6% and is related to the evolution of both zeolitic and structural water. Ideally, the water lost during heating should represent 22% of the weight of the sample. Data from FTIR measurements (Figure 8.6) confirm that CO_2 is evolved during heating, even at low temperatures (119–255 °C), justifying the difference in weight loss. This faint evolution of CO_2 in the low-temperature range

perfectly overlaps H_2O evolution and possibly represents the onset of the structural collapse of weddellite at low temperature (150 °C). This is possibly related to the stabilization of α-COA, as reported by Izatulina and Zhao [27,28], even if from the XRPD analysis, no COA, calcium carbonate or lime were detected in this temperature range, probably due to values below the detection limits. Therefore, this lower value must be cautiously considered the temperature limit for weddellite stability for storage purposes. The two water release curves can be roughly recognized: the first, with a maximum at 152.8 °C; the second, with a maximum at 200.9 °C from FTIR data. This agrees with the literature [15]. The FTIR profile of H_2O release (Figure 8.6) shows a double peak in the temperature range of 70—300 °C. The first maximum is at 135 °C, the second one at 206.6 °C. The two maxima correspond to the evolution of the zeolitic and structural water. In terms of solid phases, they correspond to the dehydration steps of the oxalate, from COD to COM and then to COA. The release of H_2O from the crystal structure continues up to approximately 300 °C. Structural H_2O and the second CO_2 evolution occur at almost the same temperature, indicating that calcium oxalate sets up to collapse at a lower temperature than expected (during the massive loss of carbon monoxide and dioxide reported in the literature), approximately at 150 °C. The second weight-loss (21.6%) occurs in the range 390–550 °C, with a maximum value at 490 °C. During this step, both CO and CO_2 (Figure 8.6) are released according to the literature [15,21]. In agreement with the stoichiometric calculation, CO would lead to a weight loss of 17%, the difference with the actual one is attributed to some CO_2 that evolved during the heating, as confirmed by FTIR measurements (Figure 8.6). The maximum release temperature for CO_2 and CO are at 492.6 and 488.1 °C, respectively. A third remarkable weight loss (31.3% b) occurs between 550 and 800 °C. A split-Voigt function was used to simulate the asymmetry of experimental peaks. The maximum release of CO_2 occurs at a temperature of about 767 °C. Immediately beyond the maximum release temperature, CO_2 drops, indicating the completion of the degradation reactions of calcium oxalate, in full agreement with diffraction data. According to the literature, the CO_2 release may account for a weight loss of 27%. The difference is attributed to a partial superimposition of the second and third steps due to the relatively high heating rate. Moreover, the asymmetry could reflect a forward-backward reaction due to the reaction chamber's high CO_2 and calcium oxide substrate activities, related to lingering volatile species.

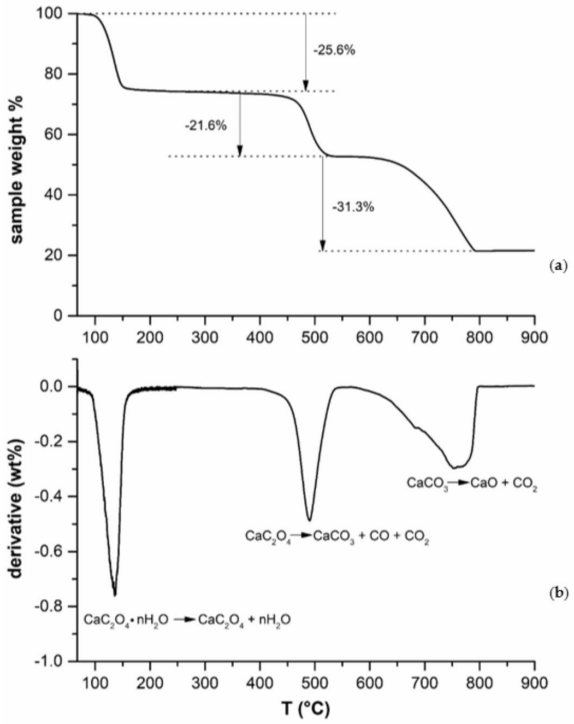

Figure 8.5 Thermogram (a) and the first derivative (b) showing the endothermic peaks related to the reactions indicated in correspondence.

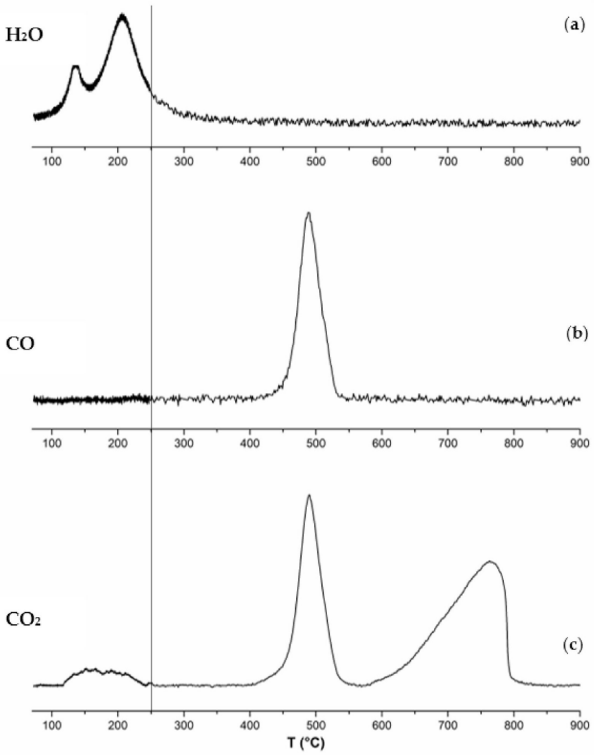

Figure 8.6 FTIR measurements of (a) H_2O, (b) CO, and (c) CO_2 release. The darker color of the experimental data on the left of the vertical line (low-temperature range) is related to the slow-rate ramp (2 ℃/min), at a temperature higher than 250 ℃, the ramp rate was increased to 15 ℃/min to simulate the heating condition of an industrial oven.

8.4 Discussion

In Table 8.2, the temperatures related to the three degradation reactions of weddellite revealed by XRPD (appearance and disappearance of the crystalline phases) and DTG (gas evolution) are summarized and compared. The transition temperature ranges agree with those from the literature [15].

Table 8.2 FTIR measurements of (a) H_2O, (b) CO, and (c) CO_2 release. The darker color of the experimental data on the left of

XRPD				TG			
Crystalline phase recognized	T (°C) Appearance	T (°C) Disappearance	Volatile Species Expected	Gases Evolved	Crystalline Phases Expected	T of Max Release (°C) of Volatile Species	Notes
COD		110-140					
COM	110-140	150-180	H_2O	1st water loss	COM	135	Some CO_2 is evolved: two concomitant peaks at 152.8°C and 200.9 °C
COA	150-180	360-410	H_2O	2nd water loss	COA	206.6	
CaCO3	360-410	680-730	CO	CO + CO_2 loss	$CaCO_3$	488.1	CO peak
						492.6	CO_2 peak
CaO	680-730		CO_2	CO_2 loss	CaO	767	Asymmetric CO_2 release peak

HT-XRPD and TGA experiments provide coherent descriptions of zeolitic and structural water release. The DTG peak related to water release overlaps the temperature range thermal-gravimetric analysis. We stress that, in TGA, a 2 °C/min ramp was chosen to emphasize the double water loss. In contrast, in HT-XRPD, we recorded patterns at narrow temperature intervals to follow the transformation of the solid phases from weddellite to whewellite and then to the anhydrous phases. Although a general shift to higher temperature occurs owing to heat and mass transfer related effects, the releases of volatile phases can be undoubtedly associated with the stabilization of the crystalline phases recorded by XRPD, following the sequence:

$CaC_2O_4{\cdot}xH_2O \leftrightarrow CaC_2O_4 + xH_2O$ (reaction R1)

where *x* is equal to 2 (weddellite to whewellite; zeolitic water loss) or 1 (whewellite to anhydrous Ca-oxalate; structural water loss);

$CaC_2O_4 \rightarrow CaCO_3 + CO + CO_2$ reaction R2a (and reactions R2b, R2c, and R2d)

corresponding to the transition from anhydrous Ca-oxalate to calcite (first decarbonation reaction), accompanied by carbon monoxide and dioxide release and not, as suggested in some literature [20, 29], by carbon monoxide production only. In these circumstances, CO oxidation should be catalyzed to obtain pure and reusable CO_2. However, the methods, to our knowledge, involve fine metal oxide powders (ZnO, for instance) and may induce pyrophoric effects. As an alternative, gas separation should be provided for obtaining a pure CO_2 or CO gas flux. In an oxidant atmosphere, reactions R2c and R2d are the most likely to explain the presence of carbon dioxide;

$CaCO_3 \leftrightarrow CaO + CO_2$ (reaction R3)

corresponding to the calcite to lime reaction (second decarbonation reaction). Activation energies (Table 8.3) for the processes have been evaluated using the Coats-Redfern integral method [30-33] derived for non-reversible reactions at non-isothermal conditions (Figure 8.7). The results of the analysis are reported in Table 8.3, along with the order of the reaction estimated based on the least-square fitting agreement between the model and observations, as described by Sukarni [30]. Moreover, in CO_2 production, the reaction mechanism are classified following the method described by Dollimore [34]. However, this evaluation does not claim to be absolute: the Coats-Redfern approach is hardly suitable for the determination of reaction mechanisms and correct kinetic analysis of a single experimental curve requires an a priori knowledge of the true activation energy [35,36].

Table 8.3 Activation energies (E_{att}) and orders of the reactions (*n*) were evaluated by applying the Coats-Redfern method. The mechanism of reaction was hypothesized, when possible, using the approach described by Dollimore et al [34,37]

Experimental Evidence	E_{att} (kJ/mol)	*n* (Best Fit)	Possible Reaction Mechanisms	Notes
1st H_2O release	241	2	not determined	The mechanism cannot be proposed due to the low value of α_{max} obtained from the Coats-Redfern method
2nd H_2O release	−22	0	not determined	The mechanism cannot be proposed due to the low value of αmax obtained from the Coats-Redfern method
CO release	118	1	not determined	The mechanism cannot be proposed due to the low value of αmax obtained from the Coats-Redfern method. Overlaps the 1st CO_2 release
1st CO_2 release	234	2	2nd order decay	Overlaps the CO release
2nd CO_2 release	51	0	1D diffusion	-

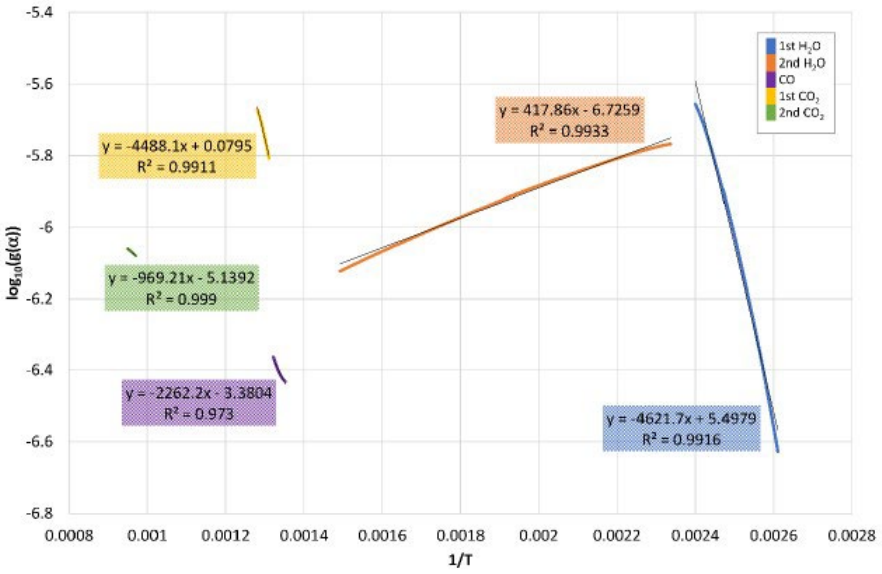

Figure 8.7 Analysis of TG data applying the Coats-Redfern method. The g(α) function is given by $1 - (1 - \alpha)(1 - n)/(1 - n)T2$ if $n \neq 1$ or $\log10(1 - \alpha))/T2$ if $n = 1$.

The magnitude of the activation energy values inferred here is comparable to those found in the literature [16,17,31]. The occurring discrepancies are attributed to the experimental setup differences in heat and mass transfer, sample particle size, and catalytic effects of the impurities present in the system. Thermal degradation of weddellite occurs through multi-step transformations. Some overlapping of the processes occurs in water release reactions (first and second release are not fully separated), in CO_2 release reactions at low temperature, and in the combined CO—CO_2 evolution, wherein the maximum release rates of CO and CO_2 occur at 488 and 492.6 ℃, respectively. All of these overlapping processes may affect the evaluation of the activation energies of a single process. As an example, the second water release shows a negative activation energy value. This negative value is probably due to the double interference effects of first water release and CO_2 feeble release at low temperature on the second water release process. At the same time, it is apparent that this reaction corresponds to the structural water loss, which seems unlikely to be a barrierless reaction. A comparison of TGA results with HT-XRPD reveals a temperature shift towards higher values in the former, confirming the severe dependence of the kinetics of the reactions on the heat transfer rate and, in general, on the experimental setup.

8.5 Conclusions

In conclusions, the feasibility of CO_2 long-term storage in crystalline oxalate stable at room temperature and pressure has been proven on microcrystalline weddellite samples from the ascorbate promoted CO_2 capture green reaction. Although a direct comparison of TGA and XRPD results confirms the severe dependence of the reactions' kinetics on the heat transfer rate and, in general, on the experimental setup, some CO_2 release from calcium oxalate occurs at relatively low temperature (150 ℃). This must be considered the higher storage temperature for calcium oxalate to avoid the release of CO_2 back to the environment. Apart from this, COA guarantees that the mass of CO_2 is safely stored until the first decarbonation temperature is reached and a CO + CO_2 mixture is released. At this step, a gas separation would be required to decouple pure CO_2 from CO. Then, starting from the onset of the second decarbonation reaction (550 ℃

for the setup tested), pure CO_2 can be retrieved in pure form from COA, leaving a crystalline calcium oxide ready for further technological applications.

8.6 References

1. T. Eggleton, A Short Introduction to Climate Change, Cambridge University Press, **2012**
2. NASA: climate change and global warming, *Earth Sci. Commun.* **2018**.
3. Stenhouse, M.; Arthur, R.; Zhou, W. Assessing environmental impacts from geological CO2 storage, *Energy Procedia* **2009** 1895–1902.
4. Smith, R.G.; Smith, I.J.; Smith, B.D. A novel strategy for sequestering atmospheric CO_2: the use of sealed microalgal cultures located in the open-oceans *Renew. Sustain. Energy Rev.* **2018**, 83, 85–89.
5. Lackner, K.S. A guide to CO_2 sequestration *Science* **2003**, 1677–1678.
6. Gadikota, G.; Swanson, E.J.; Zhao, H.; Park, A.H.A. Experimental design and data analysis for accurate estimation of reaction kinetics and conversion for carbon mineralization. *Ind. Eng. Chem. Res.* **2014**, 536664–6676,
7. Pastero, L.; Curetti, N.; Ortenzi, M.A.; Schiavoni, M.; Destefanis, E.; Pavese, A. CO_2 capture and sequestration in stable Ca-oxalate, via Ca-ascorbate promoted green reaction. *Sci. Total Environ.* **2019**, 1232–1244.
8. Pastero, L.; Marengo, A.; Boero, R.; Pavese, A. Non-conventional CO_2 sequestration via Vitamin C promoted green reaction: Yield evaluation. *J. CO_2 Util.* **2021**, 44, 101420.
9. Deutsch, J.C. Ascorbic acid and dehydroascorbic acid interconversion without net oxidation or reduction, *Anal. Biochem.* **1997**, 58–62.
10. Zhu, Y.; Yu, J.; Brecht, J.K.; Jiang, T.; Zheng, X. Pre-harvest application of oxalic acid increases quality and resistance to Penicillium expansum in kiwifruit during postharvest storage, *Food Chem.* **2016**, 190, 537–543
11. Kim, E.J.; Lee, J.C.; Baek, K.; Abiotic reductive extraction of arsenic from contaminated soils enhanced by complexation: arsenic extraction by reducing agents and combination of reducing and chelating agents *J. Hazard. Mater.* **2015**, 454–461.
12. Chen, F.-H.; Tseng, T.-Y. Formation of High-Tc Superconducting Bi-Pb-Sr-Ca-Cu Oxide Films by Spray Pyrolysis of an Oxalate Suspension. *J. Am. Ceram. Soc.* **1990**, 73, 889–892.
13. Gurrieri, S.; Siracusa, G.; Calí, R. Thermal decomposition of CaC_2O_4 H_2O. Determination of kinetic parameters by DTG and DTA. *J. Therm. Anal. Calorim.* **1974**, 6, 293–298.
14. Frost, R.L.; Weier, M.L. Thermal treatment of whewellite—a thermal analysis and Raman spectroscopic study. *Thermochim. Acta* **2004**, 79–85.
15. Hourlier, D. Thermal decomposition of calcium oxalate: Beyond appearances. *J. Therm. Anal. Calorim.* **2018**, 2221–2229.
16. Szekely, T.; Varhegyi, G.; Till, F.; Szabo, P.; Jakab, E. The effects of heat and mass transport on the results of thermal decomposition studies: Part 1. The three reactions of calcium oxalate monohydrate. *J. Anal. Appl. Pyrolysis* **1987**, 71–81.
17. Price, D.; Dollimore, D.; Fatemi, N.; Whitehead, R. Mass spectrometric determination of kinetic parameters for solid state decomposition reactions. Part 1. Method; calcium oxalate decomposition. *Thermochim. Acta* **1980**, 323–332.
18. Kloprogge, T.; Boström, T.E.; Weier, M.L. In situ observation of the thermal decomposition of weddelite by heating stage environmental scanning electron microscopy. *Am. Miner.* **2004**, 245–248.
19. Boldyrev, V.V.; Nevyantsev, I.S.; Mikhailov, Y.N.; Khairetdinov, E.F. On the mechanism of thermal decomposition of oxalates. *Kinet. Katal.* **1970**, 367–373.
20. Kociba, K.J.; Gallagher, P.K. A study of calcium oxalate monohydrate using dynamic differential scanning calorimetry and other thermoanalytical techniques. *Thermochim. Acta* **1996**, 277–296.

21. McAdie, H.G. Simultaneous Differential Thermal Analysis and Thermogravimetric Analysis Using the Open-Pan Type of Sample Holder. *Anal. Chem.* **1963**, 1840–1844.
22. Al-Maskari, N.; McAdams, D.; Reddy, J. Modeling of a biological material nacre: Waviness stiffness model. *Mater. Sci. Eng. C* **2017**, 772–776.
23. Barrall, E.M.; Rogers, L.B. Differential thermal analysis of organic samples. Effects of geometry and operating variables. *Anal. Chem.* **1962**, 1101–1106.
24. Lee, Y.F.; Dollimore, D. The identification of the reaction mechanism in rising temperature kinetic studies based on the shape of the DTG curve. *Thermochim. Acta* **1998**, 75–81.
25. Anderson, E.M.; Ericsson, I. Thermal degradation of organic polymers using different metals as the pyrolysis filament. *J. Anal. Appl. Pyrolysis* **1981**, 35–47.
26. Conti, C.; Brambilla, L.; Colombo, C.; Dellasega, D.; Gatta, G.D.; Realini, M.; Zerbi, G. Stability and transformation mechanism of weddellite nanocrystals studied by X-ray diffraction and infrared spectroscopy. *Phys. Chem. Chem. Phys.* **2010**, 14560–14566.
27. Izatulina, A.R.; Gurzhiy, V.; Krzhizhanovskaya, M.G.; Kuz'Mina, M.A.; Leoni, M.; Frank-Kamenetskaya, O.V. Hydrated Calcium Oxalates: Crystal Structures, Thermal Stability, and Phase Evolution. *Cryst. Growth Des.* **2018**, 5465–5478.
28. Zhao, W.; Sharma, N.; Jones, F.; Raiteri, P.; Gale, J.D.; Demichelis, R. Anhydrous Calcium Oxalate Polymorphism: A Combined Computational and Synchrotron X-ray Diffraction Study. *Cryst. Growth Des.* **2016**, 5954–5965.
29. Echigo, T.; Kimata, M.; Kyono, A.; Shimizu, M.; Hatta, T. Re-investigation of the crystal structure of whewellite [$Ca(C_2O_4)\cdot H_2O$] and the dehydration mechanism of caoxite [$Ca(C_2O_4)$ $3H_2O$]. *Mineral. Mag.* **2005**, 77–88.
30. Sukarni, S.; Widiono, A.E.; Wulandari, R.; Prasetiyo, A.; Puspitasari, P. Thermogravimetric Study on the Thermal Characteristics of *Tetraselmis chuii* Microalgae Pyrolysis in the Presence of *Titanium dioxide*. *Key Eng. Mater.* **2020**, 156–163.
31. Coats, A.W.; Redfern, J.P. Kinetic Parameters from Thermogravimetric Data. *Nat. Cell Biol.* **1964**, 68–69.
32. Freeman, E.S.; Carroll, B. The Application of Thermoanalytical Techniques to Reaction Kinetics: The hermogravimetric Evaluation of the Kinetics of the Decomposition of Calcium Oxalate Monohydrate. *J. Phys. Chem.* **1958**, 394–397.
33. Doyle, C.D. Kinetic analysis of thermogravimetric data. *J. Appl. Polym. Sci.* **1961**, 285–292.
34. Dollimore, D. The application of thermal analysis in studying the thermal decomposition of solids. *Thermochim. Acta* **1992**, *347*–23.
35. Ebrahimi-Kahrizsangi, R.; Abbasi, M. Evaluation of reliability of Coats-Redfern method for kinetic analysis of non-isothermal TGA. *Trans. Nonferr. Met. Soc. China* **2008**, 217–221.
36. Málek, J.; Criado, J.M. Empirical kinetic models in thermal analysis. *Thermochim. Acta* **1992**, 25–30.
37. Dollimore, D.; Evans, T.; Lee, Y.; Wilburn, F. Correlation between the shape of a TG/DTG curve and the form of the kinetic mechanism which is applying. *Thermochim. Acta* **1992**, 249–257.

Chapter 9

Conclusions and Recommendations

The main objective of this research has been the characterization of MSWI BA/FA chemical and mineralogical composition and its relationship with the leachable pollutants, and to propose effective treatments and recycling methods. The main conclusions and recommendations for future research related to the thesis sections are as follows:

9.1 Bottom ash

The work on BA mainly focused on assessing the efficacy of a novel treatment involving steam ("steam washing"). The BA characterization in terms of composition and pollutants release as a function of particle size, previously performed by the group, allowed the definition of three main subclasses ($s > 4.75$ mm, $4.75 > s > 1$ mm, $s < 1$ mm), for which different combinations of treatments were tested. The coarser BA are composed by mostly inert material (such as ceramics, aggregates, etc..) and do not require strong treatments to meet the law limits for direct reuse building materials technologies according to Italian law, while the finer fractions are more prone to dangerous leaching and are more difficult to stabilize completely. The steam washing was developed in order to exploit one of the products of the waste incineration, i.e., the steam, coming from the circuit dedicated to the production of electricity used in urban district heating; this energy resource is always available in all Waste-to-Energy plants equipped with a cogeneration system and may be used to treat the ash directly at the plant, by combining the relatively high temperature with the solvent power of water. The application of this treatment at laboratory scale was tested for the coarse BA fractions. Its efficacy in reducing the leaching of the BA main pollutants (chloride and Cu) with short time of exposure (240 s) was confirmed for $s > 4.75$ mm, and an intermediate class ($4.75 > s \geq 2$ mm). Overall, 60 wt% of BA was recovered for reuse directly with steam washing, however the resulting BA effective application in cement/concrete and its impact on the mechanical and hydration properties still needs to be investigated. Moreover, a markedly lower amount of wastewater was produced, when compared with the one obtained during a common water washing treatment with L/S around 5-10, in the order of 95-98 vol%.

Macroscopical observations allowed to describe the process as a combination of mild dissolution and removal of the dust on the BA grains. An effort to elucidate the steam washing mechanism at the microscale was made by Cu K-edge XAS, which provided a deep insight into the speciation and behavior of the BA most abundant PTE. In the pristine BA, Cu is present as mainly CuO microparticles, together with secondary contributions from Cu_2O, malachite and Cu_2S. After the treatment, the CuO component markedly reduces, suggesting that these particles are removed during the steam exposure. However, the translation from the microscopic to the macroscopic behavior of BA, characterized by a high heterogeneity, is not always straightforward, and further research should be done to correlate XAS data with leaching tests, for example by employing sequential extraction methods and geochemical modelling.

In the case of BA with $2 > s \geq 1$ mm, steam washing was effective in decreasing chlorides and sulfates below the Italian limit, but not Cu. On the other hand, accelerated carbonation of 60 min managed to curb all the heavy metals concentrations below the legal thresholds. In this case, a combined approach could be tested, by mixing the two fluxes (i.e., steam and CO_2) and inducing the two processes at the same time. XRPD, TGA coupled with FTIR, and SSNMR analyses show that carbonation mainly takes place in terms of formation of carbonate compounds, which are represented by calcite (major phase) with a low degree of crystallinity.

The accelerated carbonation was employed for the finer fraction, $s < 1$ mm, as flocculation hindered the application of steam washing. Chlorides and sulfates yet remained above the legal threshold. In order to improve this limitation, the introduction of deflocculants could be explored.

9.2 Fly ash

The work on FA started by thoroughly characterizing the material as a function of particle size, in a similar manner to BA. A more in-depth analysis of the heavy metals behaviors was performed, as they represent a major concern when dealing with FA, which is considered a hazardous waste. Among the analyzed heavy metals, Zn and Pb are the most abundant in any grain size class, followed by Cu, Cr, Cd and Ni, with concentration that tends to increase with a decrease of the grain size. The phase composition is constituted of salt (halite, sylvite, anhydrite and syngenite), followed by calcite, quartz and gehlenite, while 50% wt is composed of amorphous fractions. The combination of mineralogy, sequential extractions and geochemical modelling allowed to highlight how the leaching of dangerous heavy metals is dependent more on their speciation rather than simply on the total content. Indeed, heavy metal leaching is strongly correlated to speciation distribution, and in particular to the fraction (F1) associated with salt, carbonate and weak surface sorption. Leaching from speciation due to surface complexation on Al/Fe (hydr)oxide becomes relevant at acidic regime. Particle size and heavy metal content, in turn, moderately correlate with leaching. The F1-speciation as a function of particle size does not exhibit a definite trend shared by all heavy metals under investigation, therefore a comparatively modest efficiency in managing FA is expected from grain size separation strategies, with respect to BA. Still, kinetics (long-term leaching) should also be considered to fully translate in real scale the modelled and experimental results obtained, which assume that the thermodynamic equilibrium is reached. A better approximation could be obtained by performing column (dynamic) leaching tests. Moreover, further investigations should be done in order to take into account the effect of FA organic components on the leaching of contaminants (especially Cu).

The treatments were then applied on FA as a whole, by comparing the conventional batch water washing with a multiple step water washing (FH-WW). The L/S ratio was a crucial parameter, along with the number of washing cycles, for removing halite and sylvite, whereas quartz, calcite, anhydrite, and the amorphous phase remained in the solid residue. The FH-WW delivered a dry product with limited contaminant leaching with respect to that from the conventional washing at L/S = 50 for 24 h, thus providing a comparatively relevant wastewater (L/S = 5 versus 50) and time (2.5 versus 24 h) reduction. A sequential extraction method and dissolution kinetics modelling suggested that the treatment takes place through a two-step mechanism, where after a fast dissolution of the soluble phases fraction present on the FA particle surface, a slower diffusion process occurs. Dissolution kinetics was the key parameters governing FH-WW, which significantly differs from the conventional washing that takes place at quasi-equilibrium conditions. Altogether, multi-step washing with L/S = 5 was effective in reducing pollutants under the legal limits for non-hazardous waste disposal, while the legal limits for non-reactive or reusable material couldn't be completely reached, owing to the excess release of sulfate and some heavy metals (Cr, Ni). By considering the heavy metals leaching as a function of pH, an improvement can be expected if the treatment is carried out by employing a more acidic water. Moreover, the method was assessed by employing ultrapure water for each step, however much work is still necessary to implement a regeneration system to reuse the same water again, for example by employing a sorbent material like biochar.

The treated FA were then tested by introducing it into two different phosphate-based materials, phosphate based geopolymer and magnesium phosphate cement. This choice was induced by the good compatibility between phosphate and heavy metals, since the related salts are characterized by a very low K_{sp}. In addition, these materials are limited by the high costs of the traditional reagents, and thus can benefit

by their substitution with FA. When washed FA substituted metakaolin in PBG, a progressive decrease of the mechanical properties was observed (up to 75%). A combined approach involving XRPD, SEM-EDS, SSNMR and IR was adopted to describe the mineralogical changes and the structural modifications of the geopolymer networks, proving that FA displays a different reactivity compared with metakaolin, behaving preferentially as a source of alkali that compete with the aluminosilicate MK fraction by precipitating crystalline and amorphous phosphates. At 10 wt% of metakaolin substitution with fly ash, the extent and reticulation of the amorphous geopolymer matrix was preserved, and the mechanical properties were retained. At higher waste content (30–50% wt), the fast kinetics of the acid-base reactions involving the fly ash reactive phases prevail over the metakaolin dealumination, and the nature of the material shifts to an alkali-phosphate cement/phosphate-geopolymer composite. This behavior, together with the development of porosity and presence of low-strength phases in the ash, led to a decline in the mechanical performance with increasing amount of substitution. To increase the degree of FA substitution, possible additives could be tested, for example the introduction of soluble Al (i.e., using Al-phosphate in the reactant solution) to compensate for the lower amount of Al present in the FA, with respect to MK. Regardless, the stability of the material with respect to pollutants leaching should be thoroughly investigated before proposing PBG as a valid recycle opportunity.

The study of FA introduction into MKPC was more focused on assessing the waste reactivity in the system, since the reaction conditions are much less harsh than in PBG, by employing both an “inert” formulation, where FA replaces both magnesia and KDP (i.e., acting as an aggregate), and a “reactive” formulation, thus replacing magnesia only (i.e., acting as a binder component). An extensive spectroscopic analysis, in terms of SSNMR and XAS Zn K-edge demonstrated that, in both situations, dissolution/precipitation reactions involving some fly ash components occur. A fraction of Zn, the most abundant heavy metal in the waste, becomes bound to phosphate, together with Al, while the dissolution of sulphates determined the precipitation of K_2SO_4. A model sample obtained through a suspension of FA in a KDP saturated solution confirmed these results, proving the mainly amorphous character of the reaction products through an XRPD and ^{31}P SSNMR investigation. In terms of the main MKP reaction pathway, isocalorimetry, XRPD and SEM suggest that MSWI-FA determined an increase in the amorphous/crystalline MKP ratio, although the exact mechanism has not been identified. The mechanical properties markedly increased when FA was considered reactive (up to 50%), together with an efficient reduction of heavy metals leaching, thus proving that MKPC can be a promising matrix for the MSWI-FA incorporation. However, a more detailed study involving more formulations should be conducted to isolate the contribution of FA with respect to other parameters (i.e., amount of water and KDP), which have a major impact on the cement characteristics and properties.

Overall, the two employed approaches suggest that it is unlikely to find a single material able to withstand a large amount of treated FA, and it is more reasonable to consider different destinations as potential recycle opportunities, each accommodating a fraction of the residue. This in keeping with the still not negligible pollutants content of washed FA, together with a significant less volume with respect to BA.

9.3 Carbon dioxide

The work on CO_2 involved the investigation of the thermal stability of weddellite crystals resulting from a novel green method for CO_2 capture and sequestration in stable calcium oxalate by ascorbic acid reducing action. This study was prompted by the necessity to evaluate the dehydration, decarbonation, and the possible production of unwanted volatile species during heating, to forecast the reuse of oxalates as solid-state reservoir of pure CO_2 and CaO in a circular economy perspective or, eventually, their disposal. The combination of *in-situ* high-temperature X-ray powder diffraction and thermogravimetric analysis unravelled

an early CO_2 release at low temperature (119–255 °C) together with structural water evolution, which must be taken into account when considering storage conditions. Pure CO_2 was released only above 550 °C, while between 390–550 °C, a two-component mixture of carbon monoxide and dioxide was evolved, requiring oxidation of the former or gas separation to reuse pure gases. The next steps are represented by the scale-up of the ascorbate promoted CO_2 capture in oxalate, which till now has been only tested at lab scale, and investigate its application in the wastewater treatment, as heavy metals precipitation method.